

# UC Riverside

## UC Riverside Electronic Theses and Dissertations

### Title

Quantum Transport in Graphene Heterostructures and Few Layer Graphene

### Permalink

<https://escholarship.org/uc/item/7xt5n0bt>

### Author

Wu, Yong

### Publication Date

2016

Peer reviewed|Thesis/dissertation

UNIVERSITY OF CALIFORNIA  
RIVERSIDE

Quantum Transport in Graphene Heterostructures and Few Layer Graphene

A Dissertation submitted in partial satisfaction  
of the requirements for the degree of

Doctor of Philosophy

in

Physics

by

Yong Wu

March 2016

Dissertation Committee:

Dr. Marc Bockrath, Chairperson

Dr. Shan-Wen Tsai

Dr. Nathaniel Gabor

Copyright by  
Yong Wu  
2016

The Dissertation of Yong Wu is approved:

---

---

---

Committee Chairperson

University of California, Riverside

## Acknowledgments

First and foremost, my sincerest gratitude goes to my advisor Professor Marc Bockrath, a kind and patient mentor. During the past six years, I not only learned valuable skills for doing research but also how to be a physicist from you. Marc inspired me a lot in physics. You were always available to discuss physics and gave many enlightening instructions. You have walked me through an amazing journey of my Ph.D. career, from a foreign student, to a researcher. I really feel grateful and fortunate to be your student.

I would also like to thank the members of my defense and candidacy examining committees: Professor Shan-Wen Tsai, Professor Nathaniel Gabor, Professor Jing Shi, Professor Jory Yarmoff and Professor Alexander Balandin. I want to give my special thanks to Professor Jeanie Lau and Professor William Goddard for the wonderful collaboration.

I owe also a great debt of gratitude to my co-workers Bin Cheng, Si-ping Han and Cheng Pan. I thank Peng Wang, Tengfei Miao and Bin Cheng for teaching me a lot of research skills as senior students. I especially thank Bin, Tengfei and Cheng Pan for many discussions when we kept inspiring each other. A gratitude also goes to our lab mates: Yi Wu, Juan Aguilera, Oleg Martynov, Adrian Nosek, Sean Nelson, Nan Zhang, Rui Lv and the former group members: Brian Standley, Sinchul Yeom, Anthony Mendez and Honest Makamba. Without the help from these people, this thesis would be much shorter.

Over the last five years my friends in Riverside have made life colorful even in the darkest periods. I would like to thank Jun Xu, Zilong Jiang, Bin Cheng, Cheng Pan, Peng Wang, Dong Gui, Fengling Wang, Xu Xu and many other friends. Especially gratitude goes to Tengfei who helped me a lot in my darkest period here. I want to give my special thanks

to Catherine Sun. I also want to thank my uncle and aunt in San Diego. They gave me a warm home-feeling here in US.

Finally, I want to thank my family: my parents, my sister and my brother-in-law for their support, love and encouragement. Since I was a boy, my sister always liked to teach me some math and physics knowledge which leads me to the physics research. My parents give me their endless and unconditional love. My mother always encourages me to do what I want to. My curiosity must be inherited from my father who passed away three years ago. Eventually, that kind of curiosity leads me to science, to here. He is the guider and mentor of my life. His memories live on forever in my heart.

In memory of my father

To my mother

With love and eternal appreciation.

## ABSTRACT OF THE DISSERTATION

Quantum Transport in Graphene Heterostructures and Few Layer Graphene

by

Yong Wu

Doctor of Philosophy, Graduate Program in Physics  
University of California, Riverside, March 2016  
Dr. Marc Bockrath, Chairperson

This thesis describes low temperature transport experiments designed to study graphene itself and its heterostructures. The external modifications, such as one dimensional periodic potentials, boron nitride (BN) substrate and mechanical strain, will modify the transport properties by changing graphene's band structure. Graphene with different layers (bilayer, trilayer) will also have different physics. At first, we study the graphene under one dimensional periodic potentials. We use DNA linker to assemble the nanotubes as gate to get a one dimensional periodic potentials. The devices with graphene on top of nanotube gate are studied. The transport controlled by the one dimensional periodic potentials are measured and analyzed. The second part of work is about trilayer graphene aligned with BN with a small rotation angle. The periodic lattice of BN modified the graphene by forming the moiré pattern and commensurate state. We studied the effect of electronic interactions between different Dirac points and with magnetic field as well as electric field. Then transport study on the strained bubbles in graphene is reported. We study the pseudo magnetic field formed by the strained graphene. The fourth part of work is about

the hetero-structure of black phosphorus (BP) and graphene. Some interesting anisotropic transport behaviours are introduced from BP to graphene. At the end, an ultra clean bilayer graphene device is reported. In this device, we observe fractional quantum hall effects. The even denominator fractional quantum hall state will be reported first time in an encapsulated bilayer graphene sample.

# Contents

<b>List of Figures</b>	<b>xii</b>
<b>1 Introduction</b>	<b>1</b>
1.1 Introduction . . . . .	1
1.2 Theoretical overview of graphene . . . . .	4
1.2.1 Monolayer Graphene . . . . .	4
1.2.2 Bilayer Graphene . . . . .	8
1.3 Graphene on BN . . . . .	9
<b>2 Device Fabrication Techniques</b>	<b>11</b>
2.1 Introduction . . . . .	11
2.2 Layer Stacking Transfer technique by using Elvacite . . . . .	11
2.3 Layer Stacking Transfer technique by using Elvacite/PVA and Thermal Release Tape . . . . .	16
2.4 The dry transfer method by PDMS . . . . .	19
2.5 The etch process using the ICP (The Inductively Coupled Plasma System) Etch System . . . . .	21
2.6 Device Contacts Fabrication and the Edge Contacts . . . . .	25
2.7 Low Temperature Transport Measurement . . . . .	27
<b>3 Graphene Under One Dimensional Periodic Potentials</b>	<b>32</b>
3.1 Abstract . . . . .	32
3.2 Introduction . . . . .	33
3.3 Device Fabrication . . . . .	39
3.4 Estimation of Periodic Potentials . . . . .	48
3.5 Electron Beam Collimation . . . . .	55
3.6 Quantum Transport Data . . . . .	62
3.7 Conclusion . . . . .	66
<b>4 Trilayer Graphene</b>	<b>69</b>
4.1 Abstract . . . . .	69
4.2 Introduction . . . . .	70

4.3	Trilayer Graphene BN Superlattice - Additional Dirac Points . . . . .	77
4.4	Two Gates Pattern at Different Magnetic Field . . . . .	82
4.4.1	Dual Gate Sweep Pattern at $B = 9$ T . . . . .	82
4.4.2	Dual Gate sweeps Pattern at $B = 7$ T . . . . .	91
4.4.3	Dual Gate Sweep Pattern at $B = 5$ T . . . . .	95
4.5	The Non-linear Massless Landau levels under Electrical Field at Low Magnetic Field . . . . .	96
4.5.1	The Evolution of Massless Landau levels with Magnetic Field . . . . .	96
4.5.2	The Non-linear Massless Landau levels under Electric Field at Low Magnetic Field . . . . .	96
4.6	Gaps of the Different Landau Levels . . . . .	102
4.7	Landau Fan of the Superlattice - The Hofstadter Butterfly . . . . .	103
4.7.1	The Hofstadter Butterfly without Electric Field . . . . .	104
4.7.2	The Hofstadter Butterfly with Finite Electric Field . . . . .	109
4.8	The Commensurate State of Bilayer, Trilayer Graphene Aligned with BN . . . . .	115
4.9	Conclusion . . . . .	118
<b>5</b>	<b>Quantum Transports In Strained Graphene</b>	<b>120</b>
5.1	Abstract . . . . .	120
5.2	Introduction . . . . .	120
5.3	The Graphene Bubbles Formed During Transfer Process . . . . .	122
5.4	Line Strain Defect Device Fabrication . . . . .	123
5.5	The Coulomb Blockade Cross the Line Strain Defect . . . . .	126
5.6	Transport with the line strain defect grounded . . . . .	134
5.7	One Dimensional Conducting Channel . . . . .	138
5.8	Temperature Dependence . . . . .	139
5.9	Conductance Changing with the Magnetic Field . . . . .	147
5.10	The Triangle Bubble Strain Defect and Other Bubbles . . . . .	151
5.11	Two parallel graphene conducting device divided by the line strain . . . . .	156
5.12	Conclusion . . . . .	157
<b>6</b>	<b>Transport in Graphene Black Phosphorus Heterostructure</b>	<b>159</b>
6.1	abstract . . . . .	159
6.2	introduction . . . . .	160
6.3	Device Fabrication and Structure . . . . .	162
6.4	The Anisotropic Transport Properties . . . . .	165
6.5	The Magneto-transport Properties . . . . .	166
6.6	Dirac Point Shifting with Magnetic Field . . . . .	171
6.7	Conclusion . . . . .	174
<b>7</b>	<b>Fractional Quantum Hall Effects In Bilayer Graphene</b>	<b>177</b>
7.1	abstract . . . . .	177
7.2	Introduction . . . . .	178
7.3	Integer Quantum Hall Effect . . . . .	179
7.4	Fractional Quantum Hall Effect . . . . .	188

7.5	FQHE by plotting $R_{xx}$ versus Filling Factor and Magnetic Field . . . . .	194
7.6	Conclusion . . . . .	203
<b>8</b>	<b>Conclusions</b>	<b>207</b>
	<b>Bibliography</b>	<b>208</b>

# List of Figures

1.1	Structure of mono-, bi-, tri-layer graphene . . . . .	4
1.2	The lattice and Brillouin zone of graphene . . . . .	5
1.3	The band structure of graphene . . . . .	7
1.4	The tight binding parameters of bilayer graphene . . . . .	8
1.5	Graphene on top of BN . . . . .	9
2.1	The transfer stage . . . . .	13
2.2	Dry transfer using elvacite . . . . .	14
2.3	The steps of transfer process . . . . .	15
2.4	The transfer process by using PVA and Elvacite . . . . .	17
2.5	The picture of sample after develop in the water . . . . .	18
2.6	The PDMS . . . . .	19
2.7	The transfer process of PDMS . . . . .	20
2.8	The sample making process . . . . .	23
2.9	The etching process . . . . .	24
2.10	Edge contacts fabrication . . . . .	25
2.11	Our devices edge contacts fabrication . . . . .	26
2.12	The DC measurement setup . . . . .	29
2.13	The AC measurement setup . . . . .	30
2.14	The schematic of refrigerator . . . . .	31
3.1	Electrons propagate without (a) and with (b) periodic potentials. . . . .	33
3.2	Graphene schematic and Dirac cone energy band structure with periodic potentials . . . . .	35
3.3	The collimation of electrons . . . . .	37
3.4	Additional Dirac points under periodic potentials . . . . .	38
3.5	Hall conductivity vs. carrier density for graphene under 1D periodic potentials	39
3.6	Using DNA linkers to make parallel SWNTs . . . . .	41
3.7	The table of different DNA linker sequence . . . . .	42
3.8	The process of making parallel SWNTs on SiO <sub>2</sub> wafer . . . . .	45
3.9	The SEM picture of parallel SWNTs . . . . .	46
3.10	The schematic of device fabrication process . . . . .	49

3.11	Side view and top view of device fabrication process . . . . .	50
3.12	SEM pictures of devices . . . . .	51
3.13	Contacts on devices . . . . .	52
3.14	The schematic of sample with two gates . . . . .	53
3.15	The simulation of the periodic potential controlled by two gates . . . . .	55
3.16	The simulation of the periodic potential controlled by two gates with different parameters . . . . .	56
3.17	The simulation of periodic potential controlled by two gates with another different parameters . . . . .	57
3.18	The schematic diagram of collimation . . . . .	58
3.19	The data of collimation 1 . . . . .	59
3.20	The data of collimation 2 . . . . .	60
3.21	The analysis of collimation data . . . . .	61
3.22	Color plot of data with magnetic field . . . . .	61
3.23	Data under magnetic fields . . . . .	62
3.24	The dual gate sweep data and Landau fan . . . . .	64
3.25	The Landau fan diagram of tube gate versus $B$ . . . . .	65
3.26	Dual gates data with extra Dirac point features . . . . .	66
3.27	Line traces from the dual gate sweep data . . . . .	67
3.28	The Landau fan of top gate voltage versus $B$ with different tube gate voltage . . . . .	68
4.1	Two landau fan diagrams form a "butterfly" pattern . . . . .	70
4.2	The morié pattern . . . . .	71
4.3	The Hofstadter's butterfly . . . . .	74
4.4	The Wannier diagram . . . . .	75
4.5	The line trace of $R_{xx}$ versus carrier density $n$ . . . . .	78
4.6	Color plot of longitudinal resistance versus two gates . . . . .	80
4.7	The color plot of $\log R_{xx}$ . . . . .	81
4.8	The line traces along different Dirac points . . . . .	83
4.9	Color plot of $\log R_{xx}$ . . . . .	84
4.10	Color plot of $\Delta \log R_{xx}$ . . . . .	85
4.11	Color plot of $\Delta \log R_{xx}$ at small area . . . . .	88
4.12	The transitions and the corresponding schematic diagram with different filling states . . . . .	90
4.13	Two gates versus the $\Delta \log R_{xx}$ at $B = 8$ T (a) and $B = 7$ T (b) separately. . . . .	91
4.14	Filling factor and $D$ versus the $\log R_{xx}$ at $B = 7$ T . . . . .	92
4.15	Filling factor and $D$ versus the $\log R_{xx}$ at $B = 5$ T . . . . .	94
4.16	Filling factor and $D$ versus the $\log R_{xx}$ at $B = 5$ T . . . . .	97
4.17	Filling factor and $D$ versus the $\Delta \log R_{xx}$ at $B = 3$ T . . . . .	99
4.18	Filling factor and $D$ versus the $\Delta \log R_{xx}$ at $B = 2$ T . . . . .	101
4.19	Filling factor and $D$ versus the $\Delta \log R_{xx}$ at $B = 1.5$ T . . . . .	101
4.20	$R_{xx}$ versus the carrier density $n$ at different temperature . . . . .	102
4.21	Color plot of $\Delta \log R_{xx}$ versus the filling factor and electric displacement field . . . . .	103
4.22	The Hofstadter butterfly of $\log R_{xx}$ versus the top gate (ground the back gate) . . . . .	104
4.23	The Hofstadter butterfly of $\Delta \log R_{xx}$ . . . . .	105

4.24	The part of the Hofstadter butterfly of $\Delta \log R_{xx}$ . . . . .	107
4.25	The second Dirac point Landau levels . . . . .	108
4.26	The Hofstadter butterfly Landau fan pattern at finite small electric field $D=0.025$ V/nm . . . . .	109
4.27	The butterfly pattern at $D = 0.25$ V/nm and at $D = -0.25$ V/nm . . . . .	111
4.28	The details of the fan diagram . . . . .	113
4.29	The details of fan diagram . . . . .	114
4.30	The formation of the commensurate state and incommensurate state . . . . .	115
4.31	The dependence of Frenkel-Kontorova potential with rotation angle $\theta$ . . . . .	118
4.32	The table of possibility of commensurate state for different rotation angle in different graphene (mono-, bi-, tri-layer) . . . . .	119
5.1	Valleytronics affected by the pseudo magnetic field. . . . .	121
5.2	The SEM pictures of bubbles . . . . .	122
5.3	The AFM picture of strain defects. . . . .	123
5.4	The size of line defects measured by AFM . . . . .	124
5.5	BN/Graphene/BN sandwich structure on $SiO_2$ substrate . . . . .	125
5.6	The device structure . . . . .	125
5.7	The measurement setup . . . . .	127
5.8	The DC bias voltage vs. the back gate voltage and plot the $dI/dV$ . . . . .	128
5.9	Zoom in figure of $dI/dV$ . . . . .	129
5.10	The line trace of $dI/dV$ VS $V_g$ . . . . .	130
5.11	The line trace of $dI/dV$ vs $V_{sd}$ at $V_g=24.6V$ . . . . .	131
5.12	The $V_{xy}$ signal . . . . .	132
5.13	The schematic diagram of another device . . . . .	133
5.14	The data of current across the line strain . . . . .	134
5.15	SEM picture of device . . . . .	135
5.16	The disappearing of diamonds with grounding the line strain . . . . .	136
5.17	The data taken along the line strain defect of two different devices . . . . .	137
5.18	Figure shows how charges move along the line defect . . . . .	138
5.19	The level spacing at different gate voltage . . . . .	139
5.20	The coulomb peaks changing with temperature . . . . .	141
5.21	Temperature dependence of coulomb peaks at different bias voltage . . . . .	142
5.22	The data after two different thermal cycles . . . . .	143
5.23	Two sets of data of same device after several thermal cycles . . . . .	145
5.24	The schematic of two different modes $V_{xy}$ scattering before and after thermal cycle . . . . .	146
5.25	The differential current cross the line strain with $V_g$ as X and B as Y . . . . .	147
5.26	The $V_{xx}$ along the line strain with $V_g$ as X and B as Y . . . . .	148
5.27	The $V_{xy}$ cross the line strain with $V_g$ as X and B as Y . . . . .	150
5.28	The triangular strain devices and data . . . . .	152
5.29	Cross-section side view of strain defects . . . . .	153
5.30	The side gate data . . . . .	154
5.31	The side gate coulomb diamonds . . . . .	155
5.32	The second kind of triangular strain device . . . . .	156

5.33	The landau fan of parallel graphene . . . . .	158
6.1	Structure of single layer BP . . . . .	161
6.2	The process of making devices . . . . .	163
6.3	Ageing of the BP surface and BP covered with graphene . . . . .	164
6.4	Experiment resistance between different contacts . . . . .	165
6.5	Simulation of anisotropic conductance (a) and resistance (b). . . . .	166
6.6	Color plot of conductance between two contacts . . . . .	167
6.7	Landau fan diagram . . . . .	169
6.8	Analysis of fan diagram . . . . .	170
6.9	Landau fan diagram shows the similar feature like monolayer graphene . . .	172
6.10	Dirac point shifting with magnetic fields . . . . .	173
6.11	Line trace of Dirac shifting with magnetic fields . . . . .	175
6.12	The line trace of Dirac shifting with magnetic fields with linear fitting . . .	176
7.1	Composite Fermions under effective magnetic field $B_{eff}$ and form BCS-like Bosons . . . . .	178
7.2	Schematic figure of the bilayer graphene device and edge contact . . . . .	179
7.3	The $R_{xx}$ vs. top gate voltage - mobility calculated from electron side is around $1,000,000 \text{ cm}^2\text{V}^{-1}\text{s}^{-1}$ . . . . .	180
7.4	The physics of quantum hall effect . . . . .	182
7.5	The landau fan . . . . .	183
7.6	$\log R_{xx}$ vs. $V_{gate}$ at different magnetic field. . . . .	184
7.7	Transverse conductance data . . . . .	186
7.8	The $R_{xx}$ and $\sigma_{xy}$ at $B=8\text{T}$ . There is a plateau with a step of $e^2/h$ at $\sigma_{xy}$ with a concomitant dip at $R_{xx}$ . For filling factor $\nu$ , the concomitant plateaus yields the value $\nu e^2/h$ . . . . .	187
7.9	Two small range Landau fan . . . . .	189
7.10	The $\sigma_{xy}$ vs. Filling Factor at different B . . . . .	191
7.11	The $\sigma_{xy}$ vs. Filling Factor at different B (range 2) . . . . .	192
7.12	The $\sigma_{xy}$ vs. Filling Factor at different B with half filling factor . . . . .	193
7.13	CPs under effective magnetic field $B_{eff}$ . . . . .	195
7.14	The CFs absorb all the magnetic field and give a zero effective field . . . . .	196
7.15	The color plot of $R_{xx}$ with B and Filling Factor . . . . .	197
7.16	The color plot of $R_{xx}$ at high magnetic field with Filling Factor . . . . .	198
7.17	The color plot of $V_{xx}$ versus the filling factor and magnetic field above 6 T .	200
7.18	$G_{xy}$ versus $\nu$ and the color plot of $V_{xx}$ versus the B and $\nu$ . . . . .	201
7.19	The color plot of $\log R_{xx}$ . . . . .	202
7.20	The color plot of $\log R_{xx}$ at the hole side . . . . .	204
7.21	The color plot of $\log R_{xx}$ with a subtracted background and the concomitant $G_{xy}$ versus $\nu$ . . . . .	205

# Chapter 1

## Introduction

### 1.1 Introduction

When I joined our research group in 2010, graphene was already a hot research topic in condensed matter physics. In the past six years, this area is moving forward very fast and getting more and more interesting. I am very excited to have a chance to be part of it.

From an application standpoint, graphene has been proven to have many possibilities, for example, as a switch [60], graphene transistors [57], graphene speakers [58] and many other possible applications.

As a first year graduate student who came from China to US, I really did not realized how widely the application of graphene in the future would be. Actually, I could not understand the most of the papers about graphene at that time. But as a physics student, the main thing that attracted me to this area was its apparent theoretical simplicity. After being a member of our group, the beauty and simplicity of the quantum transport data

really attracts my attention. Usually, the device quality can be determined to be good or not easily by seeing whether the data looks beautiful and clean. All of the simple, uniform behavior comes from the elegant physics in the graphene. Electrons in monolayer graphene can be described by a Dirac Hamiltonian,

$$\hat{H} = \hbar v_F \hat{\sigma} \vec{k} \quad (1.1)$$

the  $\vec{\sigma}$  is the sublattice pseudo spin and  $v_F$  is the Fermi velocity in graphene.

As an introduction, the rest of this chapter will introduce the theoretical overview of graphene (including mono-, bi-, tri-layer graphene). And some very important experimental techniques which dramatically increase the quality of devices.

In Chapter 2, the most general techniques used to prepare samples and make devices will be introduced. The BN substrate [13], transfer techniques and edge contact technique [66] make obtaining very high quality devices possible.

In Chapter 3, we use DNA linker molecules to assemble the nanotubes [22] [47] as gate electrodes to apply one-dimensional periodic potentials. The distance between each nanotube can be controlled precisely by the DNA-linker we use. Theory has predicted the graphene's behavior under periodic potentials [55]. We also measure the transport behavior of this system. The data of our devices shows the anisotropic group velocities (collimation).

Chapter 4 is mainly about trilayer graphene aligned with BN with a small rotation angle. It is a work about the Hofstadter butterfly [24]. Seven Dirac points are observed from the experiments for the first time. The Landau-fan like feature that appear to emanate from extra Dirac points have some similarities and some differences from phenomenon observed

in monolayer [25] [56] [67] or bilayer graphene [14]. The transitions between LLs at high magnetic field and low magnetic field make this system very interesting.

Chapter 5 will introduce transport studies on strained graphene arising from bubbles and folds. Both theory [21] and STM experiments [31] [38] have proven the existence of pseudo-magnetic fields in strained graphene. In our experiments, the transport study across the line strain in the graphene proves it acts like a "quantum dot". The pseudo-magnetic fields due to the line strain may selectively pass electrons of particular valleys, enabling the realization of valleytronics devices. Transport study over other strain bubbles, like triangular bubbles, circular bubbles and polygonal bubbles will also be reported.

In Chapter 6, hetero-structures of black phosphorus (BP) and graphene are studied. From our results, some anisotropic behavior is introduced from the BP to graphene. Magneto-transport studies will also be reported.

Chapter 7 is about the fractional quantum Hall effect (FQHE) in a bilayer graphene system. It is in a high quality device with field effect mobility around  $1 \text{ M cm}^2\text{V}^{-1}\text{s}^{-1}$ . Several FQH states are observed, such as  $\nu = 1/3$ ,  $\nu = 2/5$  and an even denominator FQH state  $\nu = 1/2$ . The  $\nu = 1/2$  state has been reported at a suspended bilayer graphene [30]. But it is first time observed in an encapsulated graphene. An unambiguous plateau at  $\nu = 1/2$  in the transverse resistance with a concomitant dip in longitudinal resistance is shown in our data.

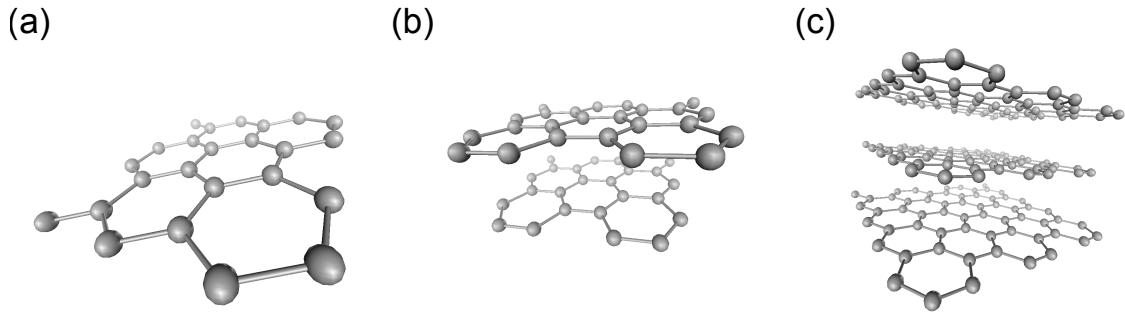


Figure 1.1: The structure of (a) graphene, (b) AB staked bilayer graphene and (c) ABA stacked trilayer graphene.

## 1.2 Theoretical overview of graphene

### 1.2.1 Monolayer Graphene

Graphene is a one atom thick layer of carbon atoms arranged on a honeycomb structure. Its mother material - graphite, a three dimensional lattice of carbon, became widely known after the invention of the pencil in 1564. Graphite is basically layers of graphene stacked together by the van der Waals forces between each layer. But graphene was only isolated by a simple and clever tape exfoliation technique [52] after 440 years after pencil was invented.

The electronic band theory of graphene was developed by P. R. Wallace in 1947 [65]. To understand the band structure of the monolayer graphene, we start from the Bravais lattice. The Bravais lattice of graphene has two unit lattice vectors,

$$\vec{a}_1 = \left( \frac{\sqrt{3}a}{2}, \frac{a}{2} \right)$$

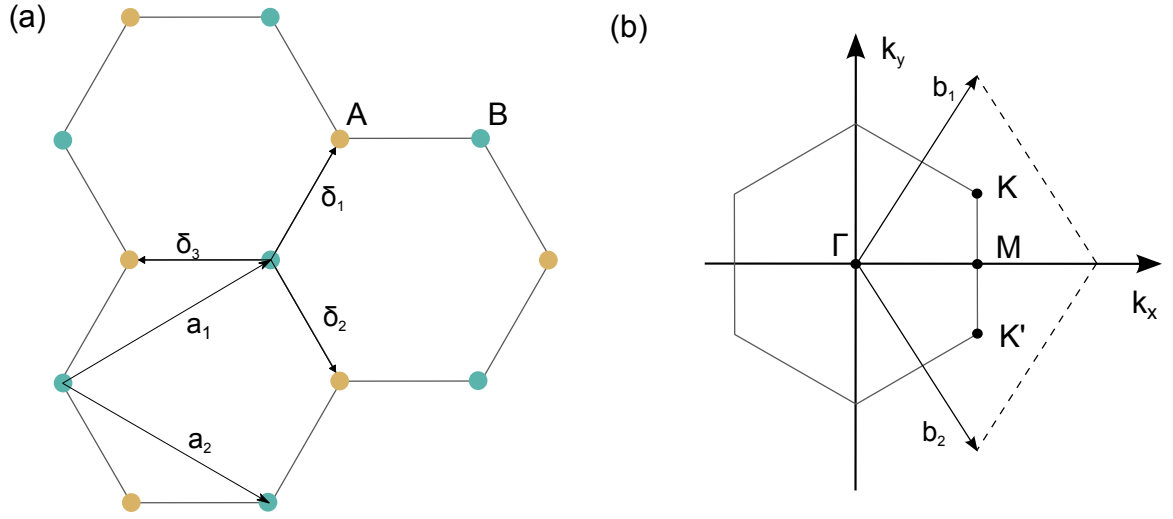


Figure 1.2: The honeycomb lattice (a) and its Brillouin zone (b).

$$\vec{a}_2 = \left( \frac{\sqrt{3}a}{2}, -\frac{a}{2} \right)$$

where  $a = 2.46 \text{ \AA}$ . The reciprocal lattice vectors  $\vec{b}$  can be found in solving

$$\vec{a}_i \cdot \vec{b}_j = 2\pi\delta_{ij},$$

$$\vec{b}_1 = \left( \frac{2\pi}{3a}, \frac{2\sqrt{3}\pi}{3a} \right)$$

$$\vec{b}_2 = \left( \frac{2\pi}{3a}, -\frac{2\sqrt{3}\pi}{3a} \right)$$

Two carbon atoms are inside one-unit cell, which are part of the A and B sublattices. The trigonal planar structure around one atom is due to the  $sp^2$  hybridization between one s orbital and two p orbitals (Figure 1.1). The formation of a  $\sigma$  bond between carbon atoms which are separated by  $1.42 \text{ \AA}$  is also a result of the  $sp^2$  hybridization. The

robustness of the graphene lattice structure depends on the  $\sigma$  band. These bands have a full filled shell (four valence electrons filled with other four electrons from nearest atoms). That is why they have a deep valence band. Although the  $\sigma$  bond contribute the robustness of the graphene, but the electrons are so tightly bound that they don't contribute to the electronic transport. The last p orbital ( $z$  direction), which is perpendicular to the planar structure, can bind covalently with neighbor carbon atoms which leads to a  $\pi$  band. The  $\pi$  band determines the low energy electronic structure of graphene. Due to each p orbital having one electron, the  $\pi$  band is half filled.

The  $\pi$  electrons are still tightly bound, so the electronic structure can be well described by a tight-binding model. Using the nearest-neighbor hopping approximation, the tight binding Hamiltonian is,

$$\hat{H} = \gamma_0 \sum_{\langle i,j \rangle, \sigma} (a_{i,\sigma}^\dagger b_{j,\sigma} + \text{H.C.}) \quad (1.2)$$

where  $\hat{a}^\dagger$  ( $\hat{a}$ ) and  $\hat{b}^\dagger$  ( $\hat{b}$ ) create (annihilate) an electron on sublattice A or B, respectively. The  $\gamma_0 \approx 2.8eV$  is the hopping energy. One can rewrite the Hamiltonian in the basis of the wave function amplitudes on the A and B sublattices,  $(\psi(a), \psi(b))$ . We then have the vectors connecting the nearest neighbors,

$$\vec{\delta}_1 = \frac{a}{2} \left( \frac{1}{\sqrt{3}}, 1 \right)$$

$$\vec{\delta}_2 = \frac{a}{2} \left( \frac{1}{\sqrt{3}}, -1 \right)$$

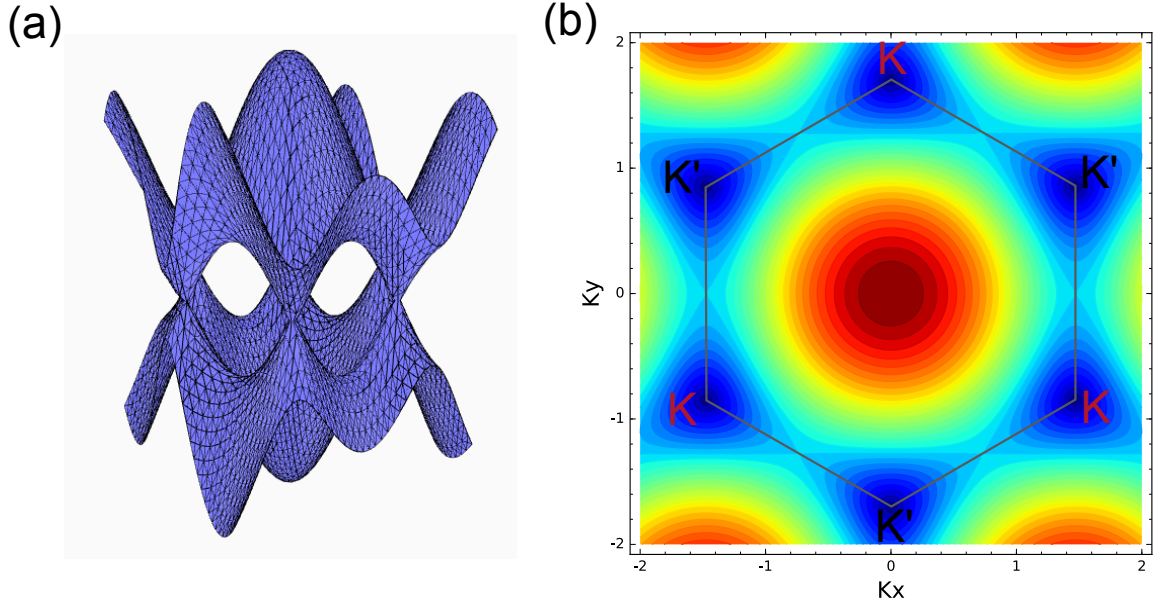


Figure 1.3: (a) Energy band of the  $\pi$ -bands in monolayer graphene. The band structure has a large gap at the  $\Gamma$  point, but is gapless at the Brillouin zone corners (K and K'). (b) The contour density plots of energy band on  $k_x$ - $k_y$  plane. It shows the degeneracy of K and K' points and the BZ boundary.

$$\vec{\delta}_3 = \frac{a}{2} \left( \frac{1}{\sqrt{3}}, 0 \right).$$

Thus, we can get the Hamiltonian,

$$\hat{H} = \gamma_0 \begin{pmatrix} 0 & \sum_j e^{i\vec{k}\cdot\vec{\delta}_j} \\ \sum_j e^{-i\vec{k}\cdot\vec{\delta}_j} & 0 \end{pmatrix} \quad (1.3)$$

with eigenvalues given by

$$\varepsilon_{\pm}(\vec{k}) = \pm \gamma_0 \sqrt{3 + 4\cos\left(\frac{\sqrt{3}ak_x}{2}\right)\cos\left(\frac{ak_y}{2}\right) + 2\cos(ak_y)}. \quad (1.4)$$

Using equation 1.4 the band structure can be plotted in Figure 1.3.

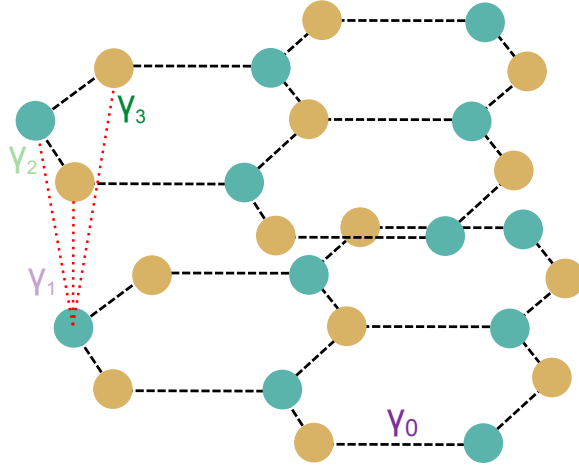


Figure 1.4: The tight binding parameters on bilayer graphene.

The energy at the K and K' points are zero ( $\varepsilon(K) = 0, \varepsilon(K') = 0$ ). At low energy scale, close to the K or K' points ( $\vec{k} = \vec{K} + \vec{q}$ ), with  $|\vec{K}| \gg |\vec{q}|$ , the eigenvalues can be expanded as,

$$E_{\pm}(\vec{q}) \approx v_F \vec{q}. \quad (1.5)$$

Equation 1.5 reveal one of the most interesting aspects of the graphene - its low energy excitations are massless Dirac Fermions.

### 1.2.2 Bilayer Graphene

This kind of tight binding approach can also be used in the stacks of finite numbers of graphene layer. The simplest one is bilayer graphene [48].

The tight binding Hamiltonian can be written as [50]

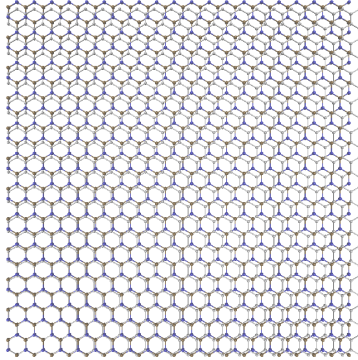


Figure 1.5: The graphene (gray layer) on top of BN.

$$H_{bilayer} = \gamma_0 \sum_{\langle i,j \rangle, m, \sigma} (a_{m,i,\sigma}^\dagger b_{m,j,\sigma} + \text{H.C.}) \quad (1.6)$$

$$- \gamma_1 \sum_{j,\sigma} (a_{1,j,\sigma}^\dagger a_{2,j,\sigma} + \text{H.C.}) \quad (1.7)$$

$$- \gamma_3 \sum_{j,\sigma} (b_{1,j,\sigma}^\dagger b_{2,j,\sigma} + \text{H.C.}) \quad (1.8)$$

$$- \gamma_4 \sum_{j,\sigma} (a_{1,j,\sigma}^\dagger b_{2,j,\sigma} + a_{2,j,\sigma}^\dagger b_{1,j,\sigma} + \text{H.C.}). \quad (1.9)$$

The low energy dispersion can be written as,

$$\varepsilon(p)^2 = (v_F p)^2 + \frac{\gamma_1^2}{2} + \frac{\Delta^2}{4} \pm \sqrt{(v_F p)^2 (\gamma_1^2 + \Delta^2) + \frac{\gamma_1^4}{4}}. \quad (1.10)$$

### 1.3 Graphene on BN

Hexagonal boron nitride (hBN) is also a planar honeycomb lattice, the same as graphene lattice except with about a 1.8% lattice constant mismatch (lattice constant is 0.25 nm).

BN is widely used in graphene samples. One of the most important reason is its flat surface. BN has an atomically smooth surface that is relatively free of dangling bonds and charge traps. Due to the flat surface of BN, the graphene devices on top of BN have higher mobility. The BN is also an insulator. Thus, we can use it as an insulation layer to make local back gate and top gate.

Another advantage of BN substrate is it is a perfect material to modify graphene by adding a two dimensional periodic potentials. They can also form a commensurate lattice state. Finally, when the device is made to a BN/Graphene/BN sandwich structure, it is very stable and can be store for a very long time.

## Chapter 2

# Device Fabrication Techniques

### 2.1 Introduction

In this chapter, general techniques used to prepare samples and make devices will be discussed. Some details may be discussed later in the following chapters for each individual project.

### 2.2 Layer Stacking Transfer technique by using Elvacite

Graphene has been reported to have a much higher mobility when placed on BN substrates[13].

Here we use a slightly different transfer method. Instead of using the PMMA, Elvacite is used as the substrate. Elvacite 2550 is a solid bead methacrylate copolymer resin. It is designed to provide excellent adhesion to metal surfaces and is a resin with good flexibility and medium molecular weight.

At first, we need make the Elvacite solvent. The recipe is 8 grams per 50mL pure methyl isobutyl ketone (MIBK). The solvent is bottled into a glass bottle and heated at hotplate at 80°C to 100°C over night until all the powders are dissolved into the MIBK.

Second, I use a glass slide and attach the transparent 3M tape onto the glass slide. The Elvacite in its solvent is spin coated onto the glass with tape as the substrate. Typically, the spinner speed is 2000rpm and RAM is 500rpm/s. One can repeat the process twice to get thicker Elvacite on top of the glass. If thicker Elvacite is used, sometimes it is helpful to transfer in the next step (push the sample and substrate together more tight). By each spin coating, we put the glass on a 120°C hot plate for about 5 mins.

After spin coating, we mechanically exfoliate graphene onto the Elvacite/tape/glass slide, then use an optical microscope to locate good graphene. Then I cut the tape into small square pieces and make sure the graphene is in the center of this small tape.

In the meantime, BN on the SiO<sub>2</sub> wafer needs to be prepared. We also use optical microscope to find large, flat and thin BN flakes. Usually by experience, BN with light green color under white light will be thin and flat enough. Then we anneal the BN/SiO<sub>2</sub> wafer inside furnace with O<sub>2</sub> at 500°C at a flow rate of 1-2 LPM for 3 to 5 hours (For the following oxygen annealing we use the same flow rate).

Then the graphene on the Elvacite/tape/glass is aligned with boron nitride on the wafer fixed on the transfer stage by the optical microscope (Figure 2.1).

By adjusting the transfer stage, the BN on the SiO<sub>2</sub> wafer approaches the Graphene on the Elvacite. There are two stages, one is the transfer stage and the other one is the microscope stage. So we can not only adjust the position of the BN but also the position

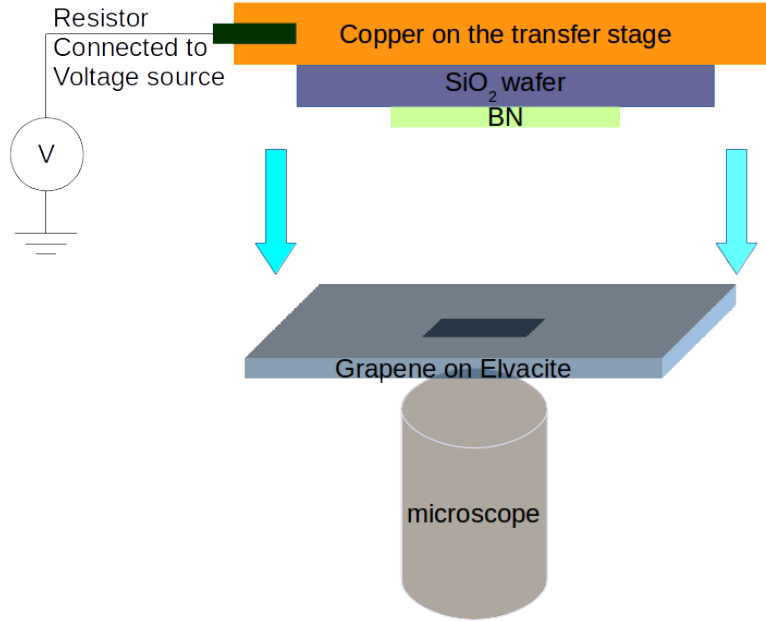


Figure 2.1: Schematic figure of transfer stage used for the layer material transfer.

of the graphene. In this way, we can make a very accurate transfer. The accuracy could be smaller than  $1 \mu\text{m}$ . When the wafer touch onto the Elvacite, we turn on the voltage supply and heat the copper of the transfer stage. The temperature will raise to about  $80^\circ\text{C}$  and heat it for 10 to 15 mins. Then the Elvacite start to melt onto the wafer. In the next step, we put the wafer into the acetone until all Elvacite dissolved.

Then the wafer will be annealed again with  $\text{O}_2$  with flow rate at  $300^\circ\text{C}$  for 4 to 5 hours. Finally, we get a very clean graphene/BN sample(Figure 2.2).

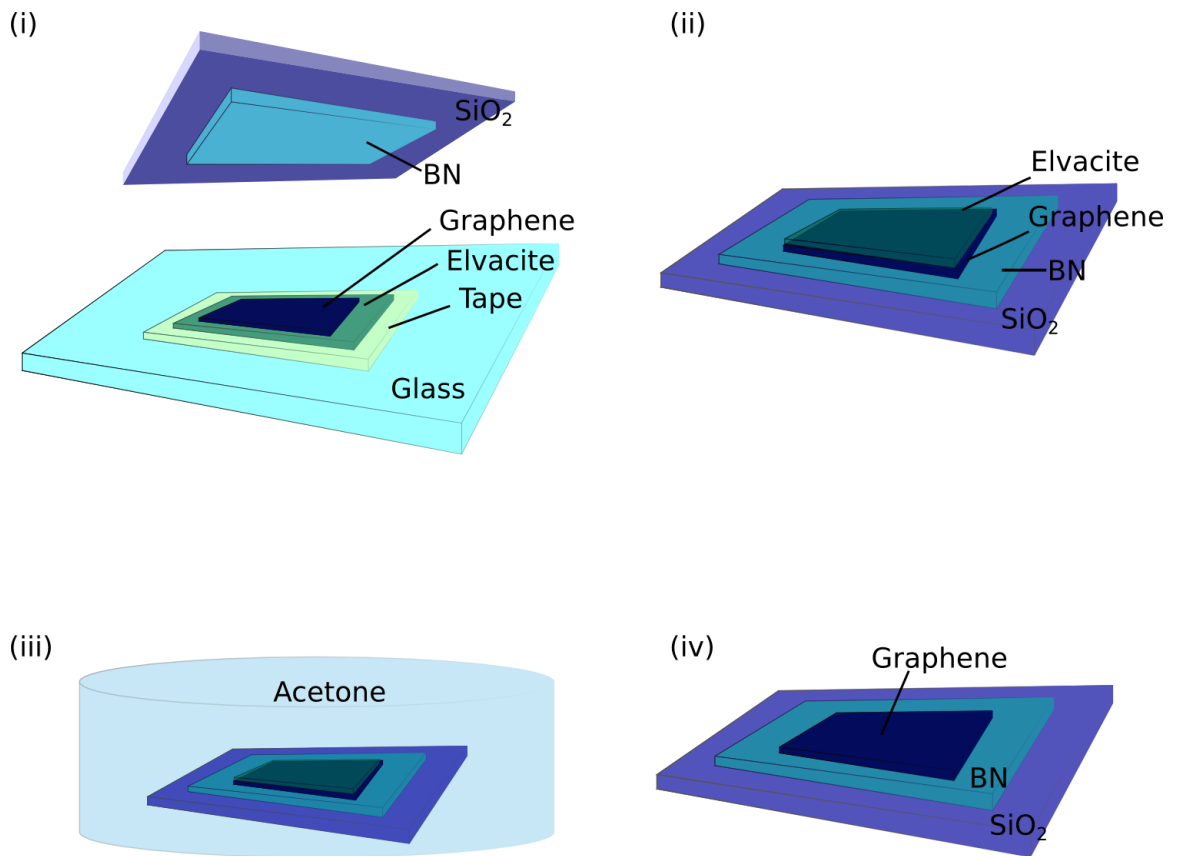


Figure 2.2: Schematic figure of transfer process I used to fabricate the BN-graphene-BN structure by using the Elvacite.

Further, if I want to make BN/Graphene/BN sandwich structure, I just need make one more transfer for the top BN and one more gas anneal after transfer.

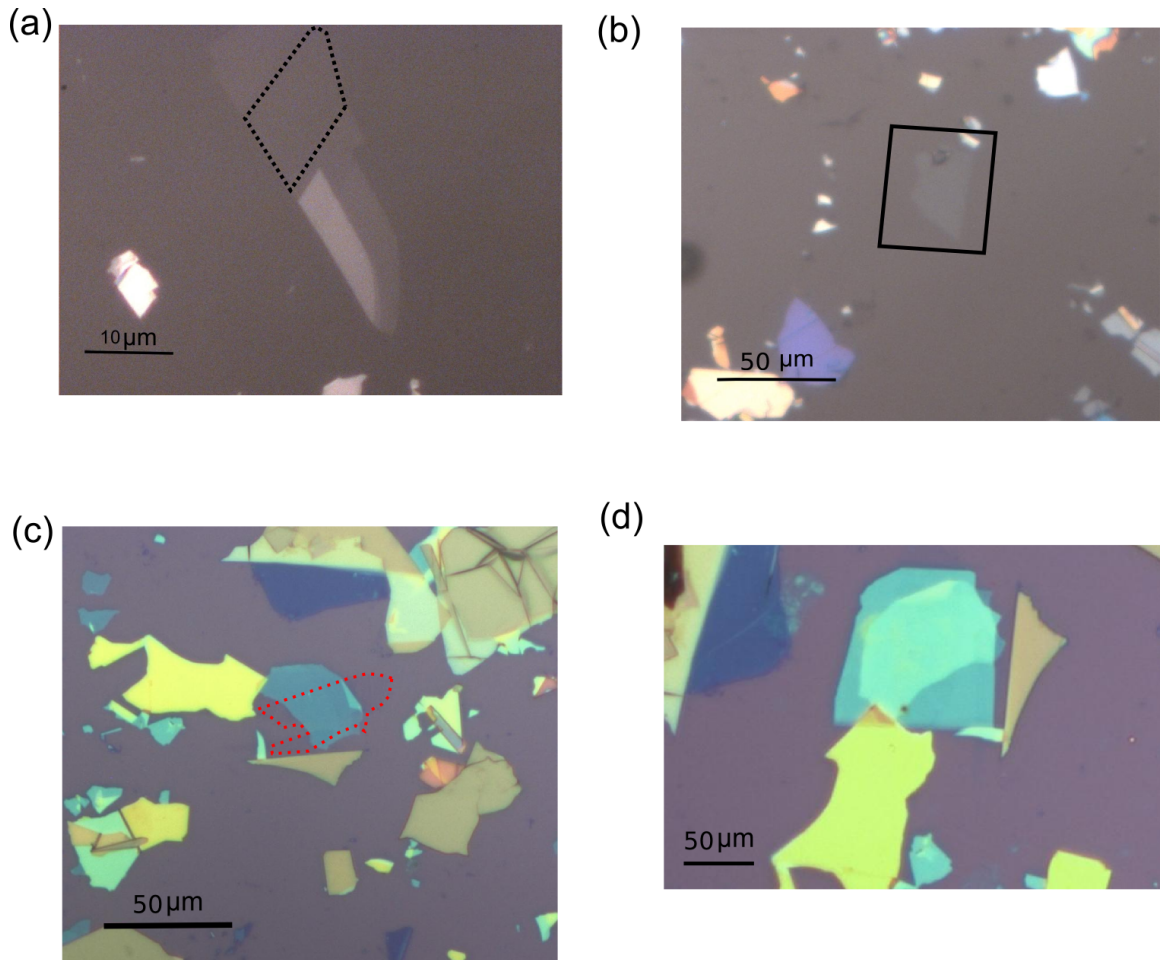


Figure 2.3: (a) Graphene on the Elvacite. Inside the black dot lines, it is a single layer graphene on Elvacite/Tape/Glass. It looks very transparent. (b) What thin BN looks like on the Elvacite/Tape/Glass. (c) The graphene already transfers onto the BN. Inside the red dot line is where the graphene is. (d) The top BN transfer to Graphene/BN structure. It is a complete BN-Graphene-BN sandwich structure.

## 2.3 Layer Stacking Transfer technique by using Elvacite/PVA and Thermal Release Tape

For different purposes, the transfer steps will be a little different. Here I will discuss several different transfer methods for different projects. The main process will be the same as discussed before and details will be different.

Sometimes the force between the target material on the glass and the substrate material on the wafer is very weak. For example, we have some contacts on the substrate material. In this case we can use one more layer water-soluble synthetic polymer PVA (Polyvinyl alcohol) between the tape and the Elvacite. The PVA can be spin coated onto the glass with tape. The spinner speed is 2000rpm and ram is 500rpm/s. I usually spin three layers of PVA. And the glass is baked at 70°C to 80°C for 5mins, between each spin coating process.

In the meantime, we use thermal release tape to attach the wafer to transfer stage. So during heating in the transfer process, the thermal release tape will release from the transfer stage and attach to the glass with the whole wafer. Then we put glass with wafer on its top into water. After overnight 80°C to 90°C baking, the PVA layer will dissolved inside the water. So the wafer with Elvacite layer will float on the water. We pick up this Elvacite layer and put it into acetone for 10 mins. The Elvacite will dissolved inside the acetone. After all these steps, we put the wafer with Graphene/BN structure into furnace and anneal the sample in O<sub>2</sub> for 4 hours. This method is shown in Figure 2.4.

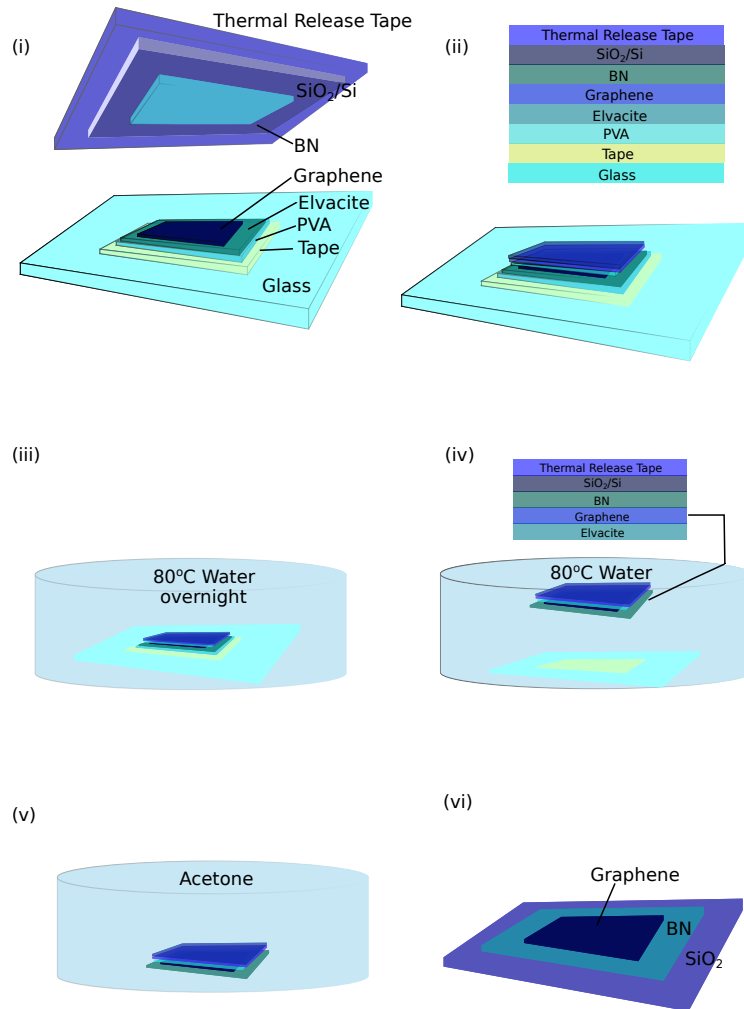


Figure 2.4: Schematic figure of transfer process I used to fabricate the BN-graphene-BN structure by using the PVA. It is very gentle to the device which is the advantage of this technique. This technique can be used to transfer layer material to some substrate already has contacts. In this transfer method, the step of PVA is optional. You can directly use thermal release tape and repeat the transfer step without putting the glass into water.

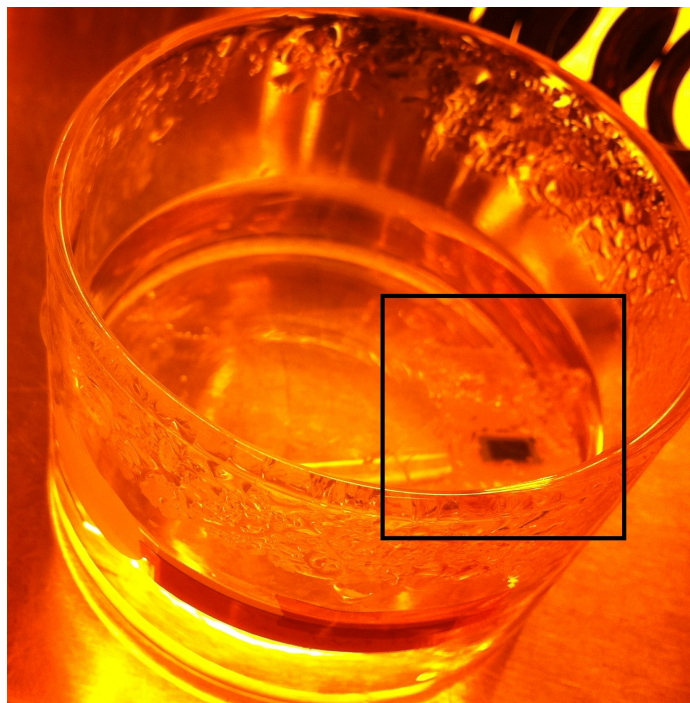


Figure 2.5: The Elvacite layer with wafer floats on the water which is the step 4 from Figure 2.4. The Elvacite layer is inside the black box in this figure.

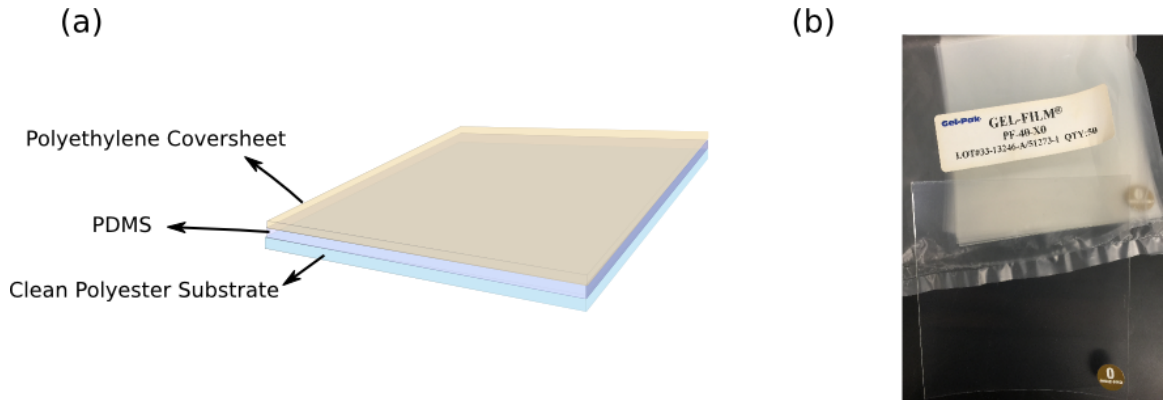


Figure 2.6: (a) The layer chart and (b) real picture of the Gel-Pak PF Film we are using.

## 2.4 The dry transfer method by PDMS

Polydimethylsiloxane (PDMS) belongs to a group of polymeric organosilicon compounds that are commonly referred to as silicones. PDMS is used for graphene dry transfer and has been proven to yield devices with a high mobility [66].

For our experiment, I ordered the Gel-pak PF PDMS film from Gel-Pak company (Figure 2.6).

This technique makes it very easy to pick up and transfer layer material more than one atom thick, like a few layers of BN. If you want to pick up and transfer graphene, you must use BN as substrate and use a layer of PPC [66].

The key of PDMS transfer technique is how fast you peel up the PDMS from wafer after they attached together. If you peel it quick enough, the PDMS will pick up the layer material, like BN, from the wafer. On the other hand, if you peel it very slowly, the layer material on the PDMS can be transferred onto the wafer (Figure 2.7).

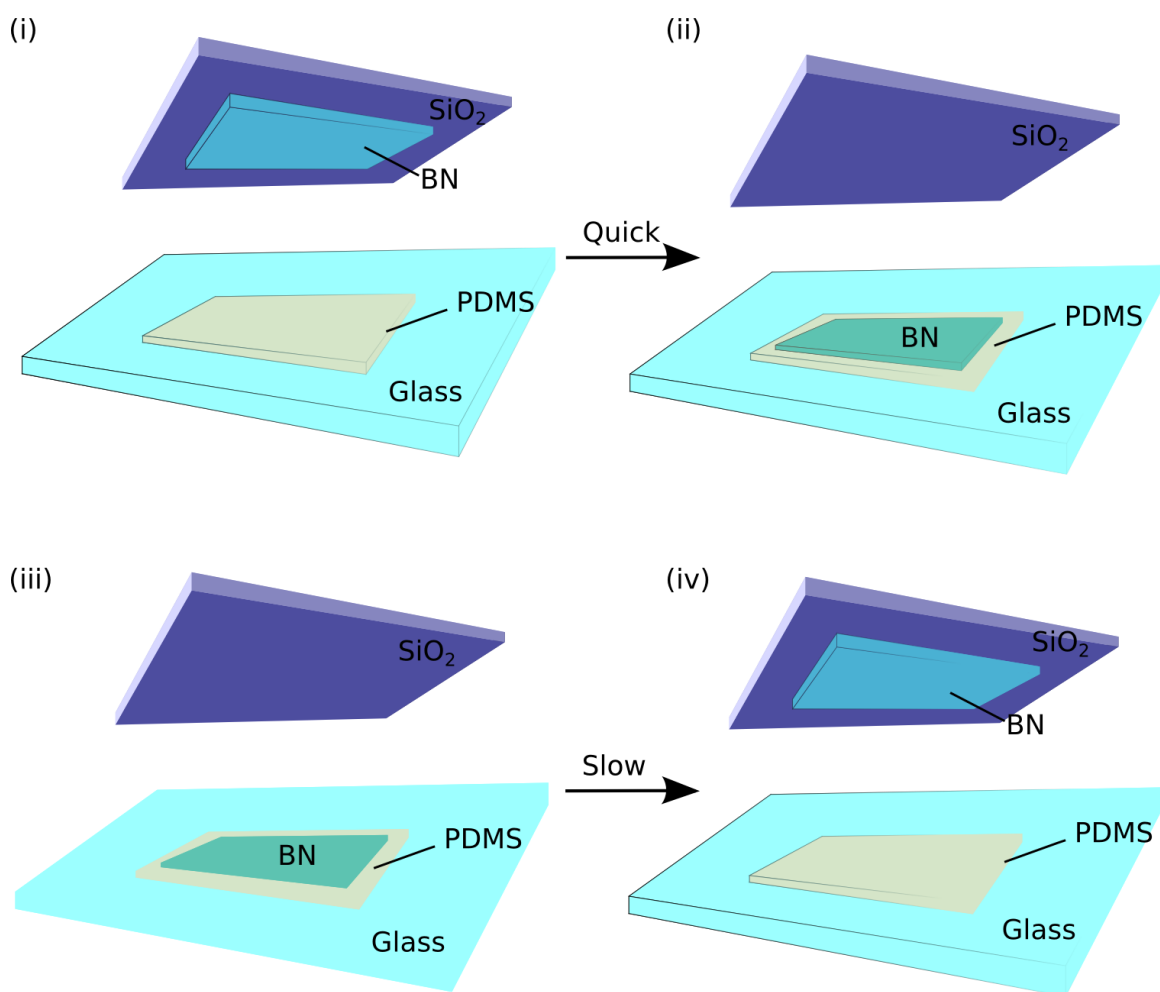


Figure 2.7: (a) to (b) is the PDMS quickly peel off from the wafer. In this way, we can pick up layer materials we want. (c) to (d) is the PDMS slowly peel off from the wafer. In this way, we can transfer the layer materials on the PDMS to wafer.

## 2.5 The etch process using the ICP (The Inductively Coupled Plasma System) Etch System

In this section, the etch process will be introduced. Basically, I only use ICP for the most etching processes.

We can use the ICP to etch both BN, Graphene, black phosphorous and their layer-stacking structures. The recipe I am using is similar for different materials. The gas is  $SF_6$  at a flow rate of 50 sccm. Here is the receipt and steps I used for the ICP etching,

- 1.Set the step time 15s (cancel the "Ignore tolerance").
- 2.Set the gas as  $SF_6$  at rate of 50 sccm.
- 3.Click "start" and let the  $SF_6$  gas flow into chamber for 15s at first (clean any possible residue gas).
- 4.Set pressure 20 mT.
- 5.Click "start". It will run for another 15s to make sure the pressure is stable.
- 6.Set the power: Forward Power 30 W and ICP power 300 W.
- 7.Click "start" for 15s.

If I can see any part of material which has not been etched totally, usually, I will run another 10s.

The ICP not only can etch the material but also can be used to flush the Edge Contact. The Edge Contact fabrication will be introduced later in this chapter. The receipt I use for flushing,

- 1.Set time 10s.
- 2.Set  $O_2$  gas at rate of 50 sccm.

3. Click "start".
4. Set pressure 15 mT.
5. Click "start".
6. Set power Forward 30 W. We only use forward power for flushing process.
7. Click "start" run for 10s.

Before the ICP etching, usually I use Electron Beam Lithography (EBL) to make a pattern on the device. At first, we need spin coat two layers Polymethyl methacrylate (PMMA) to the device. The spin speed is 4000 rpm and the ramp is 1000 rpm/s. Between each spin coating, the device should be baked at 180°C for 10 mins. If you bake it longer, it will help the PMMA become more uniform and flatter. Then I use the EBL to write the pattern. After that, the device needs to be put into the developer. Usually, people use the MIBK/IPA (ratio 3:1) solution. But here I use the Water/IPA (ratio 3:1) which is stored in the freezer at around -20 °C. The Water/IPA solution will develop the pattern at a slow rate which will help to keep the feature clean and sharp. The develop result will be better because we use the Water/IPA solution at low temperature. The develop time is around 8-10 mins for low temperature Water/IPA solution.

After all these steps, we finally can use the ICP to etch the sample to the shape we want (Figure 2.8).

Here are some devices samples etched by this technique (Figure 2.9). When you want to etch the sample to very small piece, the developing time will be very sensitive to the sample.

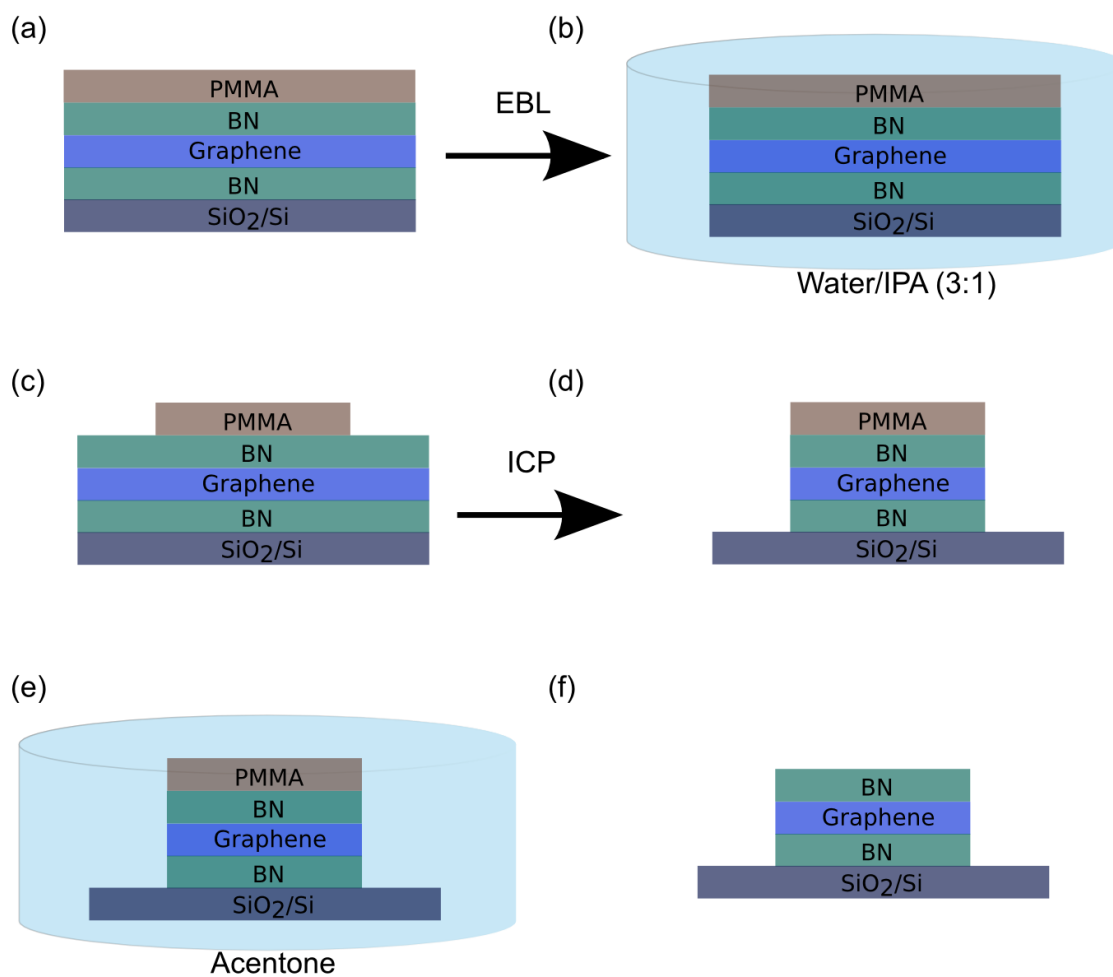


Figure 2.8: The figures step by step by using EBL and ICP to etch sample. (a) The sample with PMMA on top. (b) After EBL put the sample in the Water/IPA developer. (c) The sample after develop. (d) Using ICP to etch the sample. (e) Put the sample into acetone to remove the PMMA. (f) The BN-Graphene-BN sample after etching.

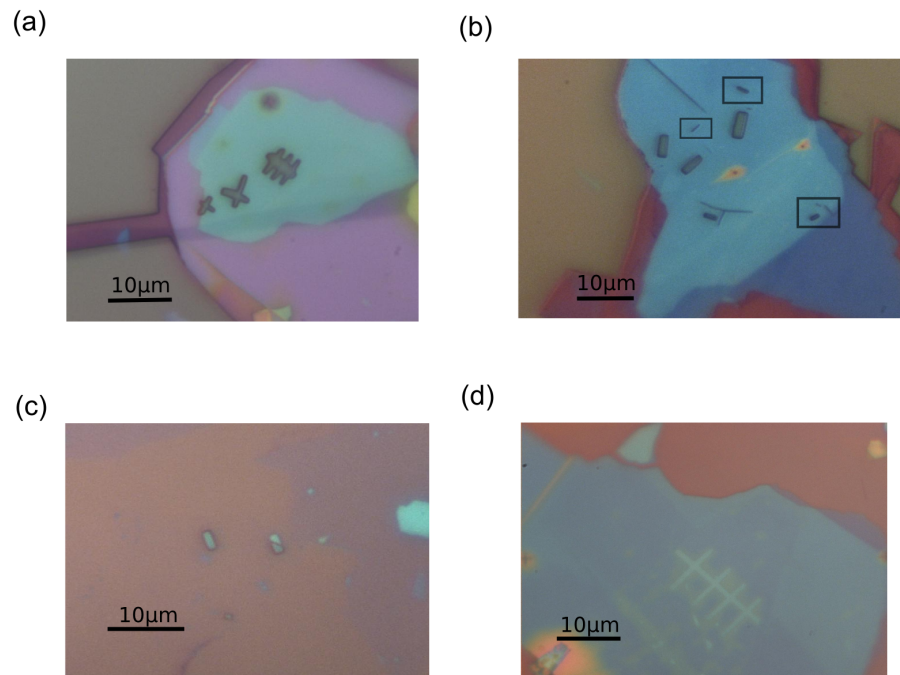


Figure 2.9: (a) The Hall Bar structure of EBL. (b) Some very small features (black box) after EBL. These features need quick develop in Water/IPA (5:1) solutions. (c) BN-Graphene-BN structure after ICP. (d) A top BN covered a hall bar structure which etched by ICP.

For example, when I etch the sample to a  $200\text{nm} \times 1\mu\text{m}$ , I will develop the sample in Water/IPA solution with ratio 5:1 at low temperature for 2 to 3 mins. If you put the sample inside the developer too long, the PMMA mask will disappear.

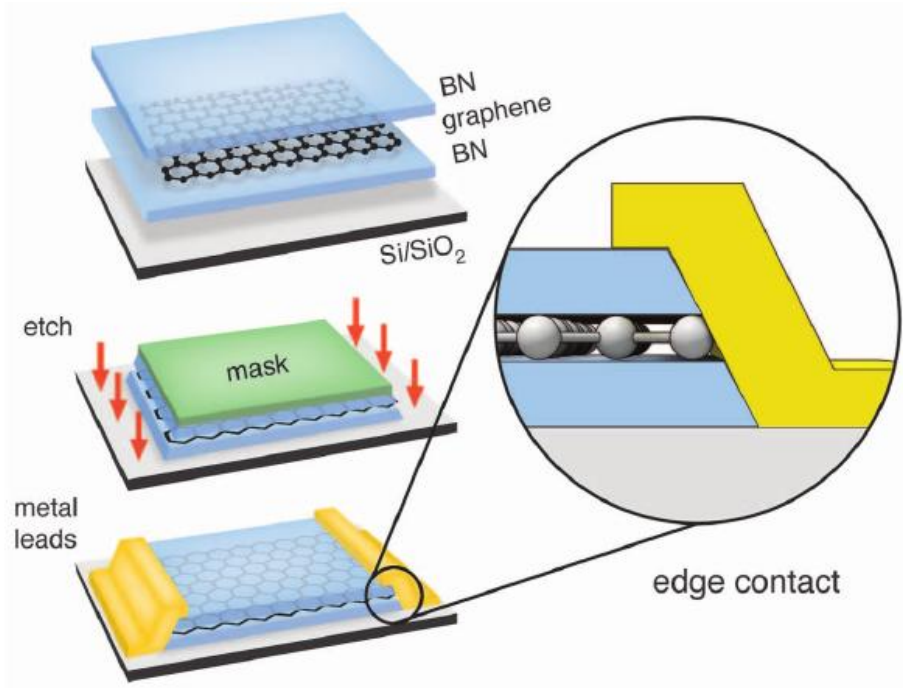


Figure 2.10: Schematic of the edge-contact fabrication process [66].

## 2.6 Device Contacts Fabrication and the Edge Contacts

After using EBL to make the contact pattern, the device will be ready after E-Beam Evaporation. Usually I will use Cr and Au. Cr is 10 nm and thickness of gold will be different from device to device.

The edge contact fabrication method was developed by the Columbia group, which makes only a one-dimensional carbon chain edge contact between metallic electrodes and the graphene [66] (Figure 2.10).

We also use this technique to make our devices (Figure 2.11).

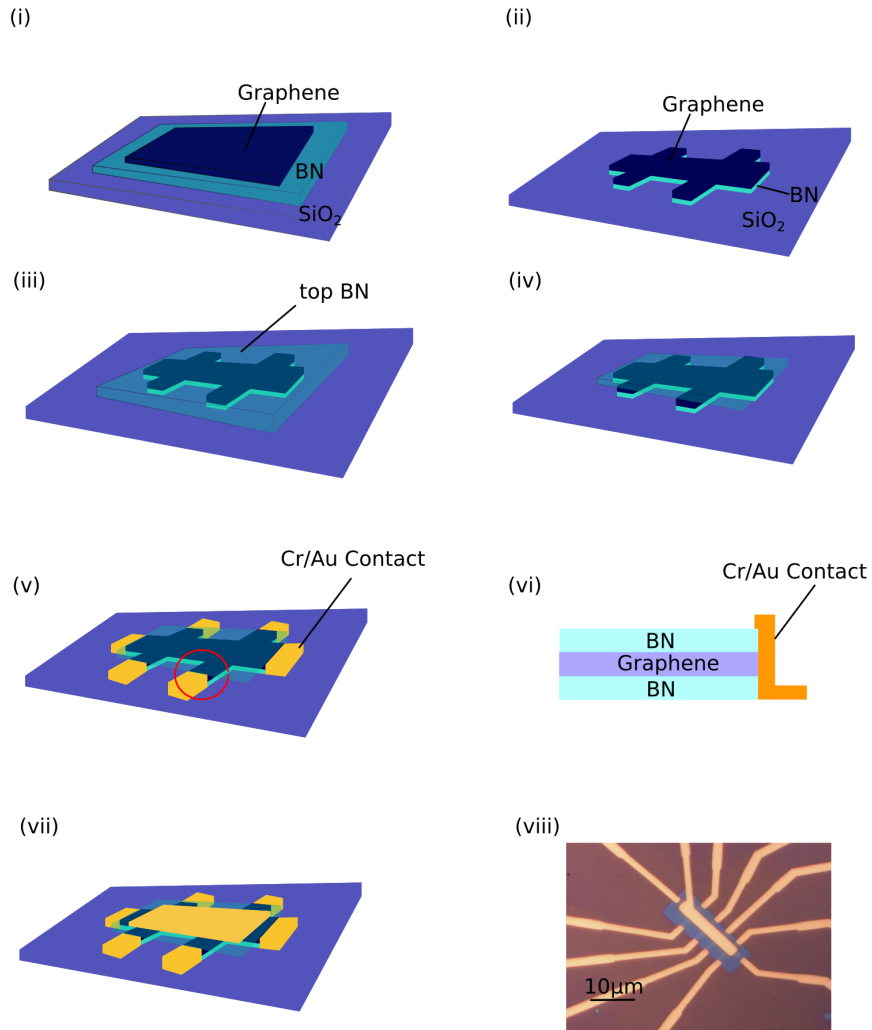


Figure 2.11: Schematic of the edge-contact fabrication of my device. (i) is the graphene on BN on the wafer. (ii) is the hall bar structure after EBL and ICP etching. (iii) we transfer another layer BN. (iv) etch it to the edge of hall bar by ICP. And flush the device by  $O_2$  in ICP. (v) Using Evaporator to make edge contacts, after the EBL. (vi) the schematic of the edge contact (red circle in (v)). (vii) make top gate by evaporator. (viii) the optic image of one of my device.

The thickness for the h-BN we using for insulating layer cannot be too thin, to avoid the tunneling current. But if the h-BN is too thick, it is very hard to tell whether the h-BN is flat enough. So the used thickness of h-BN typically is 30nm to 80nm.

In the step of the evaporation, usually people use acetone to lift off the PMMA and other part of metal. But it turns out REMOVER PG is better. So I put the sample in PG-Remover at 65°C for several hours to lift off the metal. REMOVER PG is a proprietary NMP based solvent stripper designed for efficient and complete removal of PMGI, PMMA, SU-8, and other resist films on Si, SiO<sub>2</sub>, GaAs, and many other substrate surfaces.

The other technique of evaporation I use is the angle evaporation. Sometimes the sample with a lot of layers of different material will become very thick. It is possible that the contact will break on layer structure edge.

There are two ways to overcome this situation. First one, we can grow a thicker gold contact (over 200nm dependence on your sample roughness). Second one, we can tilt the sample and do one more evaporation.

In most cases the first method will be good enough.

## **2.7 Low Temperature Transport Measurement**

For regular transport measurements, it is required to apply voltages on the device and measure the resulting currents. For the DC measurement (or DC source use as gate), we use a standard PC computer with Linux operating system with a National Instruments analog-to-digital (ADC) and digital-to-analog (DAC) converter card. The software we use is Mezurit2 which is open source and maintained by former group member Brain Standley.

The voltages are from the outputs of the DACs, which can be controlled by software (Lab View, Mezurit etc.). We use multiple DACs which allows us both use them as source-drain voltage or gate voltage. The current is measured using an Ithaco current pre-amplifier that outputs are voltage which proportional to the output current and can be ready by the ADC. In this way, we can both track the SD voltage, gate voltage and currents by Mezurit2 in real time.

The DACs can produce voltages from 10 V to +10 V with approximately 0.5 mV resolution. We have two different kinds of voltage amplifier, one is 20 times output and the other one is 10 times output. If we use voltage amplifier, the voltage range could be -200 V to + 200 V. The back gate voltage usually won't be larger than 60 V. Some papers they have increase the back gate voltage up to 140 V [43]. In this case, the result will dependent on the individual device. Some devices can bear that high and some cannot. Like we use voltage amplifier to amplify the voltage, we also can use a divider to lessen the voltage. For example, one typical bias voltage for graphene is 1 mV. So we can use a 1000 times divider connected to the DACs. If we output 1 V from DAC, then there will be 1 mV bias voltage on the device after the divider. A schematic of the simple DC measurement circuit is shown in Figure 2.12 .

To get a better signal, we also use Stanford SR830 Lock-in amplifier to apply AC voltage and measures AC voltage signal from device. The Lock-in can not only measure the AC voltage directly but also can measure the AC voltage difference between two contacts. It can output a DC voltage signal to ADC which allows us to record the signal in real time by Mezurit2. The magnification is determined by the sensitive on Lock-in, for example if

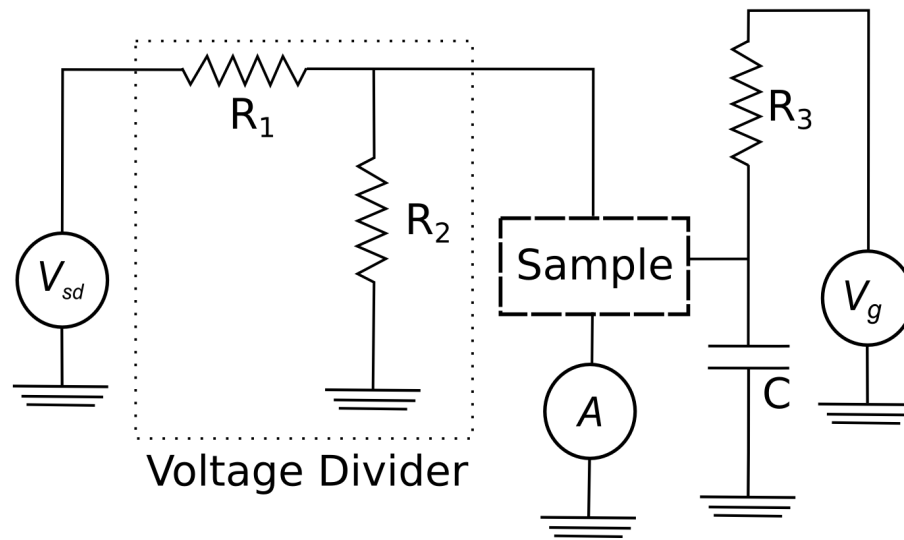


Figure 2.12: Simple DC measurement setup. The dashed line in the middle is where we put the sample. The source and drain voltage is applied on the contacts of the device via voltage divider ( $R_1$  and  $R_2$ ). The gate voltage is applied onto the Si wafer directly with a protect resistor  $R_3$  which is around  $10M\Omega$  at least. The current though the device is measured with the Ithaco current amplifier.

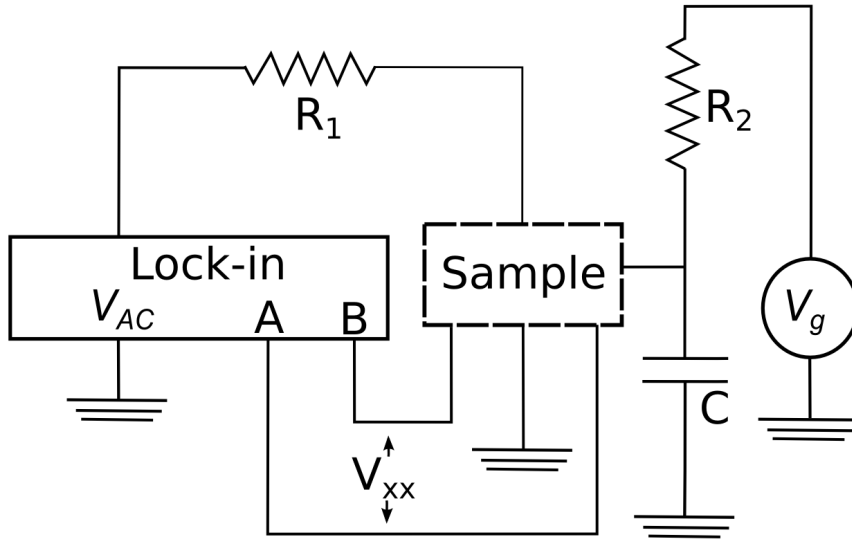


Figure 2.13: Simple AC measurement setup. A large resistor  $R_1$  connected to Lock-in AC voltage output makes it as a AC current source. We also apply the gate voltage like Figure 2.12. Two wires connected to Lock-in voltage input A and B. They can measure the voltage difference between two contacts connected to them which we called  $V_{xx}$  here.

it is 1 mV then the magnification is  $1e-3/10$ . The reason we divided it by ten is the DC output is ten times smaller than the signal detected in Lock-it itself. If you use Ithaco current amplifier to measure the current from Lock-in, at first you need change the raise time to "MIN" which means you are measuring AC signal. Second, you need time the magnification of the current amplifier. A schematic of the simple AC measurement circuit by Lock-in is shown in Figure 2.13.

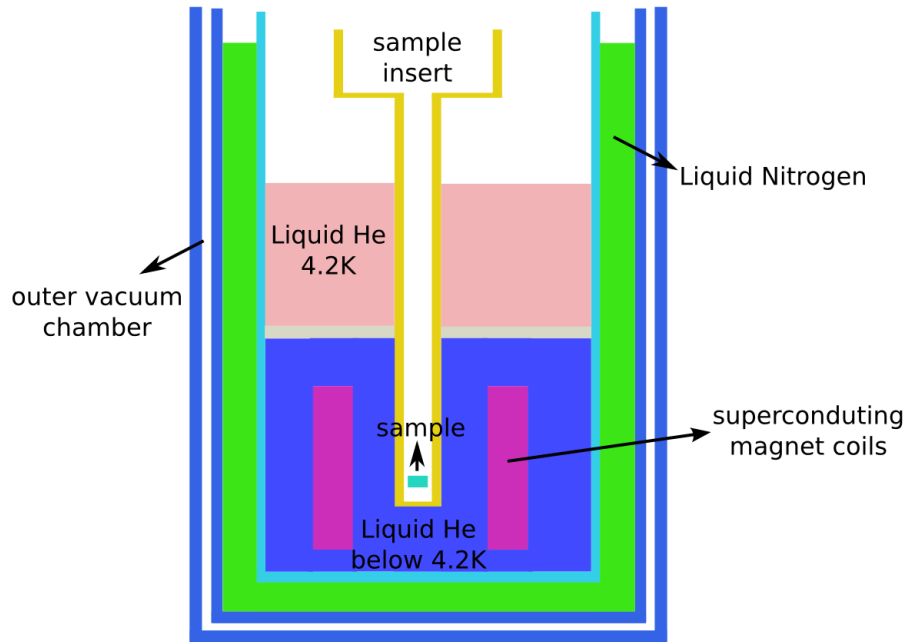


Figure 2.14: The schematic of refrigerator. The superconducting magnet coils are inside the Liquid Helium to making sure it is below its  $T_c$  temperature. So if the magnetic field is ON, the level of Liquid Helium cannot be lower than 20%.

Finally, for the low temperature measurements, we have used an Oxford refrigerator with superconductor magnets. The basic structure of this refrigerator is several independent Dewars. The outside one is the outer vacuum chamber. Then it is the liquid nitrogen reservoir. Then the 4.2 K liquid helium reservoir. Below that, it is the liquid helium below 4.2 K and this is also where the superconducting magnet coils is. The schematic of refrigerator is in Figure 2.14.

## Chapter 3

# Graphene Under One Dimensional Periodic Potentials

### 3.1 Abstract

Recently, graphene/BN superlattices have been observed to have multiple Dirac points [34] [6] [2] due to the periodic potential formed by the moiré superlattice. In this chapter, we present our related interesting work on graphene with a one-dimensional (1D) periodic potential.

Theory has predicted graphene's behavior under periodic potentials [9]. Both two dimensional and one dimensional periodic potentials will give graphene extra Dirac points as well as anisotropic behavior.

Here we use DNA linker molecules to assemble the nanotubes [22] [47] into arrays to use as gate electrodes to apply a 1D periodic potentials. This chapter will introduce the

electron collimation and transport properties in graphene when these 1D periodic potentials are applied.

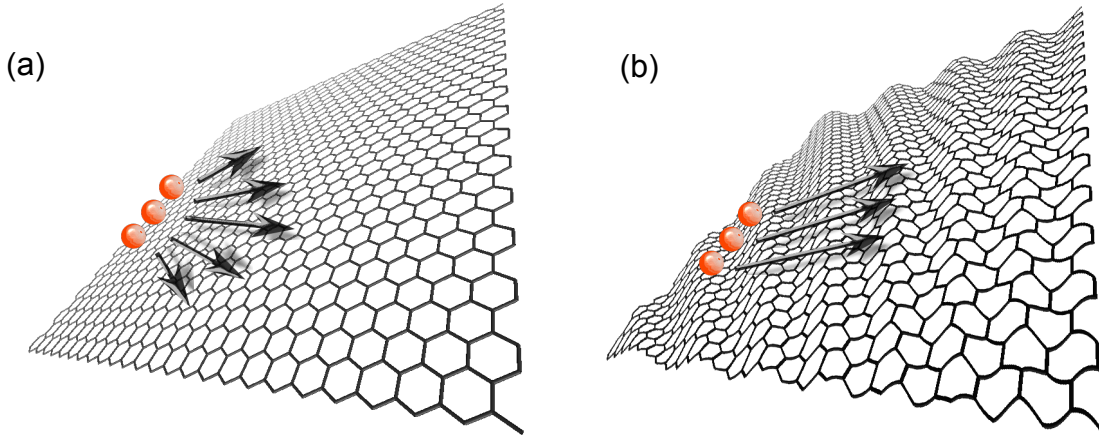


Figure 3.1: The electrons propagate without (a) and with (b) periodic potentials.

## 3.2 Introduction

Periodic potentials applied to graphene produce several interesting and unexpected charge carrier behavior. Graphene will be anisotropic under such external potentials. In the extreme case, the group velocity will reduce to zero in one direction while remaining the same in the other direction [10]. Further, new massless Dirac fermions are generated [55].

Figure 3.2 shows how the Dirac cone changes with the periodic potentials. The first figure is the pristine graphene. It has two valleys, K and K'. The energy dispersion near the Dirac point, Dirac cone, is isotropic. The next figure is graphene under 1D periodic potentials. The 1D periodic potential is a Kronig-Penney type potential along the  $x$  direction with period  $L$  and width  $w$ . Under these conditions, the Dirac cone becomes

anisotropic. The group velocity along the  $y$  direction is reduced dramatically, and the group velocity along the  $x$  direction stays the same as pristine graphene. The last figure shows the graphene under 2D periodic potentials. The Dirac cone is also anisotropic. Both group velocities in two directions have changed.

The Hamiltonian of graphene under a 1D potential  $V(x)$ , periodic along the  $x$  direction with periodicity  $L$  [55],

$$H = \bar{h}v_0(-i\sigma_x\partial_x - i\sigma_y\partial_y + IV(x)/\bar{h}v_0)$$

where  $I$  is the  $2 \times 2$  identity matrix,

using a transformation,  $H' = U_1^\dagger H U_1$ , where

$$U_1 = \frac{1}{\sqrt{2}} \begin{pmatrix} e^{-i\alpha(x)/2} & -e^{i\alpha(x)/2} \\ e^{-i\alpha(x)/2} & e^{i\alpha(x)/2} \end{pmatrix}$$

where

$$\alpha(x) = 2 \int_0^x V(x') dx' / \bar{h}v_0$$

we get

$$H' = \bar{h}v_0 \begin{pmatrix} -i\partial_x & -e^{i\alpha(x)}\partial_y \\ -e^{i\alpha(x)}\partial_y & i\partial_x \end{pmatrix}$$

$$\vec{k} = \vec{p} + \vec{G}_m/2$$

by

$$G_m = m(2\pi/L)\hat{x} = mG_0\hat{x}$$

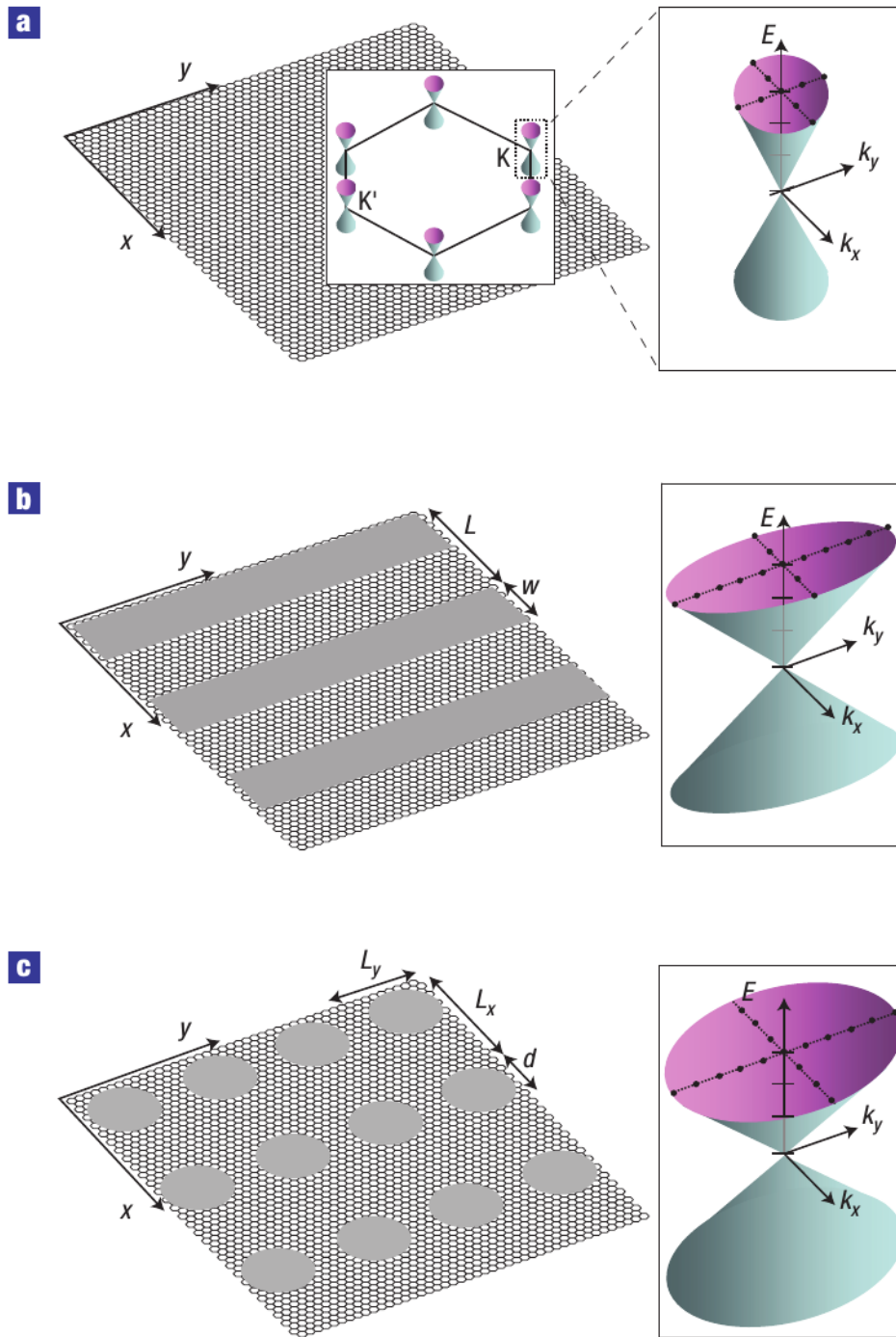


Figure 3.2: Graphene schematic and Dirac cone energy band structure of (a) pristine graphene (b) graphene under 1D periodic potentials (c) graphene under two dimensional periodic potentials [9].

and

$$p \ll G_0$$

We could treat terms containing  $\partial_y$  as perturbation since  $\vec{G}_m$  is along  $\hat{x}$ .

Hamiltonian may be reduced by using the two following basis functions,

$$\begin{pmatrix} 1 \\ 0 \end{pmatrix}' e^{i(\vec{p} + \vec{G}_m/2)}$$

and

$$\begin{pmatrix} 0 \\ 1 \end{pmatrix}' e^{i(\vec{p} - \vec{G}_m/2)}$$

we expand

$$e^{i\alpha(x)} = \sum_{l=-\infty}^{\infty} f_l[V] e^{ilG_0x}$$

in general,

$$|f_l| < 1$$

so we rewrite Hamiltonian,

$$M' = \bar{h}v_0(p_x\sigma_x + f_m p_y\sigma_y) + \bar{h}v_0 m G_0/2I$$

Comparing to the original Hamiltonian, the group velocity of charges moving along the  $y$  direction has been changed from  $v_0$  to  $f_m v_0$ . So the group velocity in this direction has become smaller than the origin Fermi velocity.

In summary, the Dirac fermion dispersion becomes anisotropic. The group velocities in two directions have become different.



Figure 3.3: Graphene under 1D periodic potentials as an electron supercollimator. [10]. In this figure, one can see how electrons propagate in graphene and in graphene under periodic potentials with differing conditions.

Further, if there is a 1D periodic potential applied to graphene like Figure 3.2b, the group velocity will be much higher in the  $x$  direction than in the  $y$  direction. In this way, the ballistic propagation of the electron beam can be achieved in graphene without spreading and diffraction. This is achieved only under periodic potentials without any waveguide or external magnetic field.

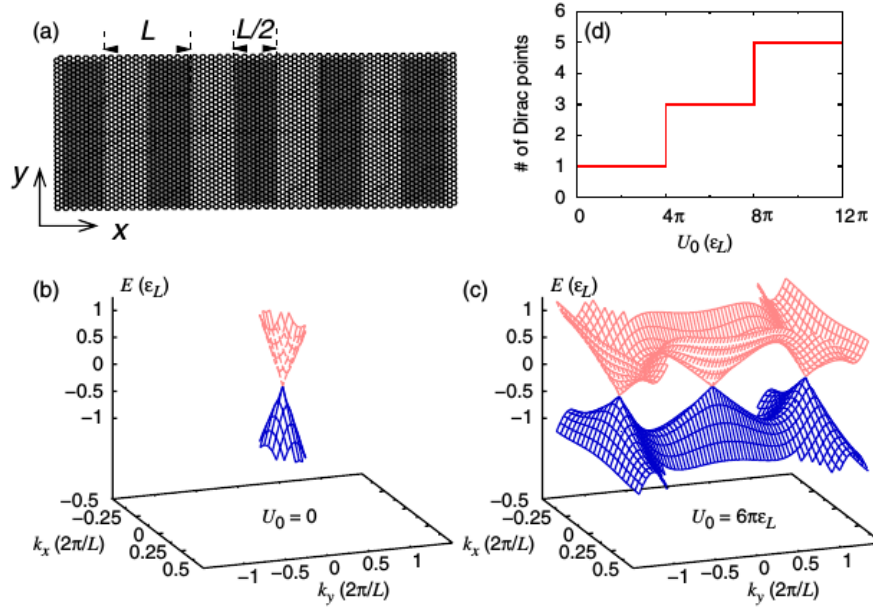


Figure 3.4: (a) The Kronig-Penney type 1D periodic potential. The strength inside the gray region is  $U_0/2$  and outside the region is  $-U_0/2$ . (b) Electron energy in units of  $\varepsilon_L = \hbar v_0/L$  near Dirac point of pristine graphene. (c) Same electron energy of graphene under 1D periodic potentials with  $U_0 = 6\pi\varepsilon_L$ . (d) Number of Dirac points in the graphene 1D periodic potentials system versus  $U_0$ . [11]

Another interesting feature is that there are additional branches of massless Dirac Fermions are generated with nearly the same electron-hole crossing energy as the original Dirac point. Because of these new degenerate zero-energy branches, the Landau Level (LL) at charge neutral point become  $4(2N + 1)$ -fold degenerate with the corresponding hall conductivity  $\sigma_{xy}$  showing a step of  $4(2N + 1)e^2/h$  [11].

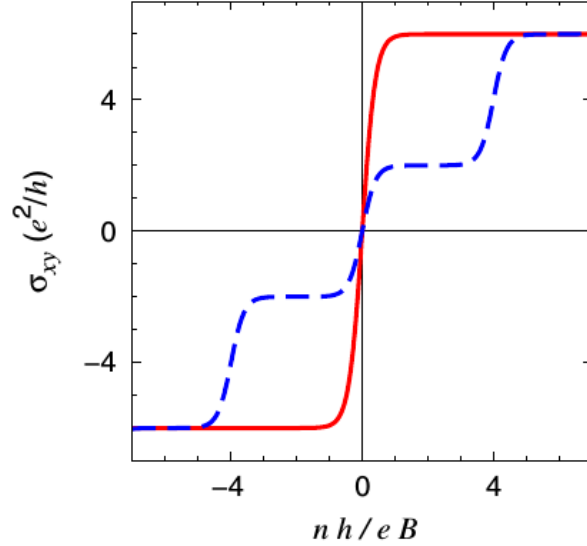


Figure 3.5: Hall conductivity vs. carrier density for graphene under 1D periodic potentials (red line) and pristine graphene (blue dashed line). The step for the red line is  $12e^2/h$  which is  $4 \times (2 \times 1 + 1)$ . [11]

### 3.3 Device Fabrication

We discussed some general experimental techniques in Chapter 2. However, the device discussed this chapter is very complicated. We are going to discuss many details about the device fabrication in this section.

At very first, we need make proper 1D periodic potentials. The easiest way might be to make some parallel metal lines on the  $\text{SiO}_2$  substrate. The problem with this approach is that it is difficult to make two metal lines close enough. The closest and thinnest metals lines using EBL might be 30 nm in width and 30 nm apart. For example, if we need at least 5 parallel lines, the size will be longer than 300 nm. In this case, the electrons will be hard to propagate without spreading and diffraction due to the mean free path and the behavior might be more like a PN junctions.

So the method we use here to create a 1D periodic potentials is to assemble parallel nanotubes by DNA-linker [22], which can achieve a nanotube separation as small as 3 nm.

At first, we order the DNA linker from INTEGRATED DNA TECHNOLOGIES. There are several different lengths we can use (Table 3.7).

Usually, I order 250 Nano mole DNA oligo for 30bp or 20bp DNA linker. The sequence of 30bp anchor is 5'- TTT ACG CTG CGA CAC GCA TGT GCG TTG GCA CGC -3'. In their website, We need click the "Custom Normalization". When choice single entry in the custom DNA oligoes. Choice "Add New" for Normalization. Choice "Full product yield, to a specified  $\mu$ Molar concentration". Enter "300"  $\mu$ Molar Concentration. Choice IDTE 7.5pH as the Buffer.

Use the same recipe to order other DNA liker, for 30bp toehold, the sequence is 5'- TTT TCG TGC GTG CCA ACG CAC ATG CGT GTC GCA GCG T -3'.

For 20bp toehold, the sequence is 5'- TTT TCG TTG TCG GCA AGA CCT CGC AAC -3'. And for 20bp anchor, the sequence is 5'- TTT GTT GCG AGG TCT TGC CGA CA -3'.

The 20bp DNA linker is around 8.5 nm long. The 30bp DNA linker is around 10 nm long. These DNA solutions must be kept in freezer. We need to melt the solution every time we use it.

First, we need make the 1xTAE Mg buffer. We have the 50xTAE (50X TAE Buffer which is Tris-acetate-EDTA is used for electrophoresis of nucleic acids in agarose and polyacrylamide gels. You can use this buffer for both genomic and large supercoiled DNA, and you can also use this as both a running and a gel preparation buffer.) in our

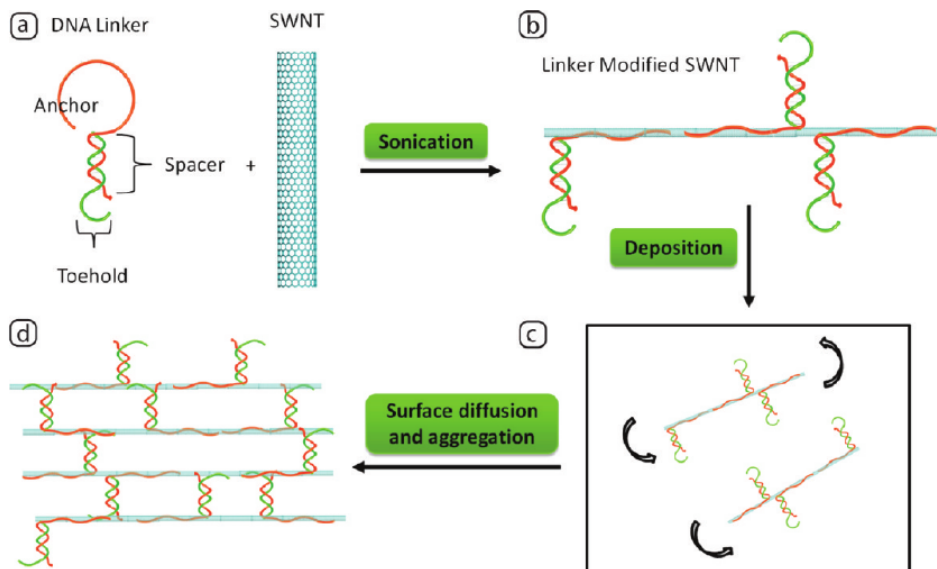


Figure 3.6: The assembly process. (a) The DNA linker is mixed with SWNTs. (b) The DNA linker connected to SWNT after sonication. (c) During the deposition process, the nanotubes can diffuse along the mica surface and assembled to (d) nanotube arrays. The DNA linker keep each SWNT in a fixed distance. [22]

lab. Then we are going to make the 10x TAE buffer. We prepare 125 mMole  $Mg^{2+}$  which is  $(125 \times 203.3)/1000 = 25.4125g$ . Mix the  $Mg^{2+}$  powders in to 200 mL 50xTAE buffer, add the water until to 1 L. So now we have the 10x TAE buffer.

Second, we make a 500  $\mu L$  DNA solution in the 1xTAE buffer. At the beginning, 32 mMole DNA anchor mixed with 35 mMole DNA toehold in a micro centrifuge tube. Put the mixer DNA tube in centrifuge for 1 min and then shaker for 1 min, then in centrifuge for another quick 10 seconds. After this step the DNA anchor are well-mixed with DNA toehold.

Strand	Sequence	Special instructions
7 bp hairpin linker	5'-GCCGGGCTTTTTTTTTTTTTTTTGGCCGGCTTTTTTTTTT TTTTTTTTTTTTTTTTTT-3'	Standard Desalting
20 bp anchor side	5'-TTTTTTTTTTTTTTTTTTTTTTTTTTTGTGCGAGGTCT TGCCGACA-3'	Standard Desalting
20 bp toehold side:		
0 base toehold	5'-TGTCGGCAAGACCTCGCAAC-3'	Standard Desalting
5 base toehold	5'-TTCGTTGTCGGCAAGACCTCGCAAC-3'	Standard Desalting
7 base toehold	5-TTTCGTTGTCGGCAAGACCTCGCAAC-3	Standard Desalting
9 base toehold	5'-TTTTTCGTTGTCGGCAAGACCTCGCAAC-3'	Standard Desalting
11 base toehold	5'-TTTTTTTTCGTTGTCGGCAAGACCTCGCAAC-3'	Standard Desalting
60 bp anchor side	5'-TTTTTTTTTTTTTTTTTTTTTTTTTTTGTGCGAGGTCT TGCCGACAACGAAAATTTTCGTTGTCTCTATCCATTGGATAG AGACA-3'	Ultramer, no purification
60 bp toehold side; no biotin	5'-TTTTTCGTTGTCTCTATCCAATGGGATAGAGACAACGAA AATTTTCGTTGTCGGCAAGACCTCGCAAC-3'	Ultramer, no purification
60 bp toehold side; internal biotin	5'-TTTTTCGTTGTCTCTATCCAATGGGATAGAGACAACGAAAA /iBiodT/TTTCGTTGTCGGCAAGACCTCGCAAC-3'	PAGE purified

Figure 3.7: Table of different DNA linker sequence. [22]

Because we ordered the 300  $\mu$ mole concentration DNA liquid. We also need DNA anchor:

$$\frac{32\mu Mole}{300\mu Mole} \times 500\mu L = 53.33\mu L$$

and DNA toehold,

$$\frac{30\mu Mole}{300\mu Mole} \times 500\mu L = 50\mu L$$

After getting a good DNA toehold and anchor mixed solution, we add 50 $\mu$ L 10xTAE and 338.4 $\mu$ L DI water until we get the 500 $\mu$ L solution.

Then this solution is put in centrifuge for 1 min, shaker for 1 min then centrifuged again 10 seconds to mix all components together.

The solution in the tube is annealed in water inside the beaker at 100°C for 30 min. After the annealing, the SWNTs powder will be dispersed into the solution. We sonicate the solution with a big power until the SWNTs powder is well dispersed inside the solution. To get the maximum power, we will fill the sonicator half full and put the tube with solution inside in the place where the maximum sonication water wave is visible.

One important tip is the water will get very hot after long time sonication. To make sure the DNA won't be damaged by high temperature, usually ice is added into the sonicator.

After this, we put the solution within special centrifuge tube for our lab's centrifuge. After 19000 rpm 90 min centrifuge, we get the solution we want in the tube. We take the top part solution into a new tube.

At the same time, we exfoliate the mica to SiO<sub>2</sub> wafer. Then drop the 15  $\mu$ L DNA solution on to the wafer. After waiting for 15 min. We then dry the wafer by KimWrap.

After that, we use the nitrogen gas gun to dry the rest of the liquid. Usually, the furnace is used to anneal and remove the DNA in 300 °C for 10 to 20 min to leave the SWNT arrays.

The next step is locating the assembled parallel SWNTs is the next step. Before we can use SEM to search for SWNTs, we need to use EBL to make an alignment pattern. Unlike the alignment pattern for graphene sample, the alignment for SWNTs will be smaller to enable more accurate alignment. The distance between two closest crossing is 10  $\mu\text{m}$ .

Now, we can use SEM (Leo SUPRA 55) to find good parallel SWNTs. If we want to get a clear SWNTs picture, the SEM needs to use in-lens mode and an accelerating voltage of 1 kV. The scan line speed must be 7 or higher.

Figure 3.8 shows the process of making parallel SWNTs on  $\text{SiO}_2$  wafer. Figure 3.9 shows the SEM picture of parallel SWNTs. (a) and (b) shows the parallel SWNTs on MICA linked by different length of DNA liker (60 bp and 20 bp separately). (c) shows the possibility of SWNTs assembled together. We not only can get some parallel SWNTs in the red box, but also other structures. (d) A bundle of parallel SWNTs on MICA. The  $\text{SiO}_2$  does not have any SWNTs on it through.

When we have an SEM image and know where the parallel SWNTs are, contacts on SWNTs are made by EBL. These parallel SWNTs are used as 1D periodic potentials for our devices.

Figure 3.10 shows the process of device fabrication. First we exfoliate the mica onto  $\text{SiO}_2$  wafer. Then drop of 15  $\mu\text{L}$  top layer DNA-SWNTs mixed solution on mica. We can use SEM to find parallel SWNTs and make contacts on them to use as parallel potentials gate. Then an insulating BN is transferred on to SWNTs area. Then we transfer

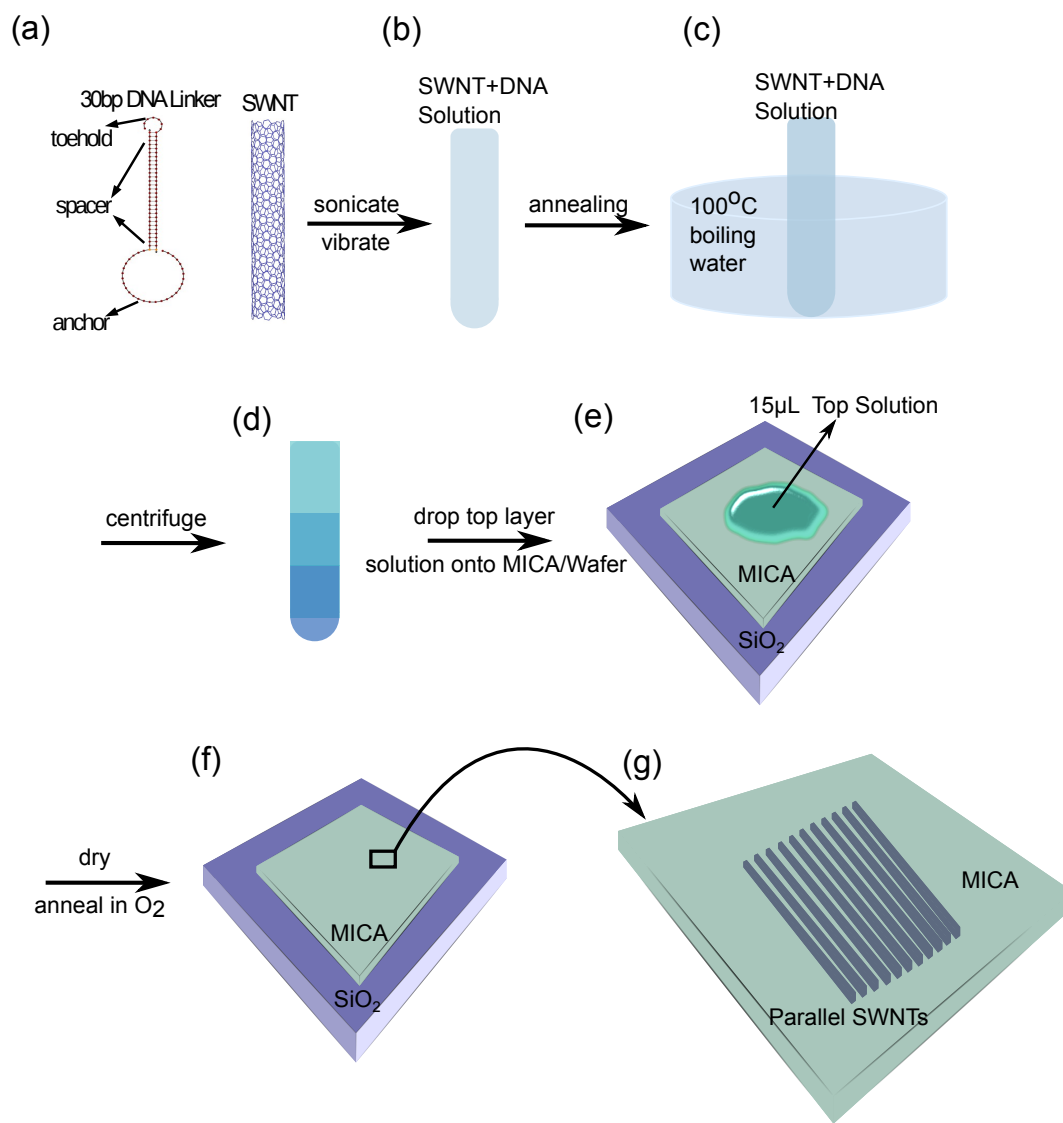


Figure 3.8: The process of making parallel SWNTs on  $\text{SiO}_2$  wafer. (a) Mix the DNA anchor and toehold solutions first. Then mix them with SWNTs. Here we use 30 bp DNA linker. The length is around 10 nm. (b) After sonication and vibration, we have a well mixed solution in the tube (making sure the temperature during sonication is low by adding ice into water). (c) Put the solution inside the  $100^\circ\text{C}$  boiling water for 30 minutes. (d) Put the tube into centrifuge for 90 min at 19000 rpm. We get a solution with several different layers in the tube. (e) Drop  $10\ \mu\text{L}$  top layer solution on the wafer. The MICA has been exfoliated on the  $\text{SiO}_2$ . (f) Dry the wafer. Then use  $\text{O}_2$  to anneal the wafer under  $300^\circ\text{C}$  for 20 minutes. (g) By using SEM, we can locate the parallel SWNTs on MICA. The distance between each SWNT is 10 nm (The length of the 30 bp DNA).

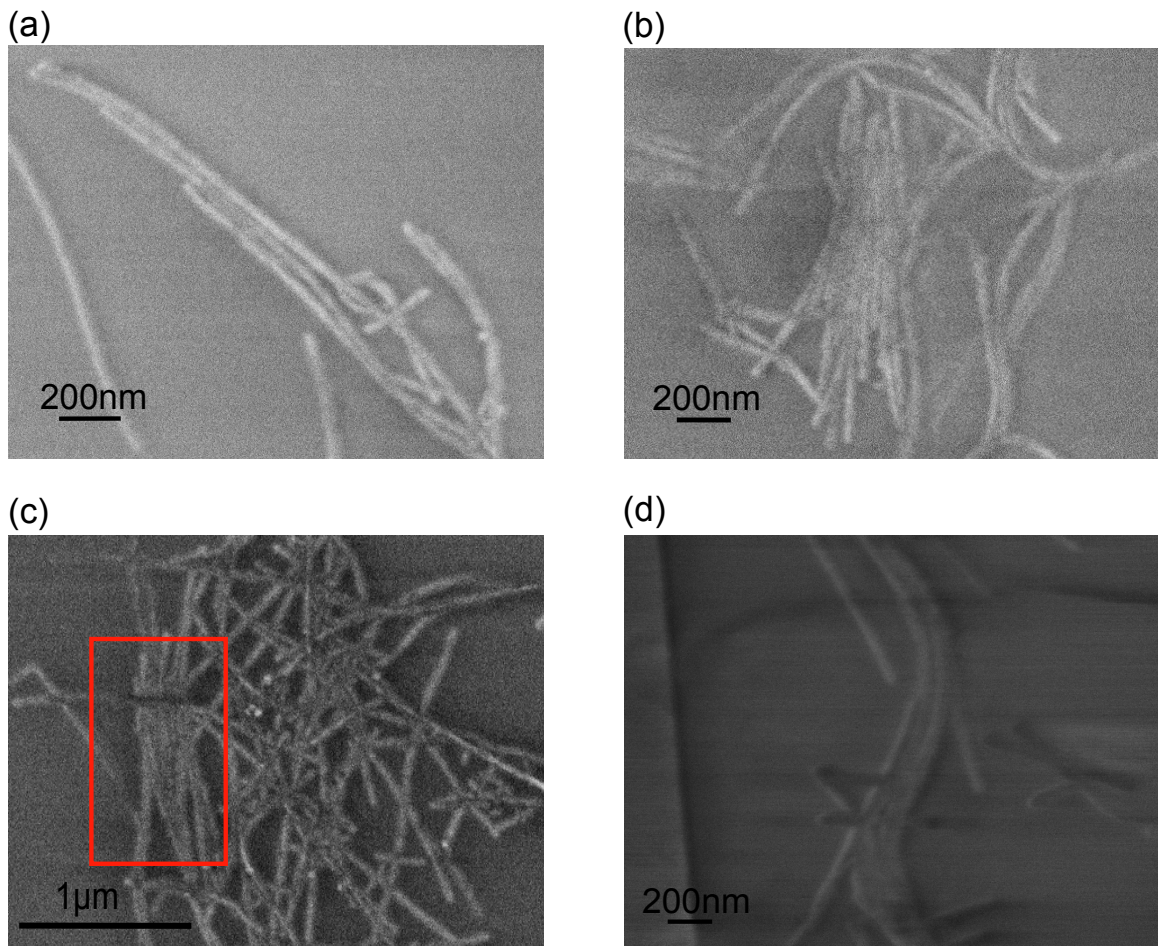


Figure 3.9: The SEM picture (In-lens Mode) of parallel SWNTs on MICA/SiO<sub>2</sub> wafer. (a) and (b) shows the parallel SWNTs on MICA linked by different length of DNA liker (60 bp and 20 bp separately). (c) shows the possibility of SWNTs assembled together. We not only can get some parallel SWNTs in the red box, but also other structures. (d) A bundle of parallel SWNTs on MICA. The SiO<sub>2</sub> doesn't have any SWNTs on it through.

graphene and make contacts on it. The figure (h) is the zoom in figure from the blue dashed line area in figure (g). The black dashed line indicates the area where is affected by parallel SWNTs gate in the graphene. Six contacts are made right close to the edge of the parallel SWNTs area. Then a top BN is transferred on to sample to make a top gate.

Because of the complicated structure of this device, we show a side view and a top view process of making device in Figure 3.11.

The schematics of (a) to (g) are the side view of device in each process, and the (i) to (vii) are the top view schematic corresponding to the side view. So in (a) and (i), we have mica exfoliated on SiO<sub>2</sub> wafer. In (b) and (ii), contacts are being made on parallel SWNTs. The distance of each SWNT is the periodic length of the 1D potentials, which can be from 8 nm to 30 nm. The periodic length can be controlled by using different DNA-linker. In (c), (d) and (iii), (iv), the first layer of BN and graphene are shown being transferred onto sample separately. In (iv), the red dashed lines indicate the area affected by parallel SWNTs gate. The scale is typically 100 nm × 500 nm. It is a tiny area.

Finally, we can make contacts on graphene now ((e) and (v)). Several contacts are made on two sides of graphene. The contacts are right next to the edge of parallel SWNTs gate area (red dashed lines). It is a very tricky process. The 1D periodic potential working area is tiny, so the contacts on graphene could be as small as 100 nm in width and as close as 50 nm to each other. This size is beyond the limitation of optical microscope. So we can't identify the features after EBL by optical microscope. And small features from EBL are sensitive to dose and beam current in EBL. The solution is every single time before making contacts, I perform a dose test and see whether the small contacts are well-defined.

After this tricky EBL process, another BN is transferred onto sample as an insulating layer for top gate. Then a top gate is made by Cr/Au used to control the carrier density on graphene ((f),(g),(vi),(vii)).

Here are some SEM pictures of real devices (Figure 3.12 and Figure 3.13). Basically, the devices talked in this chapter have a similar structure.

In Figure 3.12, (a) and (b) are contacts on the parallel SWNTs. The parallel SWNTs are inside the red dotted lines. (c) The contact on SWNTs under the first layer of BN. (d) Graphene on BN. The contacts on SWNTs under BN are still visible. Also, the parallel SWNTs are just visible inside the red box.

In Figure 3.13, (a), (b) and (c) are SEM figures with samples with contacts on graphene. The contacts on SWNTs under BN are still visible. For example, in (b), the nine small contacts are on the graphene. The two large contacts are on the SWNTs under BN. (d) A device with top gate.

### 3.4 Estimation of Periodic Potentials

The purpose of the complicated structure of device is to control the periodic potentials by the SWNT gate and control the carrier density by the top gate separately. However, the SWNTs gate will not only generate a periodic potential but also will change the average carrier density.

A screening model is used here to estimate the height of the periodic potentials and the Fermi energy of the system. Figure 3.14 shows the schematic of sample with top

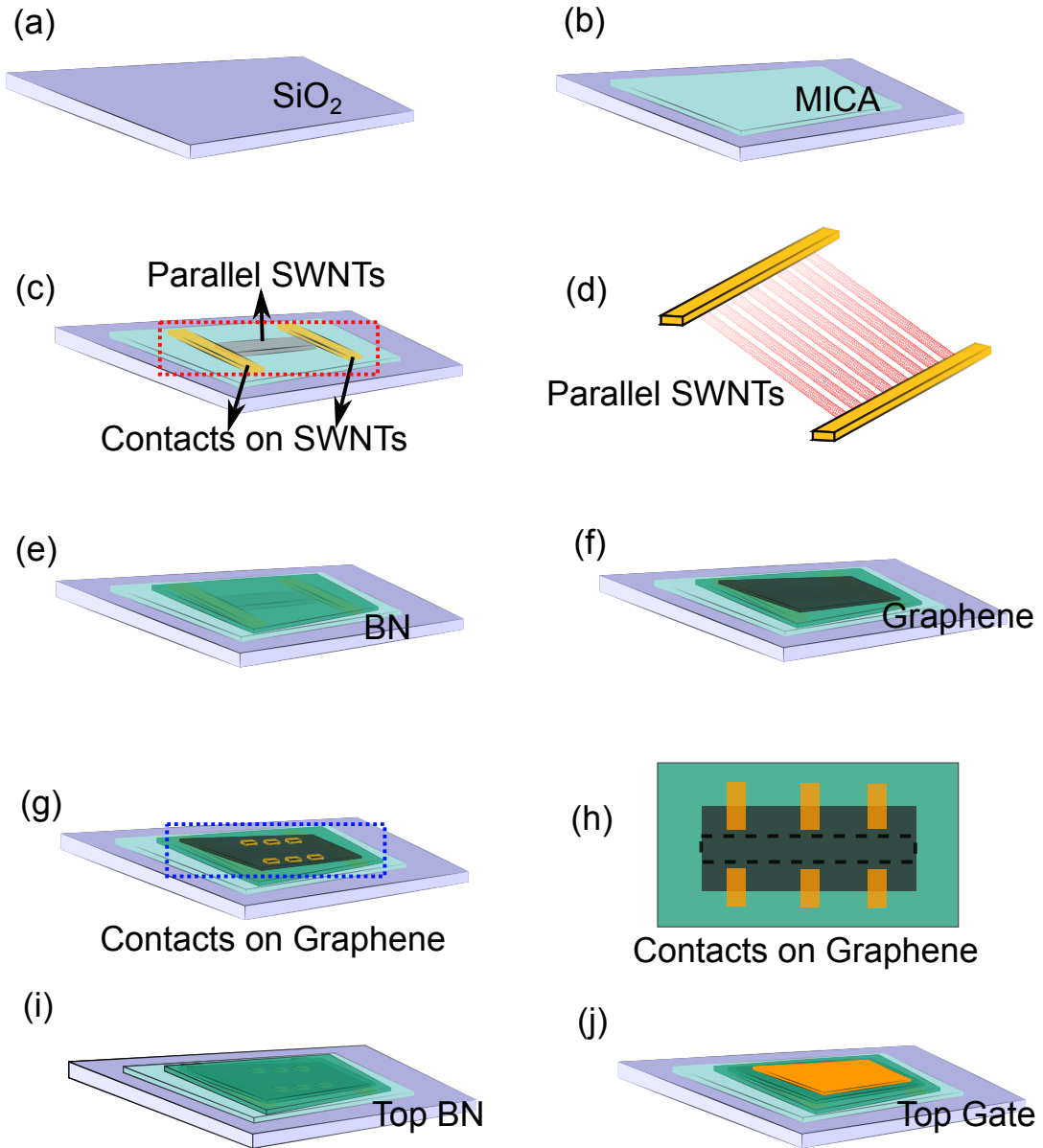


Figure 3.10: The schematic of device fabrication process. (a) The  $\text{SiO}_2$  wafer. (b) Exfoliate the mica on top. (c) Deposit the parallel SWNTs solution on top of mica. Using SEM to find parallel SWNTs and make contacts on them. The gray layer is where the parallel SWNTs are. (d) A zoomed-in figure of red dashed line in (c). (e) Transfer first layer BN as insulating layer for SWNTs gate. (f) Transfer graphene on top of BN. (g) Making contacts on Graphene. (h) The top view of blue dashed line area. We have several contacts on the edge of parallel SWNTs gate area (Black dashed line). The gray layer is graphene and green one is BN. (i) Transfer the top BN as insulating layer for top gate. (j) Make the top gate on top of BN.

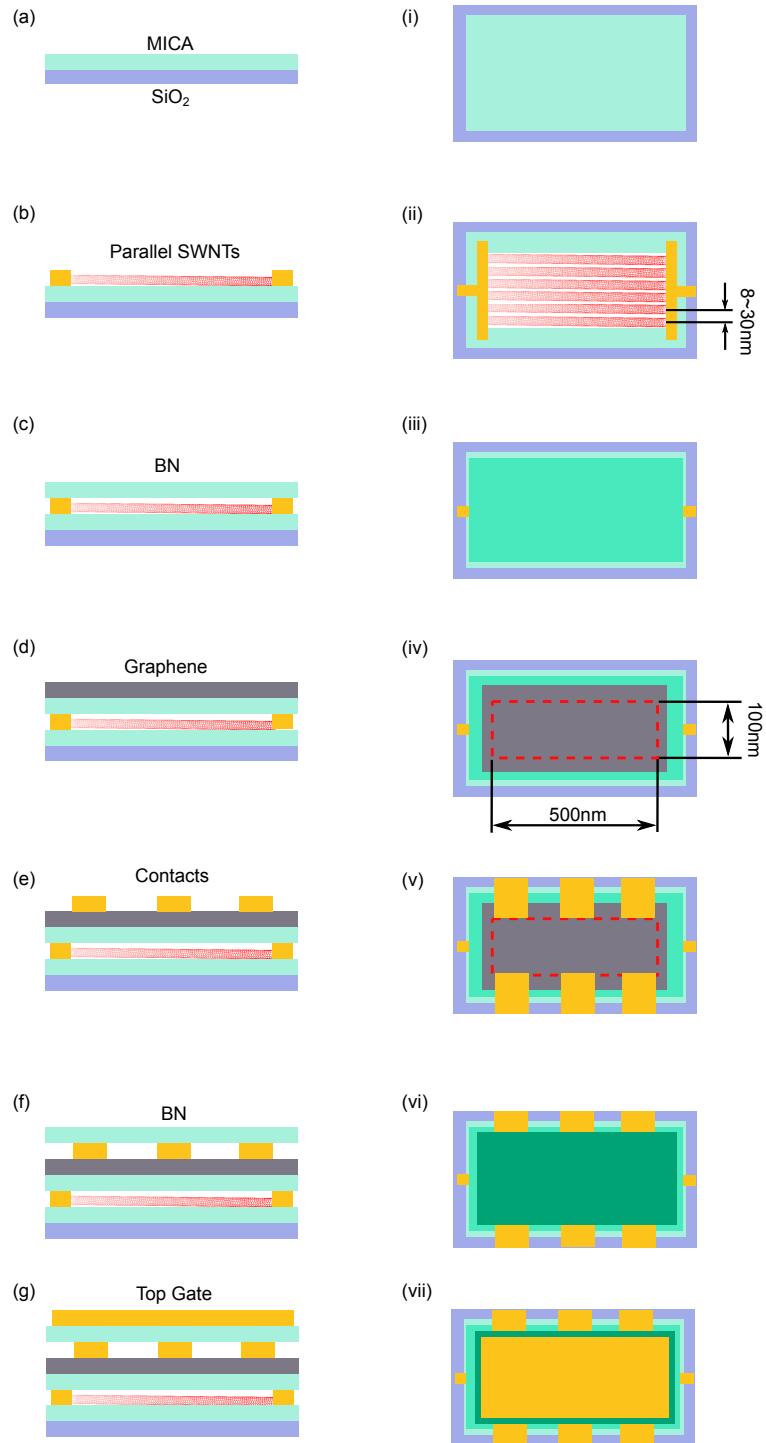


Figure 3.11: Side view and top view of device fabrication process.

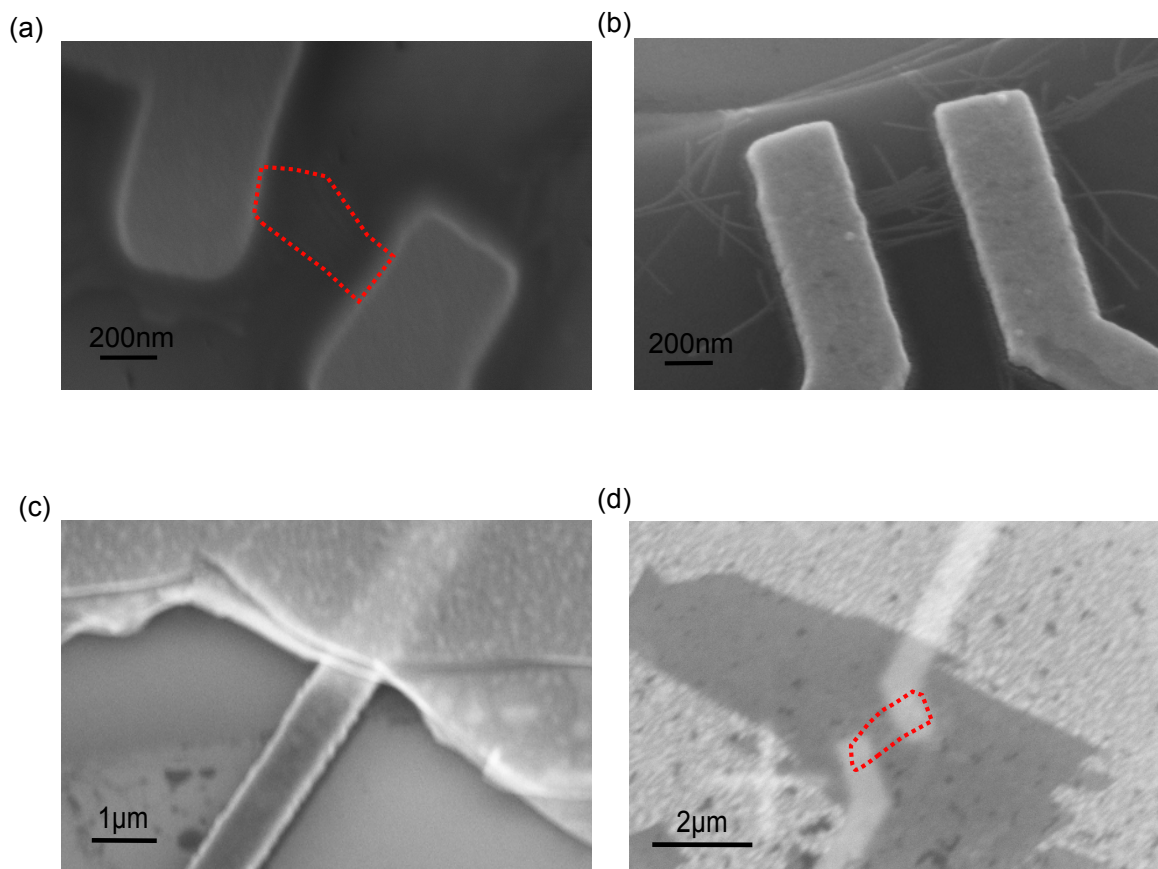


Figure 3.12: (a) and (b) are contacts on parallel SWNTs. Parallel SWNTs are inside the red dotted lines. (c) Contacts on SWNTs under the first layer of BN. (d) The graphene on BN. One still can see the contacts on SWNTs under BN. Also, the parallel SWNTs are just visible inside the red box.

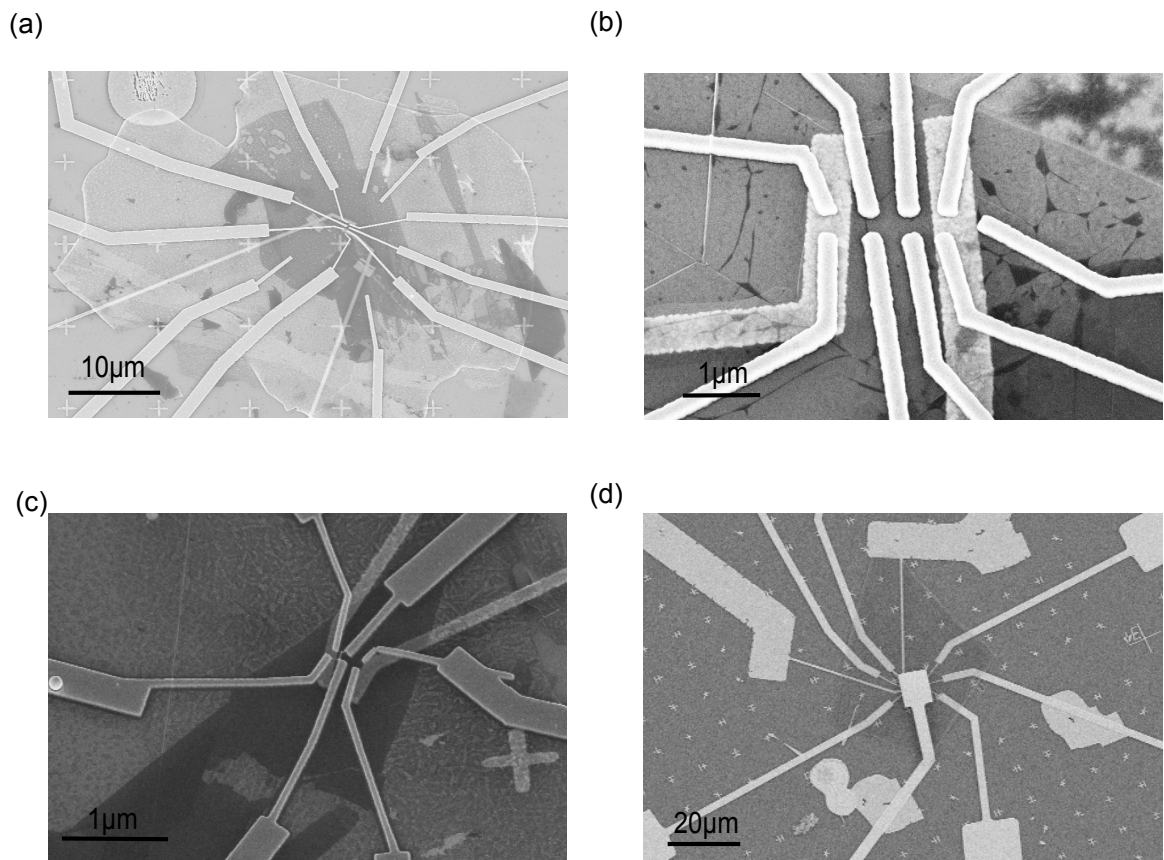


Figure 3.13: (a), (b) and (c) are contacts on graphene. The contacts on SWNTs under BN are still visible. For example, in (b), the nine small contacts are on the graphene. The two large contacts are on the SWNTs under BN. (d) device with top gate.

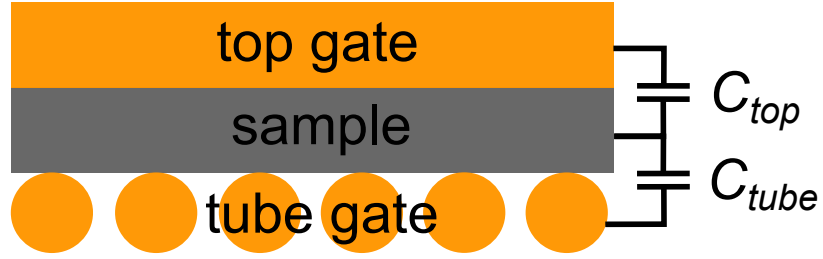


Figure 3.14: The schematic of sample with two gates. The tube gate will not only provide the periodic potentials but also a mean potential which changes the carrier density.

gate and tube gate. The two capacitance between the gate and sample are called  $C_{top}$  and  $C_{tube}$ .

At first, we estimate the carrier density,  $n_{\pm}$  is the carrier density of sample with positive or negative fluctuated fluctuations from the tube gate.

$$n_{\pm} = C_{top}V_{top} + C_{tube}V_{tube} \pm \eta C_{tube}V_{tube}$$

$\eta C_{tube}V_{tube}$  is the fluctuating contribution from the tube gate, in other words this term will be the actual periodic potential.  $\eta$  is defined as,

$$\eta = \frac{\delta n_{tube}}{n_{tube}}$$

So the Fermi energy is,

$$E_F = \hbar V_F \sqrt{\pi n}$$

$\hbar$  is the Plank's constant,  $V_F$  is the Fermi velocity in graphene.

So if the tube gate contributes a positive fluctuating carrier density, the Fermi energy is,

$$E_{F+} = \bar{h}V_F\sqrt{|\pi n_+|} * \text{sign}(n_+)$$

On the other hand, if a negative carrier density is created, the Fermi energy is,

$$E_{F-} = \bar{h}V_F\sqrt{|\pi n_-|} * \text{sign}(n_-)$$

The fluctuation of the Fermi energy will be able to written as,

$$\delta E_F = E_{F+} - E_{F-}$$

So the periodic potentials' height is,

$$U_0 = \frac{\delta E_F}{\bar{h}V_F/L}$$

L is the period of the SWNTs.

If we assume  $\eta = 0.4$  and top BN and bottom BN are both 10 nm, we can get

Figure 3.15.

This figure shows the periodic potential controlled by two gates. Figure (a) is the real scale plot. Figure (b) is the contour plot. The scale bar is the height of periodic potentials in units of  $4\pi\bar{h}V_F/L$ . So if the  $U_o$  is higher than 1, it means there are extra energy degenerated Dirac points which makes the lowest Landau level in a magnetic field degeneracy become 12 instead of 4 in graphene.

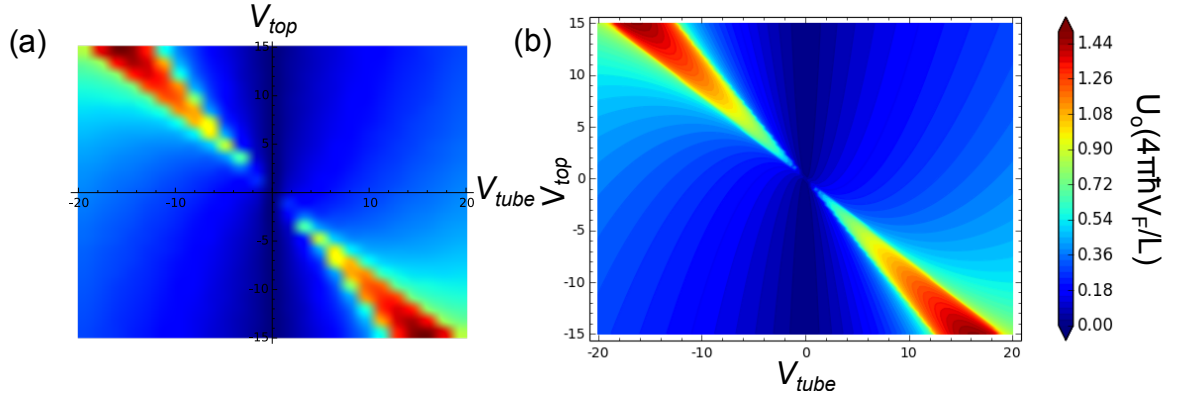


Figure 3.15: The figure shows the periodic potential controlled by two gates. (a) is the real plot of top gate versus the tube gate. (b) Contour plot of data in (a). The scale bar is the height of periodic potentials in units of  $4\pi\hbar V_F/L$ . So if the  $U_o$  is higher than 1, it means there are additional energy degenerate Dirac points which makes the lowest Landau level degeneracy in a magnetic field become 12 instead of 4 in graphene.

We can change the thickness of BN to see how the capacitance affects the periodic potential height. For top 20 nm top BN and 10 nm bottom BN, the simulation is shown in Figure 3.16.

For 10 nm top BN and 20 nm bottom BN, the simulation is shown in Figure 3.17.

### 3.5 Electron Beam Collimation

In the introduction section, we already introduced and explained that the group velocity of electrons in graphene under a 1D periodic potential will be different in the direction along the periodic potential and perpendicular to the periodic potential. In this way, the electron beam collimation will be possible without any waveguide or external magnetic field.

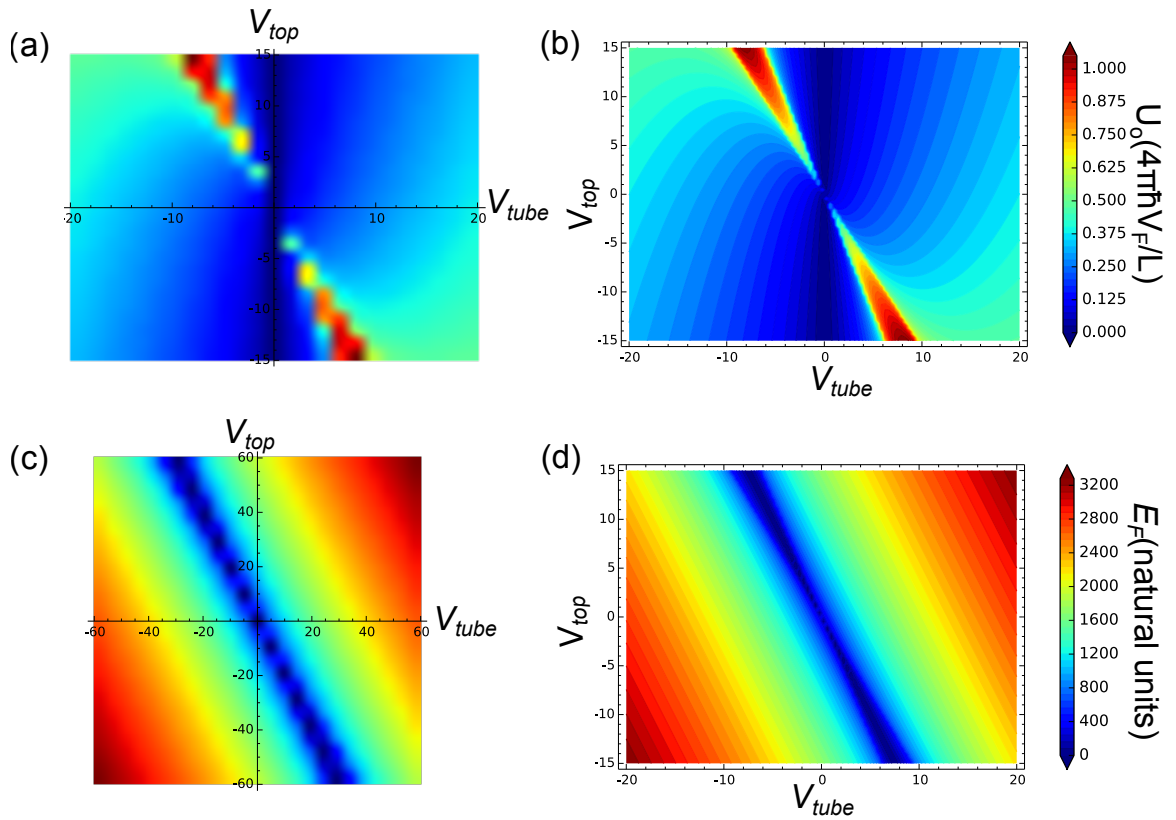


Figure 3.16: The figure shows the periodic potential controlled by two gates. (a) is the real plot of periodic potential height versus the tube gate and top gate. (b) The contour plot of same data as in (a). The scale bar is the height of periodic potentials in units of  $4\pi\hbar V_F/L$ . (c) is the real plot of Fermi energy. (d) is its contour plot.

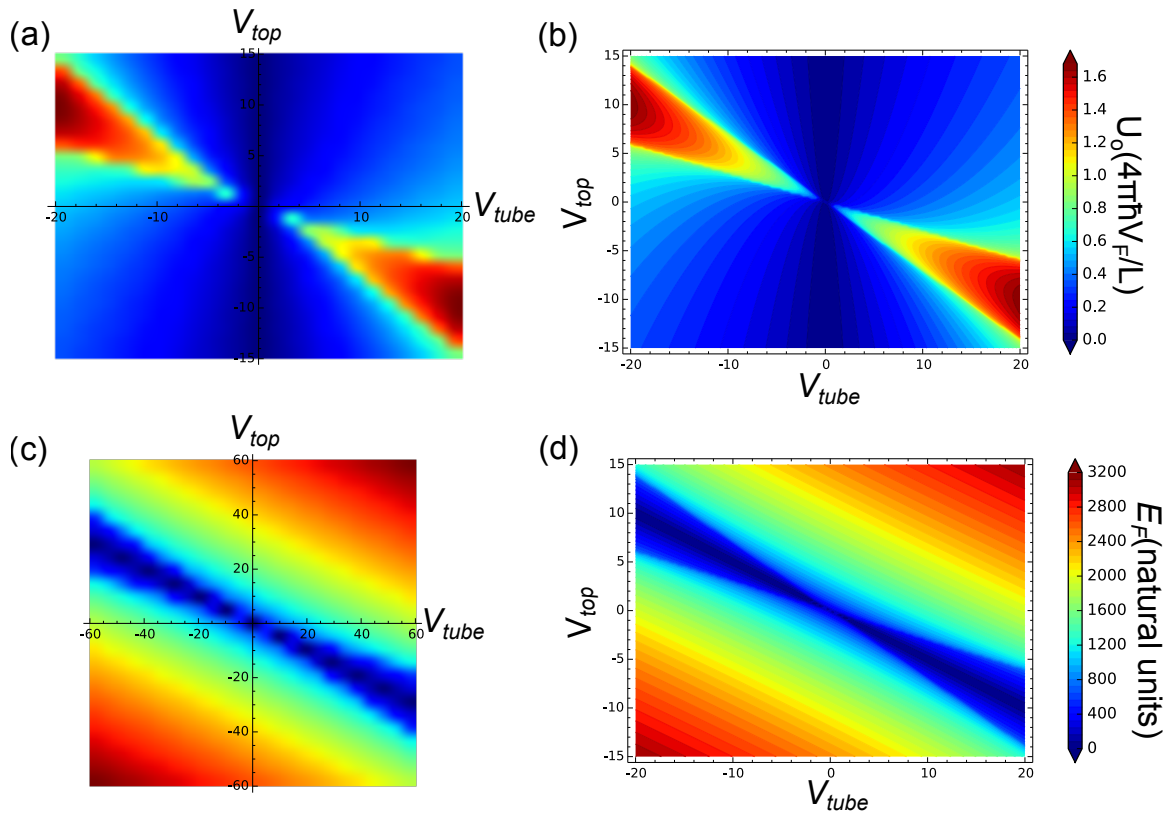


Figure 3.17: The figure shows the periodic potential controlled by two gates. (a) is the real plot of periodic potential height versus the tube gate and top gate. (b) The contour plot of same data as in (a). The scale bar is the height of periodic potentials in units of  $4\pi\hbar V_F/L$ . (c) is the real plot of Fermi energy. (d) is its contour plot.

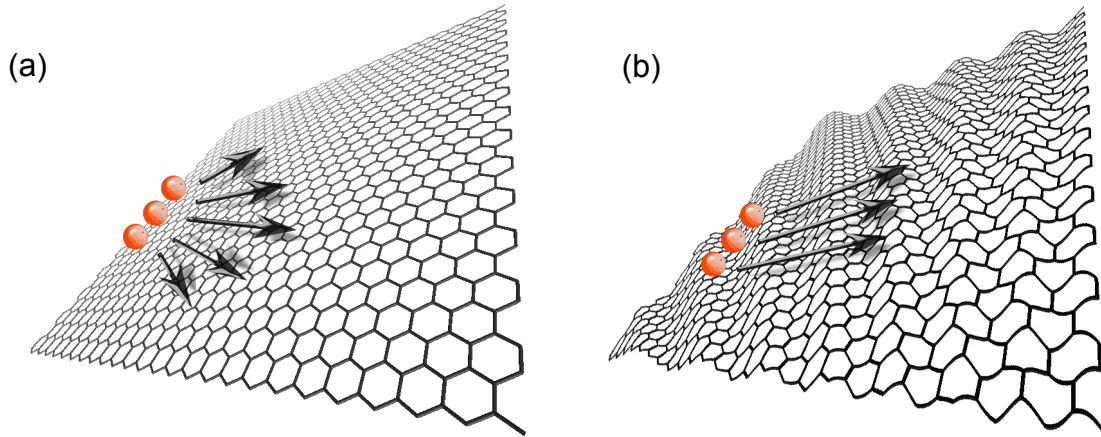


Figure 3.18: (a) Without 1D periodic potentials, the group velocity is isotropic and charges propagate in all directions. (b) With the 1D periodic potentials, the group velocity in one direction is much larger than the other one. Then the beam collimation occurs - charges propagate along one direction. The ripple here is not a ripple mechanically on graphene, but a different height of potential within the graphene.

The idea of the experiment is shown in Figure 3.18. The charges (Red dots) are propagating in graphene. Without 1D periodic potentials, the group velocity is isotropic and charges propagate in all directions. With the 1D periodic potentials (b), the group velocity in one direction is much larger than the other one. Then the beam collimation occurs - charges propagate along one direction. The ripple in Figure 3.18b is not a ripple mechanically on graphene, but a different height of potential within the graphene.

The schematic structure of a device is in shown Figure 3.19a. Two contacts are on the SWNTs gate. Three contacts are on the graphene, which are named source, 1 and 2. Figure 3.19b shows the data. A current source is applied to graphene on contact (source) and currents are being measured by the two contacts 1 and 2 on the other side.  $I_1$  is increasing when a voltage is applied onto SWNTs, while the  $I_2$  is decreasing. It means when we have an external 1D periodic potentials, charges will go to contact 1 more than contact 2. The

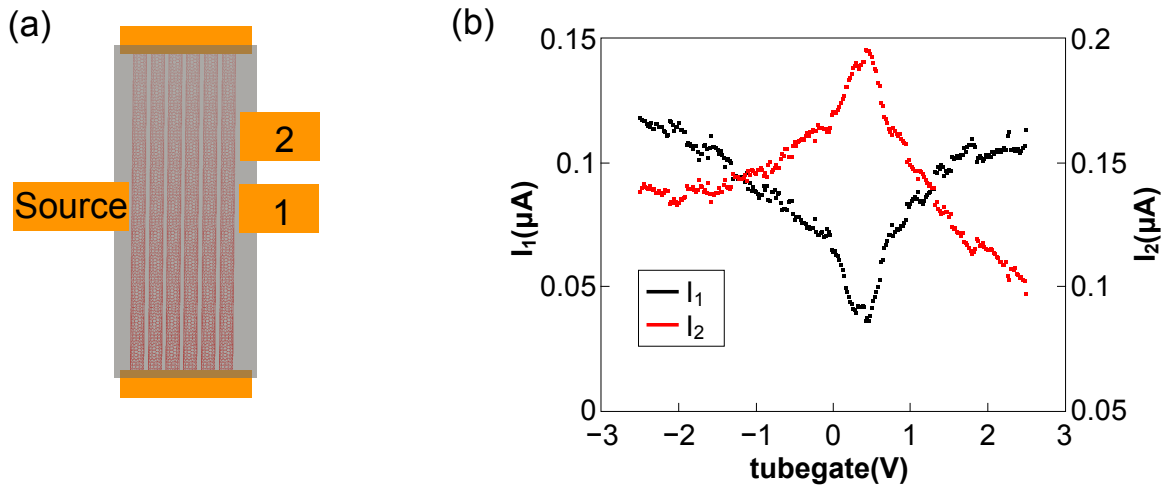


Figure 3.19: (a) The schematic of device. (b) The current on contact 1 and contact 2 changing with the periodic potentials. The  $I_1$  is increasing when a voltage is applied onto SWNTs, while the  $I_2$  is decreasing.

periodic potentials changed the distribution of currents, and the direction perpendicular to the SWNTs receives more current. This can be understood with the collimation theory.

Figure 3.20 shows another measurement setup for same device. This time the current source is applied on the one of the right contacts. Contact 2 is next to the source contact on the same side. Contact 1 is on the other side of the device from the contact. This time, the contact 2 is on the different direction with contact 1, but similar behavior occurs. The contact across from the periodic potentials collects more current when the periodic potentials is applied.

This behavior has been observed from more than one device.

Here we show results from another device, the thickness of top BN is 26 nm and the thickness of bottom BN is 13.56 nm. The space between each SWNT is 10 nm. The height of periodic potential is  $U_0 = 0.2$  eV at a tube gate voltage equals 3 V without a

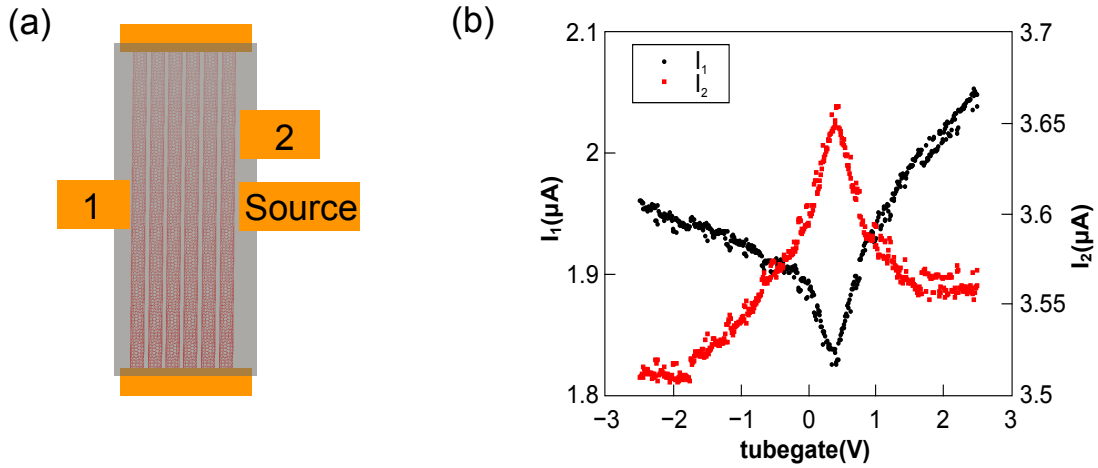


Figure 3.20: (a) The schematic of device. (b) The current source is applied as shown in figure (a).  $I_1$  is increasing when a voltage is applied onto SWNTs, while the  $I_2$  is decreasing. It means the charges go to the contact 1 more when the periodic potentials is applied.

top gate voltage. Ratio of  $I_1/(I_1 + I_2)$  at tube gate voltage equals to 0.5 V is 0.8 and at tube gate voltage equals to 3V is 0.89. The percent change is around 10% (Figure 3.21a). The percent change of electron group velocity at  $70^\circ$  from the theory [9] is also about 10% (Figure 3.21b).

This collimation is also interesting to study under a magnetic field. The current source is put on contact 1 and the current on contact 3 is measured. Some nonlinear features are shown in hole side (Figure 3.22). These feature is reminiscent of us the magnetic focusing that has been observed in graphene device [62]. Because the group velocity and Dirac band is very different between the region outside of periodic potentials and region inside of the potentials, it is possible that the transverse magnetic field changes the direction of charges and charges bounce back at the edge of the parallel potentials. The trajectories of the different modes are shown in the Figure 3.22a.

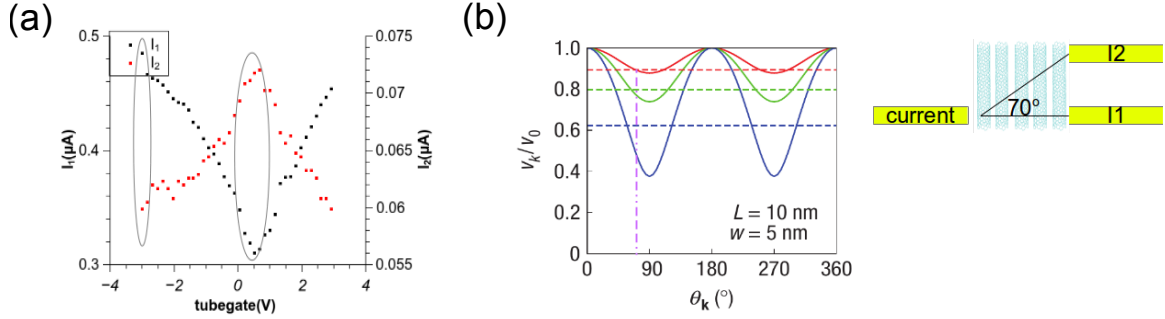


Figure 3.21: (a) The collimation data,  $I_1$  and  $I_2$  changing with tube gate. The experiment set up is the insert graph on the right. (b) The group velocity along the periodic potentials and in the  $k$  direction. The  $\theta_k$  is the angle between these two directions. At  $\theta_k$  equals to  $70^\circ$  which is indicated by a pink perpendicular line. Red, green and blue lines correspond to  $U_{1D}$  being 0.2 eV, 0.3 eV and 0.5 eV. [9]

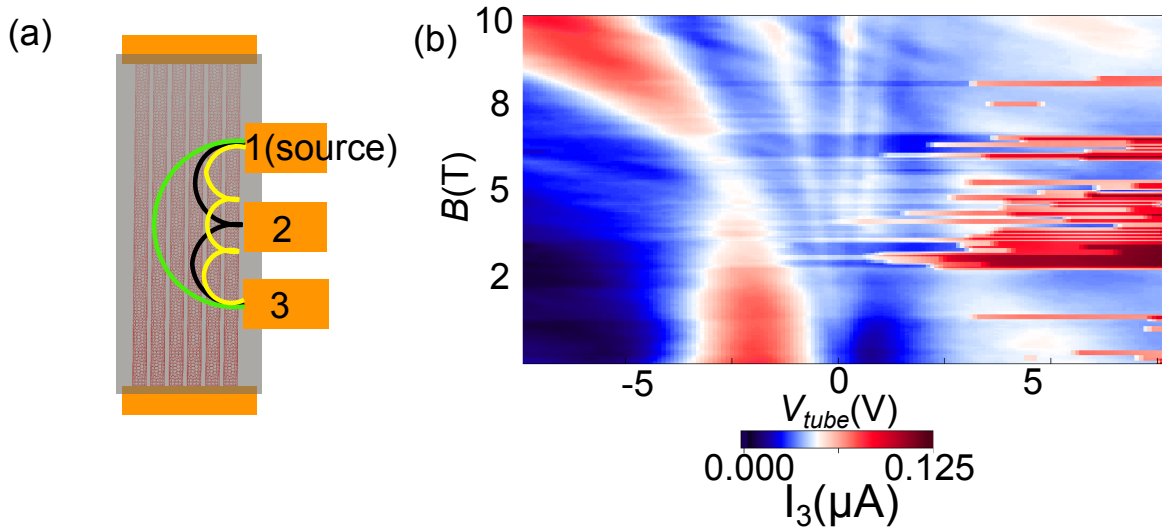


Figure 3.22: (a) Schematic of device. The lines inside show trajectories for different modes. (b)  $I_3$  plot with magnetic field as  $Y$ -axis and  $V_{tube}$  as  $X$ -axis. The non-linear feature is shown on the hole side.

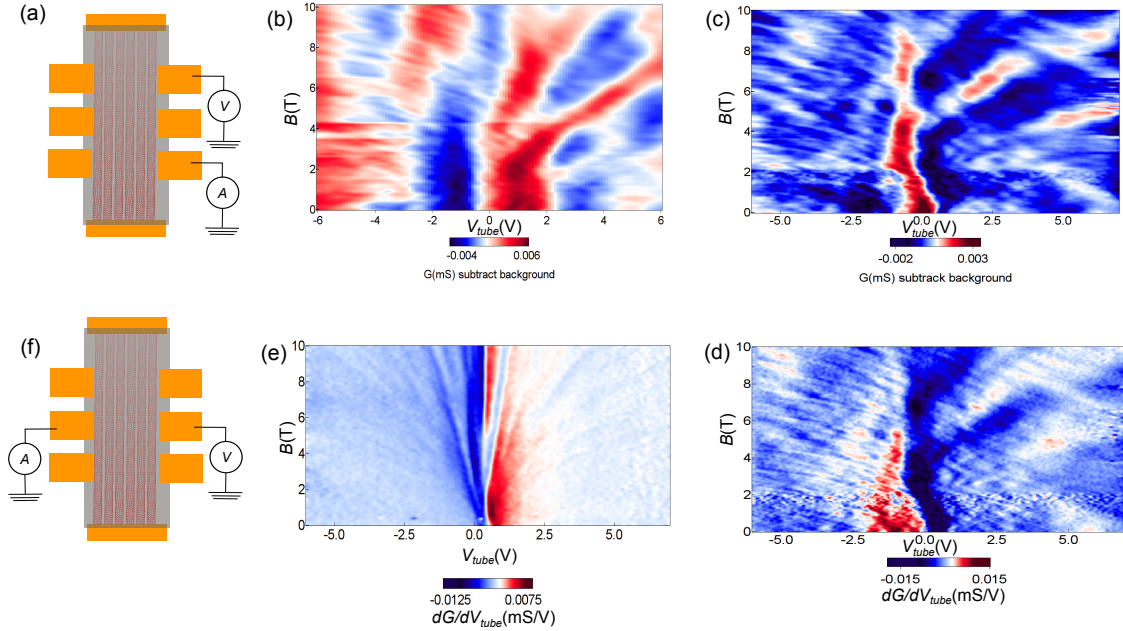


Figure 3.23: (a) The schematic measurement set up for figure (b) to (d). (b) The conductance subtracts the background with tube gate as  $X$  and magnetic field as  $Y$ . The back gate voltage is  $0V$ . (c) Same as (b) but with a  $25V$  back gate voltage. (d) Same condition as (c) but plot the  $dG/dV$ . (e) The  $dG/dV$  between two contacts shown in schematic (f).

### 3.6 Quantum Transport Data

Graphene under periodic potentials is a very interesting system. The quantum transport data also shows some unique behavior.

In Figure 3.23 shows several transport measurements under a magnetic field with a device only having tube gate and back gate.

The data in Figure 3.23 is complicated, because the back gate and tube gate are on the same side of the device. The two gates will both control the carrier density and periodic potential. In the data, there are several possible features that could arise from additional Dirac points. They could come from the periodic potential. Another possible

reason might be the periodic potential makes graphene like a multiple PN junctions. The figures from b to d are measured by the setup in a. They are very different from the figure e (setup in figure f). The anisotropic properties are obvious from these two set of data. But the features are too complicated to easily analyze, so that is why we added a top gate to control the carrier density separately.

Here we will discuss a device which is shown in Figure 3.24a and Figure 3.24b. The eight contacts shown in b marked with black stars are contacts on graphene. Blue contacts are contacts on the SWNTs gate. The orange contact is the top gate. The two green contacts are the contacts we measured here. We show a plot of conductance with top gate and tube gate in (c). There are three blue linear dip features in this figure. The horizontal feature is from the Dirac point of graphene which is only affected by top gate. The vertical feature is from the region only affected by tube gate. The feature with a slope is the Dirac point of graphene and where the carrier density is controlled by two gates. The figure d is the top gate landau fan graph with tube gate fixed at 0V. To make the feature clear, here we plot the  $dG/dV_{top}$ .

However, when we sweep the tube gate and magnetic field, the landau fan will be like Figure 3.25. This will only happen at particular top gate. In b, there are some landau level splitting features.

In Figure 3.26 is another device. The part a shows the schematic of device. The six red contacts are on graphene. Two blue contacts connected the SWNTs gate. The orange contact is the top gate. The conductance is measured between two green contacts. Figure b is the conductance vs. both two gates. The vertical dip is from the graphene

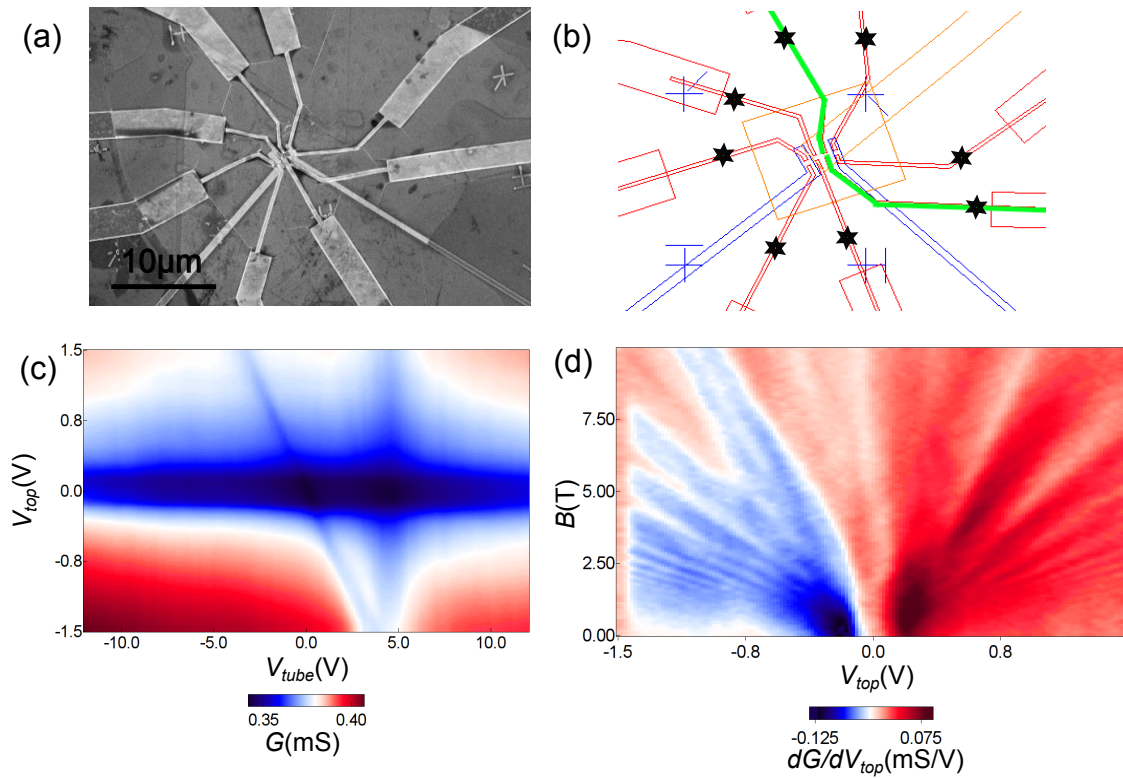


Figure 3.24: (a) SEM picture of the device. (b) Device schematic. Eight contacts with star marks are contacts on graphene. Blue contacts are contacts on the SWNT gate. The orange contact is the top gate. Two green contacts are the contacts we used for this measurement. (c) Two gates sweep plot the conductance. (d) The top gate landau fan graph with tube gate fixed at 0V. Here we plot the  $dG/dV_{top}$ .

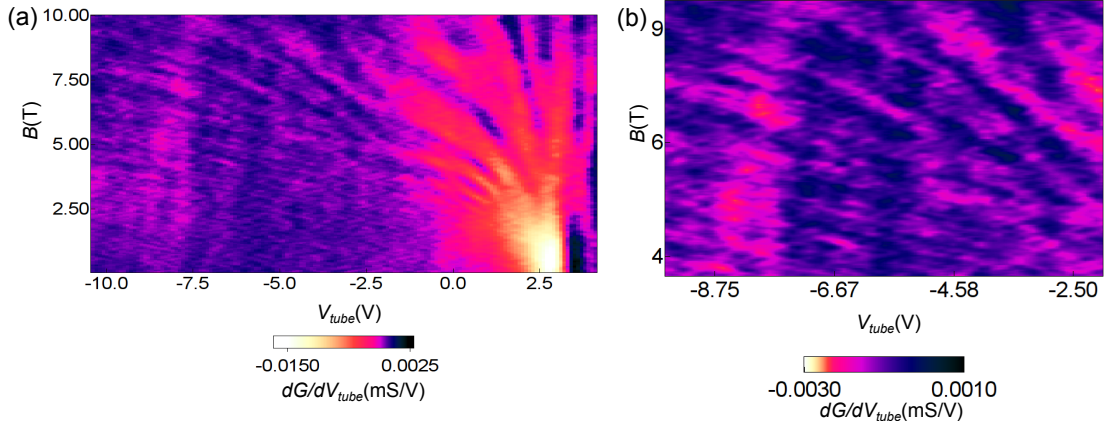


Figure 3.25: (a) Landau fan graph tube gate vs.  $B$ . (b) The splitting Landau level features. It is a zoom in figure from (a).

region where it is only affected by the top gate. The reason is that the top gate is much larger than the tube gate. To see the feature more clearly, the background subtracted data is shown in Figure c. The dashed line with circle on top points out the main Dirac point which is controlled by both two gates. Interestingly, there are four more dips on either side of the main Dirac point feature. They are marked with arrows in the graph. These dips may arise from extra Dirac points predicted by the theory.

In Figure 3.27, these graphs are the line traces of conductance vs. tube gate voltage at different top gate voltage. Except the main Dirac points, extra dips are pointed out by arrows.

In Figure 3.28, the magneto-transport measurement is performed in this device. The  $X$  axis is the top gate and  $Y$  axis is the magnetic field. There are some extra Landau levels in (a) which we applied 4V on the tube gate. Some Landau level splits at top gate -3 V and magnetic field 3.2 T. When a different tube gate voltage is applied to the device, the

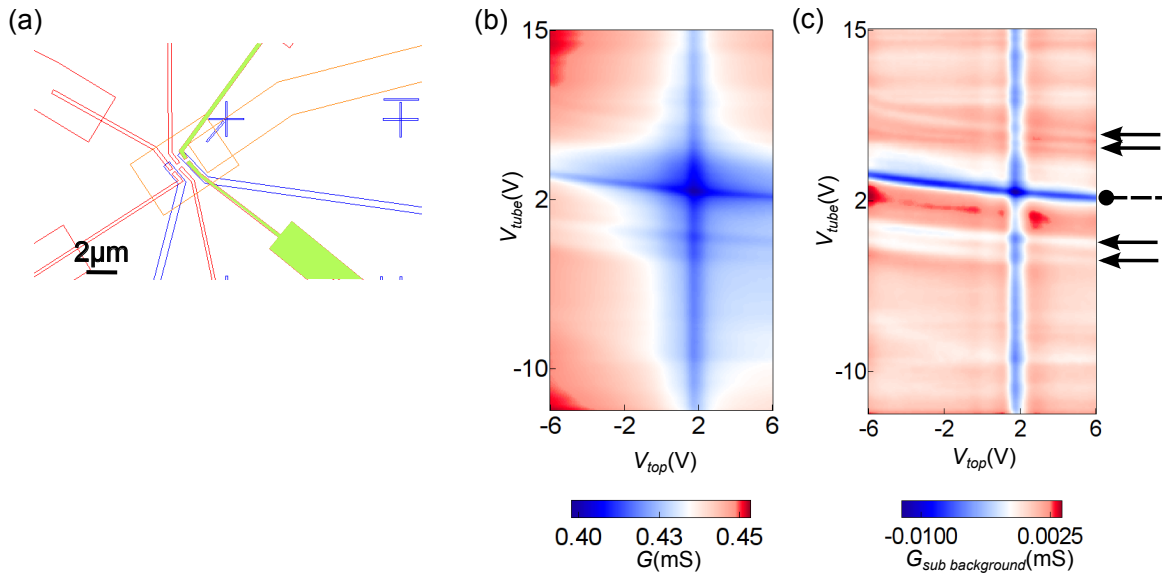


Figure 3.26: (a) Device schematic. (b) Conductance vs. two gates. (c) Same data as (b) after background subtraction. Except the main Dirac point pointed by dashed line, there are several extra dips shown by black arrows.

landau fan features have also been changed. First, the extra Landau levels have disappeared.

Second, the landau Level splitting is more strong at hole side  $B=3.75$  T.

### 3.7 Conclusion

In these 1D periodic devices, the collimation has been demonstrated. We also have some evidences of extra Dirac points.

The parallel SWNTs is also a useful experiment technique to provide 1D periodic potentials. Some interesting magneto-transport data has been observed, like extra Landau levels, Landau level splitting etc.

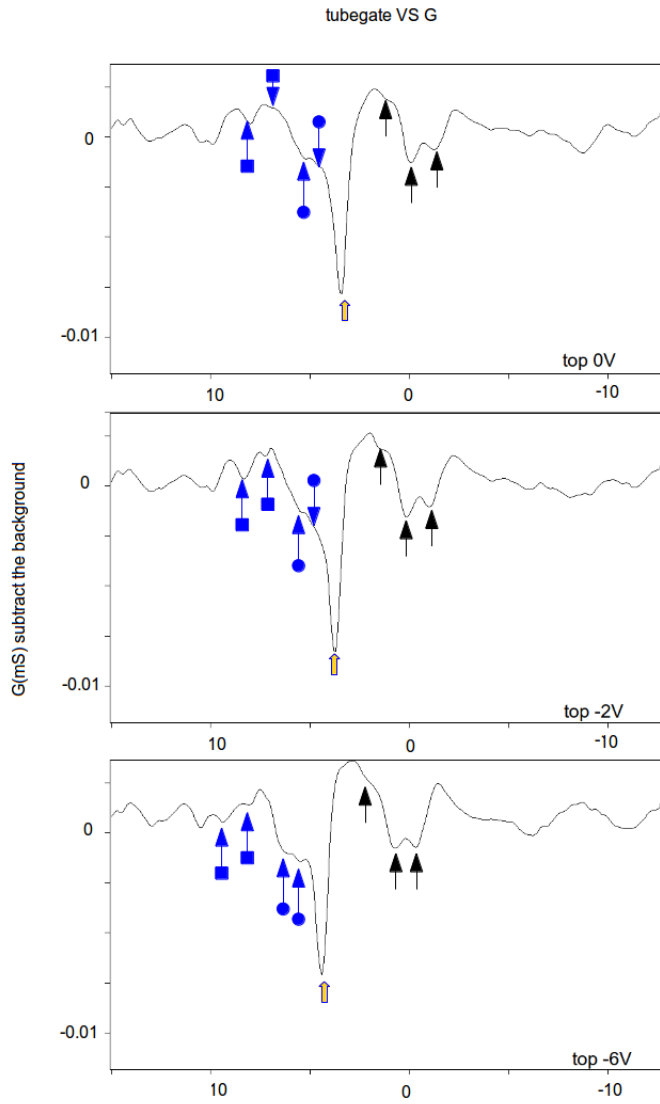


Figure 3.27: The tube gate vs. conductance at different top gate. The possible Dirac points are indicated by arrows.

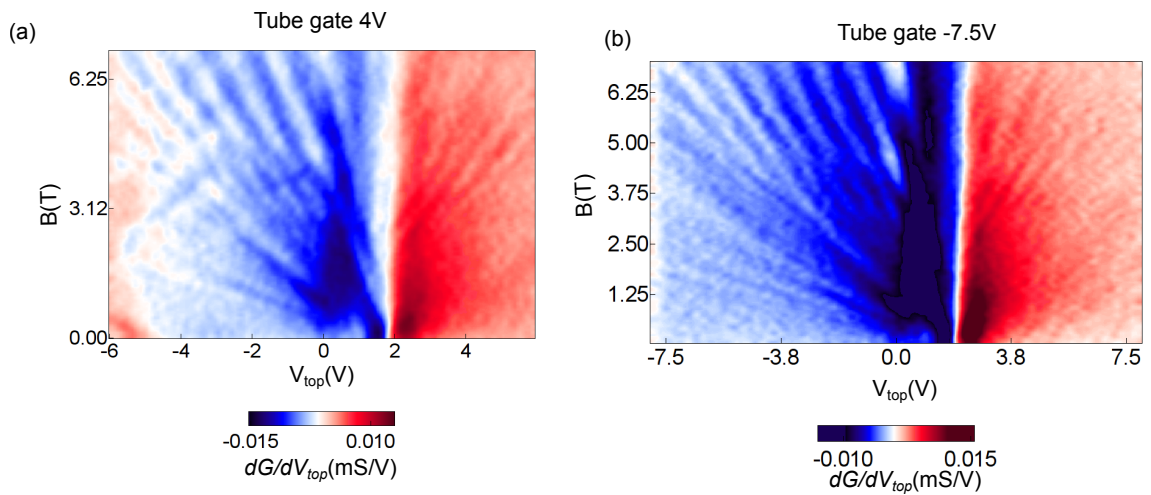


Figure 3.28: The Landau fan of top gate voltage versus  $B$  with different tube gate voltage.

## Chapter 4

# Trilayer Graphene

### 4.1 Abstract

When under a perpendicular magnetic field and a periodic potential, two-dimensional electron systems will have a self-similar fractal energy spectrum. When graphene is placed on BN with a small rotation angle, it forms such a two dimensional system [14] [25] [56] [67]. This fractal spectrum is known as Hofstadter's butterfly [24].

In this chapter, a trilayer graphene sample aligned with BN with a small rotation angle ( $0.6^\circ$ ) will be introduced. Except the main Dirac points, six additional Dirac points from mini bands and their Landau levels are formed. The Hofstadter's butterfly pattern in charge density and magnetic field, as well as its transport properties under electrical field with fixed magnetic field will be introduced.

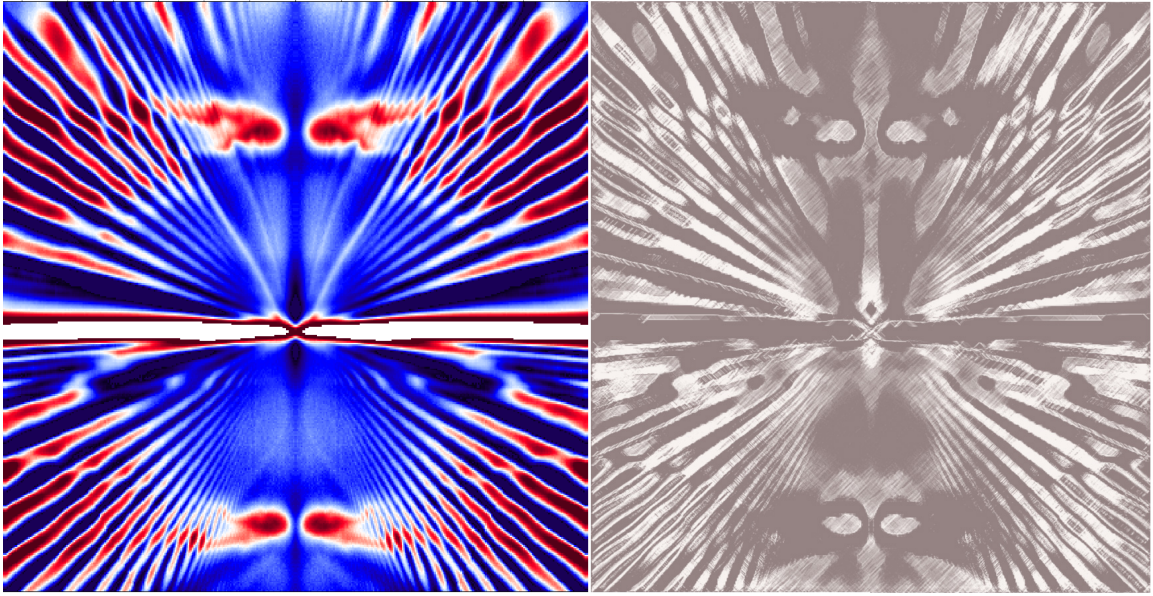


Figure 4.1: Two Landau fan diagrams form a "butterfly" pattern.

## 4.2 Introduction

The concept of Hofstadter's butterfly is originally described by an American professor of cognitive science Douglas Hofstadter (who is also a physicist) - best known as a Pulitzer-prize winner. In 1976, he calculated the energy levels of electrons under a magnetic field in a 2D lattice [24]. The most interesting thing in this system is energy bands is a fractal structure when magnetic length is of order the periodic unit cell.

In the past 40 years, people had designed different experiments to catch this butterfly. Until in the graphene/BN system, people finally get the evidence from the transport measurements. Due to the small mismatch of lattice constant in graphene ( $a = 0.246$  nm) and BN ( $a = 0.250$  nm), the superlattice form a moiré pattern providing a periodic modulation.

Figure 4.2 shows a morié pattern formed from graphene on BN with a small rotation angle. The superlattice is visible.

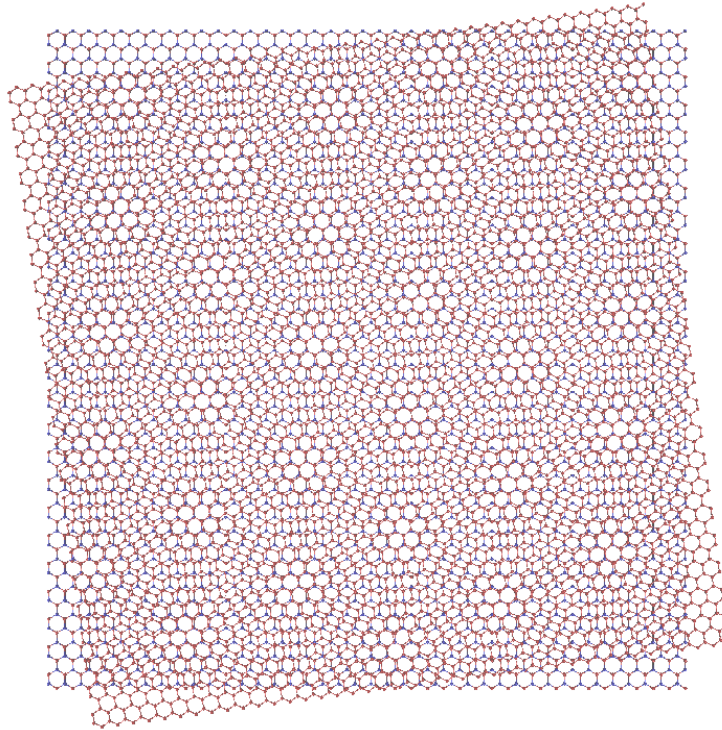


Figure 4.2: The morié pattern of a graphene layer on top of BN with a small rotation angle.

To understand the physics picture of Hofstadter's butterfly, let us start from the very beginning - the Bloch waves. A Bloch wave is a type of wave function for a particle in a periodic environment (like periodic potentials) [3]. The wave function  $\psi$  has the form,

$$\psi(\vec{r}) = e^{i\vec{k}\cdot\vec{r}} u(\vec{r})$$

where  $u$  is a periodic function with the same period as the environmental lattice.

And its band filling factor  $s$  is given by [44],

$$s = -A_0^2 \frac{\partial n(\varepsilon_F)}{\partial A_0}$$

$A_0$  is the periodic unit cell volume.

The free electron under magnetic field will have quantum cyclotron orbits (Laudau Levels) [35]. The Hamiltonian is,

$$H = \frac{(p - eA/c)^2}{2m}$$

And the energy and orbit are quantized,

$$\varepsilon(n) = (n + 1/2)\hbar\omega_c$$

The magnetic quantum flux in each orbit is,

$$\phi_0 = \frac{hc}{e}$$

and the radius of the cyclotron orbit is,

$$l_B = \sqrt{\hbar/eB}$$

so the filling factor  $\nu$  is,

$$\nu = 2\pi l_B^2 n(\varepsilon_F)$$

basically it has the similar physics like the filling factor in Bloch wave.

Combining Landau's quantum cyclotron orbits and the Bloch wave functions, Harper's equation describes this physics [23]. It is actually the competition of two length scales - the quantum magnetic orbit length  $l_B$  and the lattice constant  $a$ .

The Hamiltonian can be written as,

$$H = \frac{(\vec{p} - e\vec{A}/c)^2}{2m} + U(\vec{r})$$

resulting in the Harper's equation,

$$E\psi_l = \psi_{l+1} + \psi_{l-1} + 2\psi_l \cos(2\pi lb - \kappa) \quad (4.1)$$

From the Harper's equation 4.1, we can get the Hofstadter's butterfly [24]. When  $b$  in the equation equals to  $p/q$ , where  $p, q$  are co-primes, each LL will split into  $q$  sub-bands with  $p$ -fold degenerated. Energy bands develop fractal structure (Hofstadter's butterfly) when magnetic length  $l_B$  is of order the periodic unit cell  $a$ .

Electrons subjected to both a periodic electric field and a magnetic field can be described by the dimensionless ratio  $\phi/\phi_0$ , where  $\phi = BA_0$  is the magnetic flux per unit cell and  $\phi_0 = h/e$  is the magnetic flux quanta. The energy dispersion exhibits a complicated fractal pattern due to the incommensurate periods of the Bloch (lattice constant  $a$ ) and Landau states (magnetic length  $l_B$ ). For commensurate fields, at  $\phi/\phi_0 = p/q$ , the Landau level band splits into  $q$  subbands.

The energy gaps in the Hofstadter's butterfly can be described as Wannier diagram [68]. The equation for the location of energy gaps in Wannier diagram is,

$$\frac{n}{n_0} = t \frac{\phi}{\phi_0} + s \quad (4.2)$$

where  $t$  and  $s$  are integers.

We then may ask, what is the meaning of these two integers? The  $s$  variable is the band filling factor  $s = -A_0^2 \frac{\partial n(\epsilon_F)}{\partial A_0}$  which has introduced before, while  $t$  is the quantum hall conductance  $\sigma_{xy} = ec \frac{n(E)}{B} |_{E=E_F} = \frac{e^2}{h} t$ .

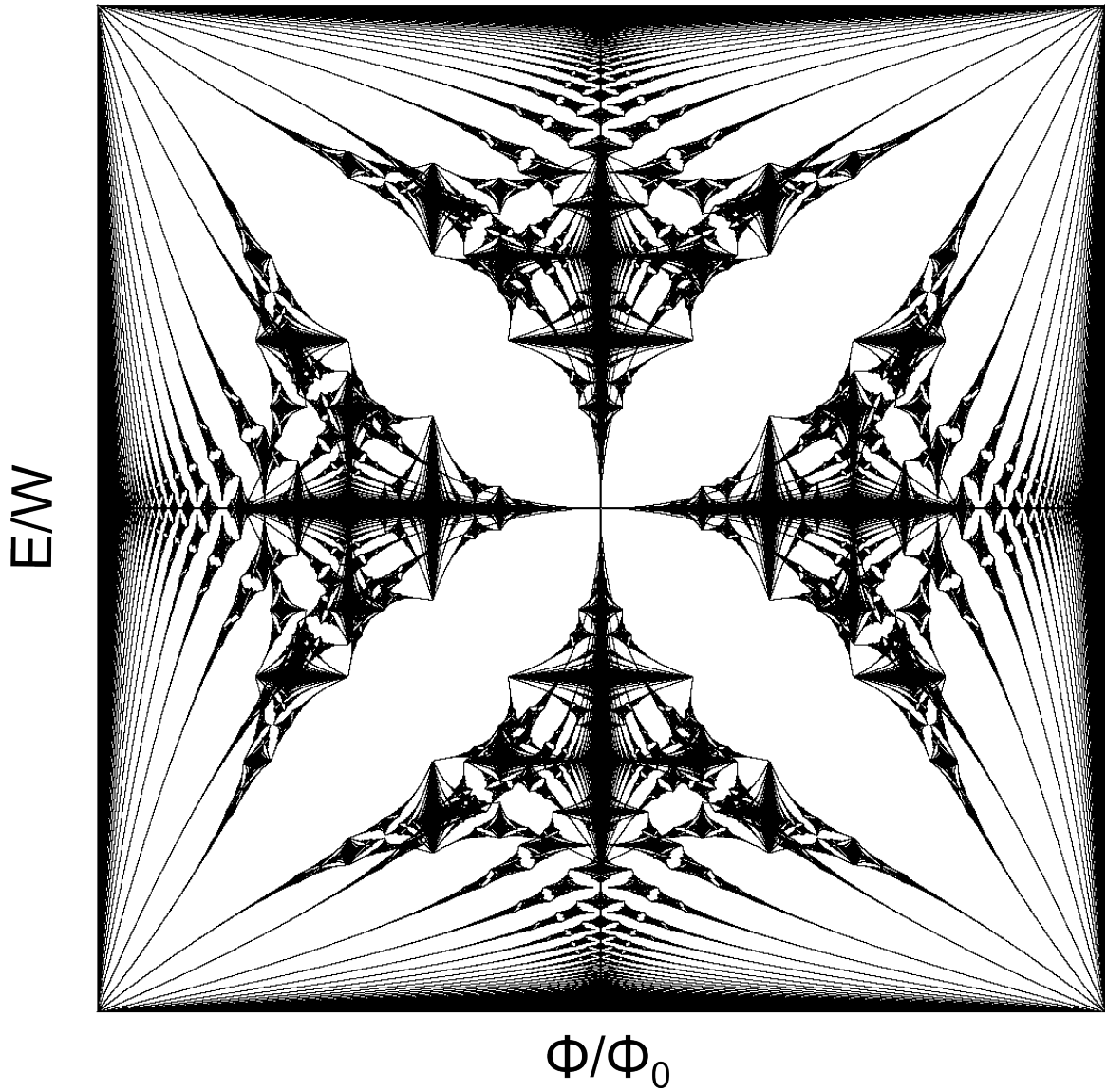


Figure 4.3: The energy diagram - Hofstadter's butterfly. The X is  $\Phi/\Phi_0$  and Y is  $E/W$ , which W is the band width.

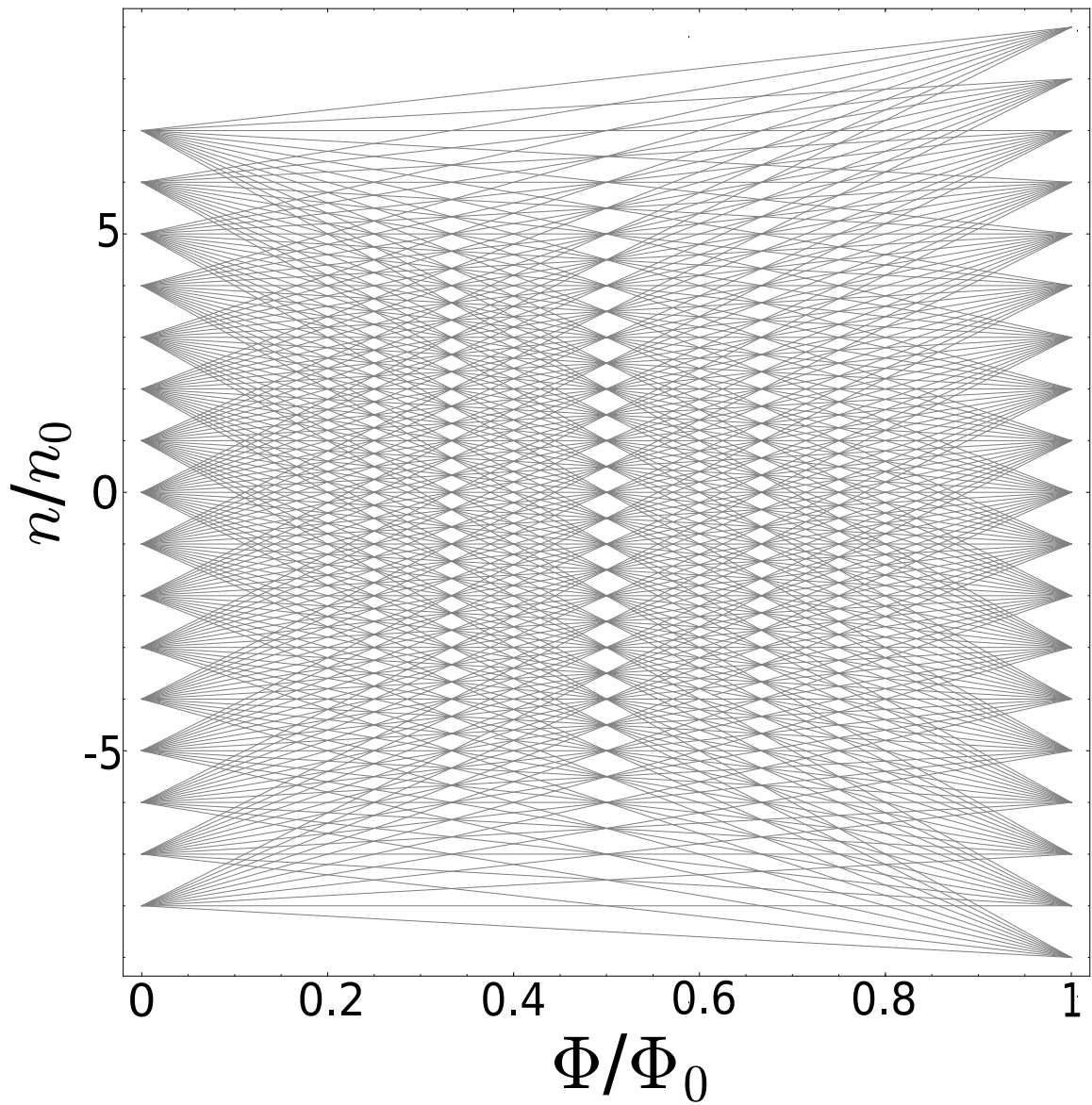


Figure 4.4: The Wannier diagram. The  $X$  axis is the ration of magnetic flux per unit cell with quantum flux. The  $Y$  axis is the ratio of carrier density  $n$  versus the  $n_0 = \frac{1}{\text{unit-cell-area}} = \frac{1}{\frac{\sqrt{3}}{2}a^2}$ .

And we have the relations,

$$\frac{\phi}{\phi_0} = \frac{BA_0}{\phi_0} = \frac{eB\sqrt{3}a^2}{2h} \quad (4.3)$$

and,

$$n_0 = \frac{1}{\text{unit-cell-area}} = \frac{1}{\frac{\sqrt{3}}{2}a^2} \quad (4.4)$$

When the magnetic length equals the superlattice scale ( $\frac{\phi}{\phi_0} = 1$ , there is 1 flux quanta per unit cell area), then  $B_0$  is equal to

$$B_0 = \frac{2h}{\sqrt{3}ea^2} \quad (4.5)$$

According to the Wannier equation 4.2 and the band filling model, the morié wavelength can be determined from the satellite Dirac point position on the carrier density axis,

$$\frac{n_{sat}}{n_0} = g_v g_s \quad (4.6)$$

the  $n_{sat}$  is the position of satellite Dirac point and  $n_0 = \frac{1}{A_0} = \frac{1}{\sqrt{3}a^2/2}$  with a the morié pattern wavelength.  $g_s$  is the electron spin degeneracy and  $g_v$  is the valley, or pseudo spin, degeneracy.

The  $n_{sat}$  can be calculated according to a standard parallel plate capacitor model to be,

$$n_{sat} = \frac{C_g(V_{sat} - V_{CNP})}{e}$$

where  $C_g$  is the geometric capacitance,  $V_{sat}$  is the voltage of the second Dirac point position and  $V_{CNP}$  is the voltage of main Dirac point. Putting this relation back into equation 4.6, and with  $g_s, g_v$  are both 2 in graphene,

$$a = \frac{8e}{\sqrt{3}C_g(V_{sat} - V_{CNP})} \quad (4.7)$$

And the morié wavelength  $a$  (superlattice wavelength) has the relation to the rotation angle  $\varphi$  between graphene and BN,

$$a = \frac{1.018a_{graphene}}{\sqrt{2.306(1 - \cos\varphi) + 0.018^2}} \quad (4.8)$$

and  $a_{graphene}$  is the graphene lattice constant which is 0.246 nm.

### 4.3 Trilayer Graphene BN Superlattice - Additional Dirac Points

This device is fabricated with a BN/Trilayer-graphene/BN sandwich structure with a top gate. The contacts are made by edge contacts technique. The trilayer graphene is Bernal- or ABA-stacked.

The line trace of longitudinal resistance  $R_{xx}$  versus the carrier density  $n$  at zero electrical field shows the multiple Dirac points in Figure 4.5. The mobility estimated from the data is  $350,000 \text{ cm}^2\text{V}^{-1}\text{s}^{-1}$  (quantum hall mobility is around 50,000 in the same units). The left inset is the hall bar structure and the measurement set up for the device. The right inset is the schematic diagram of superlattice Brillouin zone (red hexagon) and its related graphene Brillouin zone (blue hexagon) in the  $k$ -space.

From the line trace, the second Dirac point is at  $n_{sat} = 3.25 * 10^{12} \text{ cm}^{-2}$ . Putting this  $n_{sat}$  back into equation 4.6, we get

$$n_0 = \frac{n_{sat}}{4} = \frac{1}{\frac{\sqrt{3}}{2}a^2} = 0.8125 * 10^{12} \text{ cm}^{-2}$$

and

$$a = 11.921 \text{ nm} \quad (4.9)$$

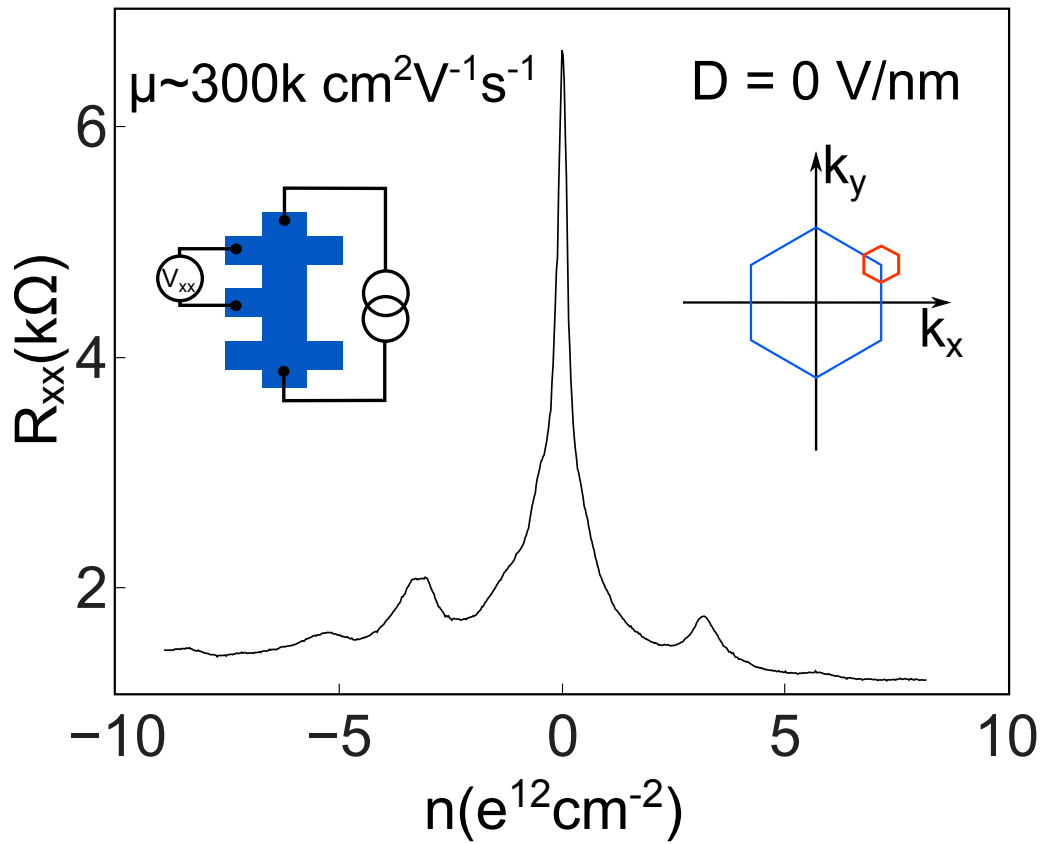


Figure 4.5: The line trace of  $R_{xx}$  versus carrier density  $n$  at  $D = 0 \text{ V/nm}$ . The mobility of device is around  $300,000 \text{ cm}^2 \text{V}^{-1} \text{s}^{-1}$ . Extra Dirac points are visible. The left inset is the device measurement set up. The right inset is the Brillouin zone of superlattice (red hexagon) and graphene (blue hexagon) in  $k$ -space.

Then we put the super-lattice wavelength back into equation 4.8, the rotation angle between trilayer graphene and BN in this sample is,

$$\varphi = 0.579^\circ \quad (4.10)$$

So the magnetic field where there is one flux quanta per unit cell area is (equation 4.5),

$$B_0 = \frac{2h}{e\sqrt{3}a^2} = 33.6T \quad (4.11)$$

Figure 4.6 shows the dual gate sweep of the  $R_{xx}$ . The electrical field on the sample changes in the figure and the extra Dirac points are more clearly visible. The Figure 4.6a is the color plot of  $R_{xx}$  versus the back gate and top gate. The main Dirac point feature is the red area in the center. The gap at main Dirac point increases when the electrical displacement  $D$  increases. The secondary Dirac points on two sides and third Dirac point at hole side is visible in this figure. To see the extra points more clearly, Figure 4.6b and Figure 4.6c are plotted. Figure 4.6b is the same data with log scale. The broadening of main Dirac point is strong along the displacement field. The additional Dirac points are more easily observed in this figure. The Figure 4.6c is basically the same as figure b but with a smaller range color bar to make small features more visible. The second, third and fourth Dirac points (7 Dirac points including the main Dirac point) for electron and hole doping are marked with the green dashed lines. The third and fourth Dirac points on the electron side are not very visible in this figure, so we zoom in on the yellow rectangle area in Figure 4.6d. The two Dirac points are marked with green dashed lines again. Figure 4.6e is the schematic diagram of the measurement set up which is a typical Hall bar  $R_{xx}$  measurement.

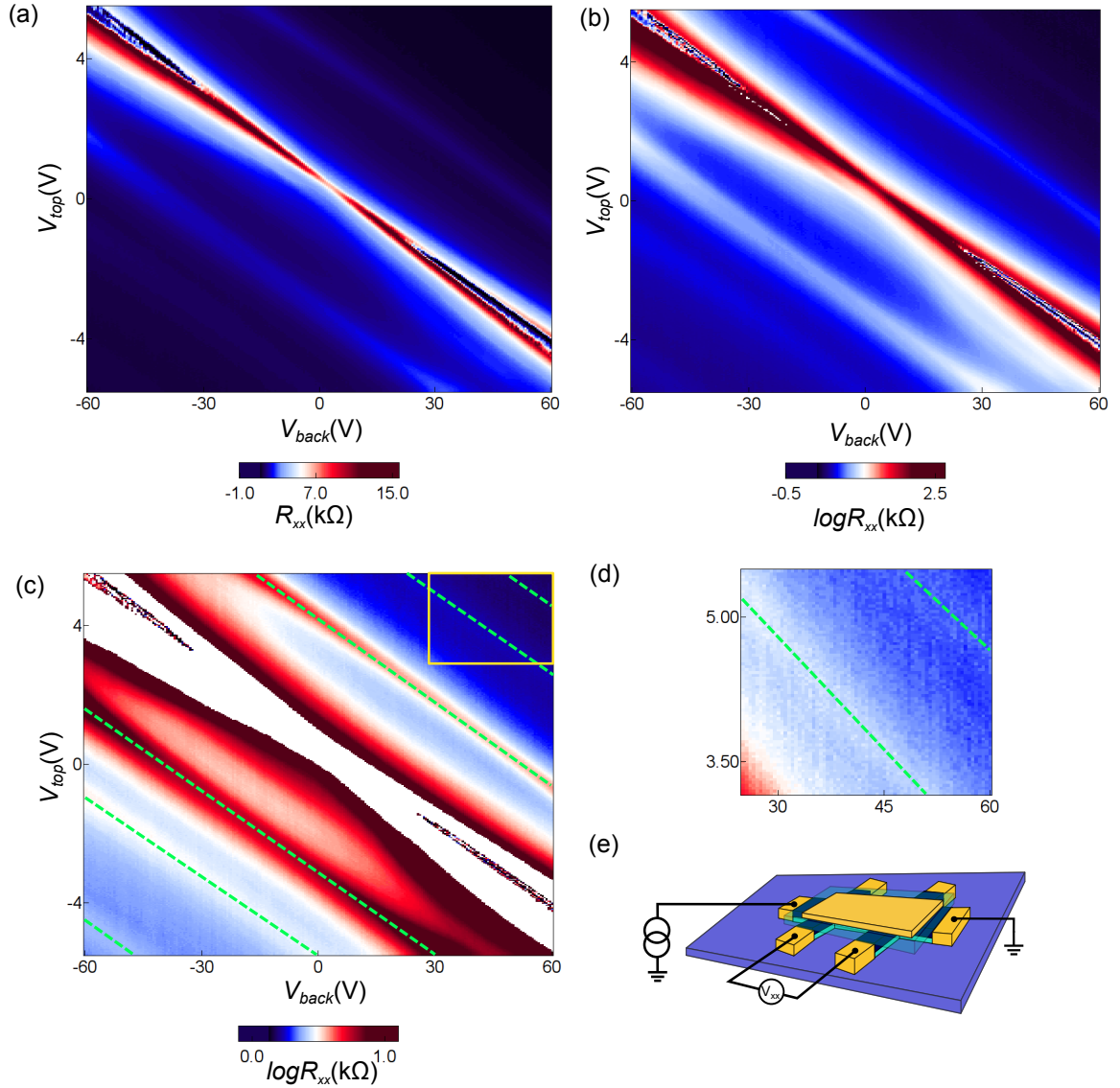


Figure 4.6: Color plot of longitudinal resistance versus two gates. (a)  $R_{xx}$  versus top gate voltage and back gate voltage. (b)  $R_{xx}$  on a log scale. (c)  $R_{xx}$  on a log scale with a different color bar. The extra Dirac points are shown in green dashed lines. There are seven Dirac points features in total including the main Dirac point. (d) Zoomed-in figure of the yellow rectangle area in (c). The third and fourth Dirac points are shown in green dashed lines. (e) Schematic graph of measurement setup.

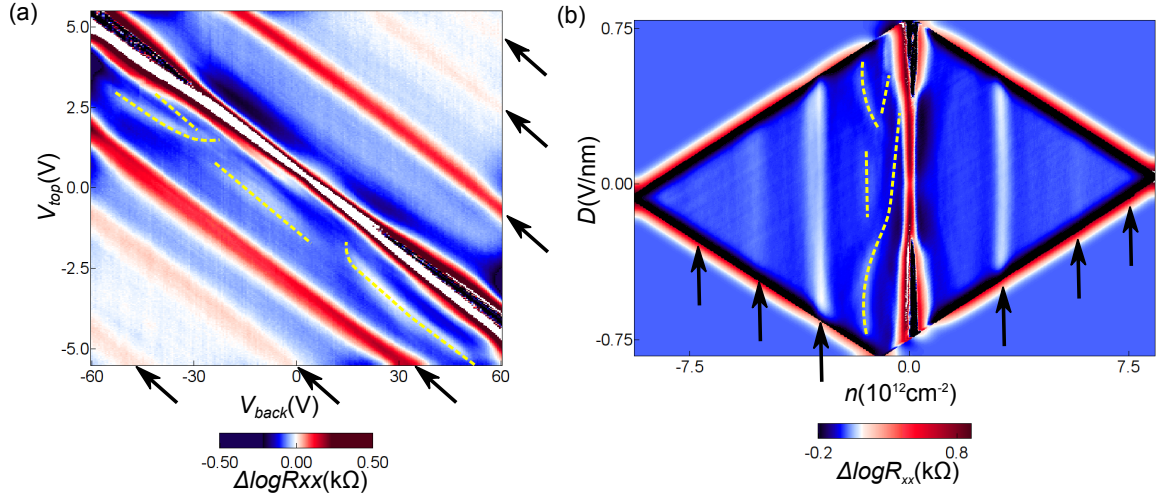


Figure 4.7: Color plot of  $R_{xx}$  on a log scale versus the two gate voltages (a), carrier density and the electric displacement field (b). The black arrows indicate the extra Dirac points. The yellow dashed lines are some features shown up after subtract the background.

To study the details more carefully, we subtract the background in the Figure 4.6 to get Figure 4.7. The left graph is the color plot of  $\Delta \log R_{xx}$  versus two gates and the right graph is the same data versus electric displacement field and carrier density. The black arrows point out the unambiguous extra Dirac points in two figures. Interestingly, some additional features are shown by the yellow dotted lines. These yellow lines are non-linear along the electric displacement field. The two yellow lines at high electric displacement field merge into the main Dirac point. And one straight feature shows at low electric displacement field and disappears when the  $D$  increasing. Moreover, this feature shows a strong electron-hole asymmetry. This feature could be from the massless band of the trilayer graphene or electron-electron strong interaction which we will talk later in following sections.

In our device, the signal from extra Dirac points on that hole side is stronger than on the electron side. It is the same as experiments reported before in single layer or bilayer graphene aligned samples as well as theory.

Figure 4.8 shows the line trace along different Dirac points in (a) - two gates versus  $\log R_{xx}$ . The figure (b) is the line trace along the main Dirac point (green line 1 in (a)) with  $D$  as X axis and  $\log R_{xx}$  as Y axis. The  $R_{xx}$  increases along the  $D$  at first then decrease. This phenomenon is observed from experiments [72] and theory [32]. The figure (c) and (d) are the line traces along second Dirac points (yellow line 2 and 3 in (a)). Figure (c) is the electron side second Dirac point line trace. There is a small dip at negative electrical field. Figure (d) is the hole side second Dirac point line trace. There is an unambiguous dip at zero electric field. The resistance increases as the electric field increases.

## 4.4 Two Gates Pattern at Different Magnetic Field

### 4.4.1 Dual Gate Sweep Pattern at $B = 9$ T

Then a dual gate sweep under a magnetic field at 9 T is taken. Semiclassically, the electron energy states will collapse onto cyclotron orbits at magnetic field which leads to Landau Levels (LLs).

Figure 4.9 shows the data under the magnetic field at 9 T. The Landau levels yield energy gaps that follow straight lines corresponding to a minimum of  $R_{xx}$ . The figure (a) is the color plot of  $\log R_{xx}$  versus the top gate and back gate. The main Dirac point is shown as the red feature in the center. Other high resistance strips may be from the

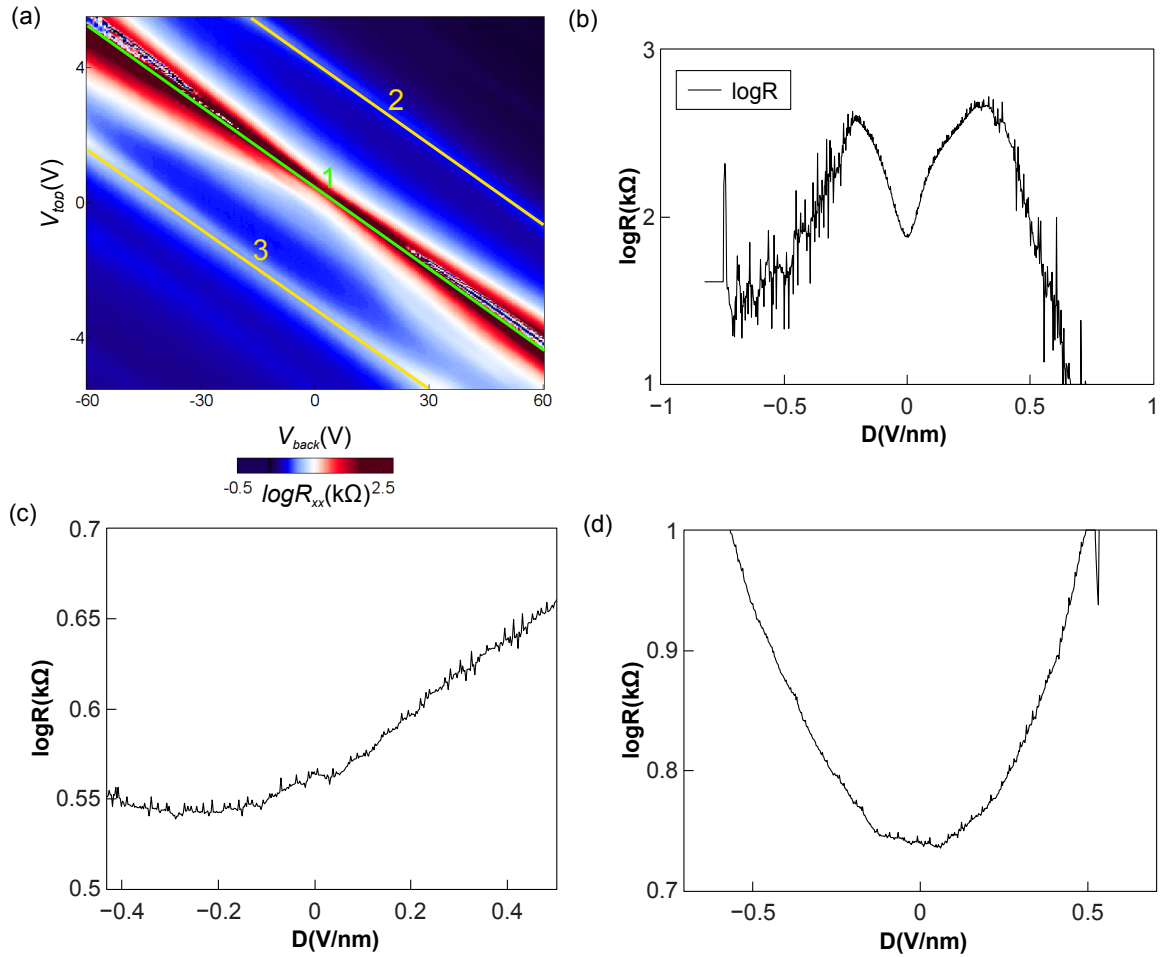


Figure 4.8: The line traces along different Dirac points. The green line 1 is along the main Dirac point (b). The yellow line 2 and 3 are along the second Dirac points (c and d). The first figure (a) color plot of  $\log R_{xx}$  versus two gates.

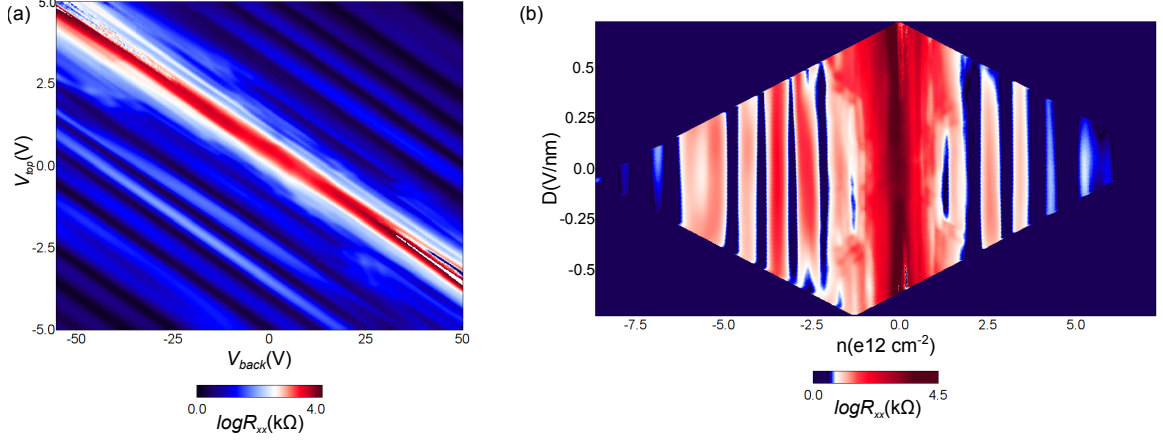


Figure 4.9: (a) The color plot of  $\log R_{xx}$  versus the top gate and back gate. Gaps between Landau Level is shown as a minimum at  $R_{xx}$  signal. (b) The color plot of  $\log R_{xx}$  versus the electric displacement field and carrier density. The Landau Level features are vertical dark color strips in the figure.

secondary Dirac points. The Landau level features are shown in the figure as dark strips. Some small features are visible near the main Dirac point. These are similar to the phase transitions that can be tuned by a transverse electric field. Similar behaviors have been reported in bilayer graphene system [37] [45]. This feature will be explained in detail later. The figure (b) is the same data of  $\log R_{xx}$  with two different axes, the carrier density  $n$  and the electric displacement field  $D$ . The Landau levels are vertical minimum strips along the carrier density. The phase transitions near the main Dirac point are tunable along the transverse electric field.

The equation we used to calculate electric field is,

$$D = (C_{TG}V_{TG} - C_{BG}V_{BG})/2\epsilon_0 - D_0 \quad (4.12)$$

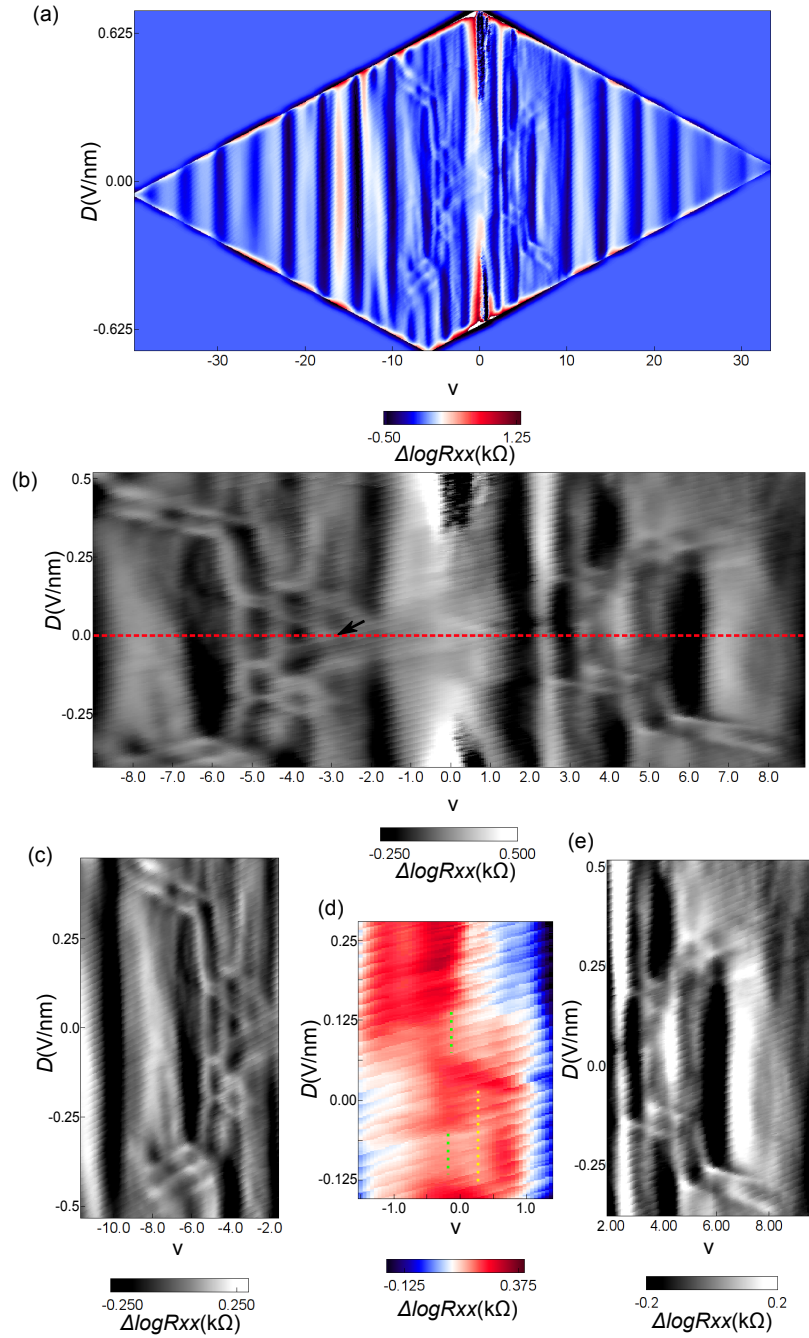


Figure 4.10: (a) Color plot of  $\Delta \log R_{xx}$  versus the filling factor and electric field. (b) The zoom-in figure of the center phase transition area. (c) Phase transition area in the hole side. (d) The transition around zero filling factor. (e) Phase transition area in the electron side.

where  $C_{TG}$  is the top gate capacitance per area,  $C_{BG}$  is the back gate capacitance per area,  $V_{TG}$  and  $V_{BG}$  are gate voltages at the top and back gates and  $D_0$  is the residual displacement field due to doping.

This equation is from the carrier density of parallel capacitors model,

$$n = (C_{TG}V_{TG} + C_{BG}V_{BG})/e - n_0 \quad (4.13)$$

where  $n_0$  is the residual doping in the equation.

And we know,

$$n = \frac{B\nu}{h/e} = \frac{Be\nu}{h}$$

so,

$$\nu = \frac{nh}{eB} \quad (4.14)$$

In this way, all the two gates data have been transferred to carrier density versus electric displacement field to study how the Landau levels changing with the electric field.

Figure 4.10a shows the color plot of  $\log R_{xx}$  with a smooth background subtracted versus the filling factor and electric field. The Landau levels still produce clear vertical dips in the figure. The phase transitions at low filling factors are unambiguous. This "X" shape phase transitions comes from the massless band of the ABA trilayer graphene. Phase transitions features are different from the transitions reported in bilayer graphene [45] [37].

Figure 4.10b is the central transition area in figure (a). The gap at filling factor  $\pm 6$  and  $\pm 2$  are larger. The trilayer graphene should have 12-fold degeneracy at zero LL energy in the absence of symmetry breaking. These degeneracies have all been broken at 9 T. The transition features are clear. They may be related to both massive band and massless band

of trilayer graphene. Two different bands contribute the filling factor together. Interestingly, unlike bilayer graphene, the transitions here show a strong hole-electron asymmetry. The red dashed line is the zero electric field. Along this line, the gaps at each integer filling factor are opened except  $\nu = -3$  which is pointed out by the black arrow ( $\nu = \pm 1, 0$  are not very visible). This behavior is also different from the bilayer. In bilayer graphene, the odd filling factors' gaps are closed at zero electric field.

Figure 4.10c and Figure 4.10e are the zoom-in figure for the hole side and electron side separately. These two figures clearly describe the asymmetric transitions between two sides. The hole side figure shows many unambiguous transitions in a complicated pattern not only at small  $D$  near  $\nu = -4$  but also at large electric field near  $\nu = -6$  and  $\nu = -8$ . The features at small electric field near  $\nu = -6$  and  $\nu = -8$  will also be interesting, because they are away from the massless band "X" feature. For the electron side, the transitions are simple comparing to the hole side. But the gap at, for example  $\nu = -3$ , is more clear on comparison to the hole side. Instead of many hexagonally shaped transition regions, the transitions at electron side are more like several lines connecting gaps.

Figure 4.10d is the area close to zero filling factor and small electric displacement field. The green dashed lines follow gaps at zero filling factor between the transitions. The yellow dashed line is interesting, because its position is right between the filling factor 0 and 1. This feature, if it is reproduced, could be from the interaction between two bands (massive and massless band) which leads to partial filling at the Landau level.

Figure 4.11 is also the color plot of  $\Delta \log R_{xx}$  but at a smaller area with a slower sweep rate. The features are basically the same, except some features are more clear. For

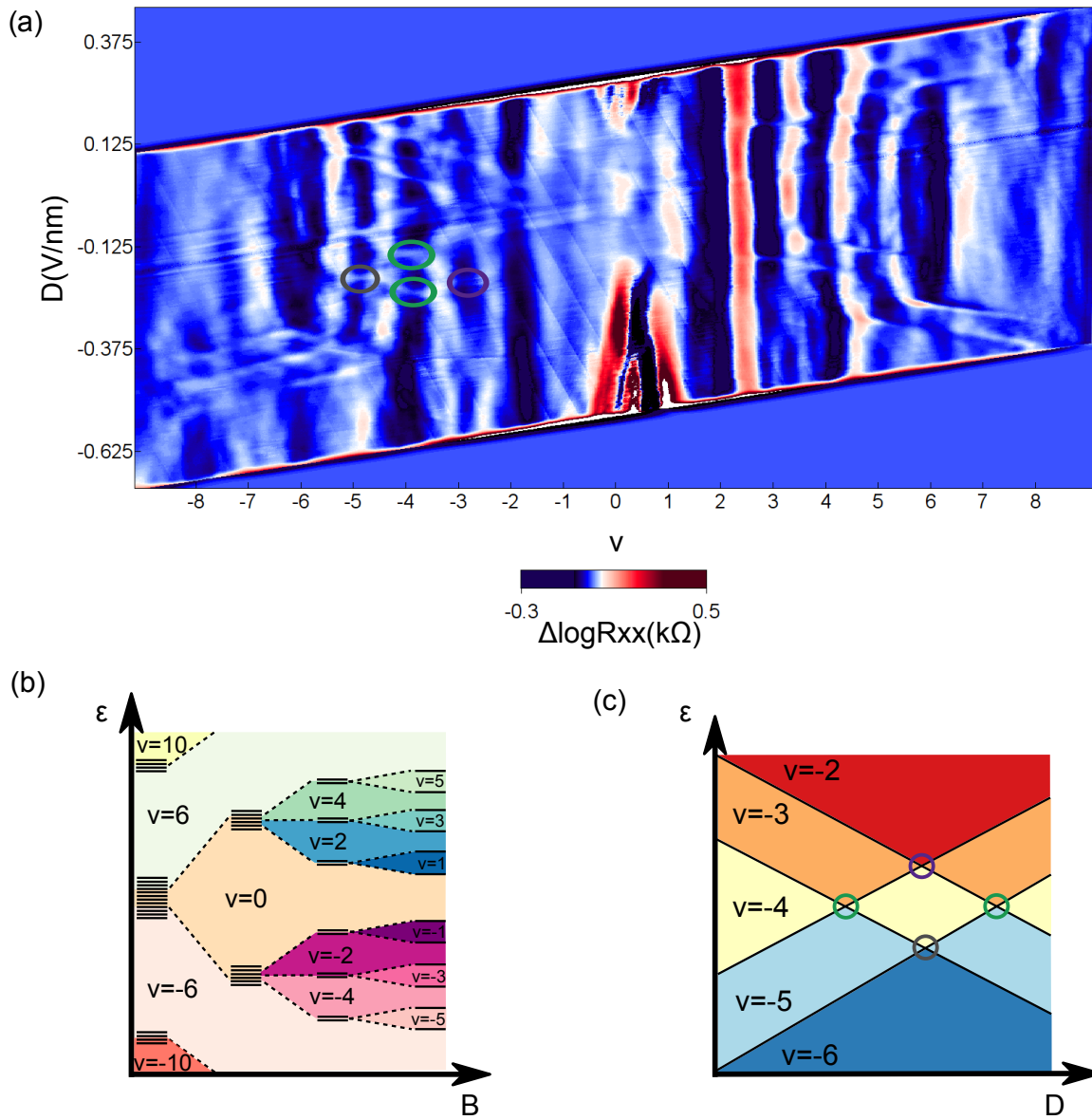


Figure 4.11: (a) Color plot of  $\Delta \log R_{xx}$  at small area. (b) The schematic diagram of 12-fold degeneracies breaking along the magnetic field. (c) The schematic diagram of phase transitions near filling factor  $\nu = -4$ .

example, some transitions look like a single line that turns into two lines in this figure. Inside the gap, like  $\nu = 6$ , there are some additional features inside.

The inset (b) in Figure 4.11 is the schematic diagram of how the 12-fold degeneracy is broken under the magnetic field. This suggests that different symmetry-breaking processes are relevant as  $B$  increases while the gaps appearing at the same time. The inset (c) is the schematic diagram of how the transitions happening around the filling factor  $\nu = -4$ . The four circles in the diagram are four different transitions. Two green circles are the transitions show in figure (a) with green ellipses. The purple circle is the transition at  $\nu = -3$  which is the purple ellipse in (a). The gray circle is the transition at  $\nu = -5$  which is the gray ellipse in (a).

To analyze these transitions, we use a simple independent two band model. The number  $m$  is the filling factor for the massive band and  $n$  is the filling factor for the massless band. We assume they will independently be filling the bands for the trilayer. So the total filling factor  $\nu = m + n$ . Because the massive band is kind of a bilayer graphene band, so it may split at particular states into two or more different bands we call  $m_1$  and  $m_2$ .

Figure 4.12 shows the possible state filling for this model. Figure 4.12a is the schematic diagram of state filling and real data at hole side. The first number in the diagram is the filling factor  $m$  in the massive band. And the second number in the diagram is the filling factor  $n$  in the massless band. There are some states, for example, the bottom one at  $\nu = -4$  has the  $m_1$  and  $m_2$ . The gray area is the area where gap closed. Figure 4.12b is the same analysis at the electron side. The electron-hole asymmetry is obvious.

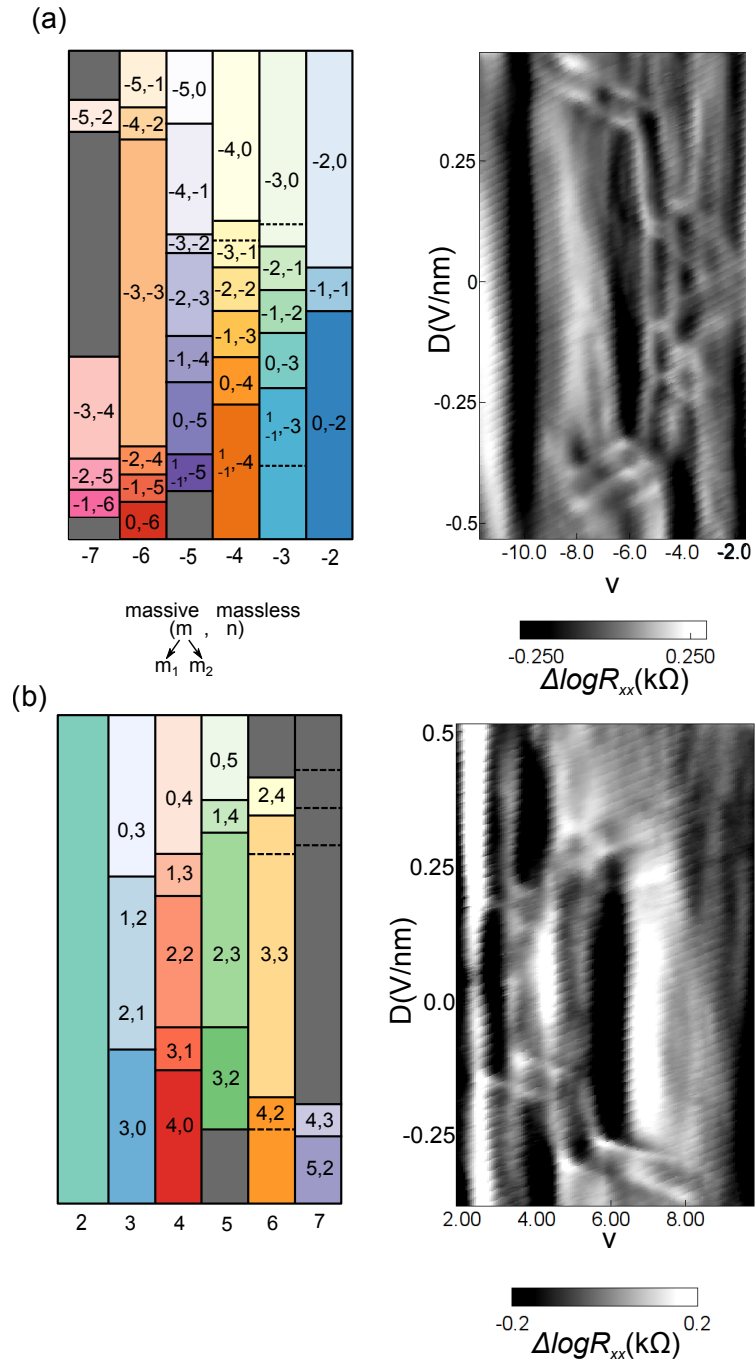


Figure 4.12: The transitions and its schematic diagram with different filling states at hole side (a) and electron side (b).

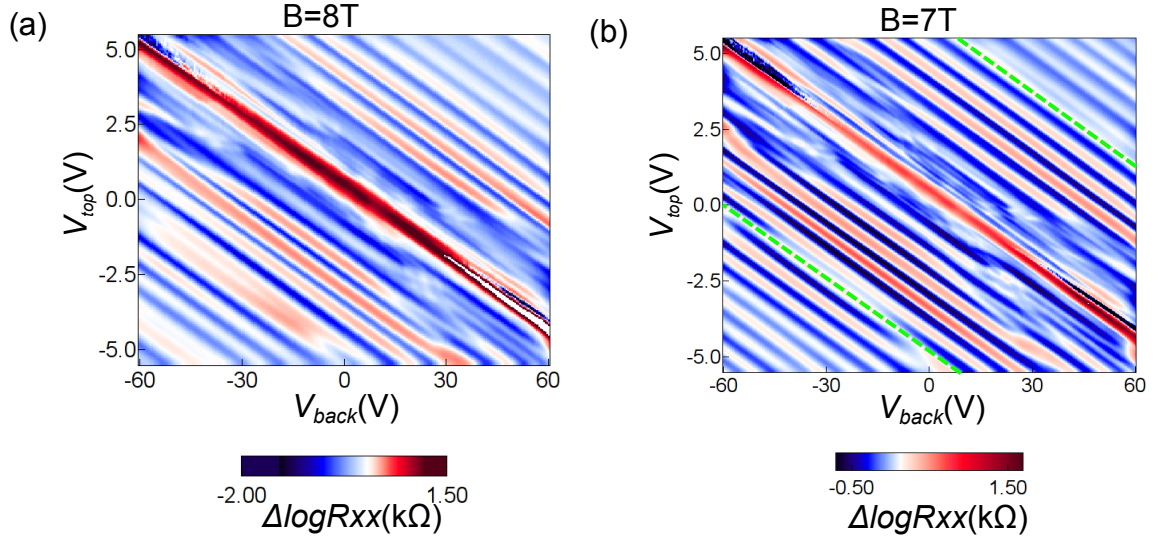


Figure 4.13: Two gates versus the  $\Delta \log R_{xx}$  at  $B = 8$  T (a) and  $B = 7$  T (b) separately.

#### 4.4.2 Dual Gate sweeps Pattern at $B = 7$ T

In this sub-section, the similar data was taken like previous sub-section but with a lower magnetic field.

At first, Figure 4.13 shows the two gates sweep versus the  $\Delta \log R_{xx}$  at  $B = 8$  T and  $B = 7$  T separately. The transitions are still visible at lower magnetic field. Some transitions at high electric field disappeared at 7 T compared to 8 T. But, at the second Dirac points (green dashed lines at figure b), the transition is different between these two.

Here, we will analysis the  $B = 7$  T data and focus on the details which are not the same as the data at 9 T.

Figure 4.14a is the color plot of  $\log R_{xx}$  versus the filling factor  $\nu$  and electric displacement field  $D$ . Figure 4.14b is the color plot of  $\Delta \log R_{xx}$ , which is (a) with a background

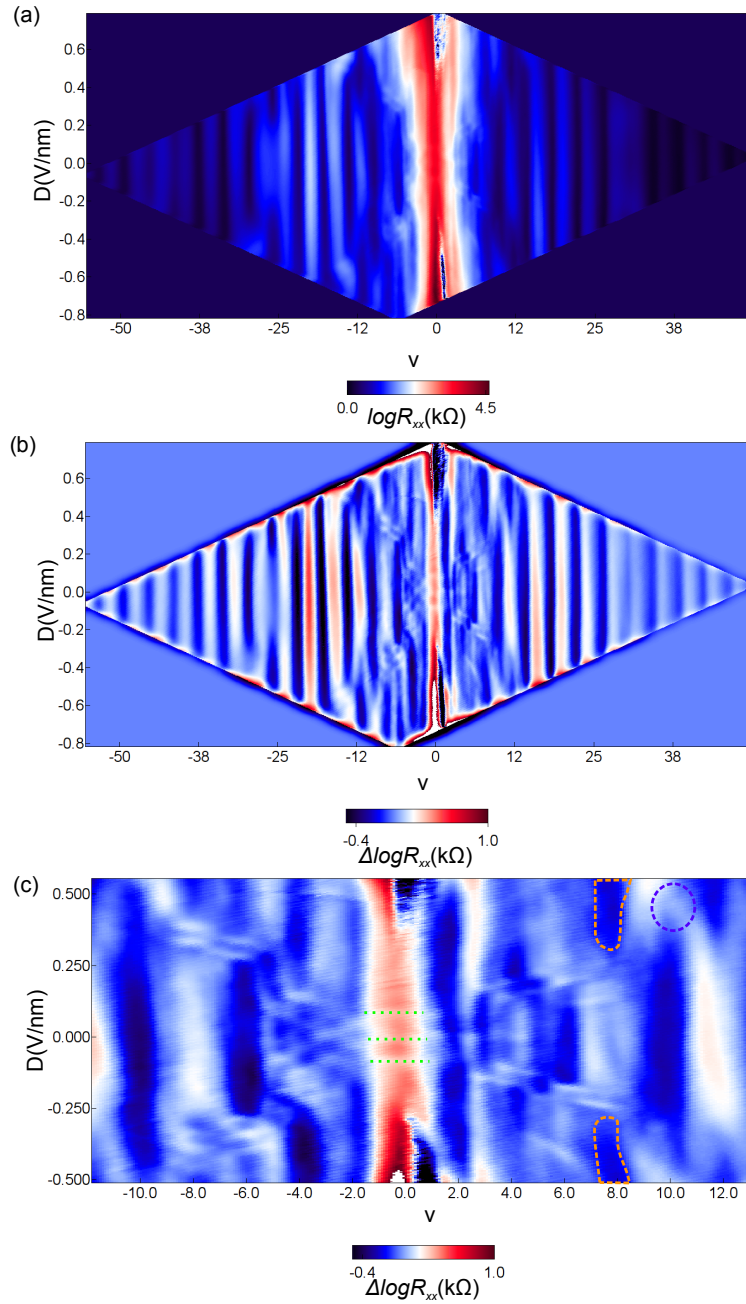


Figure 4.14: (a) Filling factor and  $D$  versus the  $\log R_{xx}$  at  $B = 7$  T. (b)  $\nu$  and  $D$  versus  $\Delta \log R_{xx}$ . (c) Center transition area of (b).

subtraction, versus the  $\nu$  and  $D$ . The "X" shape transition is visible, but it appears smaller in the plot compared to at large magnetic field. Because there will be another "X" shape non-linear transition band in the following section, we call this one Transition A (TA). This only occurs inside the  $\nu = \pm 8$ . Interestingly, there is another transition beyond this TA becomes visible at filling factor  $\nu = \pm 12$ . This one is non-linear and continuous. We call this transition transition B (TB) for the convenience. This feature is stronger at low magnetic field. We will discuss this one later. Figure 4.14c is the zoom-in figure of the TA transition area in (b). At first, as mentioned before, this transition area is smaller than  $B = 9$  T. Several repeatable details are interesting. For example, there are 3 transition lines at hole side with negative  $D$  and 2 transition lines at hole side with positive  $D$ . At electron side, they are just opposite. There are 3 transition lines at positive  $D$  and 2 lines at negative  $D$ . The two sides transitions pattern is basically the same as  $B = 9$  T. There are still some minor details difference, for example, there are another two transitions at  $\nu = 6$  (one around  $-0.5$  V/nm, the other around  $0.5$  V/nm) beyond the TA. At  $\nu = 0$ , there are three transitions cross the area from  $\nu = -1$  to  $\nu = 1$  (green dashed lines). This might come from the superlattice. The BN layer aligned with bottom graphene breaks the symmetry especially with finite electric field. That is why on one side of electric field it has 3 transition lines while on the other side it only has 2. Two gaps (orange dashed area) start to show up due to the contraction of the TA. The transitions at  $\nu = \pm 10$  are also visible but only one transition point without details.

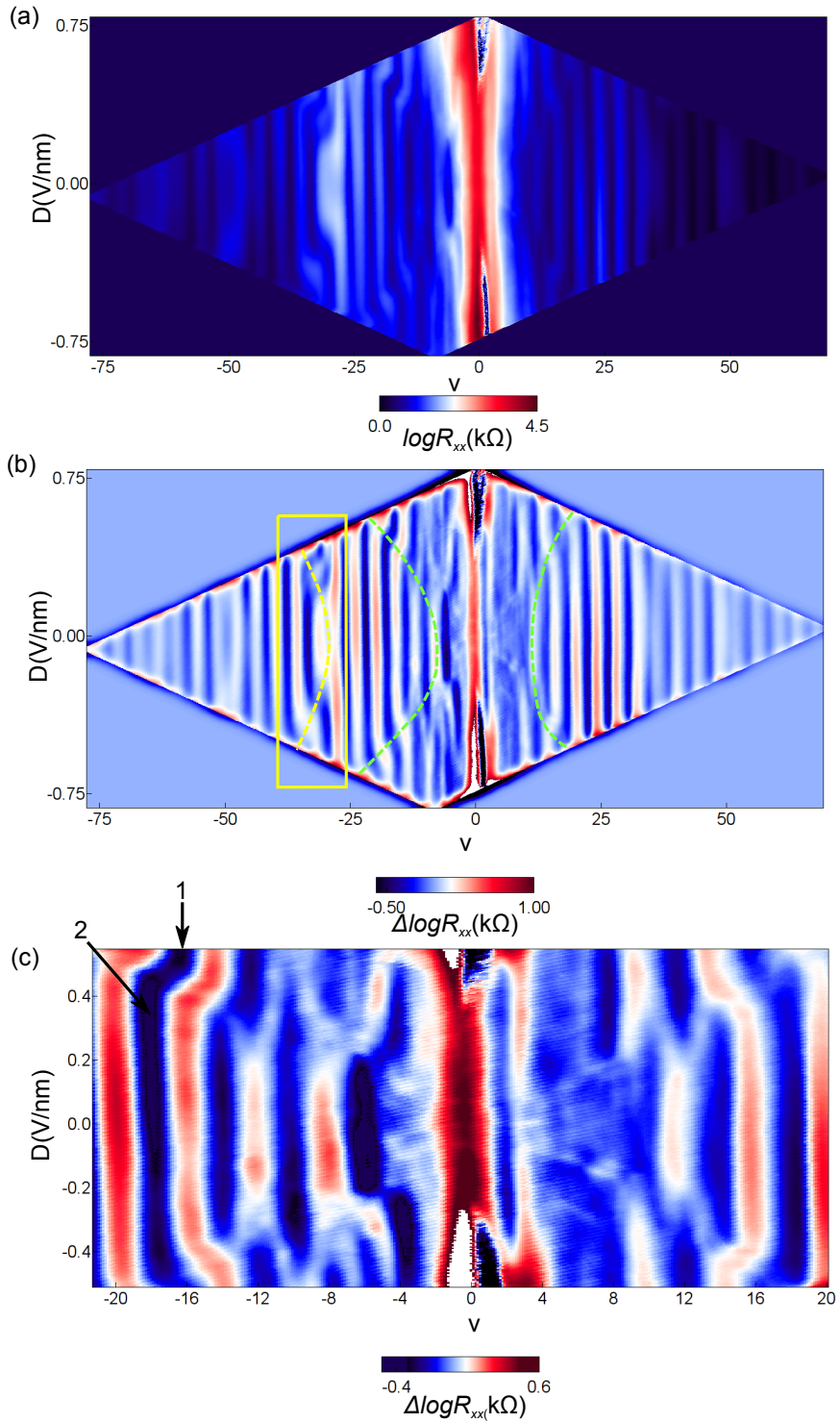


Figure 4.15: (a) Filling factor and  $D$  versus the  $\log R_{xx}$  at  $B = 5$  T. (b)  $\nu$  and  $D$  versus  $\Delta \log R_{xx}$ . (c) Center transition area of (b).

### 4.4.3 Dual Gate Sweep Pattern at $B = 5$ T

In this subsection, the data is taken in the same way but with  $B = 5$  T.

Figure 4.15a shows the color plot of  $\log R_{xx}$  versus the filling factor  $\nu$  and electric displacement field  $D$ . At the second Dirac points (around  $\nu = \pm 25$ ), there are also some phase transitions. Even at the third Dirac point (around  $\nu = -50$ ), the phase transitions are visible at high electric displacement field. Figure 4.15b is the color plot of  $\Delta \log R_{xx}$  versus the  $\nu$  and  $D$ . The TA is limited in a small area close to the main Dirac point. The TB is more clear here (two dashed green arcs). The yellow rectangle area is where the second Dirac is. A possible TB is shown in this area (yellow dashed arc). Figure 4.15c is the center transition area of (b). The TA is still visible but the details are blurred. The TA is also limited inside the  $\nu = \pm 8$ . Let us focus on the LLs near filling factor  $\nu = -16$ . Two black arrows marked with 1 and 2 are shown in figure. The arrow NO.1 is the gap outside the TB with filling factor  $\nu = -16$ . This gap shifts to the blue strip marked with the arrow 2 with filling factor  $\nu = -18$ . Considering the degeneracy of spin and valley which is 4, the shift here is a  $\pi$  phase shift.

## 4.5 The Non-linear Massless Landau levels under Electrical Field at Low Magnetic Field

### 4.5.1 The Evolution of Massless Landau levels with Magnetic Field

The phase transitions evolved with the magnetic field as discussed before. In this subsection, we will lower the magnetic field to 1.5 T and focus on the changing of the phase transition shape.

Figure 4.16 shows the evolution of the transition LLs. At high field (a and b), the TA is quantized and gives us a complicated phase transition limited inside the  $\nu = \pm 8$ . At lower magnetic field (c and d), the TA and TB are both visible and the TA is becoming weaker while TB is becoming stronger. At very low magnetic field (e and f), only TB is visible. The TB likes waves propagate along the  $X$  axis. The second/third Dirac points are fixed and interfered with the TB waves. The details of this TB transition will be discussed in next subsection.

### 4.5.2 The Non-linear Massless Landau levels under Electric Field at Low Magnetic Field

$B = 3 \text{ T}$

Figure 4.17 shows the filling factor and  $D$  versus the  $\Delta \log R_{xx}$  in (a). (b) and (c) are zoom-in figures of the black dashed rectangle and red dashed rectangle area separately. The TB type transitions are marked with black arrows in figure (b). The orange five-point star is a gap with filling factor  $\nu = -16$  and it shifts to the gap marked with an orange

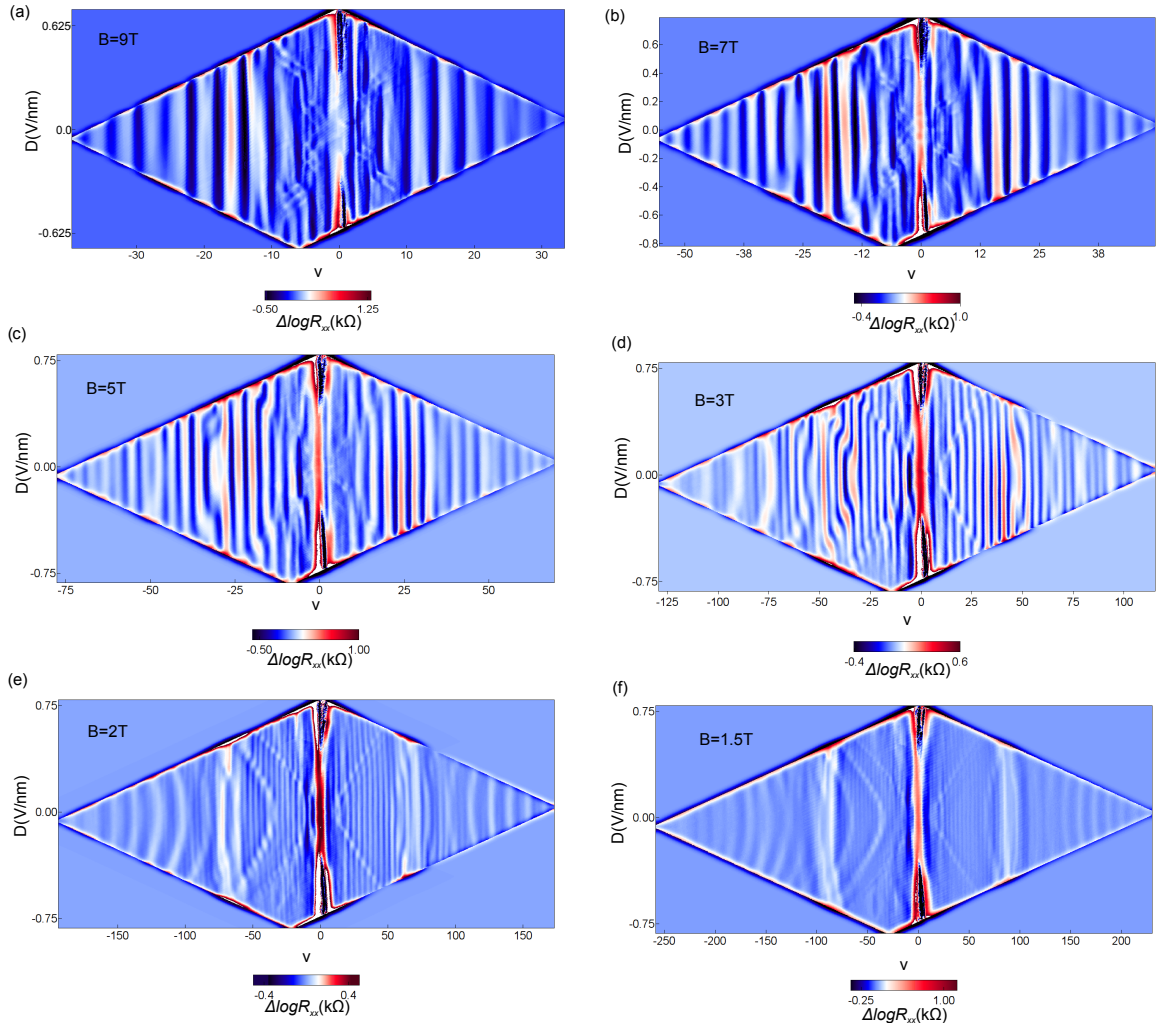


Figure 4.16: (a) Filling factor and  $D$  versus the  $\log R_{xx}$  at  $B = 5$  T. (b)  $\nu$  and  $D$  versus  $\Delta \log R_{xx}$ . (c) Center transition area of (b).

six-point star with filling factor  $\nu = -18$  after crossing the TB line. It is a shift of a step of  $\nu = 2$ . Considering the degeneracy of spin and valley, the shift is a  $\pi$  phase shift.

The position of the aqua five-point star is a gap with  $\nu = -34$ . It crosses another TB line and shifts to the aqua six-point star with  $\nu = -38$ . The step changed to 4 in this TB transition line. The same thing happens at the spring green five-point star ( $\nu = -54$ ) shifting to the spring green six-point star ( $\nu = -58$ ).

In Figure 4.17c, there are also a  $\pi$ -shift TB and a  $2\pi$ -shift TB. The purple five-point star ( $\nu = 16$ ) shifts to six-point star ( $\nu = 18$ ) and triangle ( $\nu = 16$ ) again after crossing the  $\pi$ -shift TB twice. The pale green gap shifts from  $\nu \approx 46$  to  $\nu \approx 50$  and  $\nu \approx 46$  again.

### **B = 2 T and B = 1.5 T**

Figure 4.18a is the color plot of the  $\Delta \log R_{xx}$  versus the filling factor  $\nu$  and electric displacement field D. Black arrows indicate the transitions with  $\pi$ -shift (2 transitions close to the main Dirac point) and  $2\pi$ -shift separately. The left inset is the zoom-in figure around the second Dirac point at the hole side. The right inset is the zoom-in figure around the second Dirac point at the electron side. Almost all the TB transitions appears like "waves" propagating towards the main Dirac point. But around the second Dirac points, several arcs toward the other direction are found. No matter how the magnetic fields changes, the distance between the main Dirac point and second Dirac point is fixed in carrier density scale.

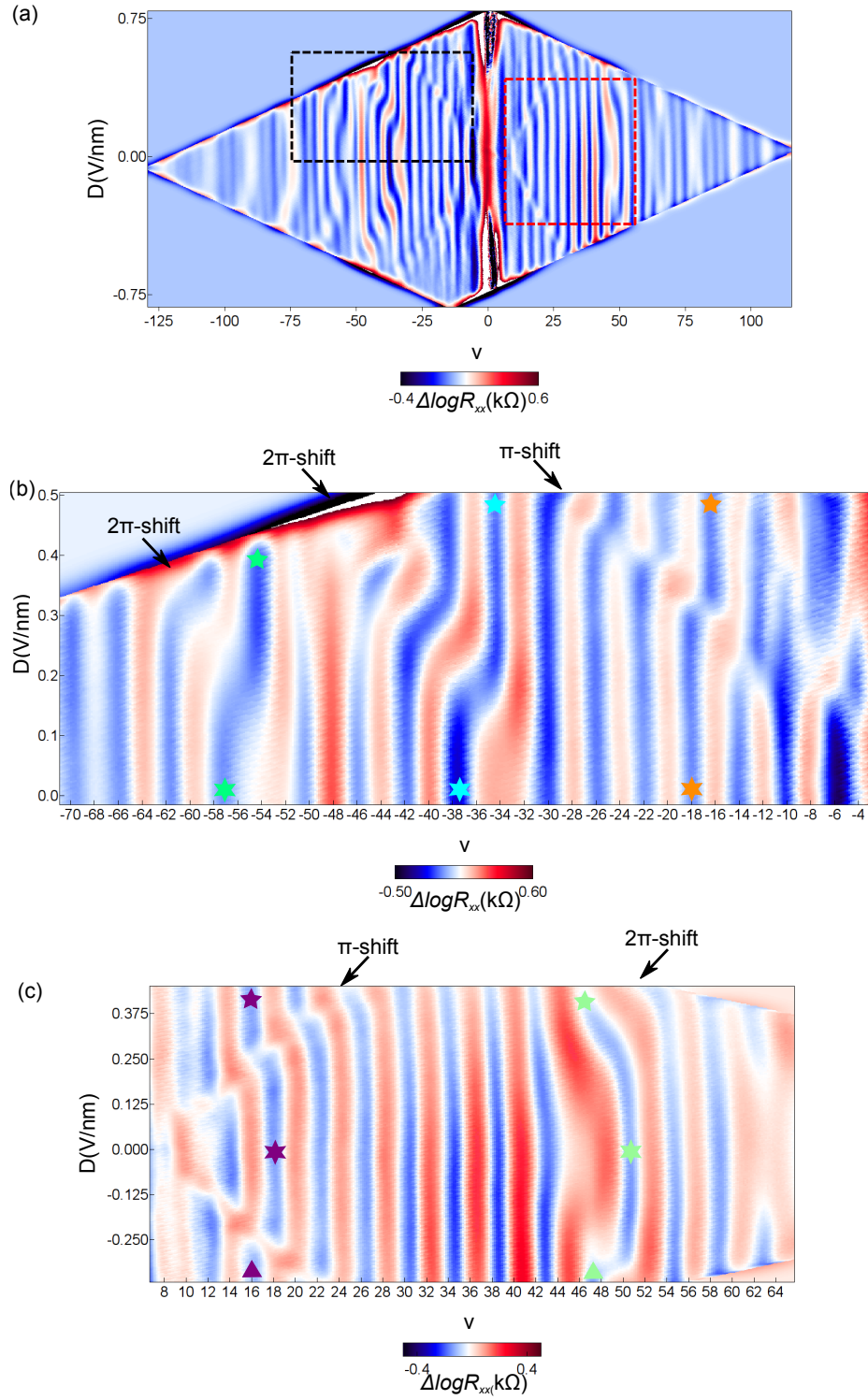


Figure 4.17: (a) Filling factor and  $D$  versus the  $\Delta \log R_{xx}$  at  $B = 3$  T. (b) The zoom-in figure of black rectangle. (c) The zoom-in figure of red rectangle.

Figure 4.18b and c are the zoomed-in figures of the red dashed rectangle and green dashed rectangle separately. In figure (b), the transition lines split into two lines instead of one. The gaps are splitted into three regions marked five-pointed star, triangle, six-points star separately. At first, the gap has a filling factor  $\nu \approx -28$ . After crossing the first line (triangle), it has a filling factor  $\nu = -27$ . Finally, the  $\nu = -26$  (six-pointed star) appears again after crossing the second transition line. The same thing happens in figure (c). The transition line becomes split at positive electric field at electron conducting side. One gap (five-points star) crosses the two TB lines at positive  $D$  (triangle and six-pointed star) and crosses one TB line at negative  $D$  (four-pointed star). The filling factor at five-points star is  $\nu = 20$ . It is 21 and 22 at triangle and six-pointed star place. Then  $\nu$  goes back to 20 after crossing the TB line at negative  $D$ . And this kind of symmetry breaking may due to the bottom graphene aligned with BN. The top graphene and bottom graphene layer feels a different potential from BN. The electric displacement field will increase the interaction between the bottom BN and bottom layer of graphene which lead to this symmetry breaking.

Figure 4.19 is the color plot of  $\Delta \log R_{xx}$  versus the filling factor and  $D$ . More arc features are visible in this figure. The left inset is the zoom-in figure around the second Dirac point at hole side. The reversed arc features are clear. The right inset is the zoom-in figure around the second Dirac point at the electron side. The backwards waves are also visible. The interference between the second Dirac points and TB is also clearly visible. The reason of backwards arcs could be there is a similar "massless" band from the secondary Dirac points just like the one from the main Dirac point.

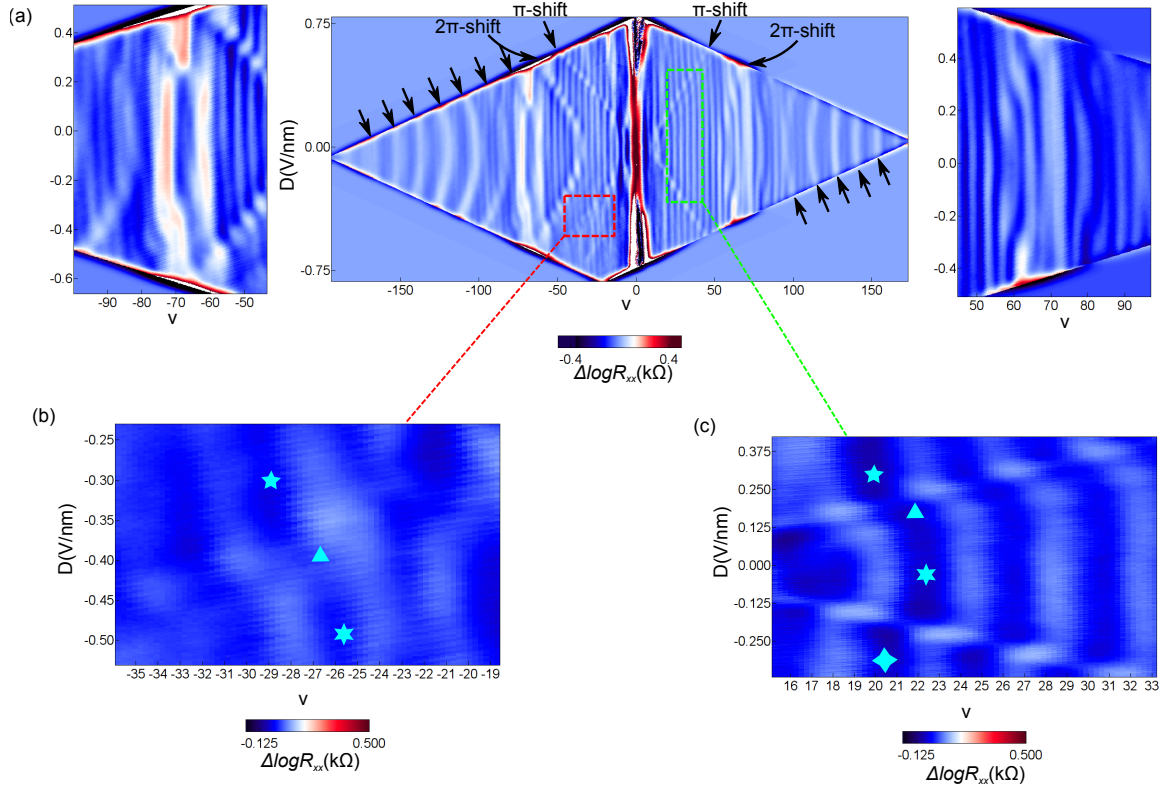


Figure 4.18: (a) Filling factor and  $D$  versus the  $\Delta \log R_{xx}$  at  $B = 2$  T. The two insets are zoomed-in figures around the second Dirac points. (b) Zoomed-in figure corresponding to the red rectangle. (c) Zoomed-in figure corresponding to the green rectangle.

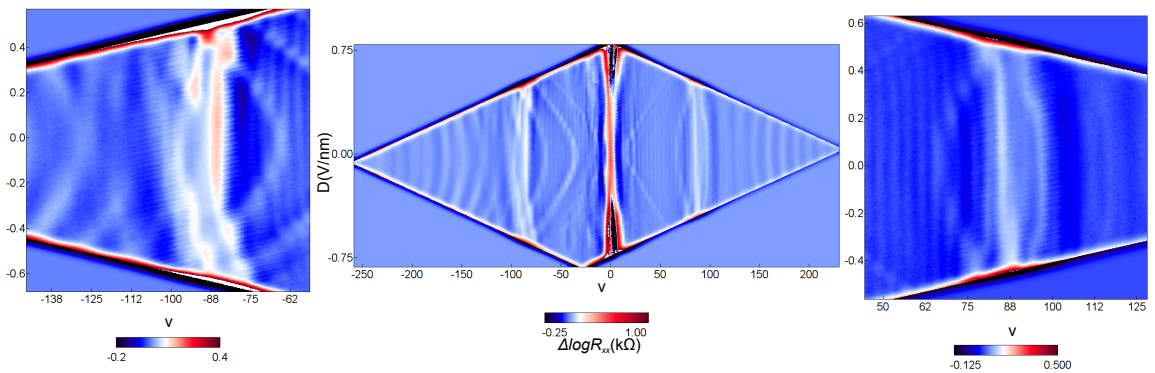


Figure 4.19: Filling factor and  $D$  versus the  $\Delta \log R_{xx}$  at  $B = 1.5$  T. The two insets are taken from around the secondary Dirac points at hole side (left) and electron side (right).

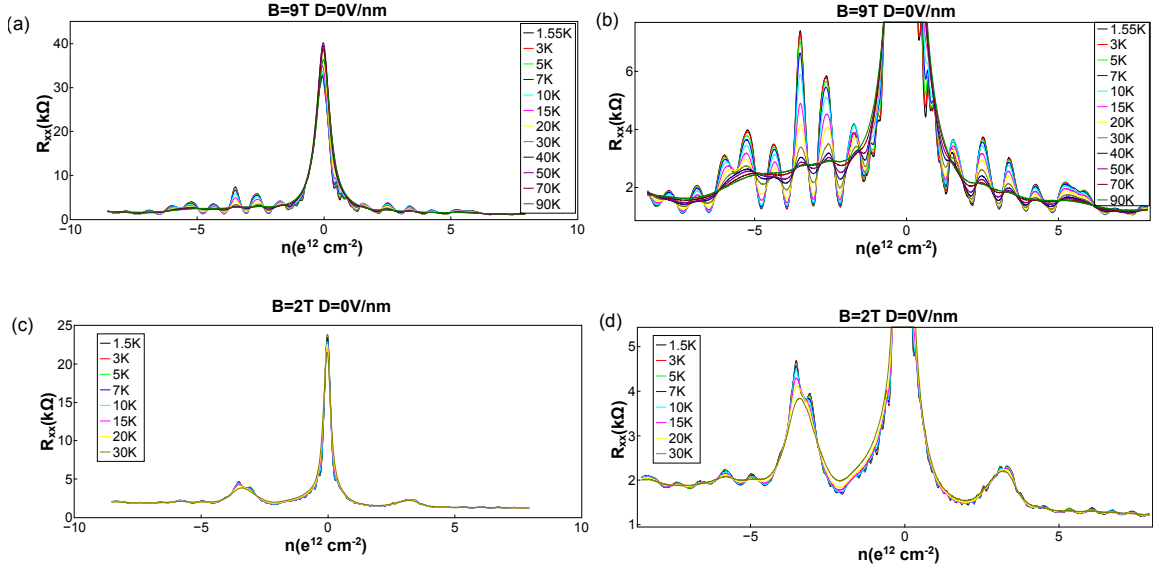


Figure 4.20:  $R_{xx}$  versus the carrier density  $n$  at different temperature. (a) and (b),  $B = 9$  T and  $D = 0$  V/nm. (c) and (d),  $B = 2$  T and  $D = 0$  V/nm.

## 4.6 Gaps of the Different Landau Levels

To get an idea of how large the gap is, a temperature dependence of  $R_{xx}$  vs. gate voltage measurements at both 9 T and 2 T are performed. Figure 4.20 shows the temperature dependence of the  $R_{xx}$  at 9 T (a,b) and 2 T (c,d). The electric displacement field at the figure is zero.

The relation between the  $R_{min}$  and gap  $\Delta E$  is

$$R_{xx}^{min} \sim \exp\left(-\frac{\Delta E}{k_B T}\right). \quad (4.15)$$

From equation 4.15, the gap  $\Delta E$  can be estimated from the fit of data  $R_{xx}^{min}$  versus  $1/T$  (Figure 4.21b). The gaps at  $B = 2$  T at hole side are given in Figure 4.21a.

The gap between two massless Landau levels is,

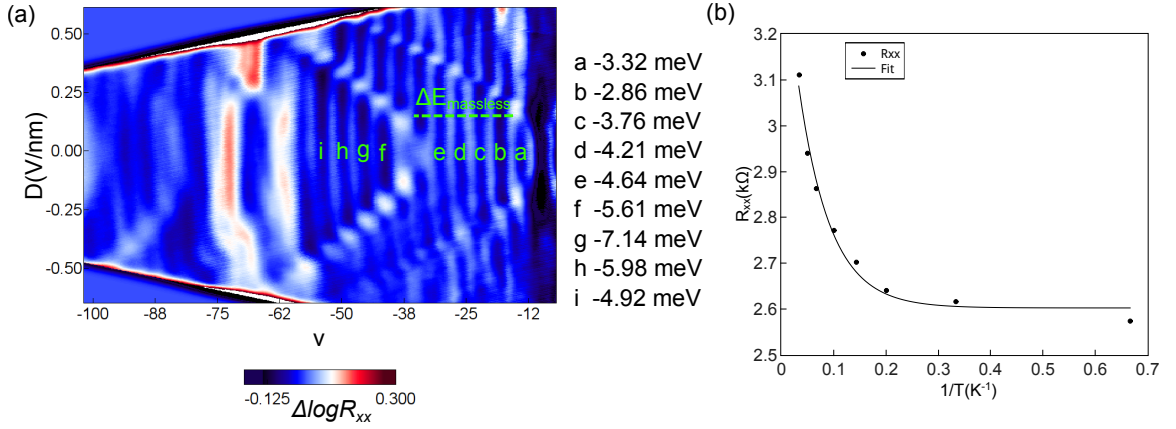


Figure 4.21: (a) Color plot of  $\Delta \log R_{xx}$  versus the filling factor and electric displacement field. The gaps are marked in the figure with a table of gap size. (b) The  $R_{xx}^{min}$  versus the  $\frac{1}{T}$ . Fitting with equation 4.15 to get the size of the gap.

$$\Delta E_{massless} = \Delta E_a + \Delta E_b + \Delta E_c + \Delta E_d + \Delta E_e = 18.7 \text{ meV}. \quad (4.16)$$

The size of other gaps is also given in the figure. In the same way, the gaps at  $B = 9$  T and  $D = 0$  V/nm are calculated, for example,  $\Delta E_5 = 1.49$  meV,  $\Delta E_6 = 8.39$  meV and  $\Delta E_{10} = 5.51$  meV ( $\Delta E_\nu$ ,  $\nu$  is filling factor).

## 4.7 Landau Fan of the Superlattice - The Hofstadter Butterfly

Here we present Landau fan measurements on this device. Similar devices have been studied incorporating both monolayer graphene and bilayer graphene. The Hofstadter butterfly features in previous system followed the Wannier diagram. But in the trilayer graphene system, the Hofstadter butterfly is different in many ways from the Wannier

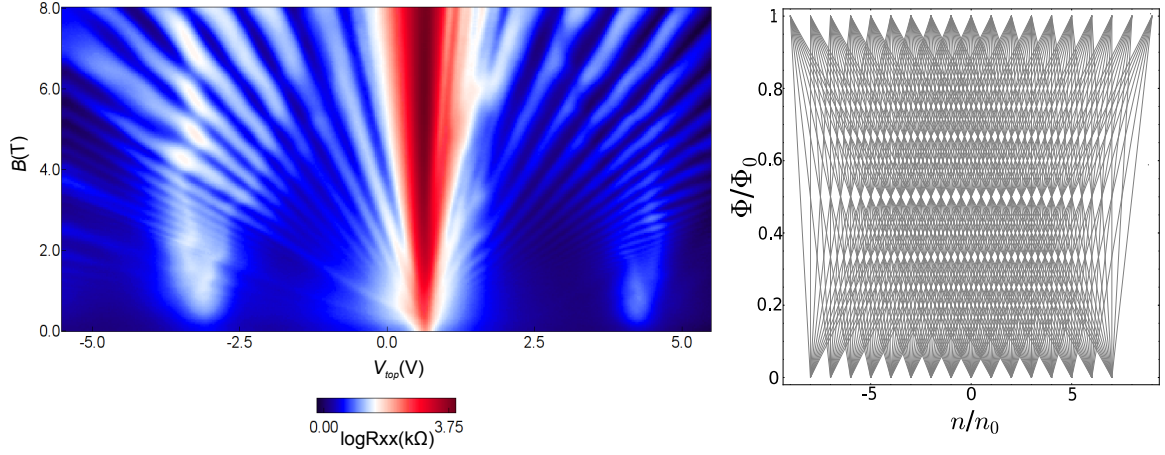


Figure 4.22: The Hofstadter butterfly of  $\log R_{xx}$  versus the top gate (ground the back gate) and magnetic field. The left diagram is the Wannier diagram.

diagram (Figure 4.22). One of the differences is the Landau levels from the extra Dirac points should be linear in the Wannier diagram, however, they are not continuous linear in the experiment data.

#### 4.7.1 The Hofstadter Butterfly without Electric Field

Now let us first discuss the Hofstadter butterfly in this device without any electric field ( $D=0$ ). From the equation 4.11, we know the  $B_0=33.6$  T.

The Figure 4.23 shows the Hofstadter butterfly by plotting the  $\Delta \log R_{xx}$  versus the carrier density and magnetic field. The bottom axis is the carrier density and the top axis is the  $n/n_0$ . The left axis is the magnetic field and the right axis is the  $\Phi/\Phi_0$ . The main Dirac point and two secondary Dirac points are very clear. The third Dirac point on the hole side is also visible around  $n = -5e12 \text{ cm}^{-2}$ . Two different Landau levels are close to the main Dirac point. We observe both features that are linear in the plot as well as ones that are

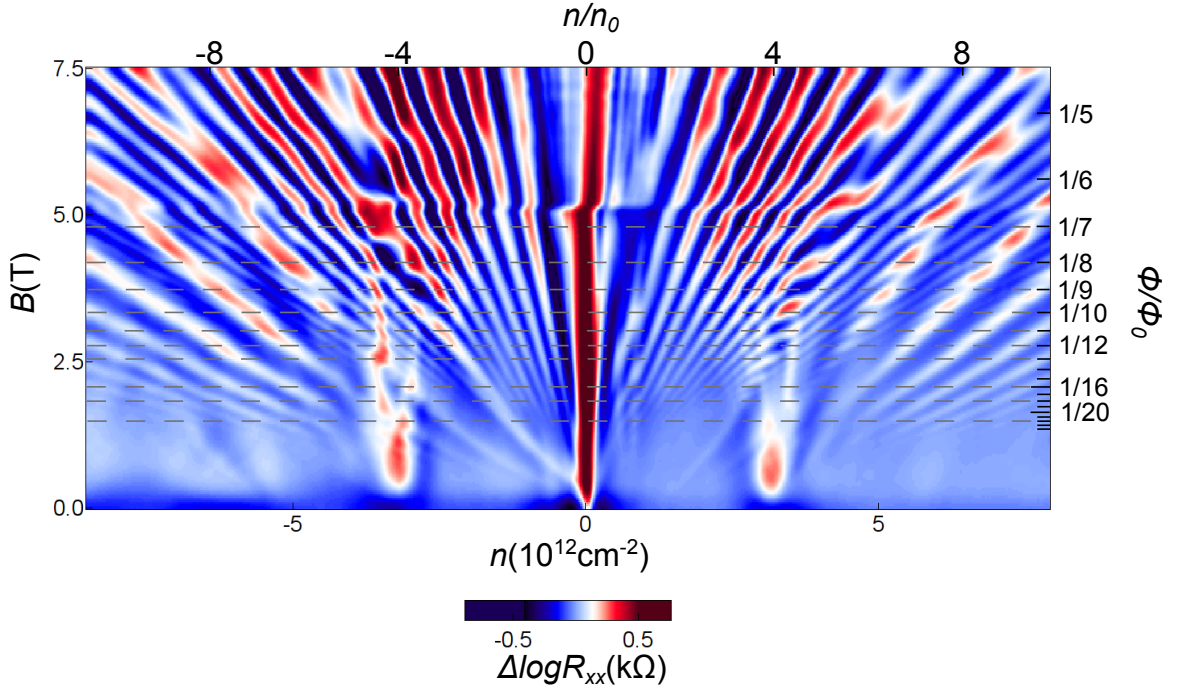


Figure 4.23: The Hofstadter butterfly of  $\Delta \log R_{xx}$ .

nonlinear. The first LLs are from the regular ABA trilayer graphene. The second non-linear LLs come from the massless band of trilayer. Similar data has been reported before [61]. Another feature is the two perpendicular LLs at the electron side right next to the main Dirac point. This feature has been predicted but not been reported on experiments yet. The Landau levels from the second Dirac points are not a simple straight line. Every single time, it will switch to a new line after crossing the massless LLs. At high magnetic field, the LLs from extra Dirac points are suppressed by the LLs from the trilayer itself. The right axis is the dimensionless parameter  $\Phi/\Phi_0$ . At  $\Phi/\Phi_0 = \frac{1}{m}$  which  $m$  is an integer, there is an enhanced signal from the crossing of the secondary Dirac point Landau fan features and the main Dirac point LLs which is confirmed by the theory and the Wannier diagram.

Figure 4.24 shows some parts of the Hofstadter butterfly pattern in previous figure. The (a) and (b) is the second Dirac points at hole side and electron side separately. The (c) is the third Dirac point at the hole side. The (d) is the LLs from the massless band near the main Dirac point (electron side).

In Figure 4.24a, the Landau level fan features from the secondary Dirac point are linear but they shift to another line every time they crosses the massless branch LLs (dashed green lines). For example, the line with indices  $t = -6$  and  $s = -4$  ( $t$  and  $s$  are integers from the Wannier equation) shift to line  $t = -4$  and  $s = -4$  after crossing the green dashed line. The variable  $t$  is related to the Hall conductance for the sub Landau levels from the secondary Dirac point. It means every time the LLs from the second Dirac point cross the massless LLs, they need fill the gaps from the massless LLs which leads to the shift to a low filling factor line. The line with index  $t = -6$  and  $s = -4$  only appear between two green dashed lines.

In Figure 4.24b, the similar things happened at second Dirac point of electron side. There are several visible LLs from the second Dirac point. The Wannier indexes are listed in the figure. The visible LLs are different from the hole side.

In Figure 4.24c, the third Dirac point is shown here. One of the most interesting features in this system is multiple extra Dirac points (7 including the main Dirac point) are able to see. But most of them is very weak and will not show in the Hofstadter butterfly Landau fan pattern. However, the one in this figure is unambiguous. Even the LLs from it are also visible in small magnetic field, but they will be dominated by other features quickly at higher magnetic field.

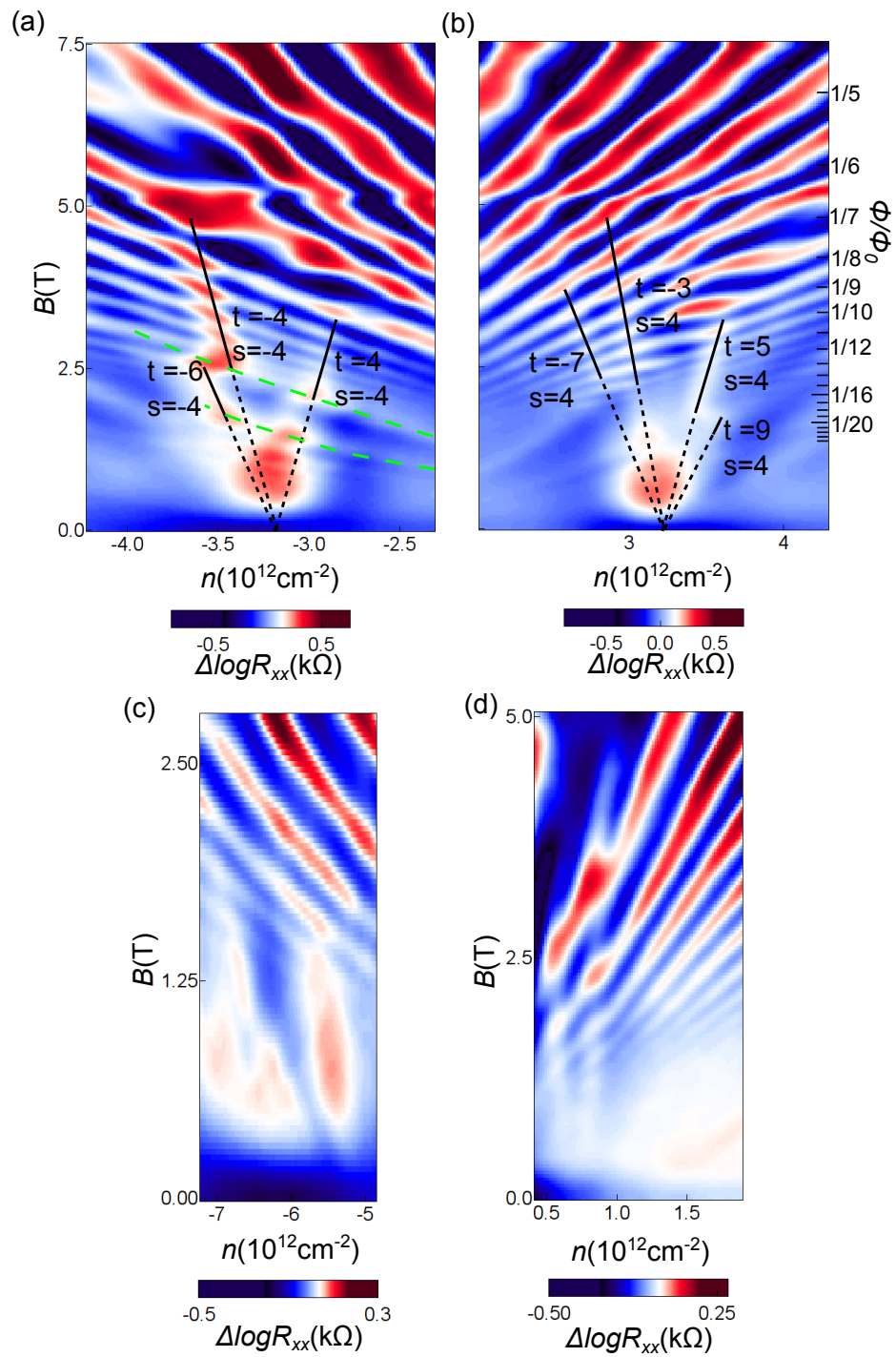


Figure 4.24: (a) The hole side second Dirac point. (b) The electron side second Dirac point. (c) The hole side third Dirac point. (d) The LLs from the massless band.

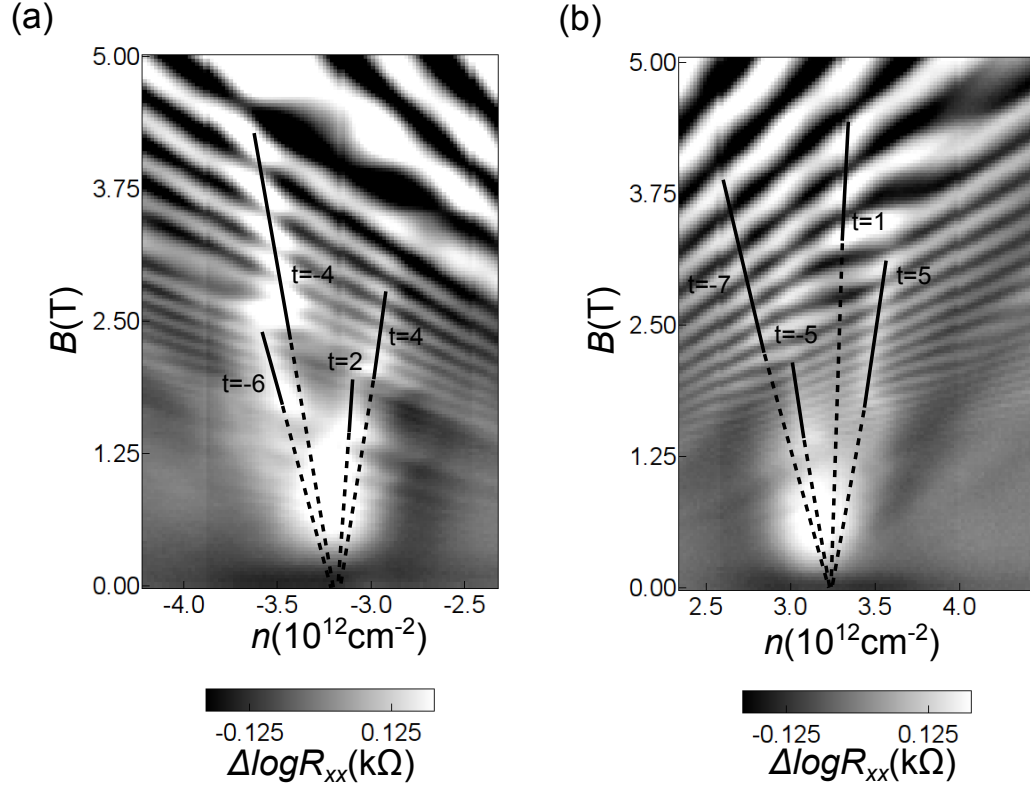


Figure 4.25: (a) The hole side second Dirac point with LLs. (b) The electron side second Dirac point with LLs.

In Figure 4.24d, the LLs from the massless band of trilayer itself are visible. These two parallel LLs are the same as predicted in the theory. They are not only visible in the low magnetic field but also cross with other LLs at higher magnetic field.

From the Figure 4.6, we know there are seven Dirac points in total. To observe them in the same Landau fan diagram, a small finite electric field ( $D=0.025$  V/nm) is applied to the device. In Figure 4.26, it shows six Dirac points in total in the fan diagram. The two black arrows next to the main Dirac point are the secondary Dirac points. The two third Dirac points are marked with four-points star. The LLs from it is also visible at

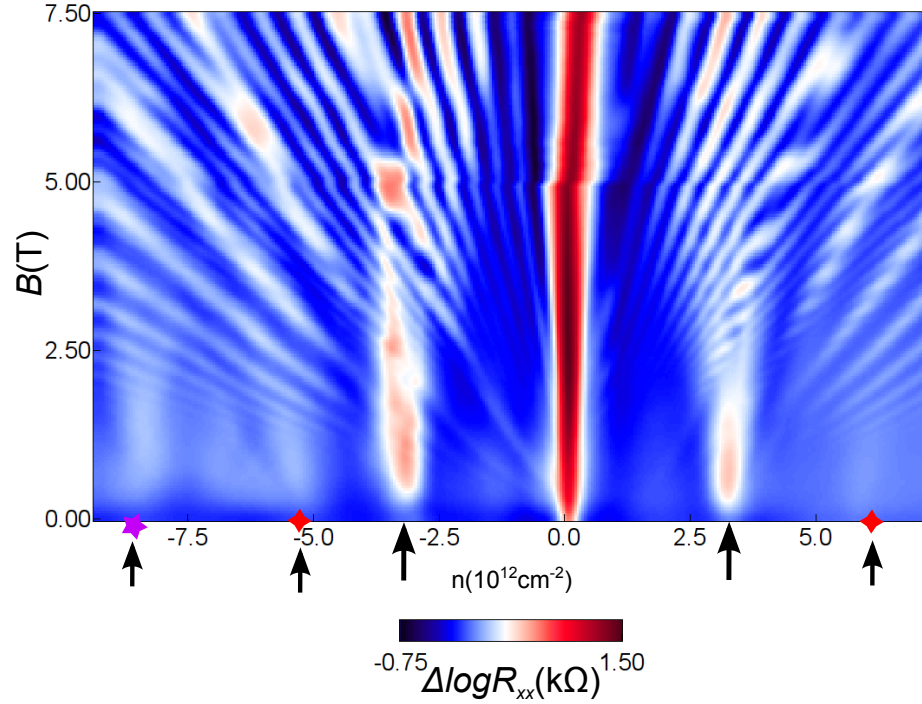


Figure 4.26: The Hofstadter butterfly Landau fan pattern at finite small electric field  $D=0.025$  V/nm. Six Dirac points and their LLs are shown in the figure.

small field. Even one fourth Dirac point is visible at far end of hole side. The LLs from it is also visible at low magnetic field.

#### 4.7.2 The Hofstadter Butterfly with Finite Electric Field

Because the device has two gates, it makes it possible to observe the influence of the electric field on the Hofstadter butterfly. In this section, the data from this experiment has been done at several positive and negative electric displacement field. The effects of the electric field has been shown in the secondary Dirac points and their LL features. Unlike the effects of electric field on bilayer graphene's Hofstadter butterfly (data from our lab mates), the trilayer system has different phenomenon.

The direction of the electric displacement field is from the top layer to bottom layer.

$$D = \pm \mathbf{0.25 \text{ V/nm}}$$

From the equation 4.12, we can fix the  $D = \pm 0.25 \text{ V/nm}$  and sweep the carrier density (equation 4.13) at different magnetic field. Interestingly, the electric field will affect the Hofstadter butterfly pattern dramatically in several ways.

Figure 4.27 is the data taken at  $D = 0.25 \text{ V/nm}$  (a and b) and  $D = -0.25 \text{ V/nm}$  (c and d). Figure b and d are the data in a and c subtract the background to make the small features more visible. The difference is easy to tell between b and d, for example, at the second Dirac point there are more extra LLs at hole side in figure b. The interference between the main LLs and second LLs are also stronger at hole side in figure b and electron side in figure c.

To see the small features more carefully, the zoom-in figures of details are shown in Figure 4.28.

The first one, Figure 4.28a, is the two Dirac points at  $D = 0.25 \text{ V/nm}$ . The LLs from the hole side second Dirac point are stronger. The numbers of LLs (at least 5 LLs visible) are more than electron side LLs (only 3 LLs). The interference between the main LLs and second LLs are also stronger at hole side.

The Figure 4.28b are the data around two Dirac points at  $D = -0.25 \text{ V/nm}$ . Instead of stronger hole side signal, the LLs at electron side are enhanced at negative displacement

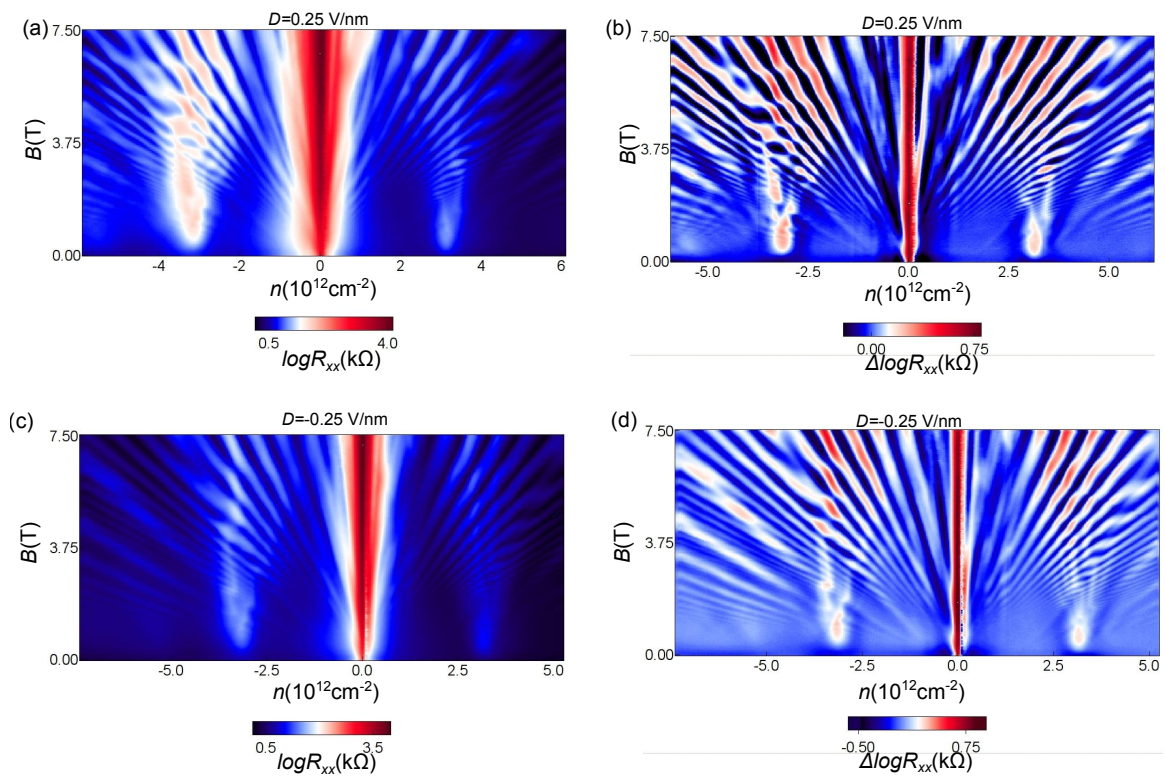


Figure 4.27: The butterfly pattern at  $D = 0.25$  V/nm (a and b) and at  $D = -0.25$  V/nm (c and d). The data with (b and d) and without (a and c) background subtraction.

field (direction: bottom to top). The number of LLs at electron side (6 or more) are more than hole side (around 3).

The Figure 4.28c shows the LLs from the third Dirac point at hole side under  $D = 0.25$  V/nm. This figure is the clearest third Dirac point LLs. There are four or more unambiguous LLs from the third Dirac point at low magnetic field. The features from third Dirac point dominated by the LLs from main or second Dirac points at higher magnetic field.

The Figure 4.28d shows two regions next to the main Dirac point at  $D = 0.25$  V/nm. At electron side, the features are from the massless band. Interestingly, some similar features appear at hole side with finite electric field.

The Figure 4.28e shows two regions next to the main Dirac point at  $D = -0.25$  V/nm. The features are a little different from the figure d.

The reason why there is a strong electron-hole asymmetry with finite electric field is related to how much the bottom layer graphene affected by the bottom BN. For example, at positive electric field the charges at hole side in Figure 4.28a is pushed down to the BN layer (bottom layer). So, in this way, the effective potential from the BN layer will be stronger than usual. That is why the hole side at positive electric field is enhanced while the electron side is enhanced at negative field.

**$D = \pm 0.5$  V/nm**

Then electric field is increased to  $\pm 0.5$  V/nm. The same measurements are taken at higher electric displacement field.

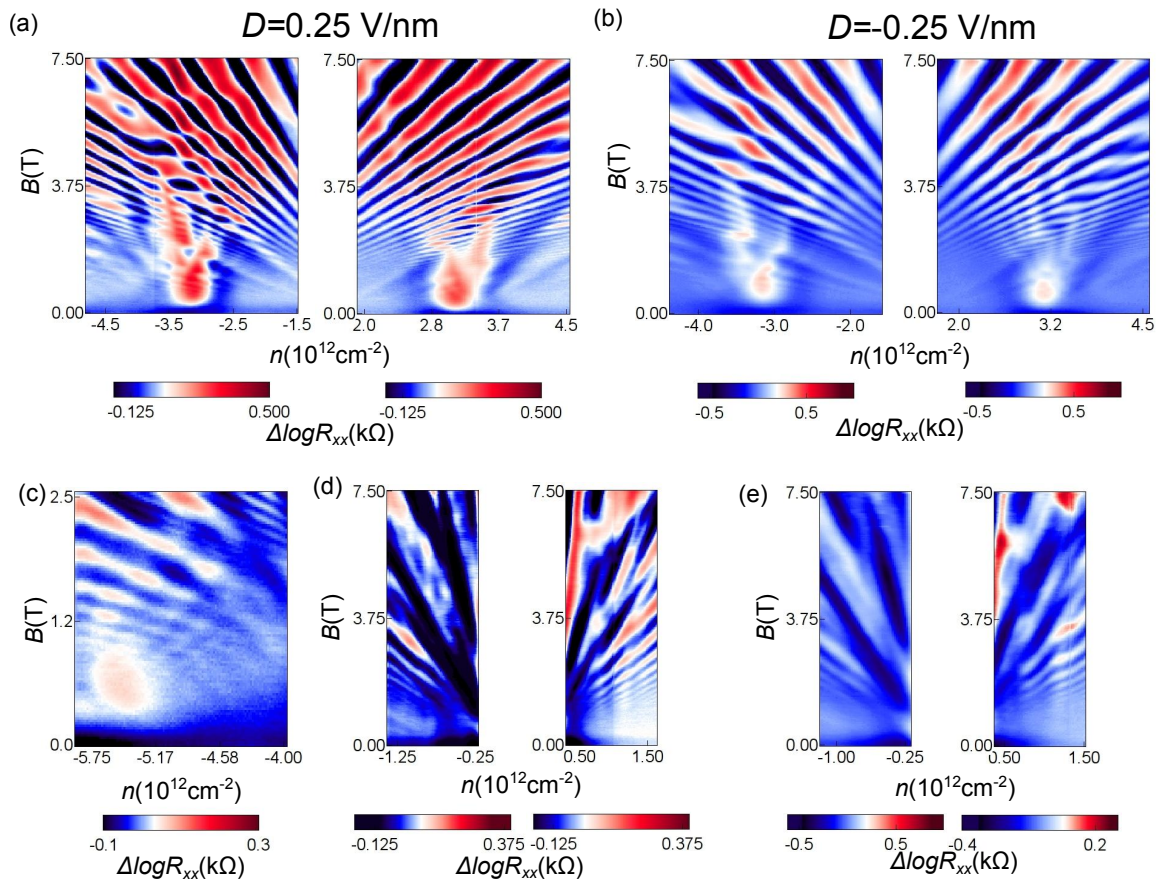


Figure 4.28: The details of the fan diagram with  $D = 0.25 \text{ V/nm}$  (a, c and d) and with  $D = -0.25 \text{ V/nm}$  (b and e).

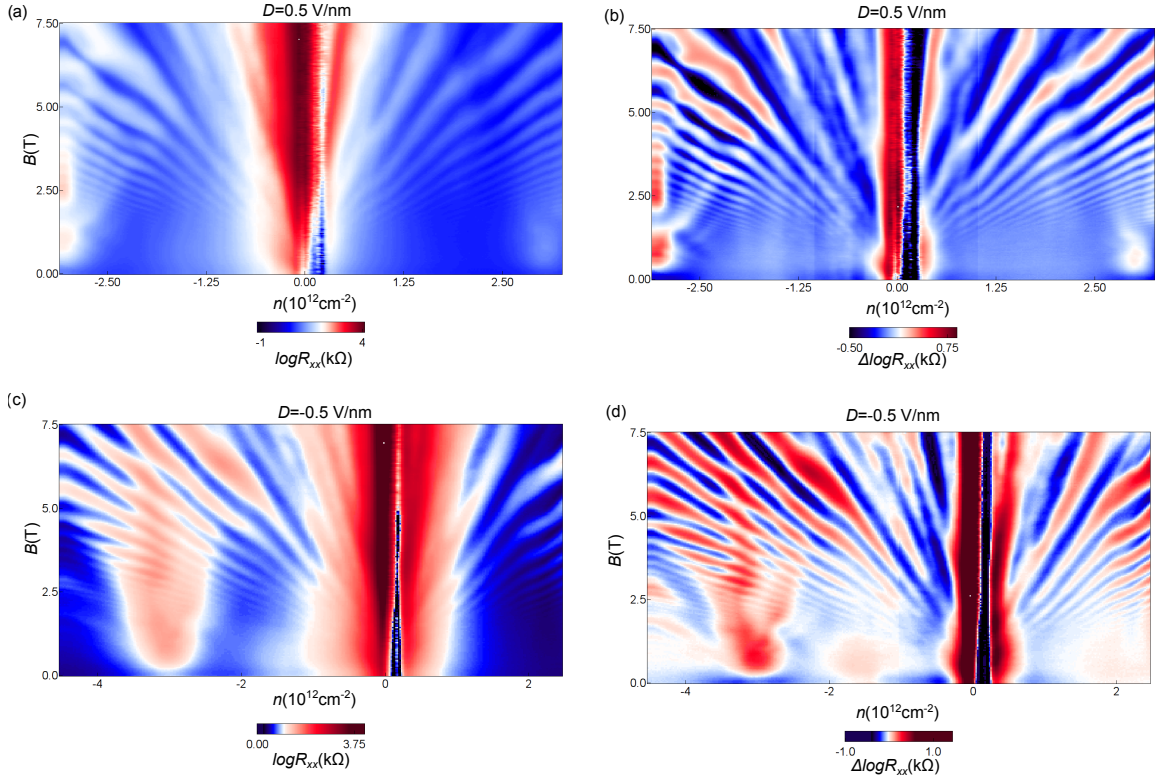


Figure 4.29: The details of the fan diagram with  $D = 0.25$  V/nm (a, c and d) and with  $D = -0.25$  V/nm (b and e).

Figure 4.29 shows the butterfly pattern at  $D = \pm 0.5$  V/nm. Figure a and b are taken at  $D = 0.5$  V/nm. The first figure is  $\log R_{xx}$  and second one is  $\log R_{xx}$  subtract the background. The second Dirac point at the hole side is enhanced which is consistent with the previous results. The figure c and d are taken at  $D = -0.5$  V/nm. Compared to the first two figures, the second Dirac point's LLs are weaker.

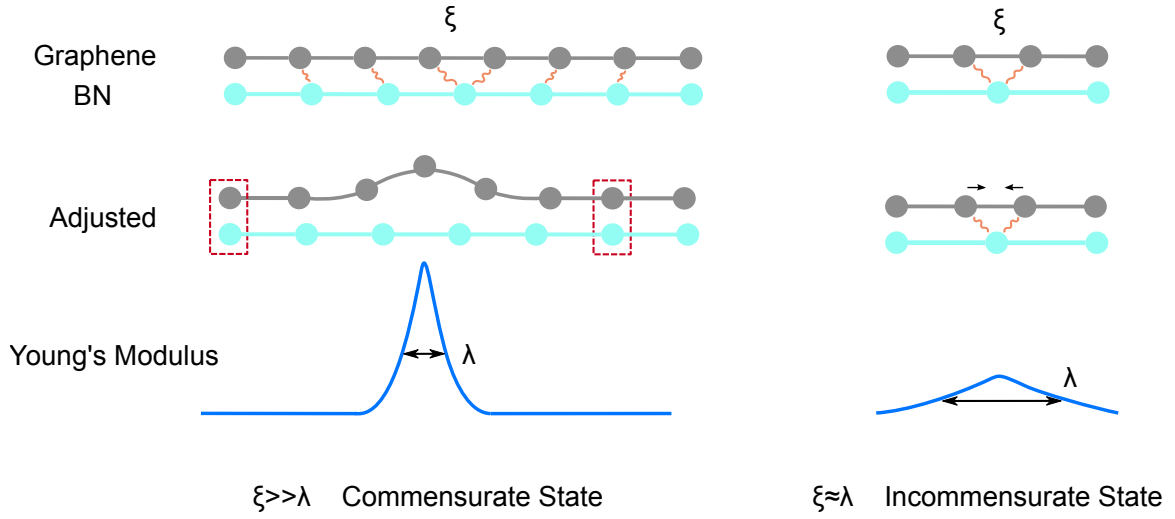


Figure 4.30: The formation of the commensurate state and incommensurate state.

## 4.8 The Commensurate State of Bilayer, Trilayer Graphene Aligned with BN

When a material is under a periodic potential, sometimes the lattice can be changed to follow the periodicity of the potential, resulting in a commensurate state. Recent study [70] shows a transition of commensurate state and incommensurate state for graphene on BN. Depending on the rotation angle between graphene and BN, they can be in commensurate state (graphene stretched) or incommensurate state (graphene almost stays the same). Only for graphene in the commensurate state, is a gap opened at main Dirac point. The study reports the transition angle between commensurate and incommensurate state in graphene is  $1^\circ$ . For angles smaller than  $1^\circ$ , the graphene is in the commensurate state (incommensurate state while rotation angle  $\leq 1^\circ$ ).

Figure 4.30 shows the formation of both commensurate state and incommensurate state. At first, the graphene is on top of BN with small rotation angle which is big superlattice wavelength  $\xi$  (left figure) and big rotation angle yields a small superlattice wavelength  $\xi$  (right figure). Because of the different van der Waals force between the graphene and BN, the graphene will adjust to fit the periodicity of the potential. This process is a kind of energy competition between the van der Waals energy and the strain energy. Until the energy is table again, two layers will "lock" to each other. If the superlattice wavelength is large enough, the graphene will form a ripple physically which leads to a domain wall. But if the superlattice wave length is small, the van der Waals energy in one period is not enough to form a strain. The graphene will only stretch a little. So in the first case, the Young's modulus will have a peak just like shown in the figure. But in the second case, the Young's modulus will not have a shape peak. The half width of the domain-wall soliton in the lattice is  $\lambda$ . So if the  $\xi \gg \lambda$ , the lattice will be in the commensurate state. Otherwise the  $\xi \approx \lambda$ , the lattice will be in the incommensurate state.

To understand the commensurate state in bilayer or trilayer graphene, we use the same model reported in the paper [70]. At first, we introduce several parameters. The lattice mismatch of graphene-hBN lattice  $\delta \approx 0.018$  and angle  $\theta$  is the rotation of the moiré pattern. And an angle  $\alpha$  is determined by,

$$\tan(\alpha) = \frac{\delta}{2\sin(\phi/2)}$$

where  $\phi$  is the rotation angle between the graphene and BN. And

$$\theta = 90^\circ - \alpha - \phi$$

At small rotation angle  $\sin(\frac{\phi}{2}) = \frac{\phi}{2} \frac{2\pi}{360} = 0.0087\phi$ , so we can get,

$$\theta = \pi/2 - \tan^{-1}(1.0345\phi^{-1}) - \phi \quad (4.17)$$

where  $\phi$  is in the unit of radians. When we know the rotation angle between the graphene and BN, the superlattice wavelength  $\xi$  can be calculated from equation 4.8. And the width of the edge dislocation core is,

$$\lambda = \frac{a}{2\pi} \sqrt{\frac{Y}{\gamma_{un}}} \quad (4.18)$$

where  $Y$  is the Young's modulus,  $\gamma_{un} = \frac{V_0}{h}$  is the unstable stacking fault energy per unit area,  $V_0$  is the amplitude of the potential relief and  $h$  is the period in the direction perpendicular to the dislocation axis.

The  $\gamma_{un}$  is proportional to the potential Frenkel-Kontorova which is given in the figure from the previous work [70]. In graphene, at  $\phi = 0^\circ$ , the  $\lambda \approx 10a \approx 2.4nm$ . For bilayer graphene, every parameter in equation 4.18 is the same except the Young's modulus. The Young's modulus in bilayer could be  $\sqrt{2}$  as much as in the monolayer (trilayer it is  $\sqrt{3}$  times). The shear's modulus  $\mu$  may dominate the strain which is roughly half of the Young's modulus.

Here we present a table to tell whether the sample is in commensurate state. For our sample, the rotation angle is  $0.58^\circ$ . According to the table, it should be in the incommensurate state. That is the reason why no gap is observed in our experiments.

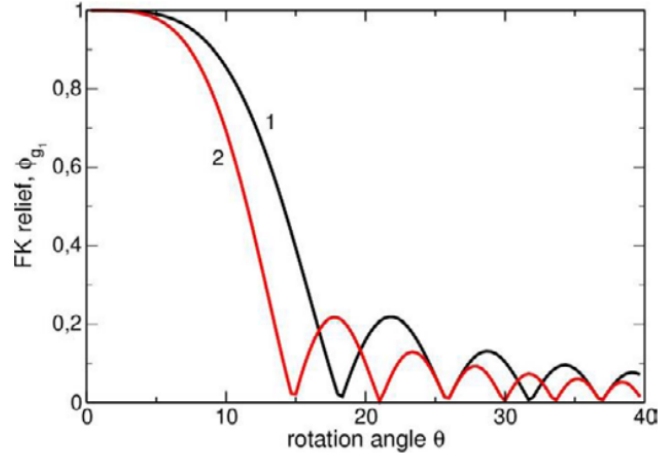


Figure 4.31: The dependence of potential Frenkel-Kontorova with rotation angle  $\theta$  [70].

Actually, the bilayer and trilayer graphene will be in the commensurate state with a low possibility (the rotation angle between graphene and BN must be very small).

## 4.9 Conclusion

In conclusion, a high mobility aligned trilayer graphene/BN sample is measured. Seven Dirac points and their Landau levels are observed. At different magnetic fields, the LLs crossing patterns change. At low magnetic fields, non-linear transitions surprisingly show up. We also measured the Hofstadter butterfly at different electric displacement fields and observed major changes in behavior depending on electric field.

$\theta(^{\circ})$	$\Phi(\text{rotation angle } ^{\circ})$	$\gamma$	$\xi(\text{super lattice})$	$\lambda_m(\text{nm})$	$\lambda_b(\text{nm})$	$\lambda_t(\text{nm})$	Mono-layer	Bi-layer	Tri-layer	Shear's modulus		
										Mono	Bi	Tri
0~5	0~0.09	1	>13.8587	2.4	3.4	4.15	Y	Y	Y	Y	Y	Y
5~17	0.09~0.3226	1~0.2	13.8587~13.195	2.4~5.366	3.4~7.6	4.15~9.28	Y	Y	Y	Y	Y	Y
>17	>0.3226	<0.2	<13.195	>5.366	>7.6	>9.28	P	P	P	P	P	P
18~19	0.343~0.3636	<0.1	13.1086~13.0179	>7.59	>10.75	>13.12	Y	P	N	Y	Y	P
24.5~27.5	0.482~0.515	<0.1	12.4408~12.0737	>7.59	>10.75	>13.12	Y	P	N	Y	Y	P
>30	>0.612	<0.1	<11.7389	>7.59	>10.75	>13.12	P	N	N	P	P	N
Other 17~30	0.3636~0.482 0.511~0.612	0.2~0.1	13.0179~12.4408 12.0737~11.7389	5.366~7.59	7.6~10.75	9.28~13.12	Y	Y	P	Y	Y	Y

Y- yes      N- no      P- possible

Figure 4.32: The table of possibility of commensurate state for different rotation angle in different graphene (mono-, bi-, tri-layer).

## Chapter 5

# Quantum Transports In Strained Graphene

### 5.1 Abstract

The graphene with strain defects has been studied both theoretically [21] and experimentally by STM [38] [31]. But it has not been observed directly by transport measurement. One of the reason is, it is not very easy to make a uniform, stable strain defect with large pseudo magnetic field. Here we report a transport study of strained graphene. This strain defect is from a bubble formed in graphene on top of BN during transfer process.

### 5.2 Introduction

Under a non-uniform stain, the graphene develops a pseudo-magnetic field [21]. It is a gauge field that has different sign for the two different valleys. This kind of pseudo-

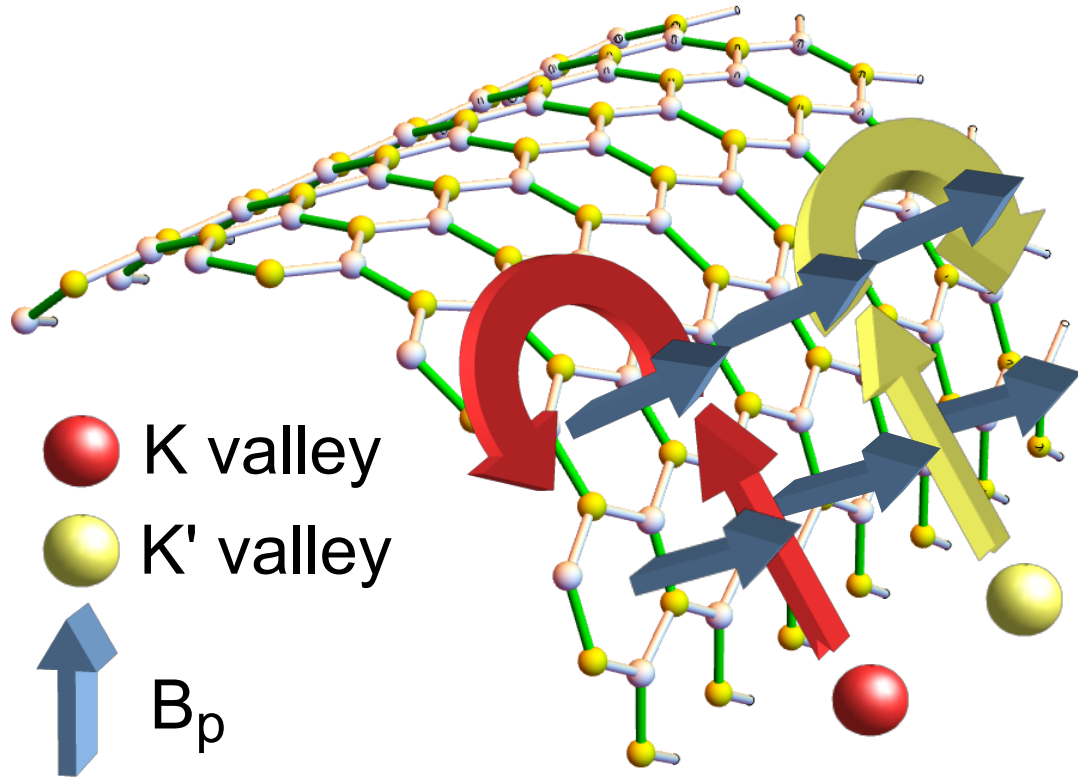


Figure 5.1: Valleytronics affected by the pseudo magnetic field.

magnetic Field has been studied by STM [38]. By using the STM tip pushing the graphene film, quantum dot behavior has been observed by AFM measurement [31]. The reason of forming quantum dots is the pseudo magnetic field can create a pseudo magnetic barrier and block the electrons. Here we report a transport study of graphene with line strain defect. This line strain can create a very large pseudo magnetic field and forms a one-dimensional conducting channel for electrons/holes. Some experiments with other strain defects will also be discussed here.

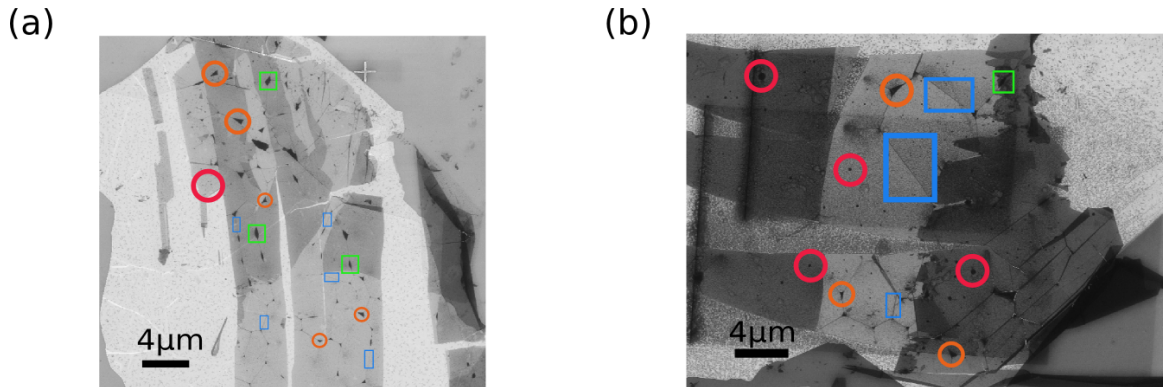


Figure 5.2: In this two pictures, there are triangle strain bubbles (orange circle), circle strain bubbles (red circle), polygon strain bubbles (green square), line strain defect (blue square).

### 5.3 The Graphene Bubbles Formed During Transfer Process

We want to study strained graphene, so we need find a good approach. Every time we transfer graphene to BN, there are at least some bubbles. For regular graphene devices, usually we avoid these areas to make high mobility devices. These bubbles which are trapped some gases and some residues inside are very good candidates to study the pseudo magnetic field caused by strain.

Differently shaped bubbles exist. Some are triangular. Some are circular bubbles. There are also polygonal and line strain defects.

Usually, line strain defects can be found connected to corner of a triangle defect. The circle bubbles are isolated from other defects. On the edge of line defect, some polygons will be found occasionally (Figure 5.2).

To measure the size of these defects, Atomic-Force Microscopy (AFM) is used. In Figure 5.3, triangle, polygon, circle and line strain defects can be seen easily. In Figure 5.4,

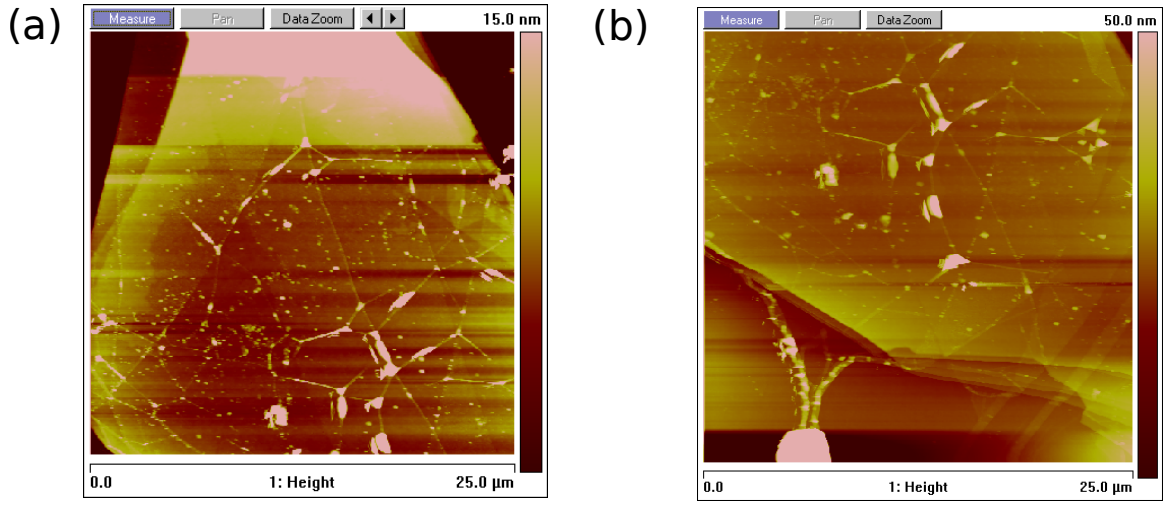


Figure 5.3: The AFM picture of strain defects.

the figures on top are AFM images and the bottom figures are height line traces of the white lines in each image in the main figure. Two blue lines corresponds to the two blue crossing. In (a), the line stain defect is not very sharp. The height is about 1 nm. In (b), this line strain defect is about 3 nm in height. In (c), the defect is sharper and looks more bright in the main figure. The height is 6 to 7 nm.

## 5.4 Line Strain Defect Device Fabrication

The line strain could have very high pseudo magnetic field on its edge, which motivated designing and making two test devices. In a room temperature measurement, I detected transverse resistance without a magnetic field which is very interesting. It turns out the transverse resistance is from scattering by the strain defect by our experiments, which will be discussed later.

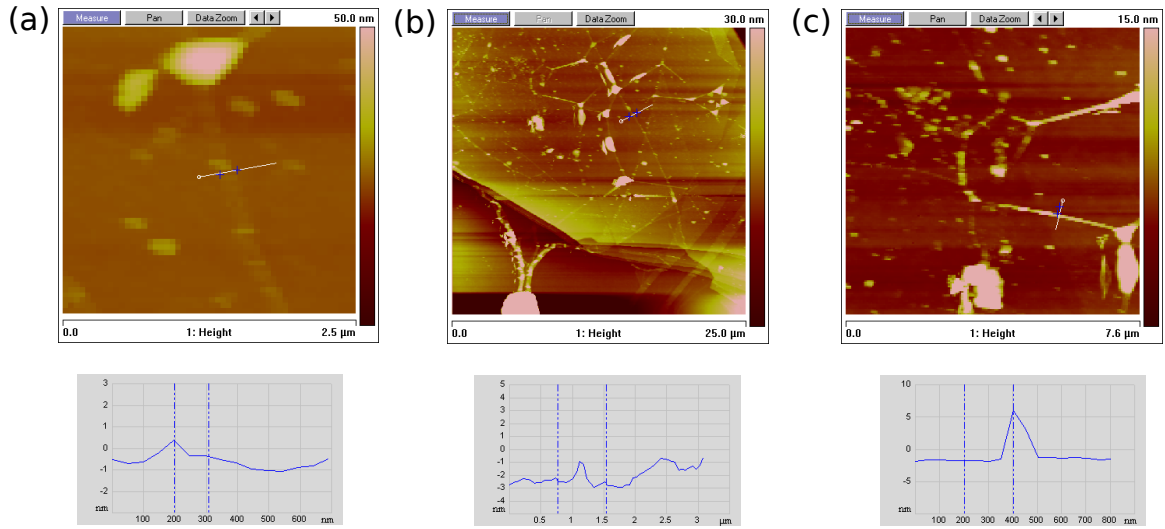


Figure 5.4: The size of line defects has been measured by AFM. The line in the figure with two blue crossing is where we measure the height. The height line trace graphs are below the main graph. Two blue lines corresponds to the two blue crossing. (a) the line stain defect is not very sharp. The height is about 1 nm. (b) this line strain defect is about 3 nm in height. (c) the defect is sharper and looks more bright in the main figure. The height is 6 to 7 nm.

First, we introduce the device fabrication. Some techniques have been introduced in the previous chapter. We will focus on additional details and some different technique for this kind of device.

Using a layer stacking technique, we transfer the BN/Graphene/BN sandwich structure on SiO<sub>2</sub> substrate. Before transferring the second layer of BN, a SEM picture was taken to locate the bubbles.

By using plasma etching, we can get a graphene sheet with a line defect in the center of it. Using an edge contacts technique, four contacts are made on the four sides of the graphene sheet. The device structure is shown in figure 5.6.

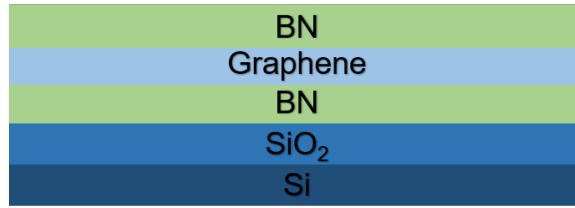


Figure 5.5: BN/Graphene/BN sandwich structure on  $SiO_2$  substrate

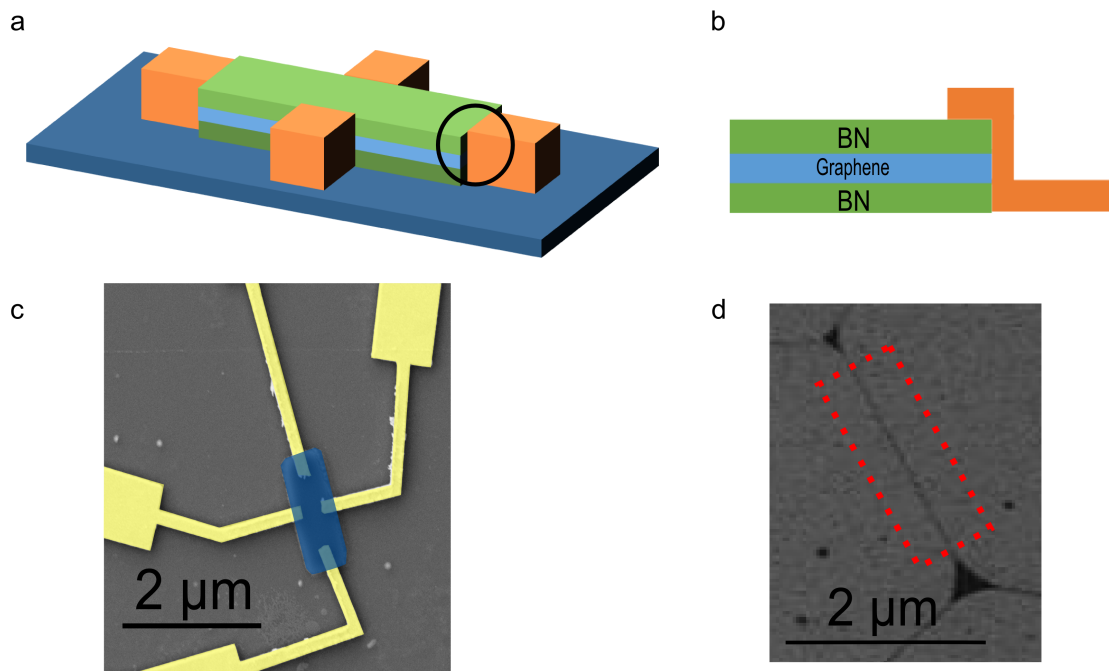


Figure 5.6: (a) The device structure. (b) The edge contact on the BN/Graphene/BN sandwich structure. (c) The SEM picture of device, you can see the four contacts on the four different sides. The top and bottom contacts are connecting to the line defect. (d) The SEM picture of the graphene. The black line inside the red box is the line strain defect.

## 5.5 The Coulomb Blockade Cross the Line Strain Defect

In this section, the low temperature transport measurement results cross the line strain defect will be discussed. Because of the pseudo magnetic barrier, we observe coulomb diamonds behaviour in the transport measurements consistent with the presence of a quantum dot in these devices.

We use the lock-in as the  $dV$  signal and another DC voltage source as the  $V_{sd}$  and measure the  $dI$  signal from the other contact (figure 5.7).

We sweep the back gate and measure  $dI/dV$  at different DC bias voltage  $V_{sd}$ . The data shows a clear coulomb diamond pattern which means the line defect behaves like a "Quantum Dot" here. Using graphene or nanotube to make quantum dots have been studied previously in many works [33] [26] [12] [46]. But for graphene quantum dots, people will etch graphene to small area in most cases [33]. Here, the reason why we observe quantum dot behaviour in graphene has a very different origin.

Here we plot the differential conductance by using the DC bias voltage as  $x$  axis and the back gate voltage on the  $y$  axis. From the figure 5.8, the charging energy is around 20 meV to 25 meV and the level spacing is around 2 meV.

Using this data we can estimate the size of the dots. The level spacing  $\Delta E$ ,

$$\Delta E \sim \frac{dE}{dk} \cdot \frac{\Delta k}{2} \sim \frac{dE}{dk} \cdot \frac{\pi}{L} \sim \frac{0.5eV}{L(nm)}$$

So  $L$  is around 200 nm.

And from the charging energy  $U$ ,

$$U \sim \frac{e^2}{C} \sim \frac{e^2}{L} \approx \frac{1.6eV}{L(nm)}$$

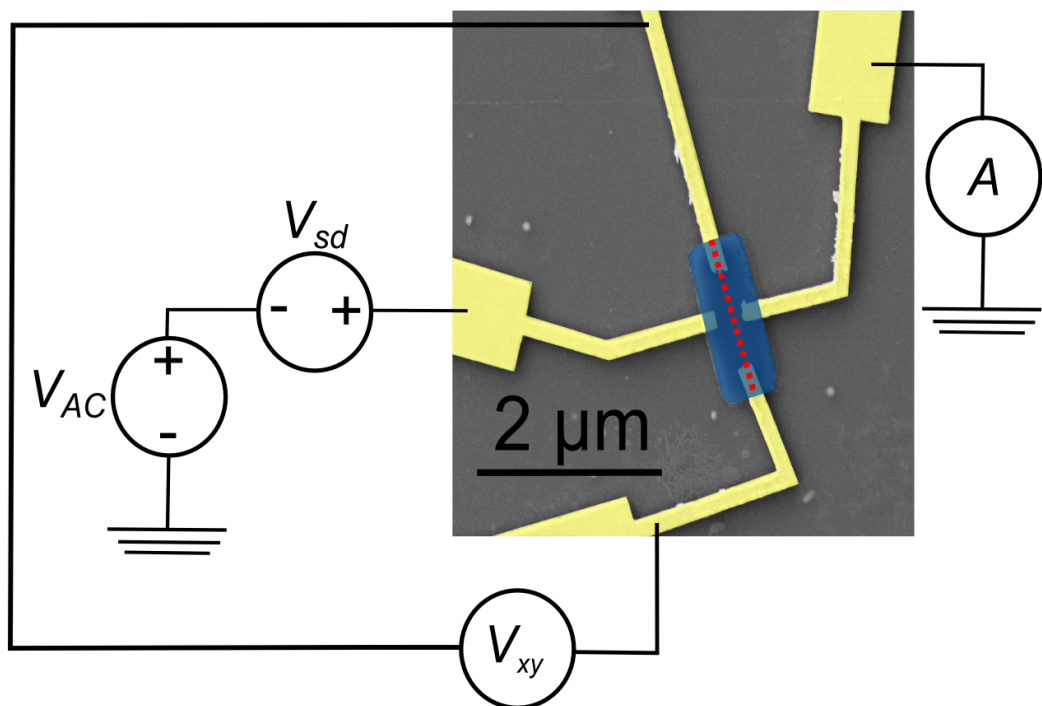


Figure 5.7: The blue area is BN/Graphene/BN sandwich structure and the red line is the line strain defect. Four contacts made on the device by using Edge Contact Technology. We use the lock-in as the  $dV$  signal and another DC voltage source as the  $V_{sd}$  and measure the  $dI$  signal from the other contact.

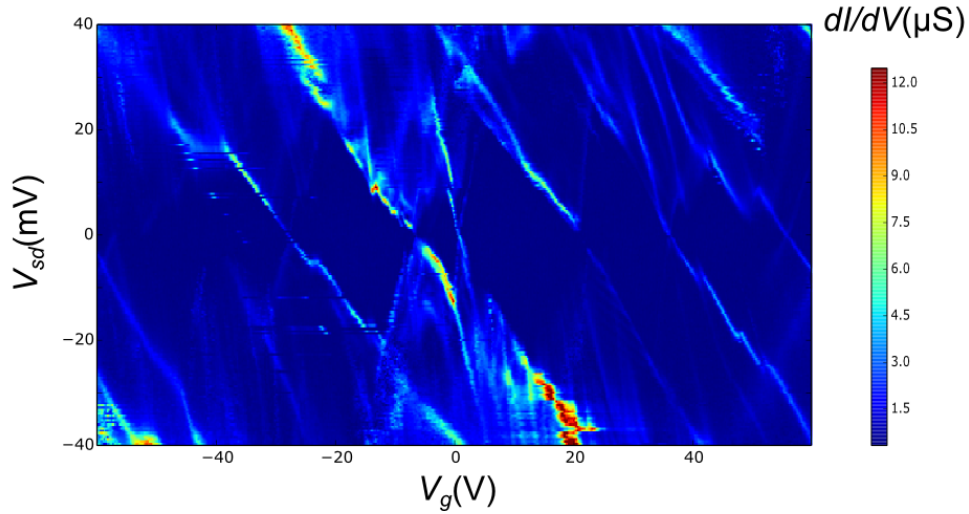


Figure 5.8: The DC bias voltage vs. the back gate voltage and plot the  $dI/dV$ . Here we are measuring the two contacts cross the line strain defect. We can see clear coulomb diamond features.

So the estimation of  $L$  from charging energy is around 100 nm.

We now discuss the transport data. The deep blue area is the differential conductance is almost zero (Figure 5.8). The bright lines here are  $dI/dV$  peaks. In this figure, there are several different sizes of coulomb diamonds which means there are several different "quantum dots" with different charging energy that are being probed in series or parallel. Both electron side and hole side have clear coulomb blockade behavior. Some clear energy levels can be seen in Figure 5.9.

Figure 5.10 exhibits a series of sharp coulomb blockade oscillations that electrons are crossed through the line strain defect at each peak.

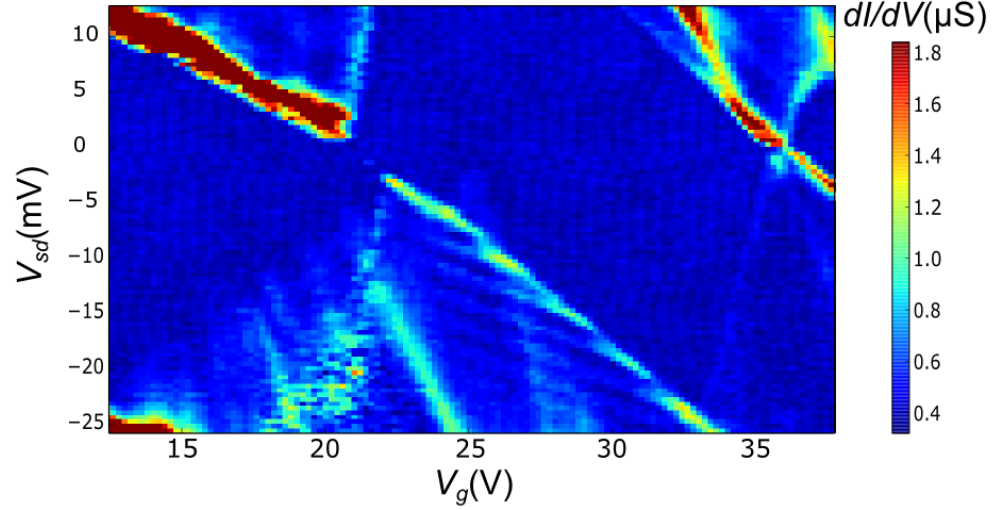


Figure 5.9: This figure is a part of the previous one. It shows a diamond and small features of the level spacing.

At the same time, we can also record the  $V_{xy}$  signal. The  $V_{xy}$  signal, interestingly, shows a similar Coulomb diamond pattern. At the center area where no electrons pass through the line defect at the  $V_{xx}$  signal, the  $V_{xy}$  is also almost zero here. It means when the electrons blocked at line stain, there are also no electrons will go to the  $V_{xy}$  electrodes. Beyond this diamond center area, the  $V_{xy}$  signal becomes larger which means some electrons have been scatted from the line strain and go to the  $V_{xy}$  electrodes.

This phenomenon (Coulomb Blockades) is strong and can be repeated by almost every working device (over 10 devices). Here we show some data from other devices (Figure 5.13). The line strain defect is the black line in the center of the device. The blue box is the graphene left after etching. There are four contacts on the device made by edge

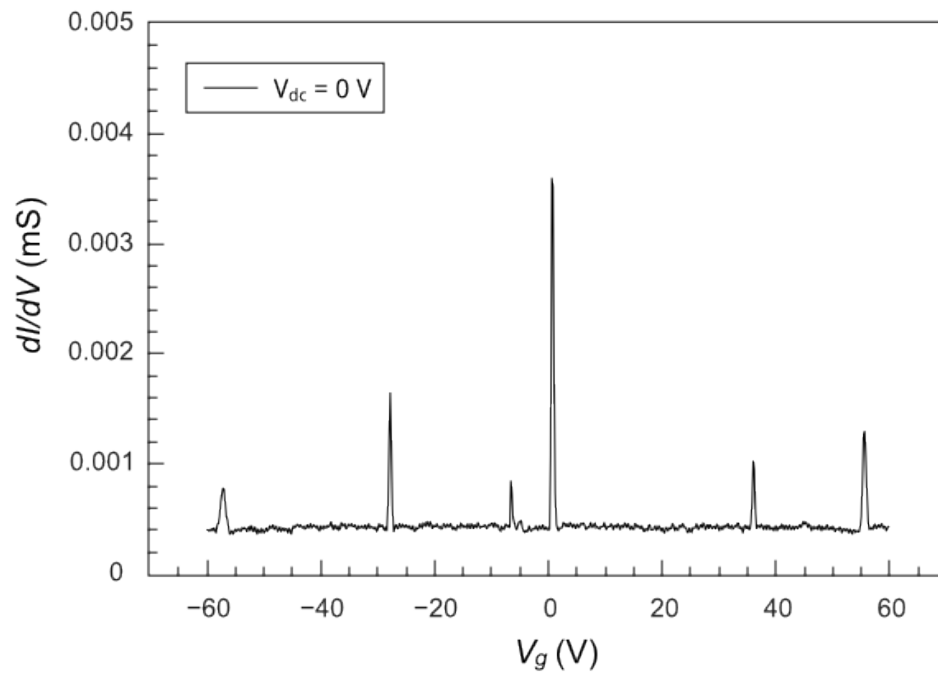


Figure 5.10: The line trace of  $dI/dV$  VS  $V_g$  when  $V_{sd}=0$ mV. We can see six coulomb peaks and at the most time the  $dI/dV$  remains around 0mS .

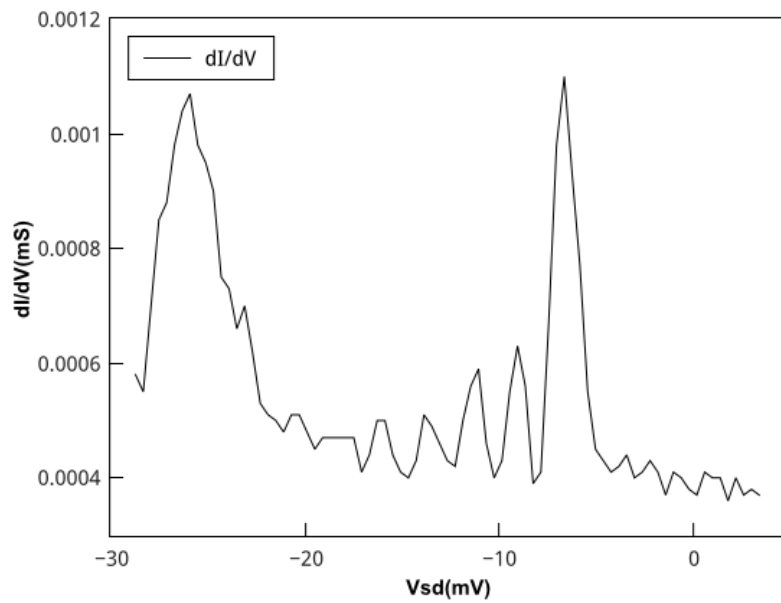


Figure 5.11: The line trace of  $dI/dV$  vs  $V_{sd}$  at  $V_g=24.6V$ . The space between the two nearest peaks are the energy level spacing of this coulomb diamond.

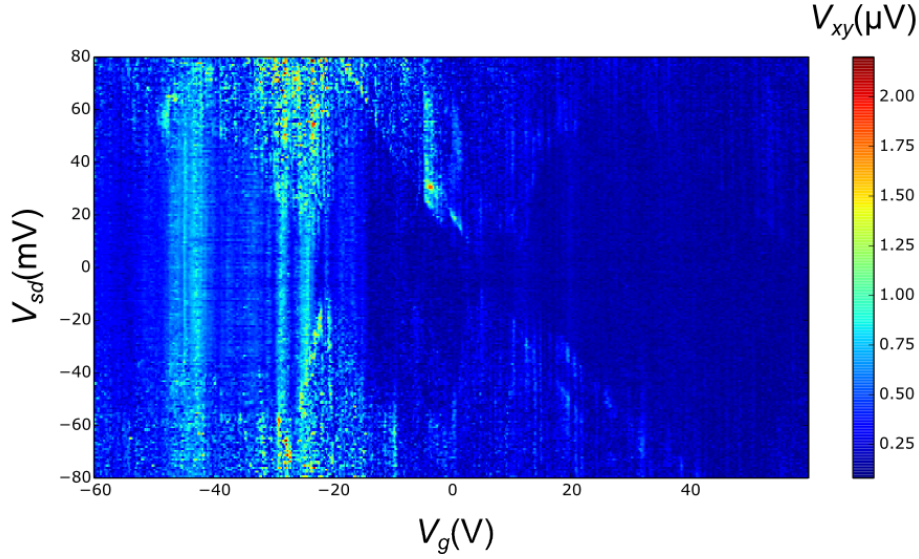


Figure 5.12: The  $V_{xy}$  signal measured by set up shown in Figure 5.7. There is a coulomb diamond shape pattern inside. And it is very similar to Figure 5.8 which prove the  $V_{xy}$  signal originates from scattering off of the line strain.

contacts technique (Figure 5.13a). The  $dI$  current between contacts 1 and 3 (cross line) with  $V_g$  as  $x$  axis and  $V_{sd}$  as  $y$  axis is shown in Figure 5.13b. There is several interesting features. First, we can see diamond shape features. But in this device the line strain did not block the electrons totally. The reason might be the strain is not high enough to give a strong enough pseudo magnetic field. Second there is a jump at around the  $V_g=0V$ . We will discuss this feature in the next paragraph. The following two figures are the data subtract the background. The diamond features are more clear.

Figure 5.14 the current across the line (red curve) and along the line (black curve) versus the back gate voltage at  $V_{sd}=0$  mV. The current across the line is measured between contacts 1 and 3. And the current along the line is measured between contacts 2 and 4 (Figure 5.13a). There is a Dirac Point feature in the current along the line defect. Because

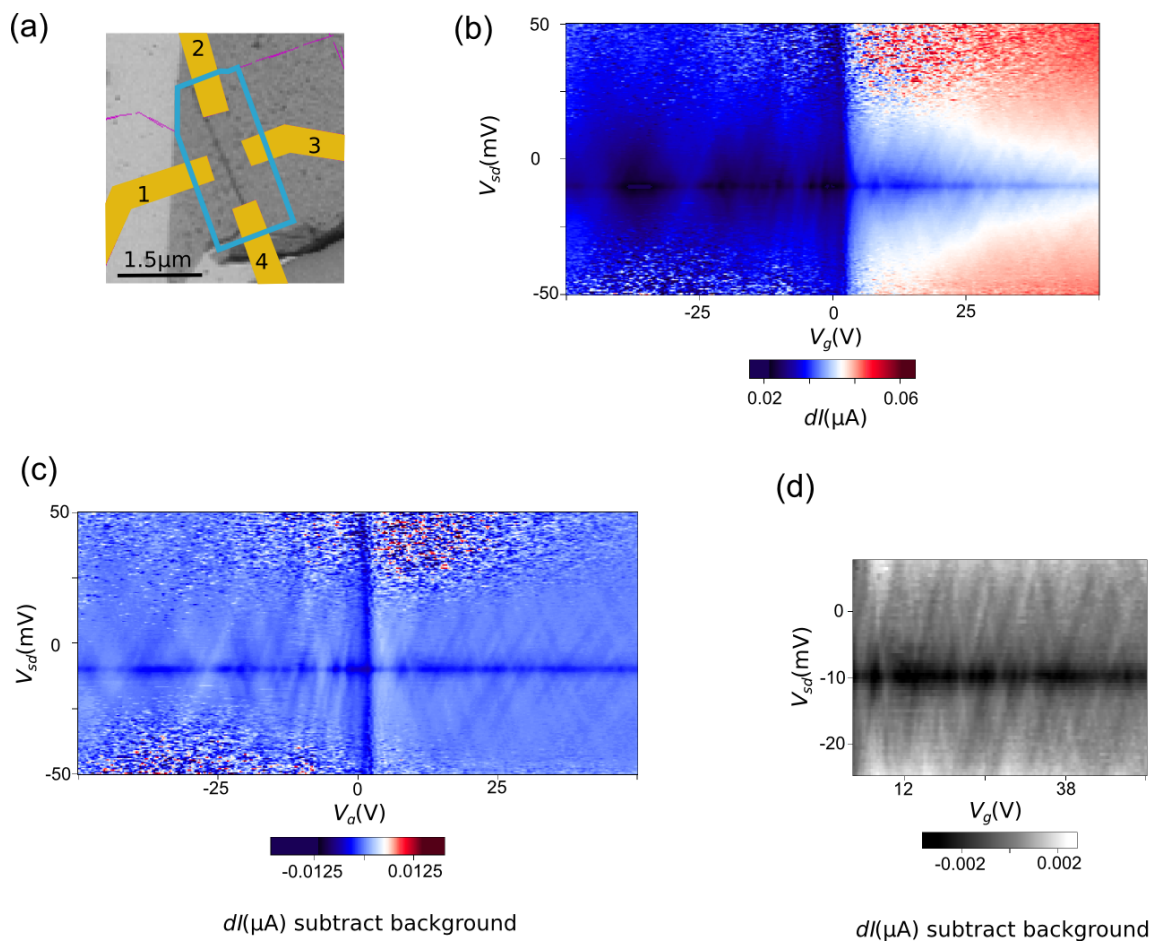


Figure 5.13: (a) The schematic of the device. The line strain defect appears as the black line in the center of the device. The blue box outlines the graphene left after etching. There are four contacts on the device made by an edge contact technique. (b) The  $dI$  current between contacts 1 and 3 with  $V_g$  as x axis and  $V_{sd}$  as y axis. There are several interesting features. First, we can see diamond shape features. Second there is a jump at around the  $V_g=0$ V. (c) The figure in (b) a smoothed background is subtracted to enhance the diamond features. (d) Zoomed-in figure of (c).

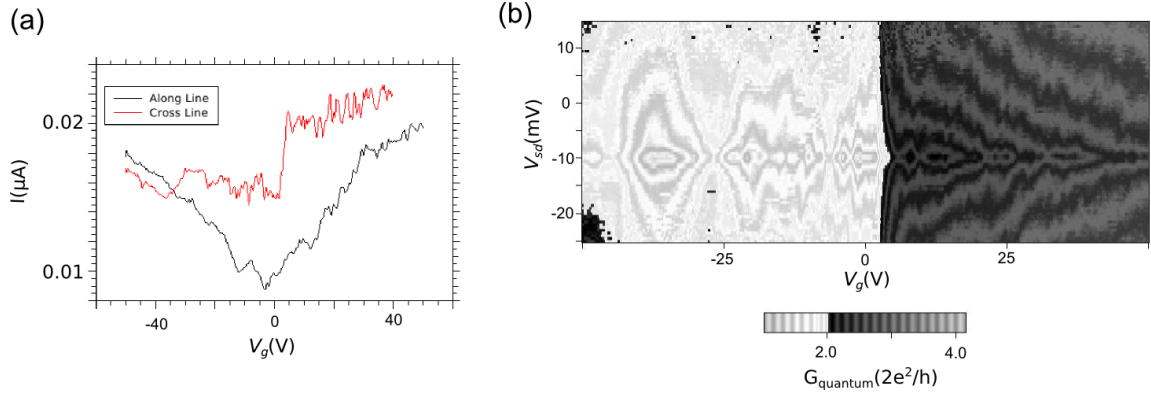


Figure 5.14: (a) The current across the line (red curve) and along the line (black curve) versus the back gate voltage. The current across the line is measured between contacts 1 and 3. The current along line is measured between contacts 2 and 4 (Figure 5.13a). There is a Dirac point feature in the current along the line defect. There is a conductance jump cross the line. (b) shows a quantum conductance changing with  $V_g$  and  $V_{sd}$ .

when the current flow along the line defect, the graphene parallel to it will contribute as an additional conducting channel. So it is just like a conducting graphene which will have a Dirac Point. For the data across the line defect, we also observe conductance fluctuations. There features are the lines in the coulomb diamonds. Also, there is also very interesting conductance jump near the  $V_g=0$  V. The Figure 5.14b shows a quantum conductance changing with  $V_g$  and  $V_{sd}$ . The jump is very clear. The quantum conductance at the side of  $V_g < 0$ V is lower than  $\frac{4e^2}{h}$  and at the side of  $V_g > 0$ V is higher than  $\frac{4e^2}{h}$ .

## 5.6 Transport with the line strain defect grounded

In this section, we will introduce a device which has several line defects and compare the transport properties across the regular line defect to the transport properties across the grounded line defect. The serial number of this device is Bubble Ac.

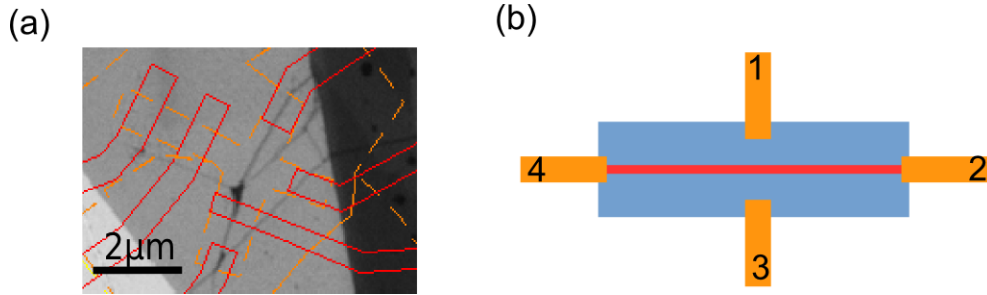


Figure 5.15: (a) SEM picture of device before transfer the top BN. (b) The schematic of device we measure.

At first, Figure 5.15 shows the real device picture and the schematic figure. The device is still a BN/Graphene/BN sandwich structure and contacts are made by edge contacts.

Then we perform the same measurement like before. The differential conductance between the line strain defect also shows some coulomb diamonds (Figure 5.16a), which proves the strain pseudo magnetic field block the electrons. In this measurement, the two contacts on the line defect are floated (Figure 5.16b). When you ground the two contacts on the line defect (Figure 5.16d), the pattern changed dramatically (Figure 5.16c). The coulomb diamonds disappear and only some lines features left. There is no coulomb diamonds mean no electron have been blocked by the line strain. It is very reasonable, because we ground the line strain defect. The electrons won't be affected by the line defect any more.

This experiment also prove that the line strain is the reason why there is coulomb blockades. The line defect is where the electrons have been blocked. In this way, we can

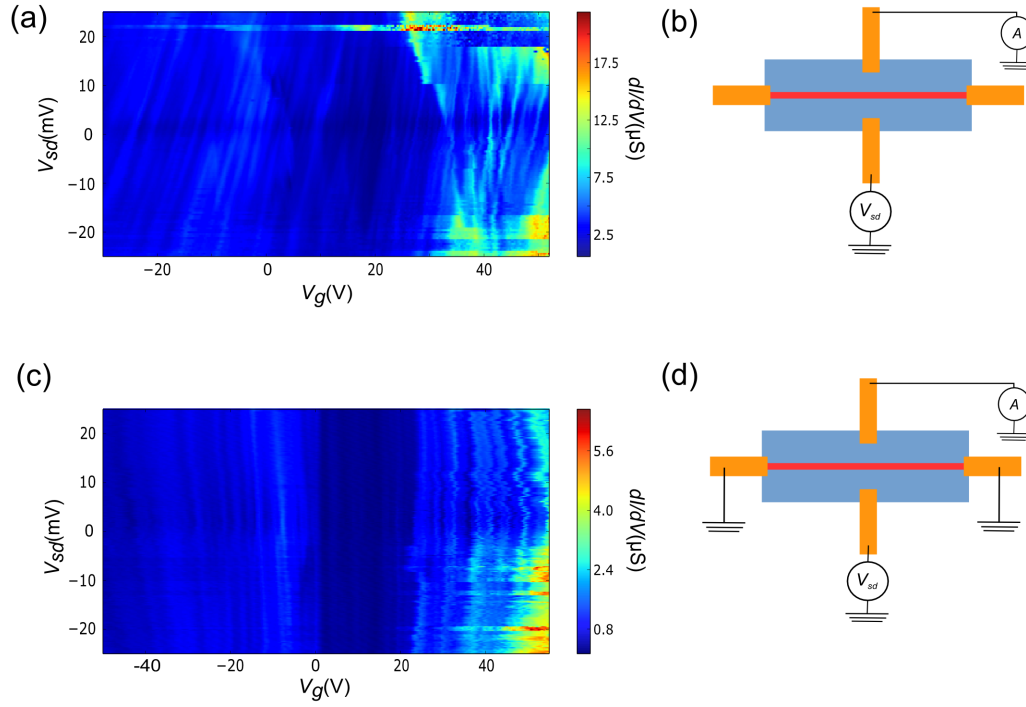


Figure 5.16: (a) The differential conductance with  $V_g$  vs.  $V_{sd}$  between two contacts cross line defect shown in (b). Two contacts connected to the line defect are floated in (b). There is some coulomb diamonds in (a). If you still measure the differential conductance (c), but ground the contacts on line defect (d) this time. The coulomb diamonds feature disappear and there are some perpendicular lines.

make sure the strain pseudo magnetic field is the reason of this phenomenon. On the other hand, our experiments prove the existence of the pseudo magnetic field by a transport study.

For the line strain devices, we not only can measure cross the line but also can measure along the line. The data looks very different from the coulomb diamonds (Figure 5.17). At first, we can see a Dirac point just like graphene on these devices. The reason is when the electrons travel along the line it won't always be blocked or scatted. Some electrons travel along the regular graphene part. That is why the data looks like taken

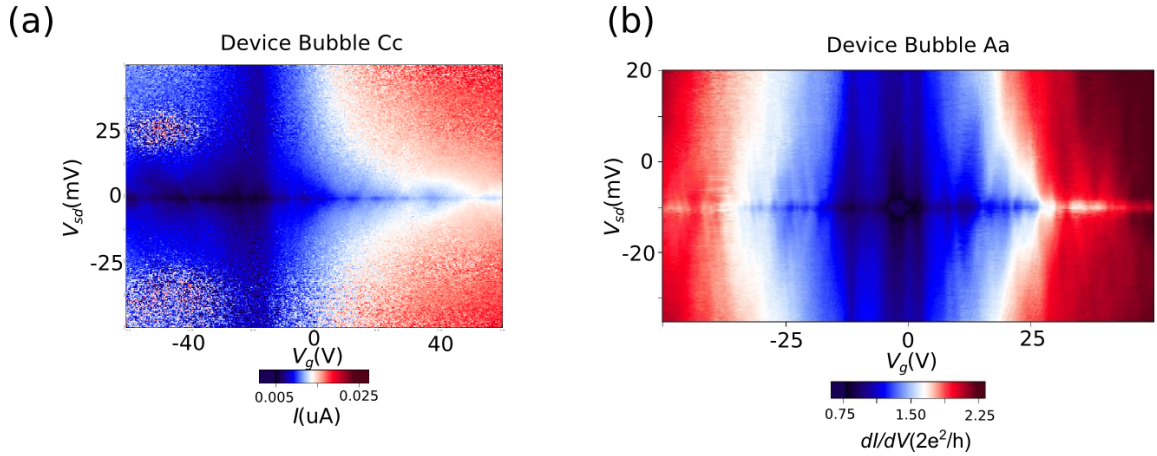


Figure 5.17: Here are the data taken along the line strain defect of two different devices. Both (a) and (b) shows a Dirac point. You can also see some coulomb diamond features. The Dirac point is contributed from the graphene part. And the coulomb diamonds are from the line defect.

in regular graphene. Second, actually it is not a regular graphene. We have a line strain defect with strong pseudo magnetic field inside. This part gives the coulomb diamond-like features in Figure 5.17.

Figure 5.18 shows the schematic of how charges moving along the line defect. There are two parts of device the regular graphene and the line strain defect in the center. Most charges will travel in the graphene part. Some others will be able to travel along or cross the line defect. The  $V_{sd}$  applied on the device along the direction of the arrow show in figure. Most of the charges (Red) will travel along the graphene. These charges will give the feature of Dirac point. Some of them (Yellow) will hit the line strain defect and bounce back to graphene area. Others (light green and dark green) may cross the line strain. These charges will contribute the coulomb diamond features. Only a few charges (Orange) will be

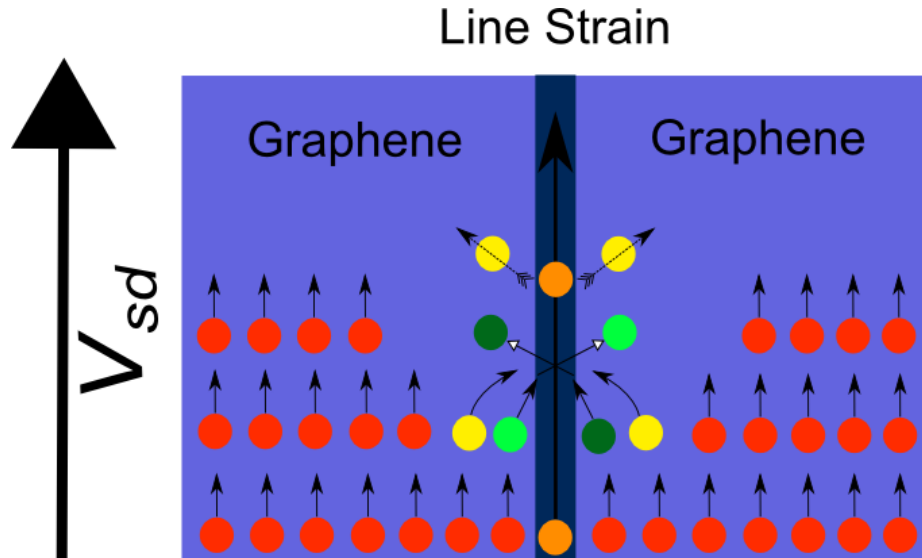


Figure 5.18: This figure shows the schematic of how charges move along the line defect. There are two parts of device the regular graphene and the line strain defect in the center. The  $V_{sd}$  applied on the device along the direction of the arrow. Most of the charges (Red) will travel along the graphene. Some of them (Yellow) will hit the line strain defect and bounce back to graphene area. Others (light green and dark green) may cross the line strain. These charges will contribute the coulomb diamond features. Only a few charges (Orange) will be able to travel inside the line strain.

able to travel inside the line strain. These charges are travelling along a one dimensional conducting channel which will be discussed later.

## 5.7 One Dimensional Conducting Channel

From the previous experiment results, the one dimensional strain defect may form a 1D conducting channel. For example, the charging energy and level spacing energy are close to nanotube devices. Their ratio is also close to the nanotube.

For graphene quantum dots, the level spacing will be sensitive to the gate voltage. Because the the level spacing is,

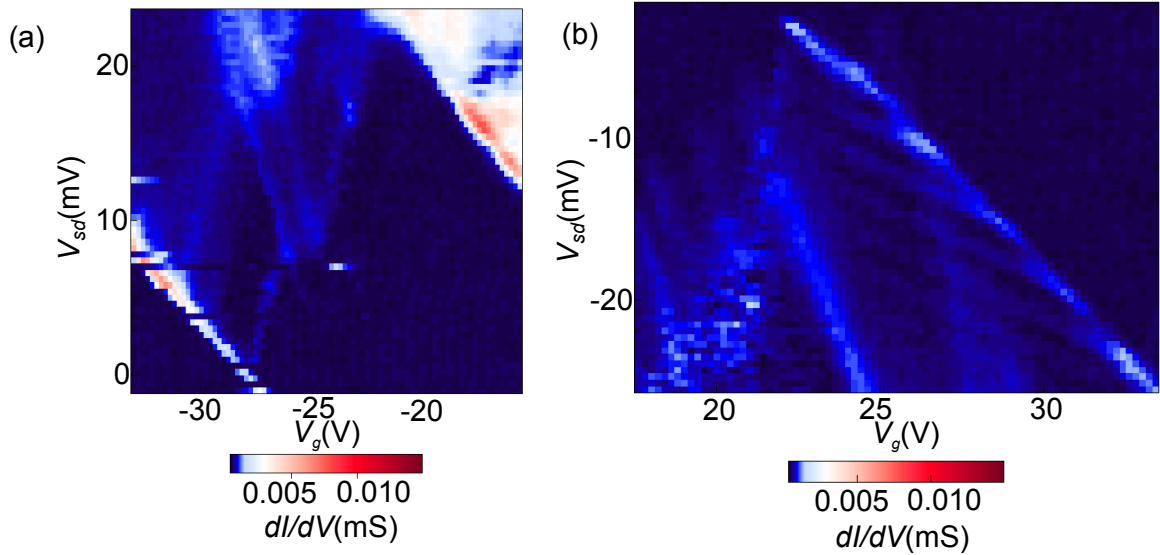


Figure 5.19: The level spacing at different gate voltage. The Dirac point is at around -10 V for this device. But the level spacing is basically the same between these two figures.

$$\Delta E \sim \frac{dE}{dk} \cdot \frac{\Delta k}{2}$$

so it will change when charges are away from the Dirac point. In Figure 5.19, level spacing is basically the same at different gate voltage. The Dirac point for this device is at around - 10 V. So the 1D strain defect behave more like a 1D dot instead of a 2D material quantum dot.

## 5.8 Temperature Dependence

In this section, we did some temperature dependence measurements.

At first, here is the experiment we tracing the coulomb peaks with temperature changing. We plot the Figure 5.20 with  $V_g$  vs.  $dI$  at  $dV=200\mu V$ . There are three main

peaks in Figure 5.20a. Both of them are broadening with temperature. The highest peak is very clear to see the height is getting smaller and smaller when the temperature increasing. There is one small peak at around  $V_g \approx 0$  V next to the highest peak. It only appears at very low temperature. The Figure 5.20b is the zoomed-in of the first high peak in (a). This peak is getting broaden from 1.4 K to 10 K. At 15 K, it is already very wide. Above 20 K, you can barely see these peaks. They are disappearing in the background.

This behaviour also follow the properties of quantum dots [46].

Then, we change the bias voltage, similar behaviours have been observed in Figure 5.21.

For quantum dot devices, they are very sensitive to temperature and will change a little after every single thermal cycle [46] [1] [29]. Our device also shows a sensitive response to thermal cycle. Figure 5.22 shows a same device after two different thermal cycles. The coulomb diamonds are still clear but the size of the diamonds have changed. It means the size of quantum dots has changed. Often quantum dots change their behavior on thermal cycling because of environmental charge rearrangement. The other reason might be after thermal contraction/expansion the strain itself will change. But after these two thermal cycles, the  $V_{xy}$  signal still be similar to what we talked early this chapter.

Then after two more thermal cycles, something starts to changing in the  $V_{xy}$  signal. The  $V_{xy}$  signal before thermal cycles have been discussed in Figure 5.12. In that figure, the  $V_{xy}$  has minimum when the charges are blocked cross the line strain.

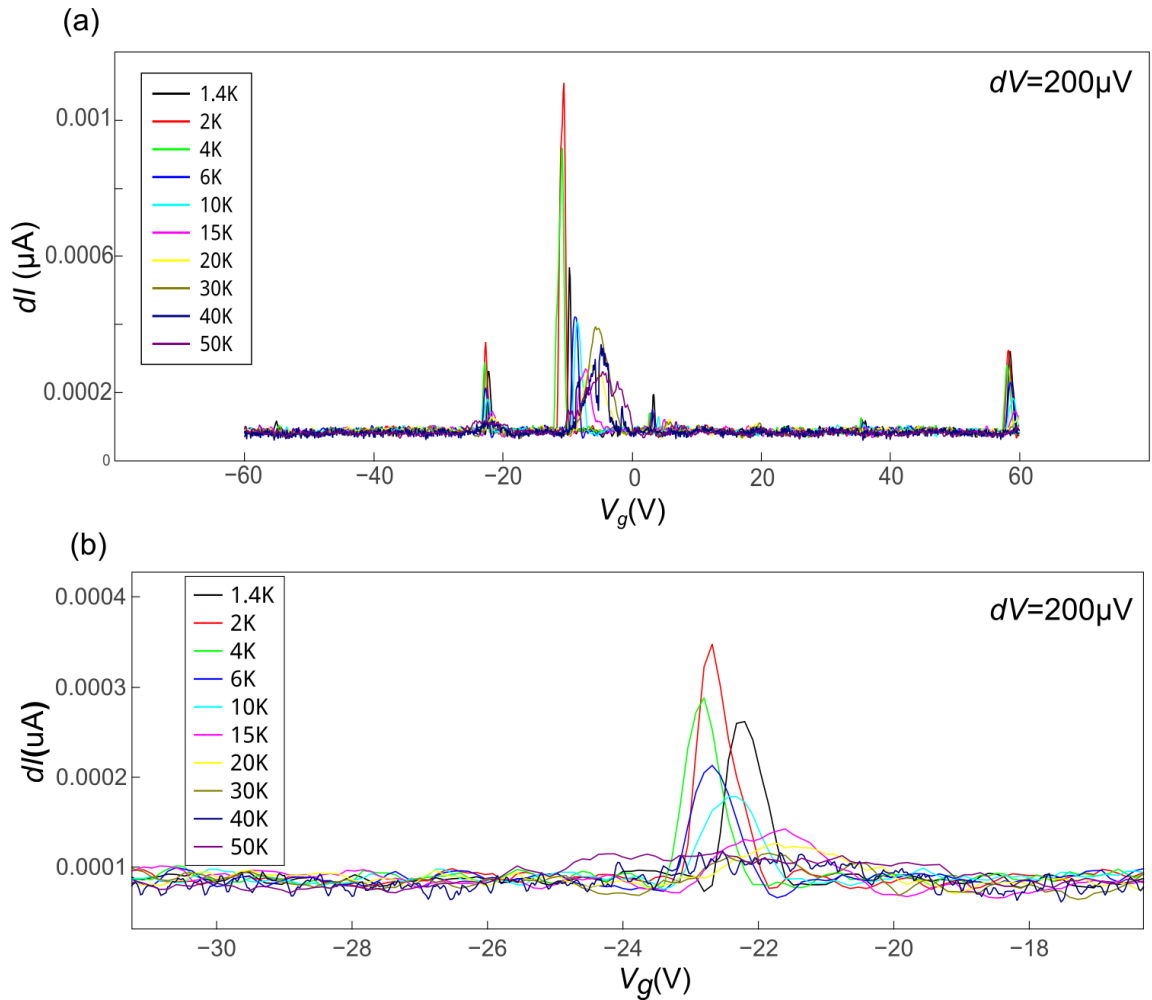


Figure 5.20: The coulomb peaks changing with temperature. (a)  $dI$  vs.  $V_g$  at  $dV=200 \mu\text{V}$ . The coulomb peaks are getting broaden by raising the temperature. (b) Zoom-in graph of the first peak of (a). The peak is getting broaden from 1.4K to 10K. At 15K, it is already very wide. Above 20K, you can barely see these peaks. They are disappearing in the background.

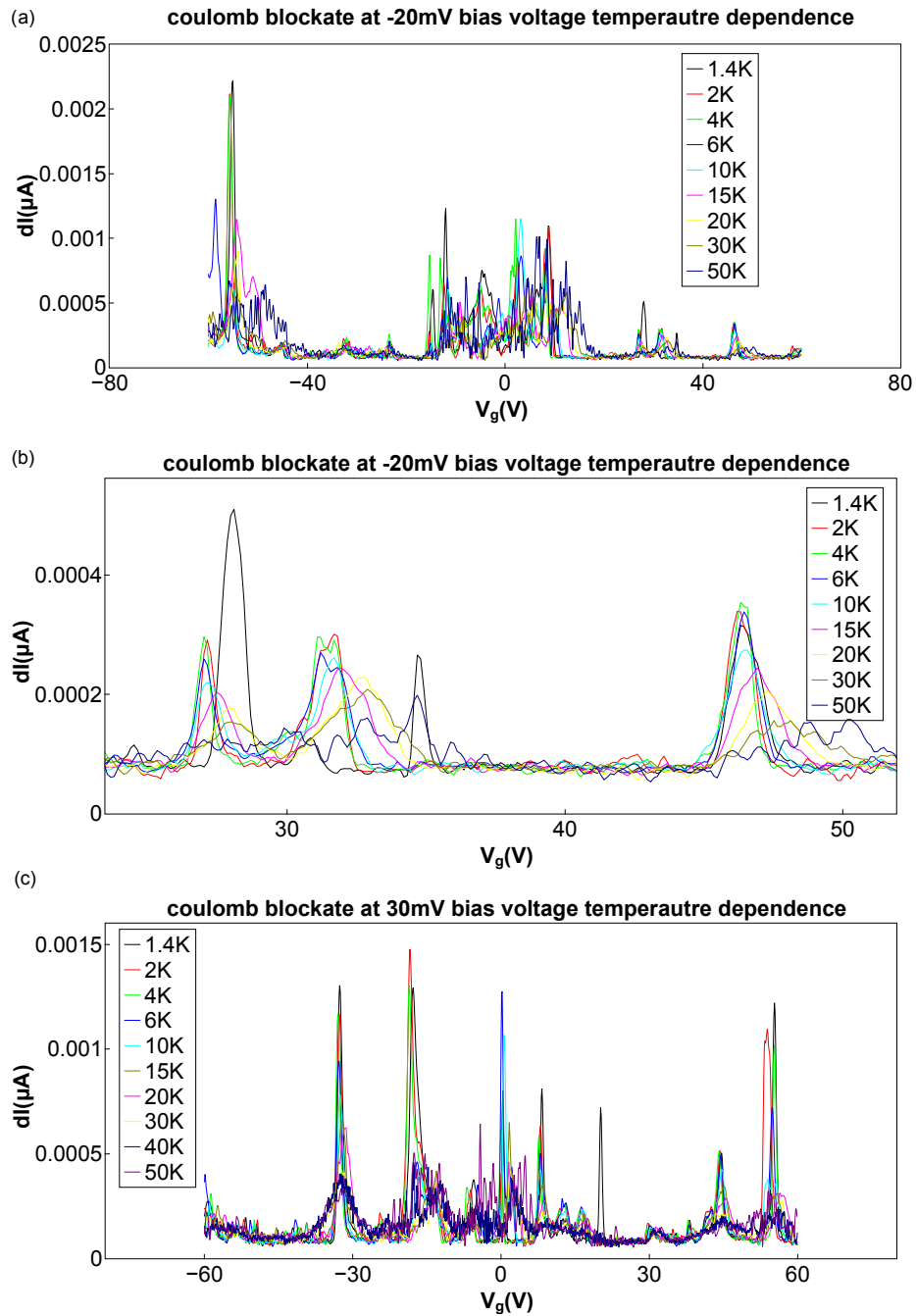


Figure 5.21: (a) Temperature dependence of coulomb peaks at -20 mV bias voltage. (b) A zoom-in figure of (a). (c) Temperature dependence of coulomb peaks at 30 mV bias voltage.

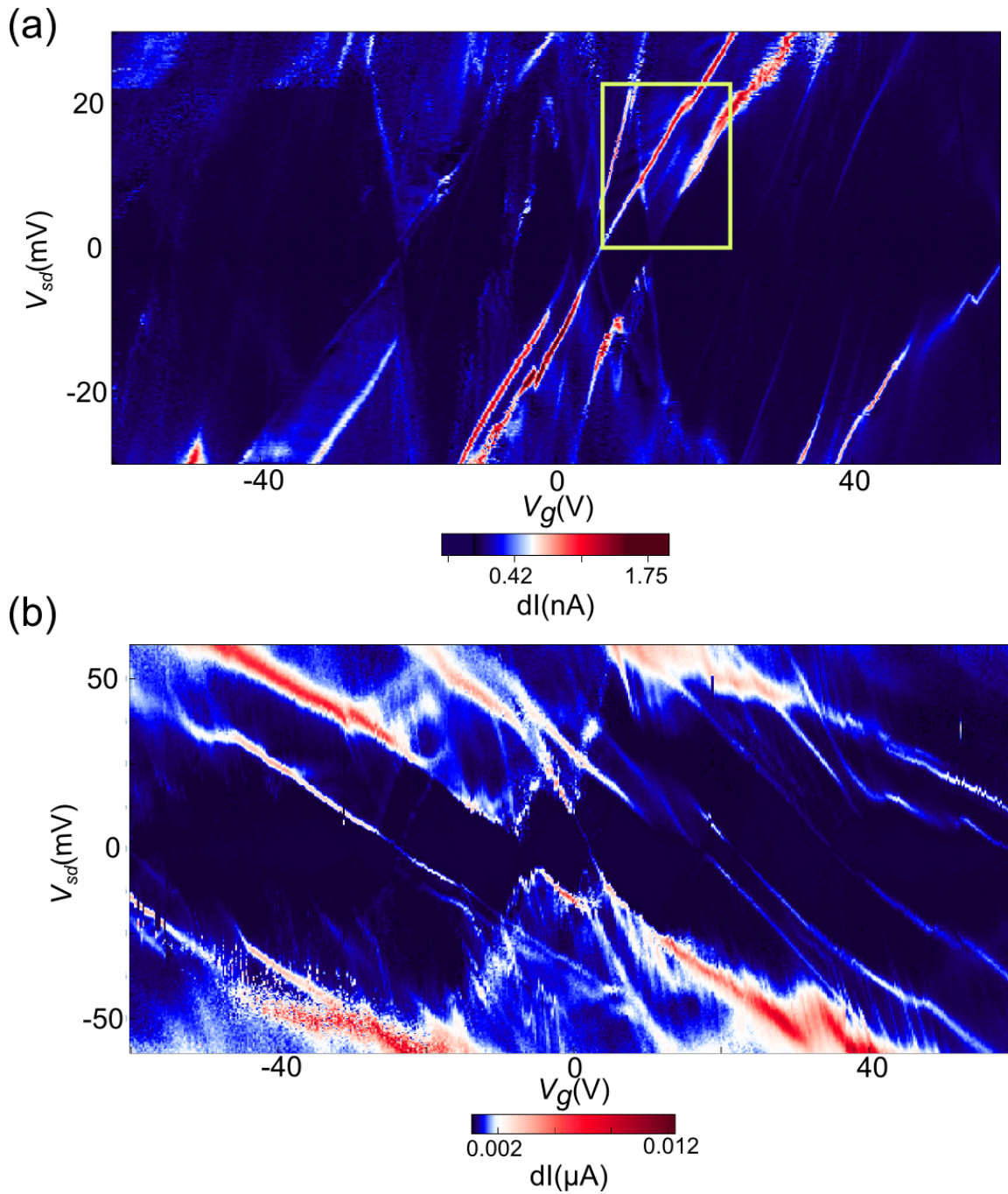


Figure 5.22: The two figures in (a) and (b) are same device after two different thermal cycles. There are still clear coulomb diamonds. These diamonds' sizes are different in every single figure which means there are more than one size quantum dots. Inside the yellow box in (a), there are some clear quantum levels.

But after several thermal cycles, the  $V_{xy}$  will have maximum when the charges are blocked cross the line strain (Figure 5.23). Figure 5.23a and Figure 5.23c are the dI with  $V_g$  as x axis and  $V_{sd}$  as y axis. The figure 5.23c and figure 5.23d are the  $V_{xy}$  for device in (a) and (c). The  $V_{xy}$  signal gets much larger than before after thermal cycle. And when the charges are blocked in (a) and (c) which is in the deep blue area in the center, the charges in xy direction are increased (red area). The coulomb diamonds pattern basically stays the same. It means both charges in two different directions are affected by the line strain.

So after the thermal cycle, the strain will change so the diamond shape changes. And the scattering from the strain will dramatically increase. But the strain will still be there and dominate the transport features.

Figure 5.24 shows the schematic of the two different  $V_{xy}$  scattering modes before and after thermal cycle. (a) is the scattering mode before thermal cycle. (b) is the scattering mode after thermal cycle. In Figure 5.24(a) the red dots are charges in the graphene of source side. The purple dots are charges already cross the line strain and go to drain contact. These purple charges contribute the quantum dot behaviour (coulomb diamond feature). The green dots are charges cross the line strain and stay inside the 1-D channel. They go to the contacts on the sides eventually. The orange dots are charges already cross the line strain on the other side of graphene but flow along the line strain defect. The  $V_{xy}$  signal in this case is contributed by green and orange charges. In Figure 5.24b, the red dots and pink dots are charges in the graphene of source side. After crossing the line strain area, the pink charges go cross the line strain and become the purple charges. But the red charges are blocked by the line strain and flow along it into two contacts on the side. So in Figure 5.24a,

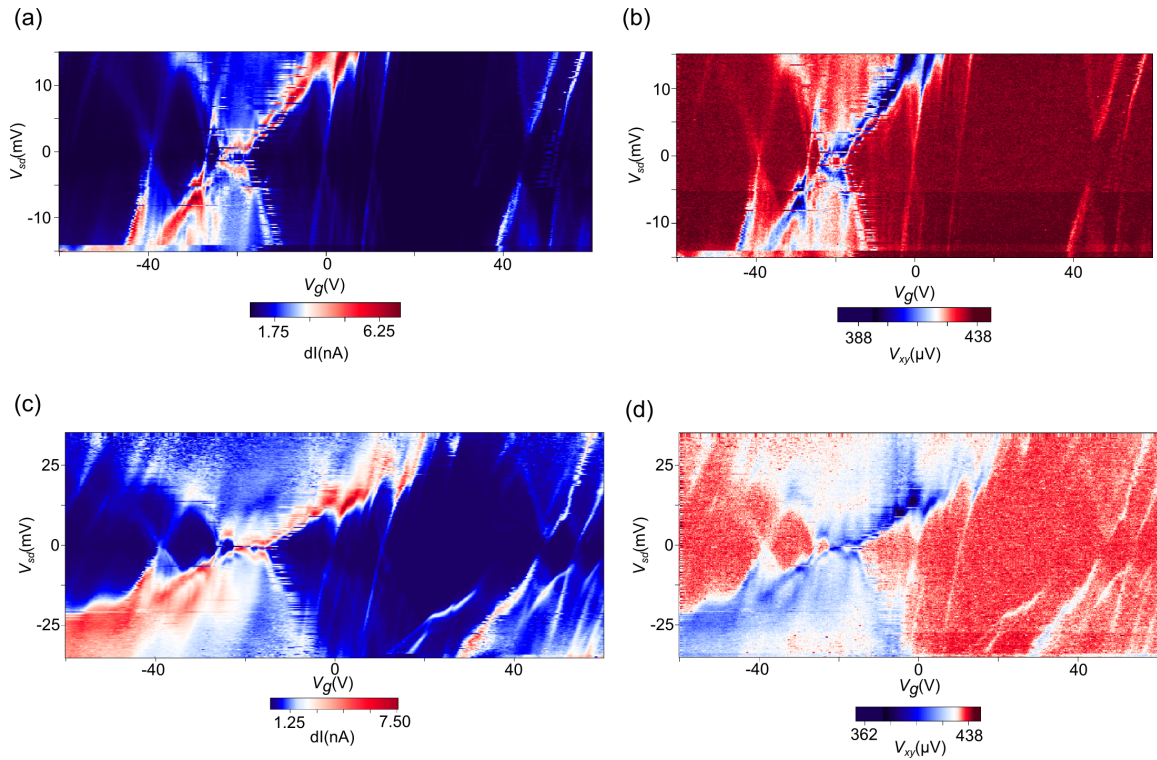


Figure 5.23: The two figures in (a) and (c) are two sets of data of same device after several thermal cycles.  $dI$  is the differential current cross the line strain defect. And the x axis is  $V_g$  and y axis is  $V_{sd}$ . There are still clear coulomb diamonds in both figures (a) and (c). These diamonds' sizes are different in every single figure which means there are more than one size quantum dots. But the shape of the coulomb diamonds in (a) and (c) are very different, which means the quantum dots have changed a lot. The figure (b) and (d) are the  $V_{xy}$  measured at same time for (a) and (c). Instead of very small signal, the  $V_{xy}$  increases a lot. And when the charges are blocked in (a) and (c) which is in the deep blue area in the center, the charges in xy direction are increased (red area). And on the other hand, the coulomb peaks in (a) and (c) will cause signal dips in (b) and (d).

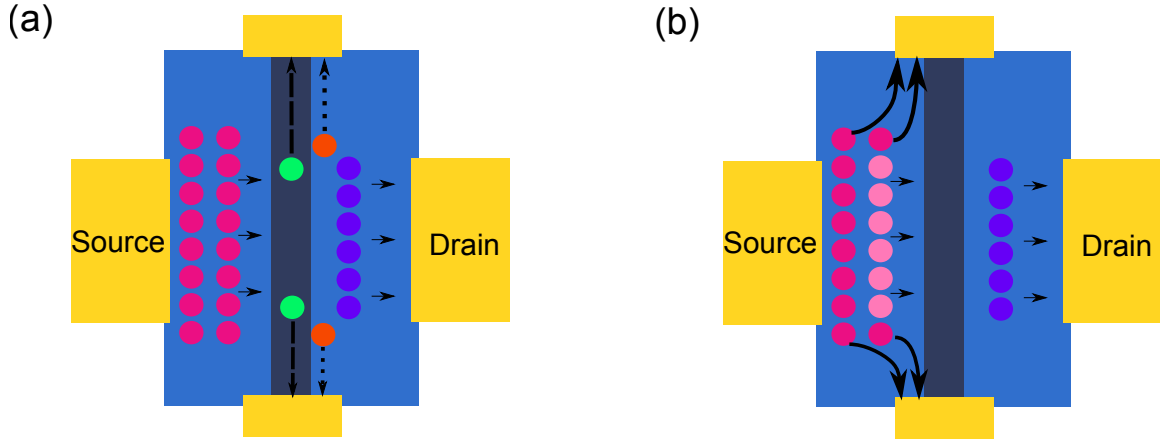


Figure 5.24: The schematic of two different modes  $V_{xy}$  scattering before and after thermal cycle. The blue big area is graphene. The grey line in the mid is the line strain. There are four contacts on four sides. (a) is the scattering mode before thermal cycle. (b) is the scattering mode after thermal cycle. (a) the red dots are charges in the graphene of source side. The purple dots are charges already cross the line stain and go to drain contact. These purple charges contribute the quantum dot behaviour (coulomb diamond feature). The green dots are charges cross the line strain and stay inside the 1-D channel. They go to the contacts on the sides finally. The orange dots are charges already cross the line train on the other side of graphene but flow along the line strain defect. (b) the red dots and pink dots are charges in the graphene of source side. Purple dots are pink charges which already crossed the line. The rest of red charges go to the contacts on the side.

the green and orange charges contribute the  $V_{xy}$  signal. The number of these two charges are proportion to the purple charges. That is why before thermal cycle, where  $V_{xy}$  signal is strong is where  $dI$  has coulomb peaks. On the other hand, in Figure 5.24b, the red charges contribute the  $V_{xy}$  signal. And the number of red charges are inversely proportional to the number of purple charges. So the  $V_{xy}$  has big value when the charges are blocked by the stain (inside the coulomb diamonds).

The reason this device has two different modes of scattering might be the stain itself is different after thermal cycle. The different stain will create different pseudo magnetic field to block the charges. And also the 1-D conducting channel will also be different.

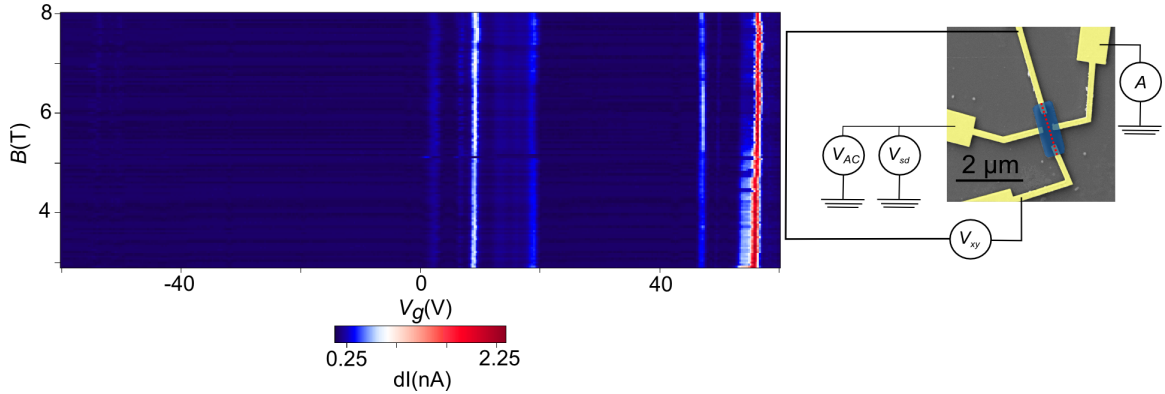


Figure 5.25: The differential current cross the line strain with  $V_g$  as X and B as Y. The coulomb peaks are straight lines along the magnetic field. The insert graph is the schematic of the measurement setup.

## 5.9 Conductance Changing with the Magnetic Field

The magneto-transport properties are very important to understand a system in quantum transport study. In this section, the data taken with magnetic field will be discussed.

Figure 5.25 is the differential current cross the line defect taken with  $V_g$  as X axis and magnetic field B as Y axis. The coulomb peaks are straight lines. This means the cyclotron orbit is smaller than size of the line strain. That is the reason why it won't be affected by the external magnetic field.

We can measure the current cross the line defect with changing magnetic field. In the same way, we also can measure the current along the line. Figure 5.26 shows the  $V_{xx}$  along the line strain with  $V_g$  as X and B as Y. There are several features in this figure. First we can see a Dirac point close to zero and this Dirac point become a gap area at high field. This part is from the graphene. Second, there are Landau levels at high field of electron

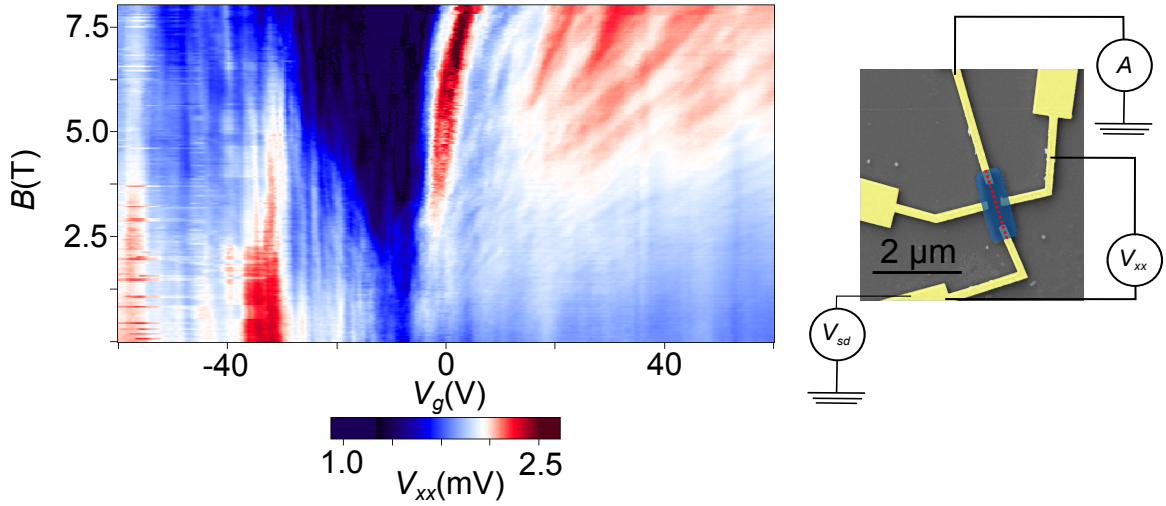


Figure 5.26: The  $V_{xx}$  along the line strain with  $V_g$  as X and B as Y. There are several features in this figure. First we can see a Dirac point close to zero and this Dirac point become a gap area at high field. Second, there are landau levels at high field of electron side. Third, there are some perpendicular line features which response to coulomb peaks both at electron side and hole side. The lines at hole side is more clear. The insert graph is the schematic of the measurement setup.

side. This feature is also from the graphene part. Third, there are some perpendicular line features which response to coulomb peaks both at electron side and hole side. The lines at hole side is more clear. This feature is more contributed by the line stain defect. The insert graph is the schematic of the measurement setup.

At the same time, we also measure the  $V_{xy}$  cross the line strain with the changing magnetic field. Figure 5.27a shows  $V_{xy}$  cross the line strain with  $V_g$  as X and B as Y. There are also several features in this figure. First we can see a large signal area at high field. Second, there are some perpendicular line features which response to coulomb peaks both at electron side and hole side. Third, there are small oscillations in the background. These oscillations are from the interference between several different transport modes called Fano

resonance [19]. In physics, a Fano resonance is a type of resonant scattering phenomenon that gives rise to an asymmetric line-shape. Interference between a background and a resonant scattering process produces the asymmetric line-shape (Wikipedia). In Figure 5.27b, the main figure is the line trace at  $B=0$  T. You can see clear feature from the coulomb peaks which is the deep dip here. The right insert figure is the schematic of the measurement setup. The left insert figure is the zoom-in graph from the red area. The resonance is clear in this insert graph.

So where does this Fano resonance come from?

At first, we need understand the Fano resonance. The Fano resonance line-shape is due to interference between two scattering amplitudes, one due to scattering within a continuum of states (the background process) and the second due to an excitation of a discrete state (the resonant process). The energy of the resonant state must lie in the energy range of the continuum (background) states for the effect to occur. Near the resonant energy, the background scattering amplitude typically varies slowly with energy while the resonant scattering amplitude changes both in magnitude and phase quickly. It is this variation that creates the asymmetric profile.

The interference could happen between the original charges and the scattering charges. The scattering charges also could have first-order scattering (scattered once), second-order scattering (scattered twice) ...

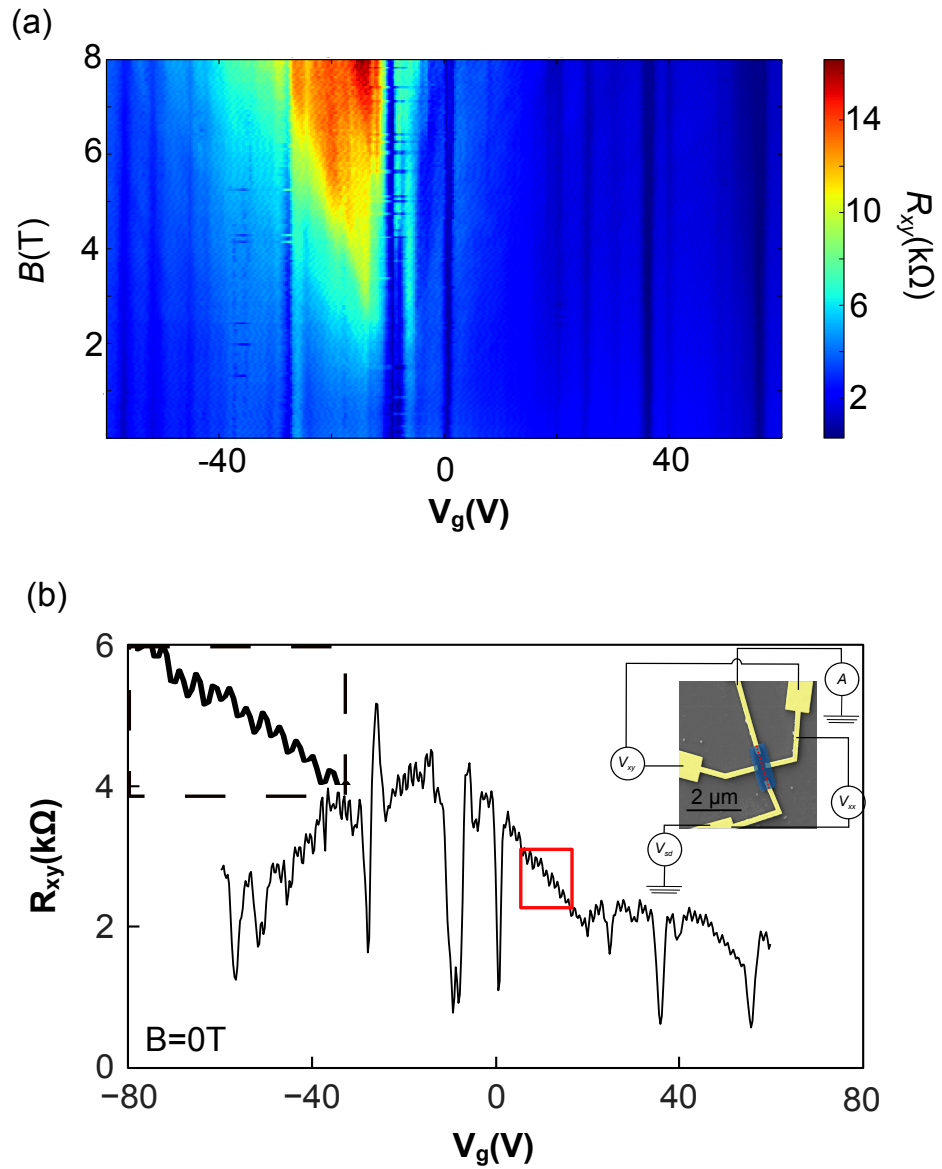


Figure 5.27: (a) The  $V_{xy}$  cross the line strain with  $V_g$  as X and B as Y. There are also several features in this figure. First we can see a large signal area at high field. Second, there are some perpendicular line features which response to coulomb peaks both at electron side and hole side. Third, there are small oscillations in the background. (b) The line trace at  $B=0$ T. There are some large dips which is from the coulomb peaks of  $R_{xx}$ . The small oscillations are some Fano Resonance between several different modes. The right insert graph is the measurement setup. And the left insert graph is the zoom-in graph of the red box area.

## 5.10 The Triangle Bubble Strain Defect and Other Bubbles

In Figure 5.2, there are many different of bubbles. According to Manchester's group [21], different shapes of strain will definitely give different pseudo magnetic field or no pseudo field at all. The way we create strain bubbles will give us many different uniform shape bubbles, like triangle, circle, polygon etc. They both are very ideal objects to study the pseudo magnetic field.

In this chapter, we mainly talked about the line strain. Actually, other shapes strain defect will have different physics inside which are very interesting. In this section, we will introduce our work on the triangle bubble strain defect and other shapes of bubbles.

The first sample is a single triangle and there are three line stain defect connected to its three corners. Figure 5.28 (a) shows the schematic of the device. There are six contacts connected to the device shown in figure. They are labelled with numbers for identification for the following discussion. Figure 5.28 (b) is the SEM picture before transferred the top BN. Inside the black box, it is the area graphene will be left after etching. There is a perfect triangle strain bubble inside. The Figure 5.28 (c) is the differential conductance between contacts 3 and 5. The x axis is  $V_g$  and y axis is  $V_{sd}$ . The contacts 3 and 5 are two contacts cross the line strain. But not like the devices we talked before, this time we have a triangle bubble in the device. So basically, the charges can go through the line defect and also the triangle bubble. We know the line defect will give a big pseudo magnetic field and block most of the charges (Coulomb Blockades). That is why we have these diamonds features in Figure 5.28 (c). But we also have a Dirac point near  $V_g=0$  V. This may due to the triangle bubble will lead some charges. The edge of the triangle bubbles will also have a high pseudo

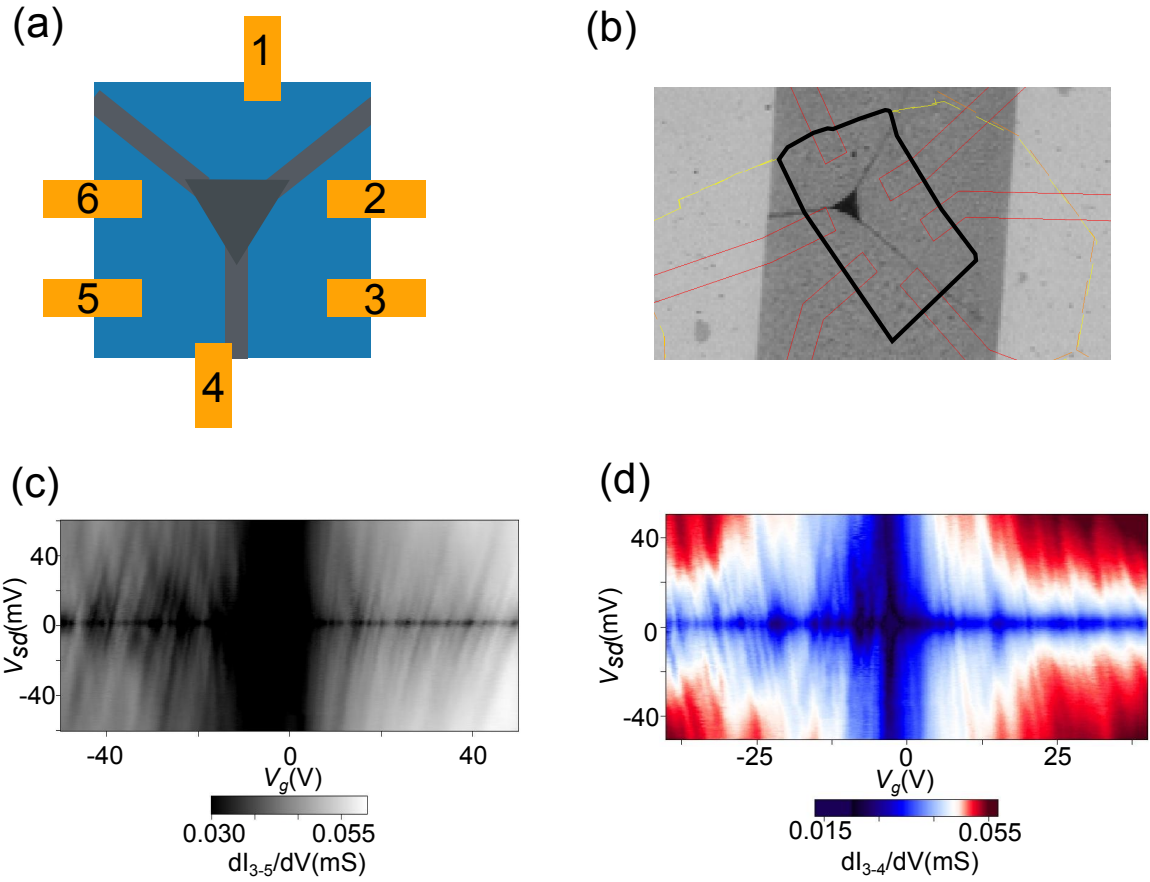


Figure 5.28: (a) The schematic of the device. Six contacts are labelled with numbers. (b) The SEM picture of the triangle defect. The black box is the etched graphene area. Six contacts (Red dashed line) are also shown here. (c) The  $V_g$  vs.  $V_{sd}$  plot the differential conductance between contacts 3 and 5. (d) The  $V_g$  vs.  $V_{sd}$  plot the differential conductance between contacts 3 and 4.

magnetic field, so the coulomb diamonds won't disappear. But the stain may be smaller so we also can see the clear Dirac point. The Figure 5.28 (d) also shows similar data for contacts 3 and 4.

Here, let's explain the structure of the strain a little. The reason why different strain bubbles will have different transport properties is the pseudo magnetic field. Stronger

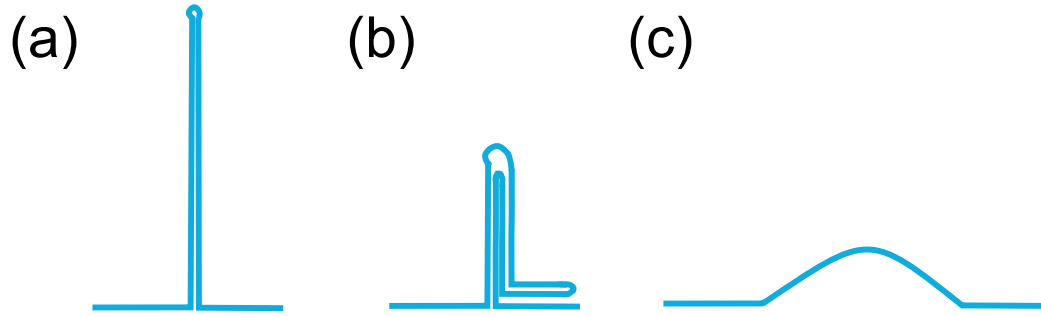


Figure 5.29: Cross-section side view of strain defects: (a) The first possibility of line strain. (b) The second possibility of line strain. (c) The triangle, circle or polygon strain bubble.

strain will have stronger pseudo magnetic field. Like Figure 5.29, the two possibilities of line strain will definitely have stronger strain than bubbles in Figure (c).

Interestingly, for this device, several contacts are not conducting. We decide to use them as side gate. Surprisingly, we also observe some coulomb diamonds and features are more clear.

Now let's introduce another triangle bubble device quickly. The schematic figure and SEM picture are in Figure 5.32 (a) and (b). The third graph is the line trace of differential current between contacts 5 and 8. The insert graph is the measurement setup. There are some coulomb peaks. So between these two contacts, the line strain defect will dominate the features. The (d) and (e) are the data of differential current through triangle bubble under magnetic field and measurement setup for (d). From (d), we can see a Dirac point and several landau levels at high field. The coulomb peaks are also there. These features could be explained by the physics picture we discussed before. And from (c) we

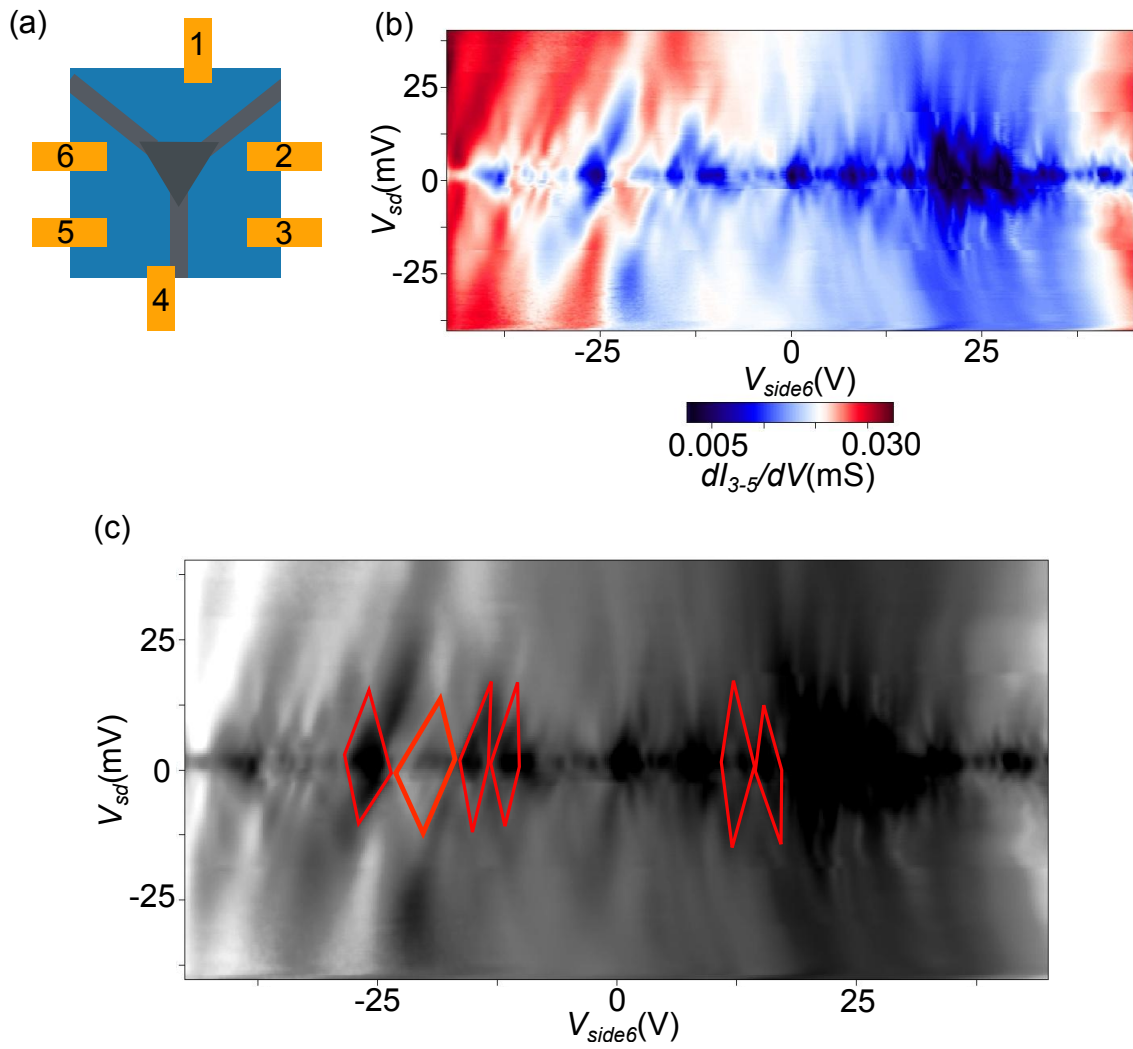


Figure 5.30: (a) The schematic of device structure. (b) The Coulomb Diamonds of differential conductance between contacts 3 and 5 by using contact 6 as side gate. (c) The gray scale of graph (b) and some coulomb diamonds are pointed out by red lines.

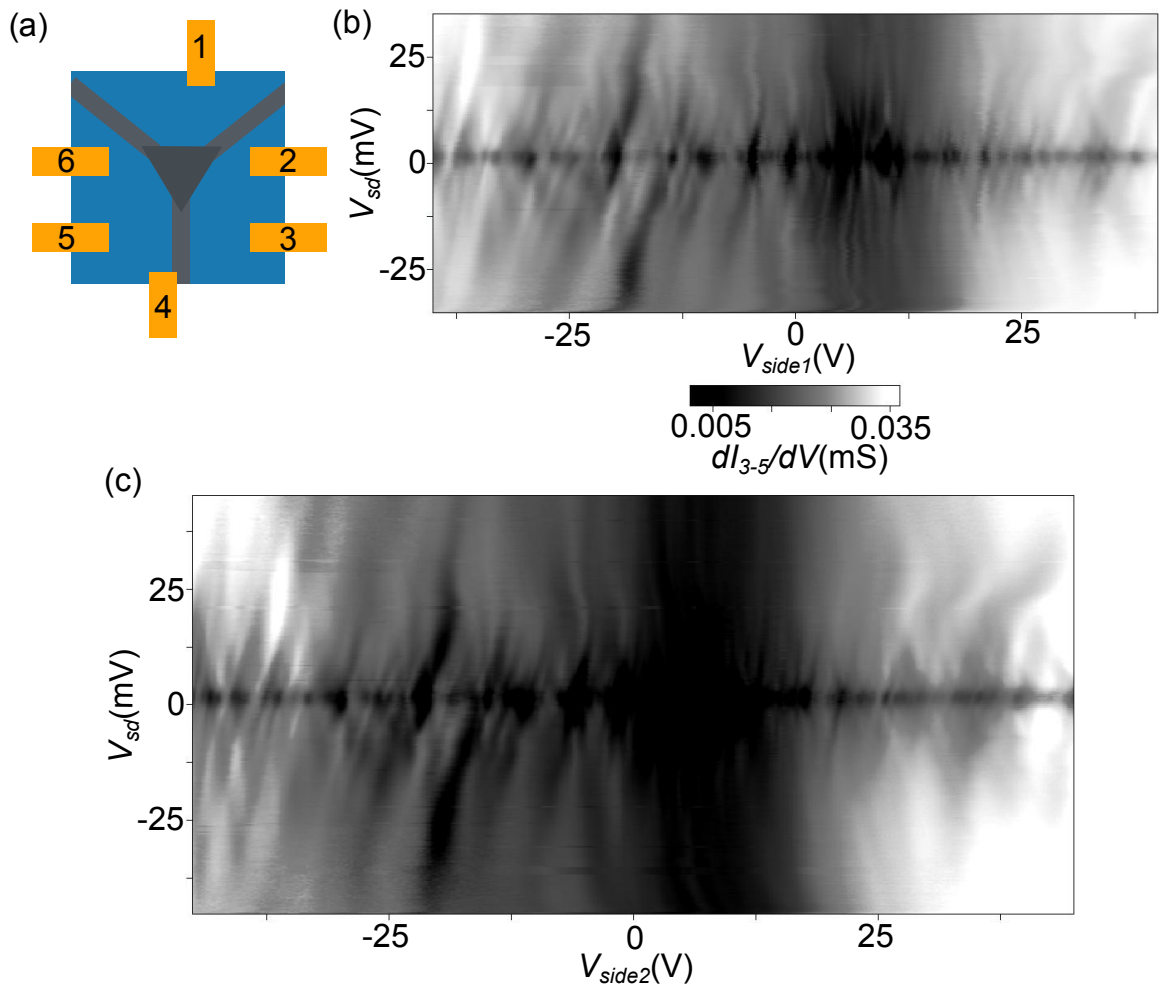


Figure 5.31: (a) The schematic of device structure. (b) and (c) the coulomb diamonds of differential conductance between contacts 3 and 5 by using contact 1 and 2 as side gates separately. The coulomb diamonds features are not very sensitive to different side gates.

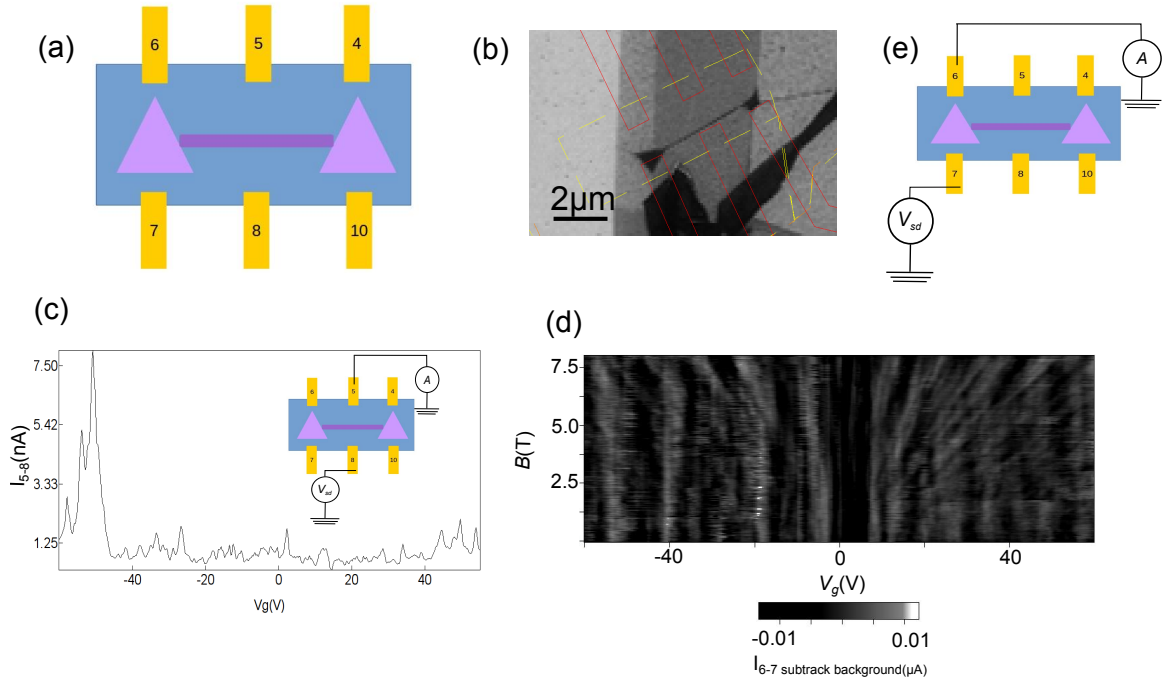


Figure 5.32: (a) The schematic of the device structure. (b) The SEM picture of the device. (c) The coulomb peaks of the differential current between two contacts cross the line in the mid. The insert graph is measurement setup. (d) The Magnetic field vs. back gate voltage and plot the differential current through two contacts cross the bubble. (e) The measurement set up for (d).

know, the triangle bubble will also block the charges. It won't provide the charges a free channel.

## 5.11 Two parallel graphene conducting device divided by the line strain

From the previous experiments, people know the graphene will have higher mobility when it has a very flat substrate and graphene itself is very clean [5].

But what we do to study the strain defect will dramatically reduce the mobility. Because the graphene with strain defect won't be flat at all. But if the size of the flat graphene next to the strain defect is big enough to have a high mobility, we will have chance to have a device like the one in this section.

The device is simple. A flat graphene with the line strain in the center. Only two contacts connected on two sides along the line (insert graph in Figure 5.33). Figure 5.33 is the current between two contacts with two axes are  $V_{back}$  and magnetic field. Instead of one regular landau fan, we see two landau fans. There are also two Dirac points. The landau levels (LLs) from the right Dirac point is very clear. The LLs from the left Dirac points are more like an interference pattern.

The situation can be understood by a two parallel graphene model. The left graphene and right graphene are separated by the mid line strain defect. If these two graphene are doped differently, there will be two Dirac points and two LLs. The mid line strain is very resistive. So the two landau fan will be quite independent from each other. If there are some charges crossing the line strain defect, there might be some interference at the graphene area. This might be the reason why there are some interference pattern at the left side of the Figure 5.33.

## 5.12 Conclusion

In this chapter, we provide a way to study the pseudo magnetic field generated by stain. And the stain defect sample we use is very stable and easy to get. It is a very good system to study the pseudo magnetic field and the valleytronics.

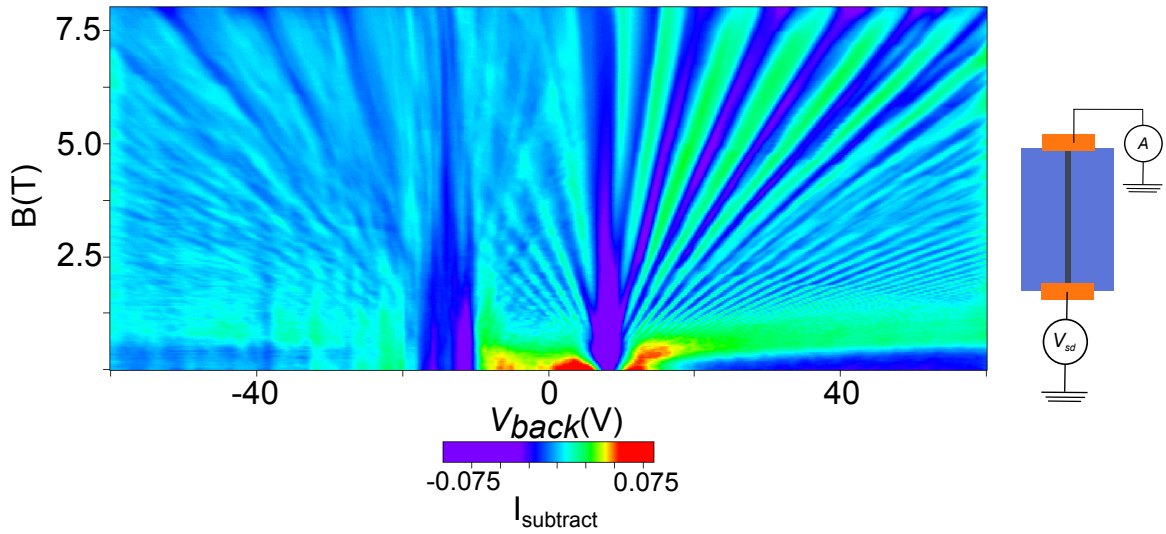


Figure 5.33: The landau fan of the device. The schematic of device and measurement setup is in the insert graph.

In our experiments, the line strain sample gives a clear result of coulomb blockades. This phenomenon is from the pseudo magnetic field resistance. We also create a one dimensional conducting channel in two dimensional Dirac fermions system.

Other shapes of strain defect will also be a good direction to study. For example, triangle strain defect bubble will be a candidate to make Nano-cavity.

## Chapter 6

# Transport in Graphene Black Phosphorus Heterostructure

### 6.1 abstract

Graphene is the first 2D layer material exfoliated on substrate [52] by Scotch tape. This Scotch tape method was later applied to other layered materials. In this way, a family of 2D materials [53] are formed, including insulators such as h-BN, semiconductors such as MoS<sub>2</sub> and WSe<sub>2</sub> and metals such as NbSe<sub>2</sub>.

Black Phosphorus (BP) joins the family since 2014 reported by Xianhui Chen, Yuanbo Zhang *et al.* [41]. As we know, graphene is isotropic in transport properties. However, the BP is anisotropic in transport properties due to its structures. In this chapter, devices with hetero-structure of graphene on top of the BN are studied. Some anisotropic

transport behaviour and unique magneto-transport behaviour have been observed and will be talked in this chapter.

## 6.2 introduction

Black Phosphorus is one of the highest mobility 2D materials except graphene. Both the Shubnikovde Haas (SdH) oscillations [40] [20] and quantum hall effect have been reported [39]. The field mobility is up to  $6,000 \text{ cm}^2\text{V}^{-2}\text{s}^{-s}$ .

In Figure 6.1, it is the structure of the BP. Single layer structure is given in figure (a). (b) and (c) give the side view and top view as long as their lattice parameters.

Due to Black Phosphorus' in plane anisotropic structure, it has a strongly anisotropic transport characteristics. The transport properties depend on the charges propagating direction and lattice direction strongly [42]. The non-local transport behaviour will also be very different in two directions [49].

Graphene, which is isotropic, may be introduced some anisotropic behaviour from BP. That is the motivation we design and perform this experiment. Further, the lattice of BP is natural born one dimensional periodic. This reminds us some possible physics inside from the periodic potentials like Chapter 3. Recently, some theory studies of this BP/Graphene system have been reported [7] [54].

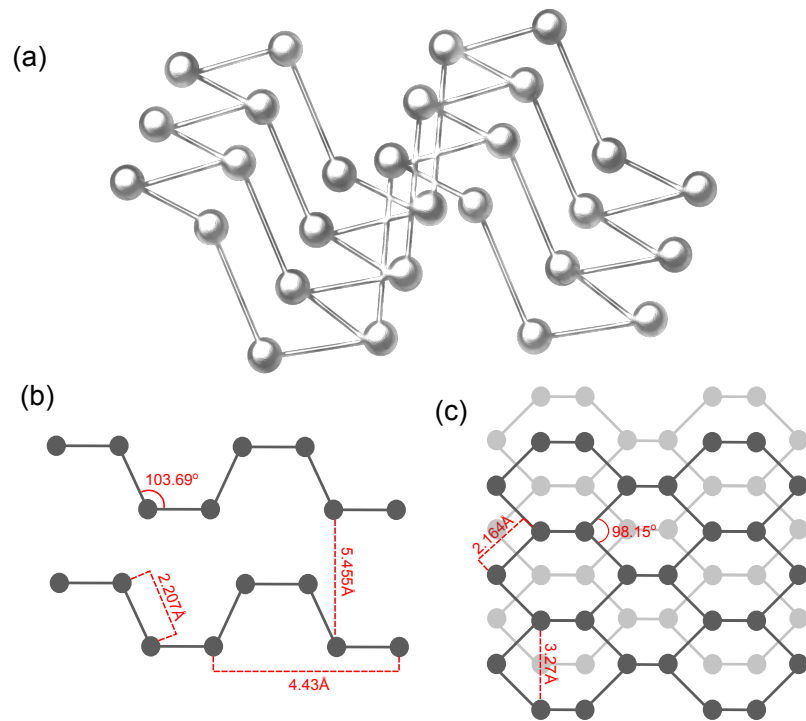


Figure 6.1: (a) Structure of single layer BP. Side view (b) and top view (c). The lattice parameters are given in the figures.

### 6.3 Device Fabrication and Structure

Black Phosphorus is ordered from 2D Materials. They are exfoliated in a glove box full of nitrogen gas inside to protect it from oxygen and water in the air. The layer structures are made by layer transfer technique talked in Chapter 2.

Figure 6.2 shows the process of making BP/Graphene devices. At the first, we need exfoliate the BP layer structure from the bulk by Scotch tape method. This process (Figure 6.2 a) must be made inside the glove box or other possible conditions without out air and water. The reason is BP is very easy to oxidize and the water vapor in the air will also damage its structure [8] quickly. Then, a graphene layer is transferred onto BP (Figure 6.2 b). This process is quickly done in the air (less than 5 min). During such a short time exposed in the air, the BP basically will stay the same [8]. The study of the stabilization of BP covered by graphene will be introduced later this section. Then the 12 Cr/Au contacts on graphene with a  $30^\circ$  angle between each of them are made (Figure 6.2 c). We transferred a BN layer on top of graphene with contacts and made a gate on top (Figure 6.2 d and e).

To verify the stabilization of BP covered by graphene, the atomic-force microscopy (AFM) technique is used.

Previous experiments have been shown the BP after exposed in the air more than 30 mins, droplet-like structures become visible on the surface of the flakes. The droplet keeps growing when the samples are kept in air [8].

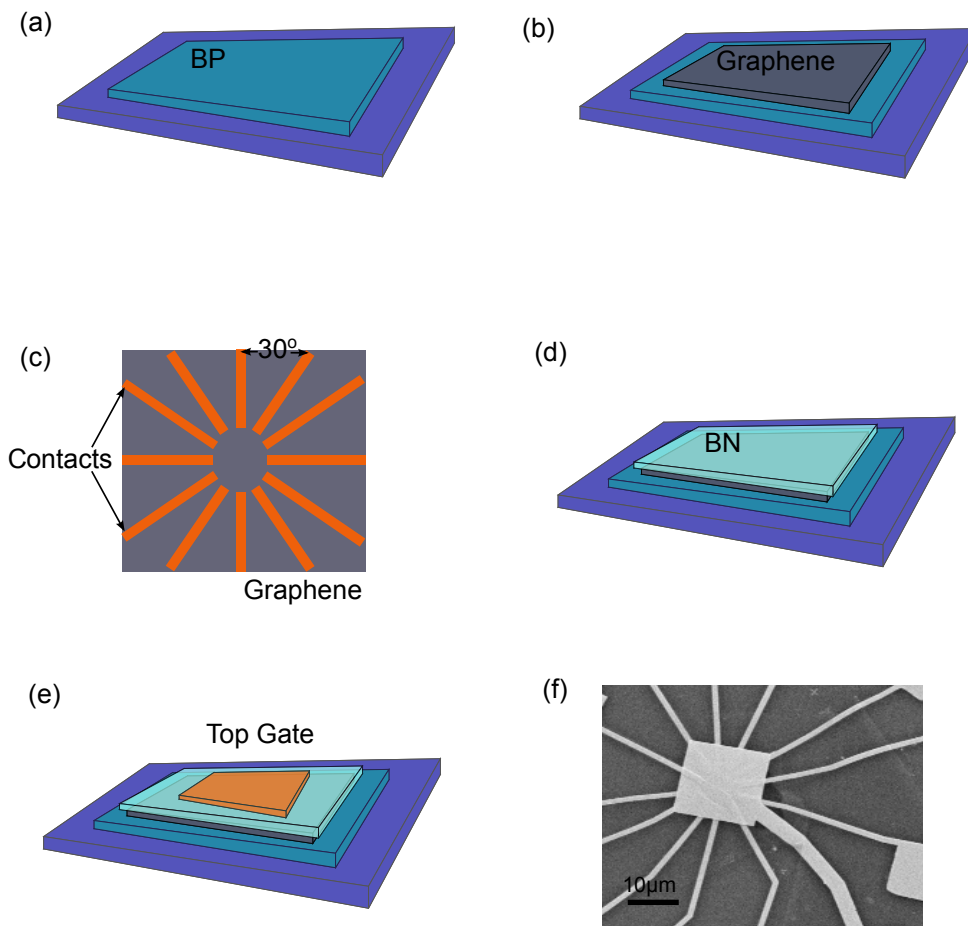


Figure 6.2: The process schematic of making devices. (a) The BP exfoliated on the  $\text{SiO}_2$  wafer inside the glove box. (b) Graphene layer was transferred onto the BP. (c) Twelve contacts with  $30^\circ$  angle between each of them are made on graphene. (d) Cover a BN on top of contacts and graphene. (e) Top gate was made on top of BN. (f) The SEM picture shown contacts on graphene and the top gate. The BP, BN and graphene layer are not very visible.

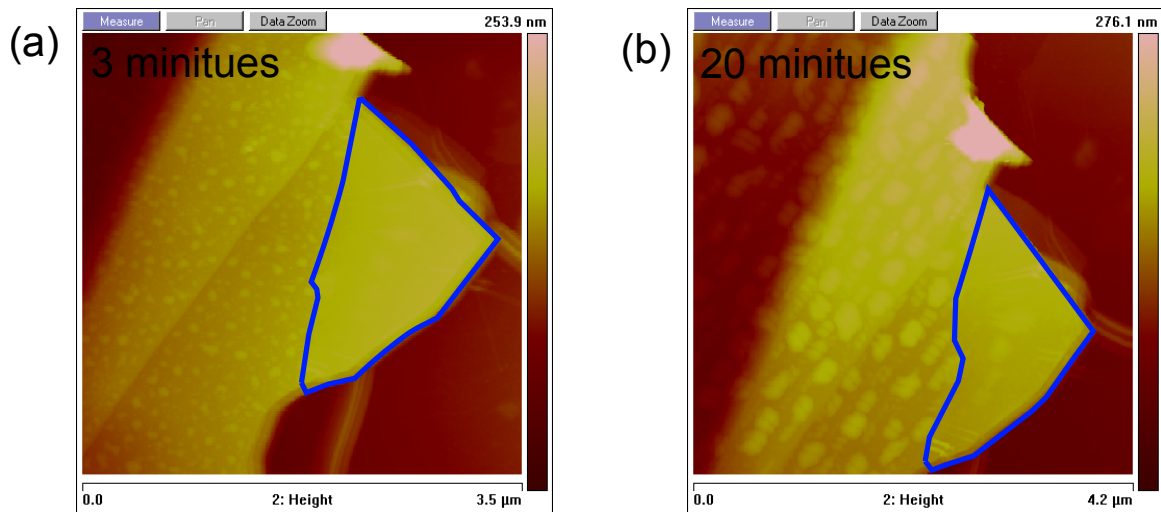


Figure 6.3: Ageing of the BP surface and BP covered with graphene (blue line area) under AFM. Some bubbles become visible at BP surface after 3 min (a) and 20 min (b). But BP covered with graphene stays the same.

This experiment is performed after graphene layer is transferred onto BP (Figure 6.2 b). The sample is put under AFM to take a real time picture to identify the changing of BP surface.

Figure 6.3 shows the ageing of BP surface. Some bubbles start to showing up and become more visible at BP surface after several minutes. But the BP covered with graphene (inside the blue line in the figure) basically stays the same after exposed in the air. Graphene protects the BP from being damaged by the oxygen and water vapour. After overnight exposed in the air, the other AFM picture is taken in the same area. The BP surface becomes very dirty but the graphene/BP hetero-structure stays clean and flat. This phenomenon is reasonable because graphene can block the air and protect the BP layer. In this way, the hetero-structure we made is stable in the air which makes every experiment easier to finish.

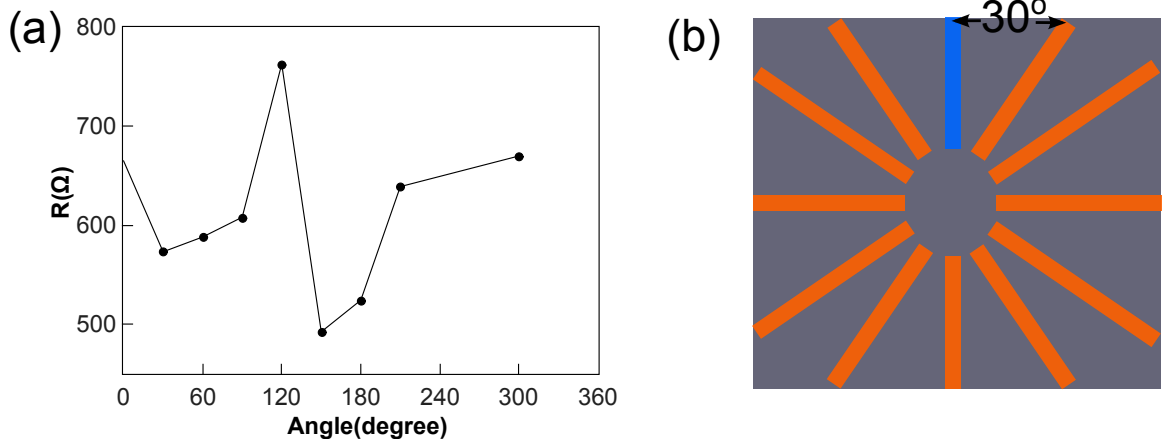


Figure 6.4: (a) Experiment resistance between different contacts and the blue contact in figure b. (b) Schematic of device. The angle degree ( $x$  axis in figure a) is the angle between measured contact and the blue contact.

## 6.4 The Anisotropic Transport Properties

To test the possible anisotropic transport properties, we perform a resistance measurement between different contacts at room temperature. The data of resistance is shown in Figure 6.4. The  $x$  axis is the angle between measured contacts. The schematic of device is shown in Figure 6.4b with one blue contact fixed in the measurement.

Here, we use a very simple model to estimate the anisotropic conductance. The current through the anisotropy system is,

$$J = \sqrt{(\sigma_{xx}^2 E^2 \cos^2 \theta + \sigma_{yy}^2 E^2 \sin^2 \theta)}$$

where we set  $\sigma_{xy} = 0$ . So the,

$$\sigma = \sqrt{(\sigma_{xx}^2 \cos^2 \theta + \sigma_{yy}^2 \sin^2 \theta)}$$

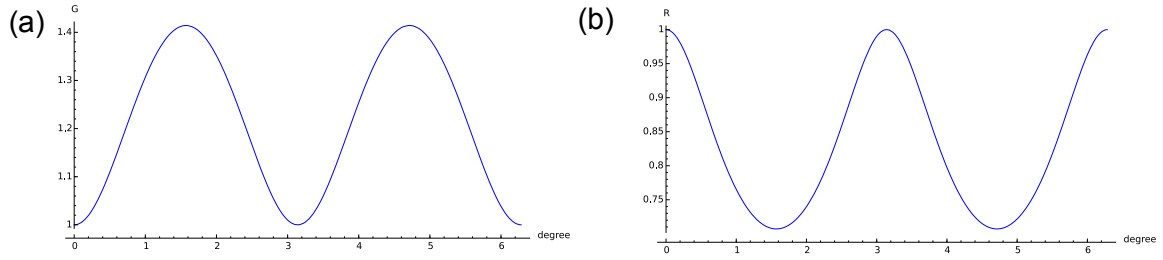


Figure 6.5: Simulation of anisotropic conductance (a) and resistance (b).

Figure 6.5 shows the simulation of anisotropic resistance and conductance. In the simulation we use natural and dimensionless units, the  $\sigma_{xx} = 1$  and  $\sigma_{yy} = 2$ . Comparing to the data taken in the room temperature (Figure 6.4), basically the data follows the simulation. It means the BP may already introduce the anisotropic behaviour into graphene. This kind of anisotropic transport properties may come from the lattice influence of BP. However, it could also be from the transport contribution of BP. To understand the inside physics, we will put the samples inside the fridge at low temperature.

## 6.5 The Magneto-transport Properties

To study the BP/Graphene hetero-structure more carefully, the low temperature magneto transport measurement is performed.

At first, the conductance measurement at low temperature with top gate and back gate is taken. The data and measurement set up presented in Figure 6.6. The data is measured between two contacts opposite to each other. The color plot of conductance between contacts shown in b versus the top gate and back gate is presented in first figure.

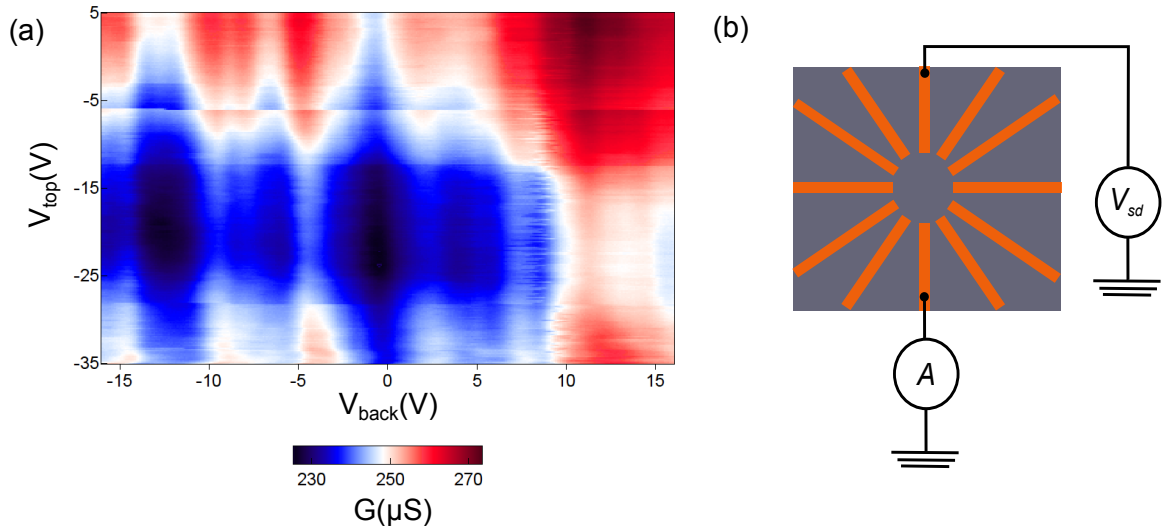


Figure 6.6: (a) Color plot of conductance between two contacts shown in (b). The  $x$  axis is back gate and  $y$  axis is top gate.

Along the top gate, there is a dip which is the Dirac point from graphene layer. This feature barely change with the back gate. But by changing the back gate, some small oscillation happens.

In the device, the BP is between graphene and  $\text{SiO}_2$ . The transport properties are mainly contributed by graphene layer and back gate influence is blocked by BP layer (because BP is also a conducting 2D material). That is why the top gate gives a Dirac point but nothing happened by changing back gate. Similar work has been done in  $\text{MoS}_2$  where the back gate has also been blocked by  $\text{MoS}_2$ . This two gates dependence (only controlled by top gate) is repeatable and independent from the angle between contacts.

A magneto transport measurement is performed. Conductance between two specific contacts changing with top gate and magnetic field is measured. The Landau fan pattern turned to be sensitive to the orientation of contacts as well as the back gate. The Landau

levels are not visible until the magnetic field reaches high enough (limited by mobility of the sample).

Figure 6.7 shows the color plot of conductance between two contacts (shown in schematic next to it) versus the top gate and magnetic field. Figure a is measured by two contacts opposite to each other and set the back gate equals zero. From the fan diagram, there are some different landau levels interference above  $B = 3.5$  T (red dashed line). The interference pattern is strong at around  $V_{top} = -12.5$  V. Three dips are visible at zero magnetic field. (b) is the landau fan measured between two contacts shown in the insert figure with back gate fixed at zero. The fan pattern is also different. The interference is stronger and more details can be observed. There are three strong "Dirac points" with their own landau levels. These landau levels cross each other and makes an interference pattern between  $V_{top}$  from -20 V to 10 V. The details of this figure will discussed separately later. For the same contacts, this time the back gate is tuned to -65 V. From the two gates data we know that the conductance is not very sensitive to back gate but still have some responses. The pattern is different from the figure (b). At first, several extra "Dirac points" are visible and the interference pattern is weaker. Some details are disappeared too. For example, the features at  $V_{top} \approx 20$  V are more like straight lines than (b). The position of dips at zero magnetic field is also moved.

Figure 6.8 shows many details from landau fan diagram in Figure 6.7b. As mentioned before, the horizontal red dashed line indicate where the LLs disappear. The several green dashed lines are where the non-linear landau levels. These features are familiar with tri-layer graphene which may indicate the landau levels may not only come from graphene

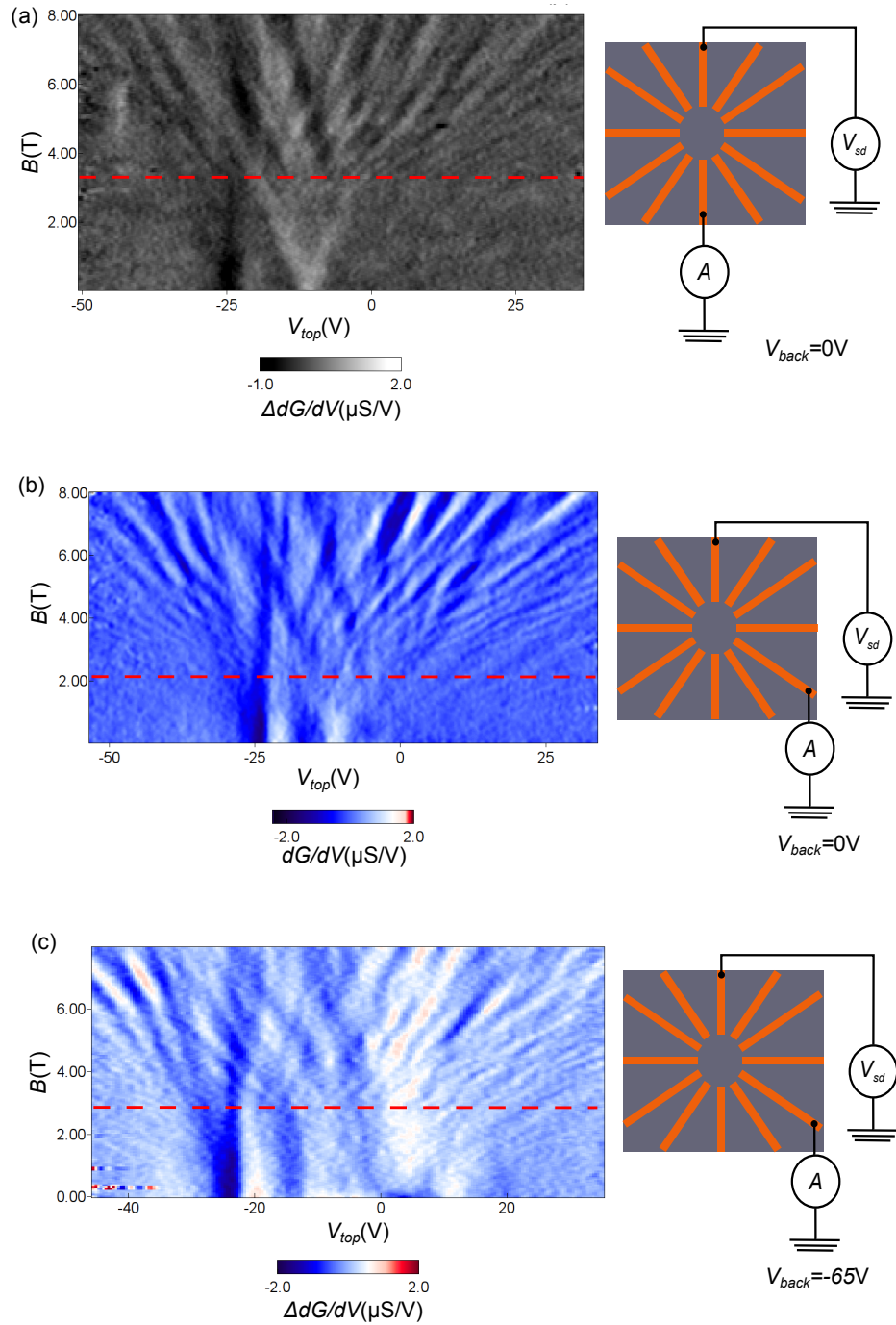


Figure 6.7: Landau fan diagram and measured contacts schematic. (a) Landau fan of  $dG/dV$  subtract the background versus the top gate and magnetic field. (b) Landau fan of two contacts shown in insert graph at back gate equals 0 V. (c) Landau fan of conductance between same two contacts as previous graph. The back gate tuned to -65 V. Red line in the figure indicates where the LLs disappear.

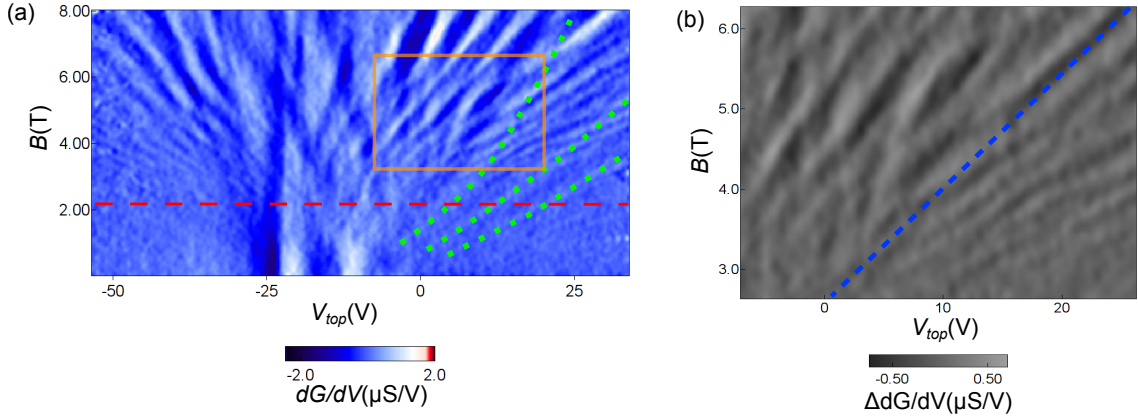


Figure 6.8: (a) Fan diagram from Figure 6.7b. The green dashed lines are several non-linear Landau levels. (b) Zoomed-in figure of orange box in (a). There are the interference pattern inside.

but also the BP. Three clear dips are visible at zero magnetic field which is deep blue color. They might be extra Dirac points due to the periodic 1D lattice of BP. The orange right-angle is where the Landau level interference happened. These patterns may be due to the different Landau levels and the electrons fill the several gaps at the same time. This area is zoomed in figure (b). The interference area is on the left of the blue dashed line. On the right of it, Landau levels become linear again.

The magneto transport properties discussed above can be repeated in several different devices. Figure 6.9 shows data from another device. Interestingly, figure (a) shows a dramatically different pattern from previous data, which is taken between two contacts shown in the insert figure next to it. It looks more like a regular graphene Landau fan. The filling factors shown in red numbers on the top are also accurate for graphene. Three green dashed lines on the top right show the possible degeneracy broken at high magnetic field. Figure (b) shows a similar Landau fan like previous devices. The two contacts used

are shown in the schematic next to the data. Some interference pattern is visible. Multiple dips at zero magnetic field is also there. The fan diagram is basically similar to the previous device.

## 6.6 Dirac Point Shifting with Magnetic Field

Another phenomenon attracts our attention. The position of Dirac point will shift with the magnetic field at particular orientation. It is a very interesting phenomenon remind us the threshold magnetic field talked in previous section. These several magneto-transport unique behaviours indicate this BP/Graphene system has some special magnetic physics inside.

This section will focus on the position of Dirac point shifting with the magnetic field. Figure 6.10 shows the color plot of conductance versus the top gate voltage and the magnetic field. The schematic is the measurement set. In (a), the low conductance area (blue area) is shifting to the left. This data is taken between two contacts in the figure while grounding other contacts. The green dashed line indicates the position of the Dirac points shifting along the magnetic field. The Dirac points shift to the left and at particular magnetic field changing to the right. In (b), the conductance is measured between two different contacts. So the orientation between the electrons propagating direction and BP lattice direction is changed. Other contacts are still grounded to prevent the signals from other parts of graphene. The color plot is still conductance versus the magnetic field and

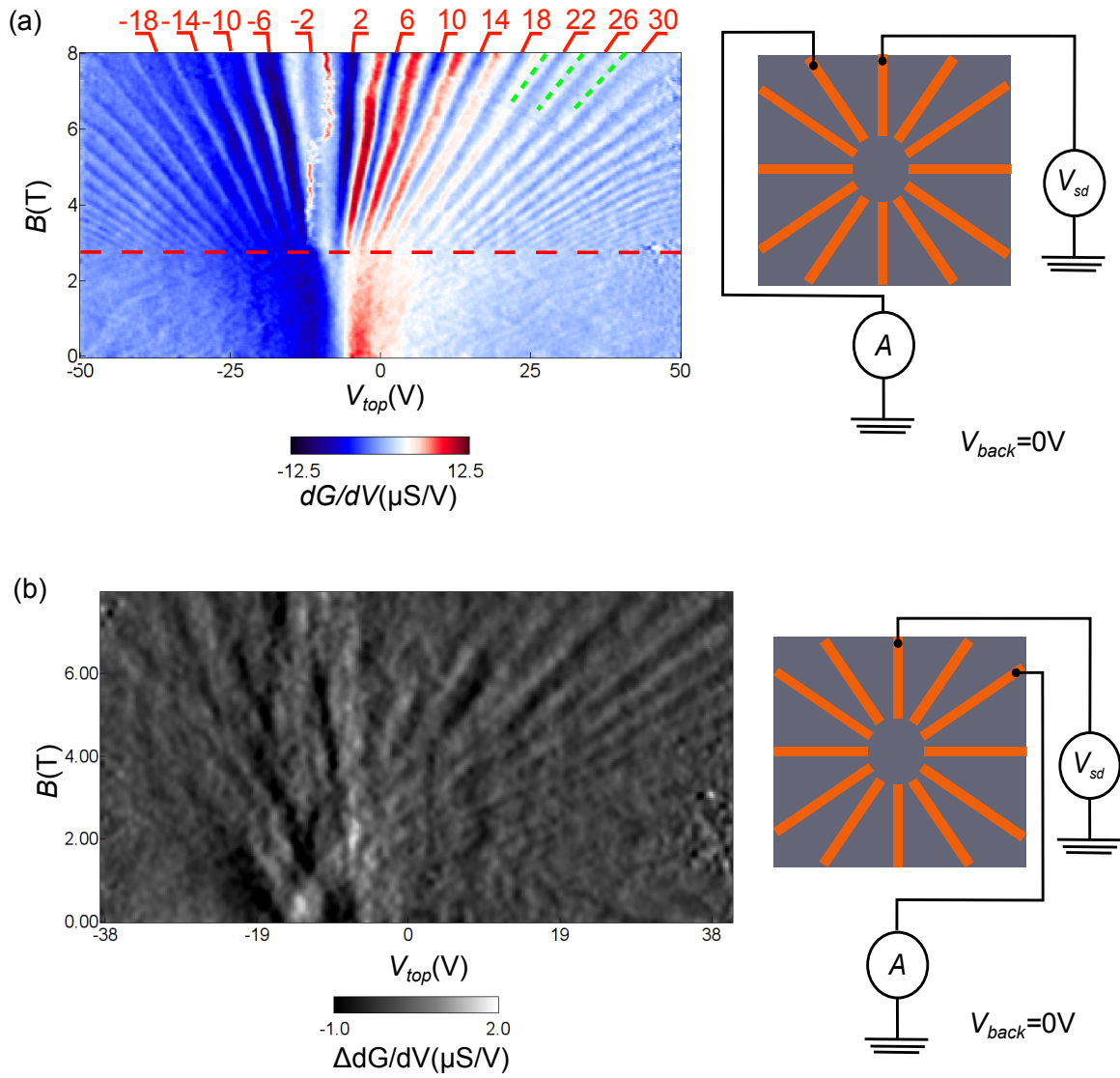


Figure 6.9: (a) Landau fan diagram shows the similar feature like monolayer graphene. Filling factors are shown in red numbers on its top. (b) Landau fan diagram between two different contacts. It is similar to previous devices.

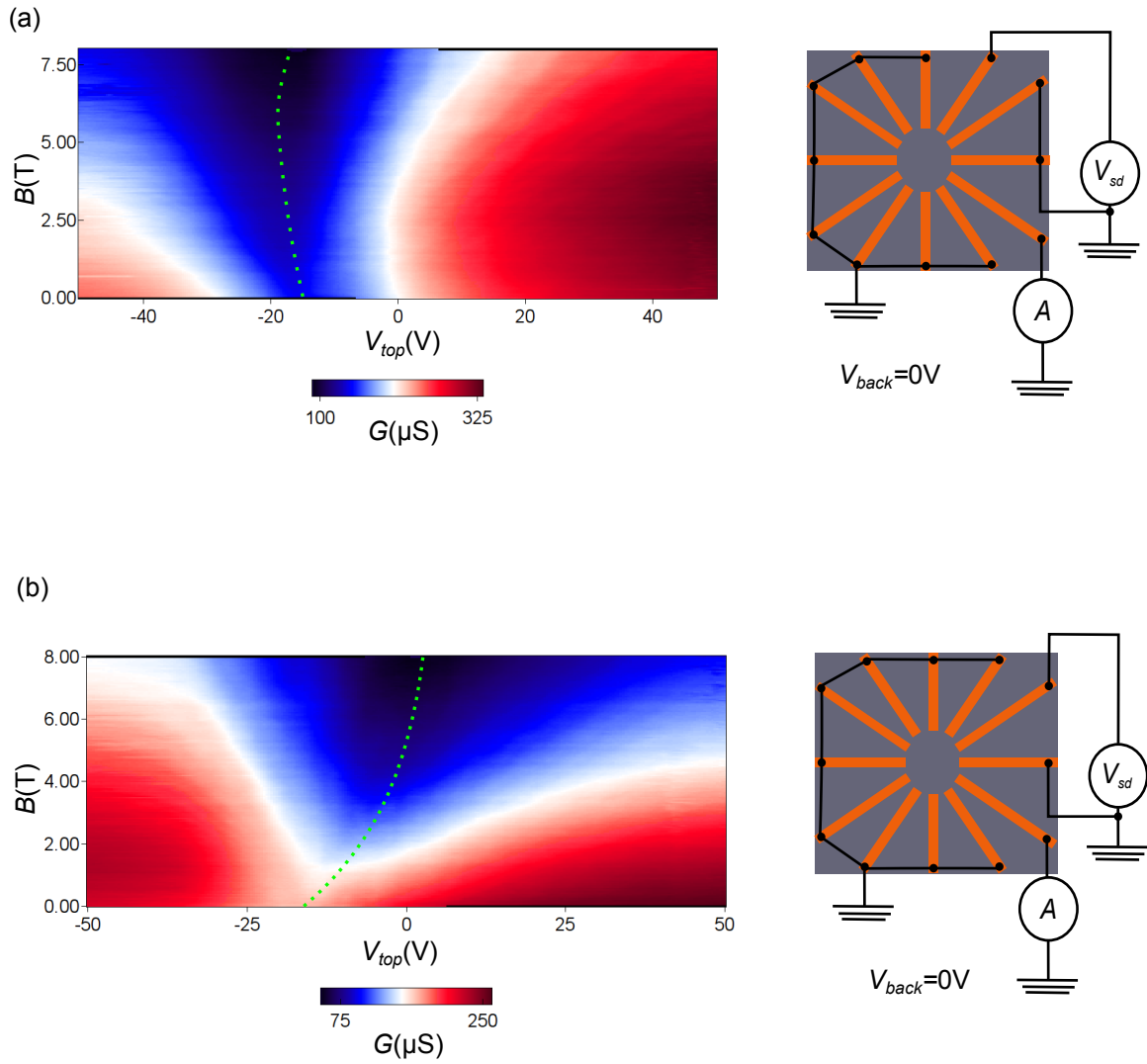


Figure 6.10: (a) Color plot of conductance between two contacts shown next to the main figure. Other contacts are grounded. The  $X$  axis is the top gate voltage and  $Y$  axis is magnetic field. The green dashed line indicates the Dirac point shifting with  $B$ . (b) Same color plot with two different contacts. Other contacts are grounded.

top gate voltage. The green dashed line is still the position of the Dirac points. This time, the green line shifts to the right all the time when the magnetic field increases.

To carefully study how the position of Dirac points changing with the magnetic field, a scatter plot of  $V_{top}$  versus  $B$  is in Figure 6.11. The blue diamonds are from the Figure 6.10 (a) and the pink triangles are from the Figure 6.10 (b). They are the top gate voltage where is the Dirac point at different  $B$ . The X axis in the graph is the magnetic field. The data from a, which is the blue diamonds in the figure, decreases with the magnetic field at first. After hopping up and down at the mid-range, the  $V_{top}$  increases at low magnetic field. However, the data from b, which are the pink triangles in the figure, is decreasing monotonously when the  $B$  decreasing. It looks like a linear relation more or less.

A linear fit is performed for data set b in Figure 6.12. The top gate voltage is the Y axis and magnetic field is the X axis. The relation between the position of Dirac points and the magnetic is,

$$V_{Dirac} = 2.089B - 13.708$$

The Dirac points shifting with magnetic field has not been reported yet. It will be an interesting direction to do some future work.

## 6.7 Conclusion

As a conclusion, the BP/Graphene hetero-structure is a interesting system. We observed the anisotropic transport properties which is introduced from BP to graphene.

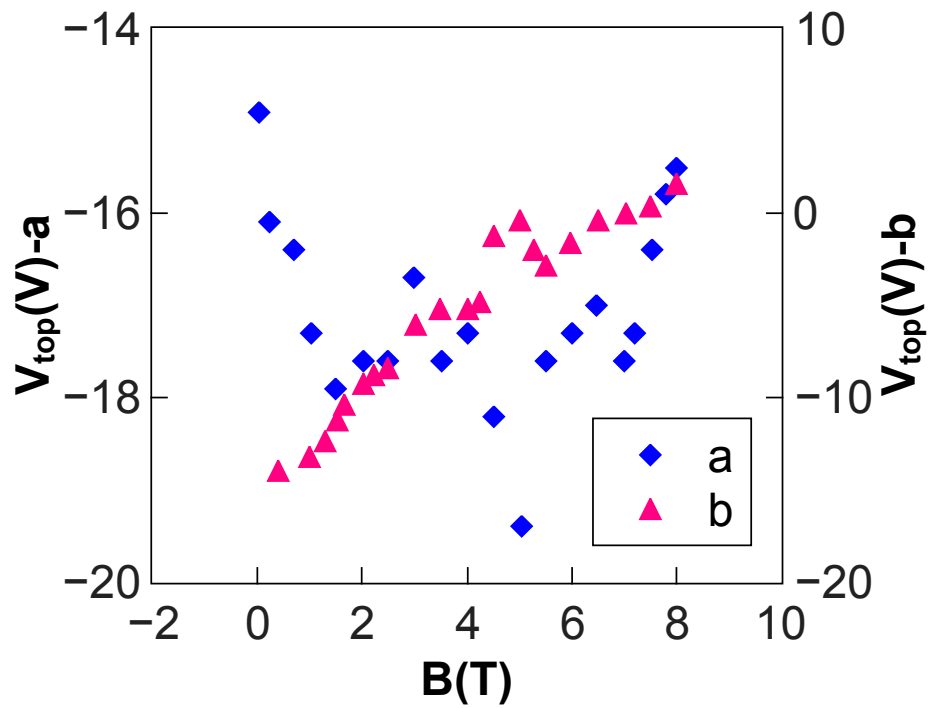


Figure 6.11: Position of Dirac points (shown as top gate voltage) at different magnetic field. The data are from two different sets. The blue diamonds (a) are from Figure 6.10-a and pink triangles (b) are from Figure 6.10-b.

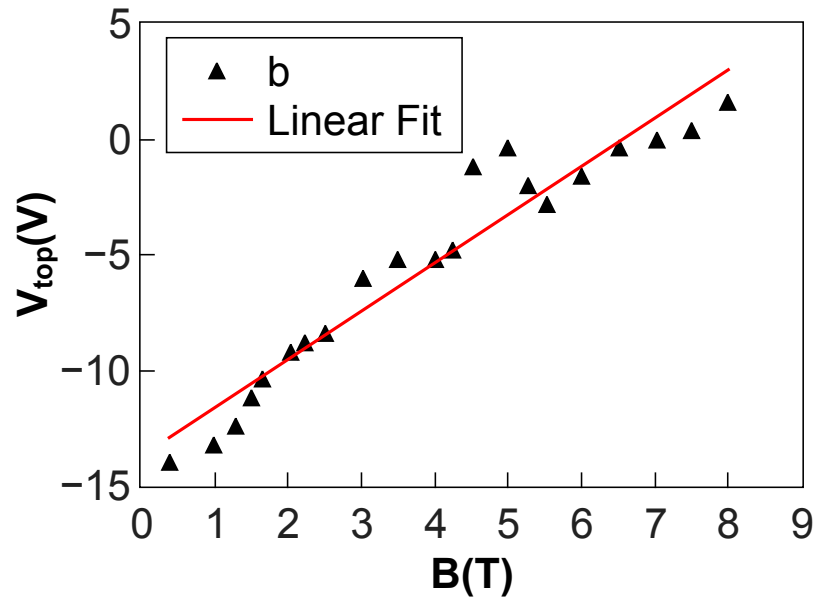


Figure 6.12: The position of Dirac points (shown as top gate voltage) at different magnetic field for data set (b). A liner relation fits well with the raw data.

This is a very charming direction to study the anisotropic graphene and will lead to many possible new physics in graphene system.

The magnetic properties from the BP are also introduced into graphene. The unique Landau fan diagram and the Dirac points shifting are the evidences of this special magneto-transport behaviour. This kind of phenomenon are not observed from experiments before. It also lacks theory calculation.

## Chapter 7

# Fractional Quantum Hall Effects In Bilayer Graphene

### 7.1 abstract

Fractional Quantum Hall Effect (FQHE) is a hot research topic for condensed matter physics for years since it had been discovered experimentally [63]. Recently, graphene as a high mobility 2D material has joined the FQHE family [18][4][15]. The fractional hall effect on graphene has been reported with an odd denominator and an even denominator. Recently, there are several experiments reported FQHE with  $\nu = \frac{1}{2}$  [30]. Their device is a suspended bilayer graphene.

In this chapter, we will report a FQHE measurement on an encapsulated bilayer graphene device. Several odd denominator and even denominator FQHE states exhibit

plateaus in the transverse resistance with a concomitant dip in longitudinal resistance. We will try to explain the experiments with composite Fermions model.

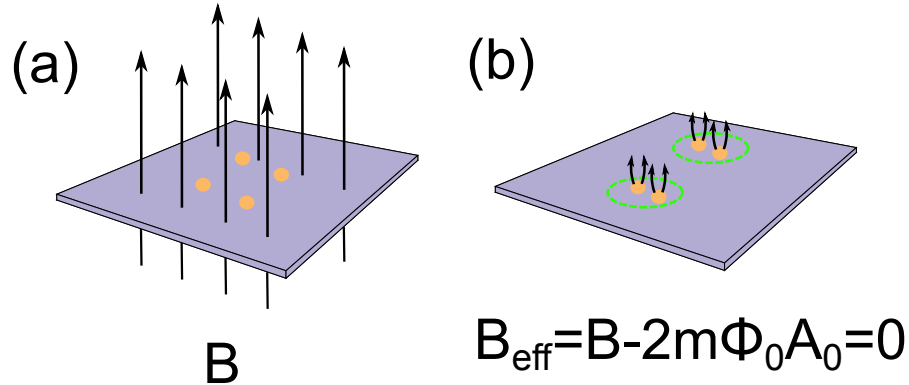


Figure 7.1: (a) Electrons under magnetic field  $B$ . (b) Composite Fermions under effective magnetic field  $B_{\text{eff}}$  and form BCS-like Bosons.

## 7.2 Introduction

Nearly 140 years ago, Edwin Hall discovered the famous Hall effect. And the quantum hall effect has been discovered at 1980 by Klaus von Klitzing [64].

The fractional quantum hall effect had first been observed experimentally in GaAs-AlGaAs heterojunctions [63], then the theoretical explanation was made [36]. However, the theory only explains the odd denominator FQH state.

Since single layer graphene device has been made in 2004 [51]. Integer QHE [71] and fractional QHE [4] [18] have been observed in graphene devices.

In this chapter, we have present data from a high mobility ( $1,000,000 \text{ cm}^2\text{V}^{-1}\text{s}^{-1}$ ) bilayer BN/Graphene/BN heterostructure device. In this device both spin and valley de-

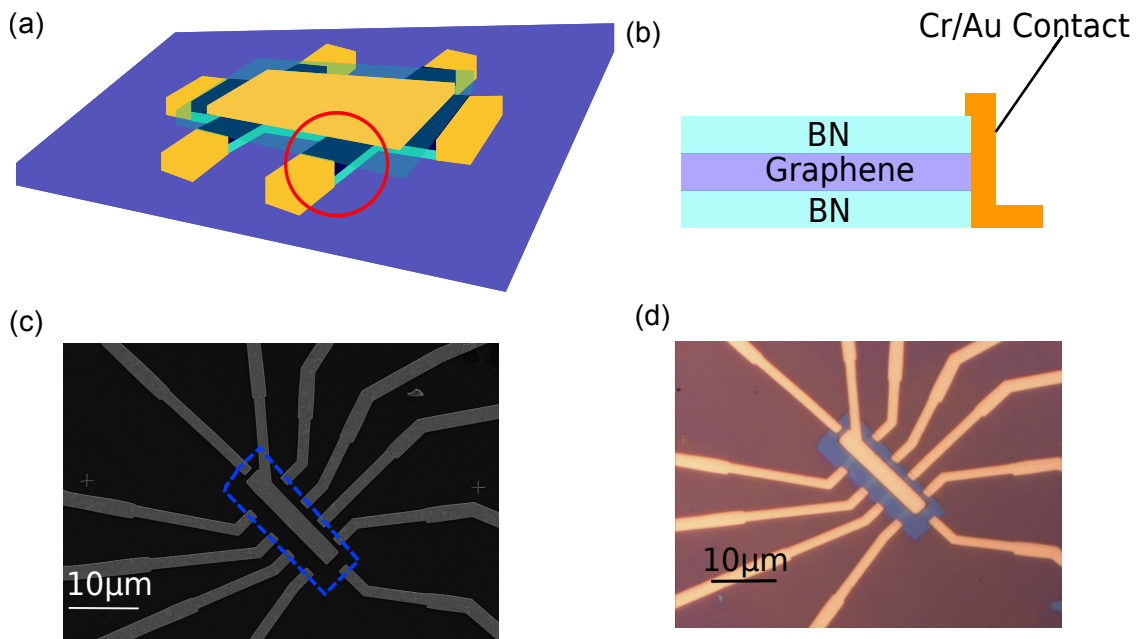


Figure 7.2: (a)(b) Schematic figure of the bilayer graphene device and edge contact. The red circle is where the edge contact is. (c)(d) SEM picture and microscope picture. In the SEM picture, graphene is inside the blue box.

generacy have been broken at low magnetic field. At  $B = 8\text{T}$ , several FQHE states have been observed with clear plateau in the transverse resistance and a concomitant dip in longitudinal resistance.

### 7.3 Integer Quantum Hall Effect

This bilayer graphene device is fabricated by transfer techniques and edge contacts introduced in Chapter 2. In Figure 7.2, there are schematic diagrams of device and the SEM as well as optics picture. Inside the red circle of (a) is the edge contact. The blue dashed lines in figure (c) is the contour of BN/graphene/BN sandwich structure.

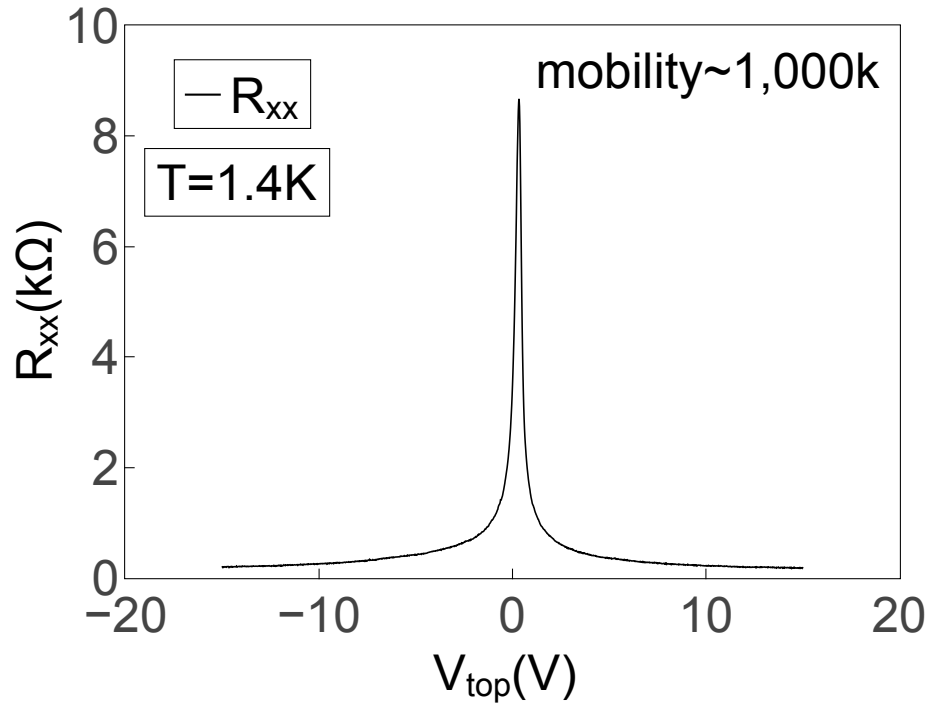


Figure 7.3: The  $R_{xx}$  vs. top gate voltage measured at 1.4K. The mobility calculated from electron side is around  $1,000,000 \text{ cm}^2\text{V}^{-1}\text{s}^{-1}$ .

At first, a cursory gate sweep transport measurement is performed. Near the Dirac point, we can estimate the field mobility.

The resistance gate dependence is shown in Figure 7.3. The mobility calculated from electron side is up to  $1,000,000 \text{ cm}^2\text{V}^{-1}\text{s}^{-1}$ . The hole side mobility is a little lower, it is around  $600,000 \text{ cm}^2\text{V}^{-1}\text{s}^{-1}$ .

In the presence of a magnetic field, the electron energy states collapse to quantized circular orbits. Between each family of states there is an energy gap. For example, solving a Schrodinger equation in a 2D system under a magnetic field, the Landau level energies are given,

$$E_n = (N + 1/2)\hbar\omega_c$$

the cyclotron frequency is,

$$\omega_c = \frac{eB}{m^*}$$

$m^*$  is the effective mass.

An integer number of LLs are exactly filled at magnetic field,

$$B_\nu = \frac{1}{\nu} \frac{nh}{e}$$

The filling factor can be written using a different expressions,

$$\nu = \frac{n}{n_B} = n \frac{h}{eB} = n \frac{\Phi_0}{B} = n2\pi l_B^2 \quad (7.1)$$

Figure 7.4 shows how the cyclotron orbit forms in 2D materials and how the density of states changes with the magnetic field.

The Figure 7.5 shows a color plot of  $\log R_{xx}$  versus  $B$  and  $V_{top}$ . The (b) is the same figure with the background subtraction. From this landau fan diagram, the data yields a quantum hall mobility around  $30,000 \text{ cm}^2\text{V}^{-1}\text{s}^{-1}$ . Originally graphene has both spin and valley degeneracy. Bilayer graphene has eight-fold degeneracy at zeroth landau level(LL) and four-fold degeneracy at other landau levels (LLs). All degeneracies have been broken at magnetic field around 5 T in this device.

For graphene, the landau level energy is given by,

$$E_\nu = \text{sgn}(\nu) \sqrt{2e\hbar v_F^2 |\nu| B}$$

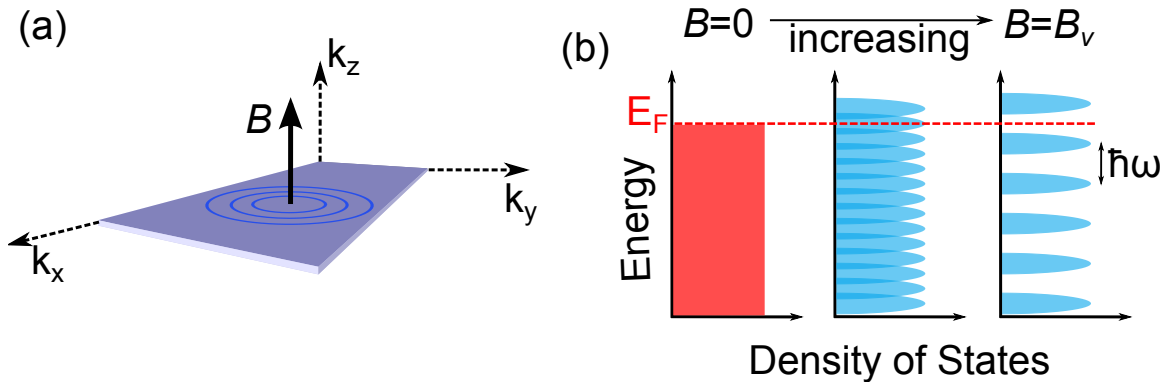


Figure 7.4: (a) Electron energy states in 2D material collapse onto cyclotron orbits in  $k$ -space under magnetic field  $B$ , separated by a well-defined gap. (b) LLs energy increase with the magnetic field. So fewer and fewer LLs are occupied if the electron density remains fixed. The faraway panel shows an integer number of LLs are exactly filled.

$\nu$  is the LL index,  $e$  is the electron charge,  $\hbar$  is the reduced Planck constant,  $v_F$  is the Fermi velocity of graphene.

This equation can be gotten from

$$l_B = \sqrt{\hbar/eB}$$

and the cyclotron frequency of Dirac Fermions,

$$\omega_c = \sqrt{2}v_F/l_B$$

The Dirac equation in Landau gauge is,

$$v_F \begin{pmatrix} 0 & \partial_y - k + Bey/c \\ -\partial_y - k + Bey/c & 0 \end{pmatrix} \phi(y) = E\phi(y)$$

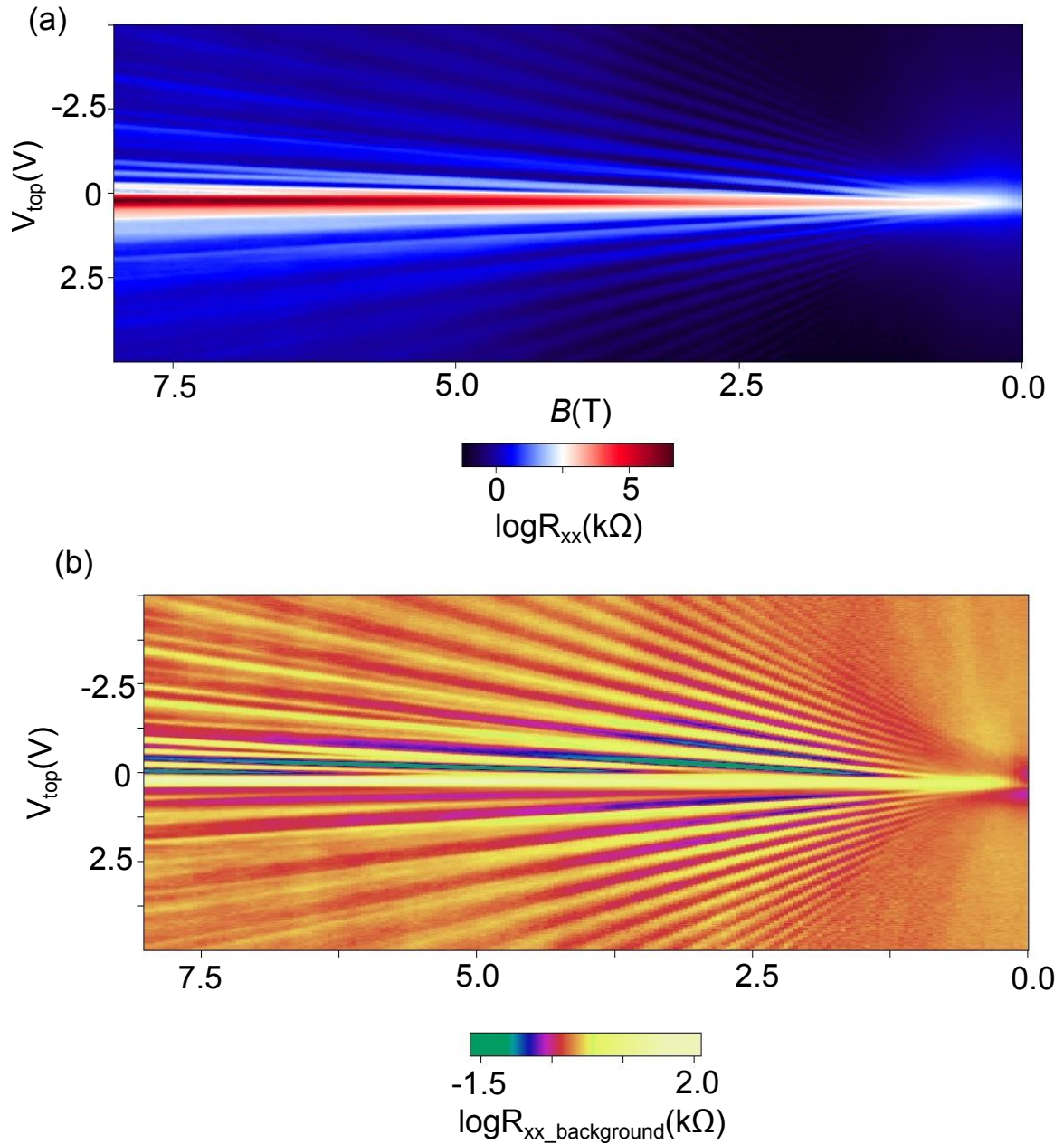


Figure 7.5: (a) The landau fan: color plot of  $\log R_{xx}$  versus  $V_{top}$  and  $B$ . (b) The landau fan data which is background subtracted. The Shubnikov-de Haas (SdH) oscillation can be observed from  $B \approx 0.3$  T.

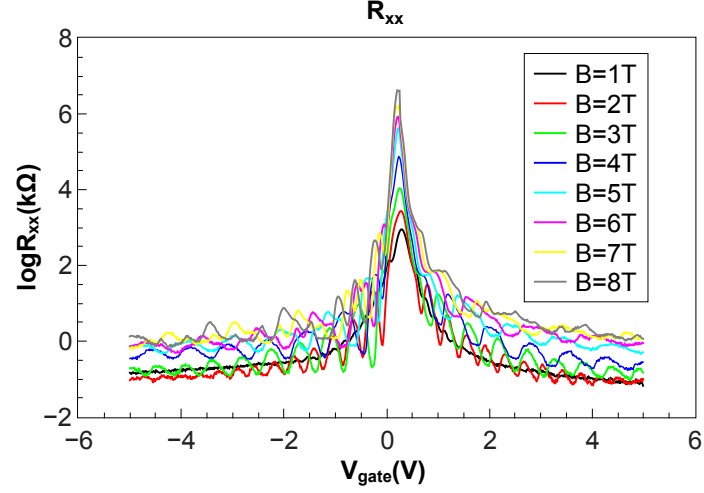


Figure 7.6:  $\log R_{xx}$  vs.  $V_{gate}$  at different magnetic field.

so the eigenvalues are

$$E_\nu = \text{sgn}(\nu)\hbar\omega_c\sqrt{|\nu|} = \text{sgn}(\nu)\sqrt{2e\hbar v_F^2|\nu|B}$$

To check the Landau level changing with the magnetic field, we plot a line trace graph at different magnetic field. Here is the figure with  $\log R_{xx}$  vs.  $V_{gate}$  at different magnetic field. The SdH oscillations are strong from 1T to 8T. The degeneracy breaks during increasing the magnetic field.

From the Figure 7.6, we can see at low magnetic field the SdH oscillations are very uniform. This is because the degeneracy here is still 4 (spin and valley). Until the  $B$  reaches higher ( $> 4T$ ), the degeneracy starts to break. Several small gaps start to show up between big gaps. At around 5 T, the spin and valley degeneracies have been broken. There are four gaps instead of one gap in a region. At 8 T, there are more features between each gap which could be the FQHE gap. The FQHE will be talked later in this chapter.

We not only have the longitudinal resistance data, but also have the transverse resistance data (Figure 7.7).

From the experiment, we can measure the  $R_{xx}$  and  $R_{xy}$  by using two lock-ins at same time.

From the conductivity tensor,

$$\sigma = \begin{pmatrix} \sigma_{xx} & \sigma_{xy} \\ -\sigma_{xy} & \sigma_{xx} \end{pmatrix}$$

we get resistivity tensor,

$$\rho = \frac{1}{\sigma_{xx}^2 + \sigma_{xy}^2} \begin{pmatrix} \sigma_{xx} & \sigma_{xy} \\ -\sigma_{xy} & \sigma_{xx} \end{pmatrix}$$

For a square 2D sample the resistance equals the resistivity ( $\rho = R$ ) so that the QHE is characterized by

$$\rho_{xx} = 0, \rho_{xy} = \frac{1}{\nu} \frac{h}{e^2}. \quad (7.2)$$

In a hall bar structure 2D sample, the length of hall bar is  $L$  and width is  $W$ ,

$$G_{xy} = -\frac{R_{xy}}{\frac{R_{xx}^2}{(L/W)^2} + R_{xy}^2} \quad (7.3)$$

and the step is  $\nu e^2/h$ .

In Figure 7.7, (a) is the color plot of  $G_{xy}$  with gate voltage and magnetic field. (b) is the line trace of  $G_{xy}$  vs.  $V_{gate}$  at different B. Conductivity plateaus appear from 1 T. Each big plateaus are gaped by  $4e^2/h$ . (c) is the zoom in figure of (b). Every step of  $4e^2/h$  in conductance plateaus with a concomitant gap in LLs energy is clear to see in the figure. At high magnetic field, the step becomes  $e^2/h$  which corresponds to the degeneracy

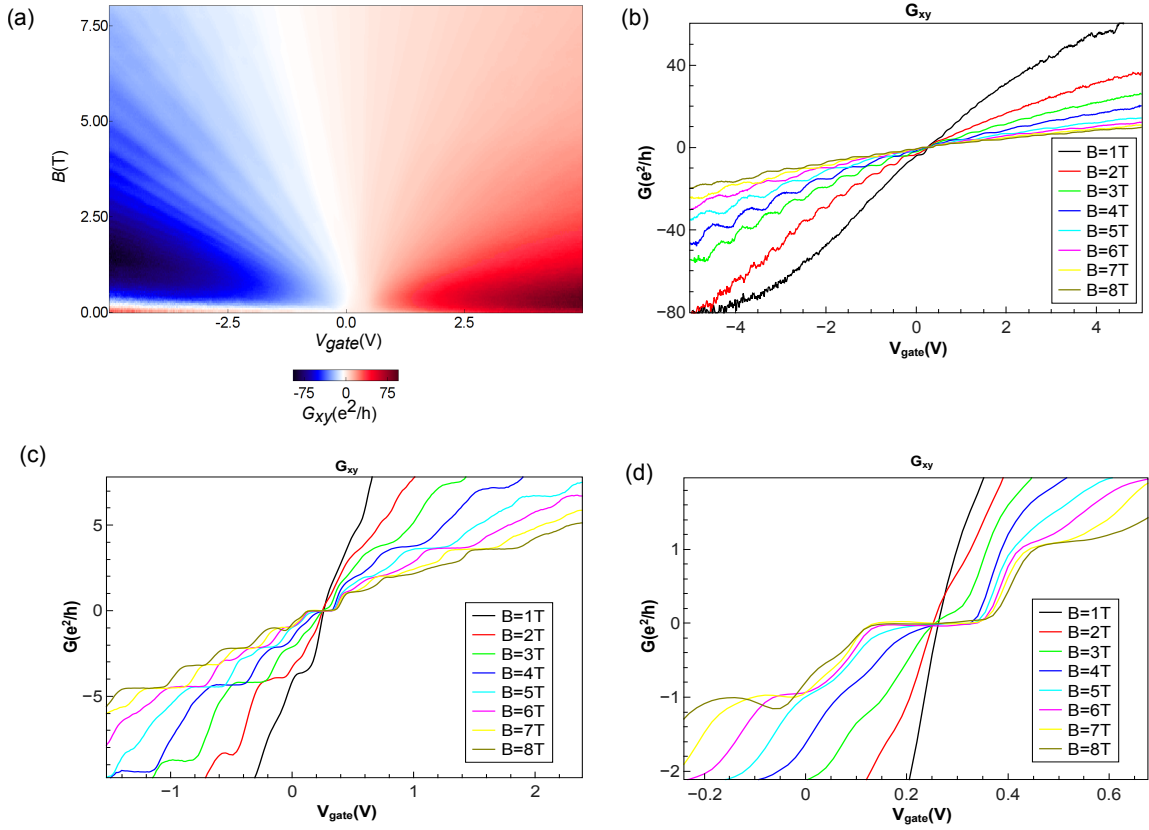


Figure 7.7: Transverse conductance data. (a) Color plot of  $G_{xy}$  with gate voltage and magnetic field. (b) Line trace of  $G_{xy}$  vs.  $V_{gate}$  at different  $B$ . (c) Zoomed-in figure of (b). Conductance step is  $4e^2/h$  at low field and  $e^2/h$  at high field. (d) The  $G_{xy}$  around the 0th LL. The plateau of 0th LL starts to appear between 3T and 4T.

broken. (d) shows the plateaus of 0th LL. It starts to appear between 3T and 4T. This is an evidence of high quality and clear device.

Figure 7.8 shows the  $R_{xx}$  and  $\sigma_{xy}$  signal at  $B=8T$ . There is a plateau with a step of  $e^2/h$  at  $\sigma_{xy}$  with a concomitant dip at  $R_{xx}$ . For filling factor  $\nu$ , the concomitant plateaus yield the value  $\nu e^2/h$ . At low filling factor, there are some extra plateaus and dips which could be signal from FQHE. FQHE will be introduced in next section.

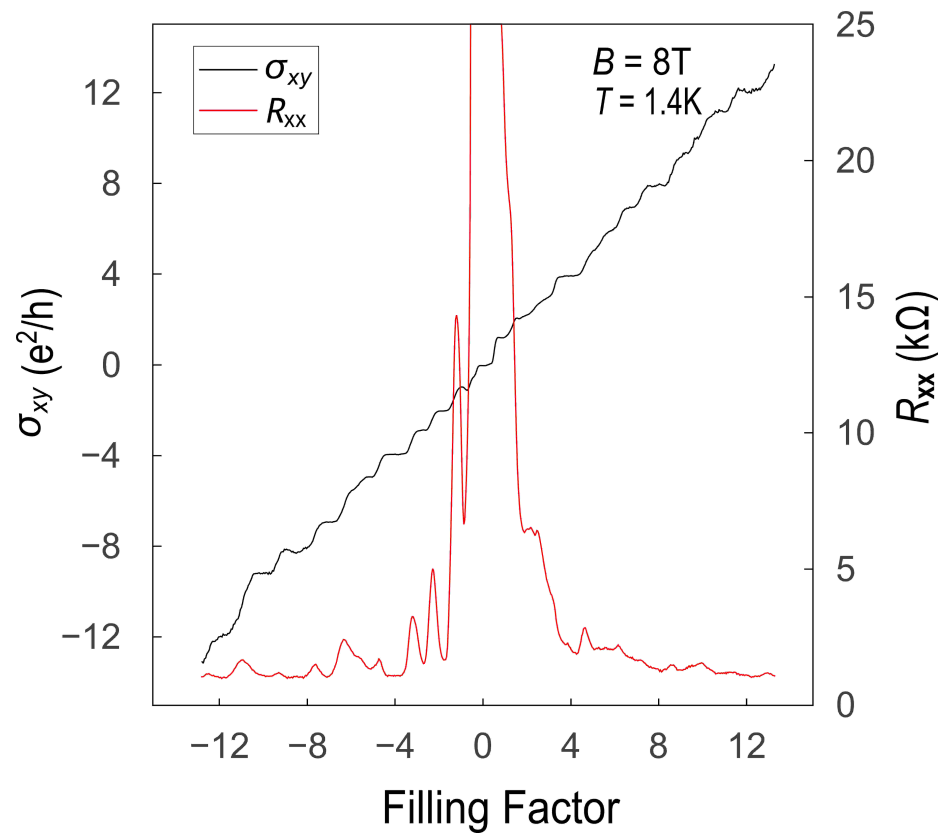


Figure 7.8: The  $R_{xx}$  and  $\sigma_{xy}$  at  $B=8T$ . There is a plateau with a step of  $e^2/h$  at  $\sigma_{xy}$  with a concomitant dip at  $R_{xx}$ . For filling factor  $\nu$ , the concomitant plateaus yields the value  $\nu e^2/h$ .

## 7.4 Fractional Quantum Hall Effect

In 1982, Daniel Tsui and Horst Stormer observed the FQHE at much higher magnetic field in the 2D material. To understand the existence of fractional quantum hall states would require the inclusion of many-body interactions into the theory.

Robert Laughlin proposed a ground state wavefunction to describe the FQHE at  $\nu = 1/m$  fractional filling [36],

$$\Psi_m(z_j, \dots, z_k) = \prod_{j < k}^N (z_j - z_k)^m \exp\left[-\frac{1}{4l_B^2} \sum_j^N |z_j|^2\right] \quad (7.4)$$

where  $m$  is an odd integer,  $z_j = x_j + iy_j$  is the location of  $j^{th}$  particle and  $l_B$  is the magnetic length. Laughlin constructed this wave function as a many-body ground state for the Hamiltonian,

$$H = \sum_j^N \frac{1}{2m_e} \left[ \frac{\hbar}{i} \vec{\nabla}_j - \frac{e}{c} \vec{A}(\vec{r}_j) \right]^2 + \sum_{j < k}^N v(\vec{r}_j - \vec{r}_k) + \sum_j^N V_{ion}(\vec{r}_j) \quad (7.5)$$

the first term is the Hamiltonian for a charged particle moving in a magnetic field.  $A$  is the vector potential associated with the magnetic field where  $\vec{B} = \vec{\nabla} \times \vec{A}$ . The second term is from the electron electron coulomb interactions,  $v_r = \frac{e^2}{r}$ . The third term is called the ion potential which is introduced to describe a background charge density that to balance out the Coulomb repulsion in order for the system to be stable.

Now let us look at our data. We took a set of data of landau fan but a smaller range and slower sweep rate (Figure 7.9). From both of the electron side and hole side,

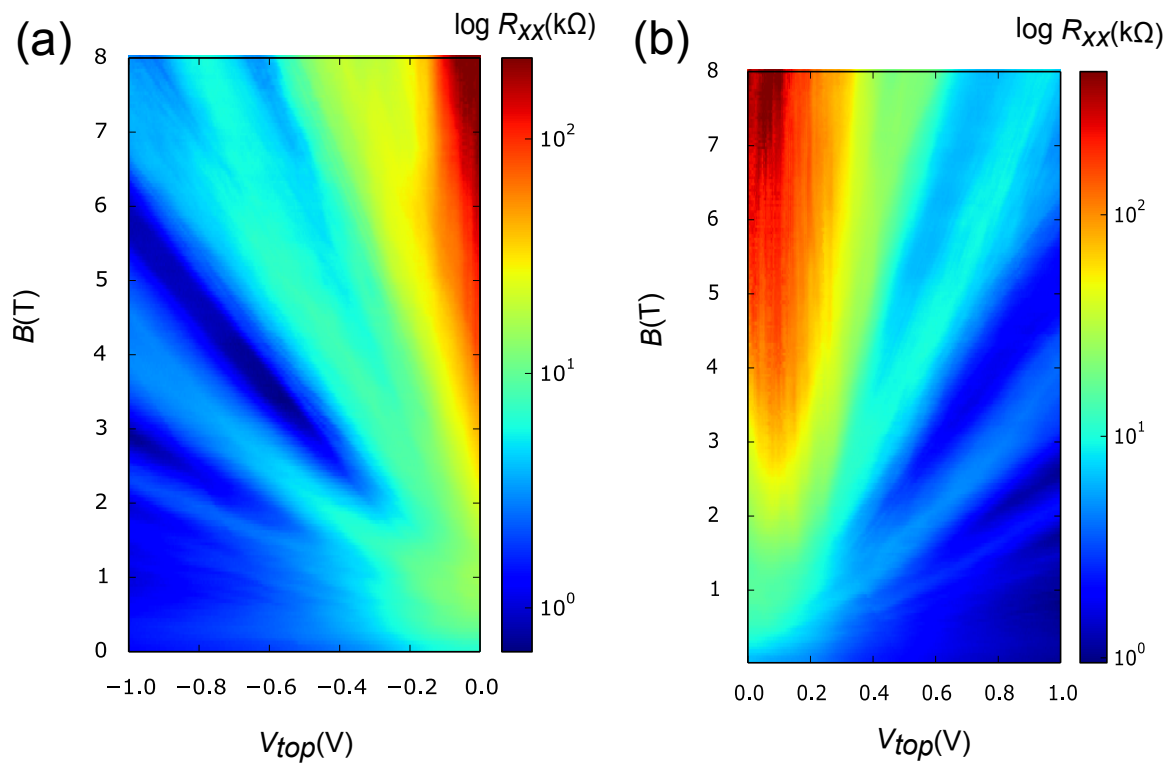


Figure 7.9: (a) The electron side of Landau fan. (b) The hole side of Landau fan.

there are several mini gaps visible between the main gaps. The line trace of  $G_{xy}$  and  $R_{xx}$  gives a clear evidence of the existing of FQH states.

Here we use SdH oscillation to fit a graph from the Landau fan data,

$$n = \frac{B}{\phi_0} * \nu = \nu B e / h \Rightarrow \frac{1}{B} = \frac{e}{nh} * \nu$$

plot  $1/B$  vs.  $\nu$  at fixed carrier density (fixed  $V_g$ ), we get linear fit slope

$$n = \frac{e}{h} \frac{1}{\text{slope}} * \text{degeneracy}$$

So, we get the relation between the  $V_g$  and carrier density  $n$ , and from

$$n = mV_g + b$$

$m$  is proportional to  $C_g$ . And we can get an accurate filling factor,

$$\nu = \frac{nh}{e} \frac{1}{B}$$

To detect the FQH states, we plot the line trace of  $R_{xx}$  and  $\sigma_{xy}$  with filling factor separately. The region of filling factor between -2 to -1 is focused (Figure 7.10) at first.

Figure 7.10 shows the  $\sigma_{xy}$  and  $R_{xx}$  versus the Filling Factor at different  $B$ . (a) and (b) is the  $\sigma_{xy}$  and  $R_{xx}$  vs. Filling Factor at a wide range of magnetic field. The extra plateaus and dips disappear while the magnetic decreasing. (c) and (d) is the  $\sigma_{xy}$  and  $R_{xx}$  versus the Filling Factor at high magnetic field. Some clear plateaus with concomitant dips are shown in the figure.

Figure 7.11 basically shows the same figure like Figure 7.10 but indicate the filling factor of the FQH states. The possible FQH states yielded value  $-3/2$ ,  $-7/5$ ,  $-4/3$ ,  $-6/5$  are shown in the figures.

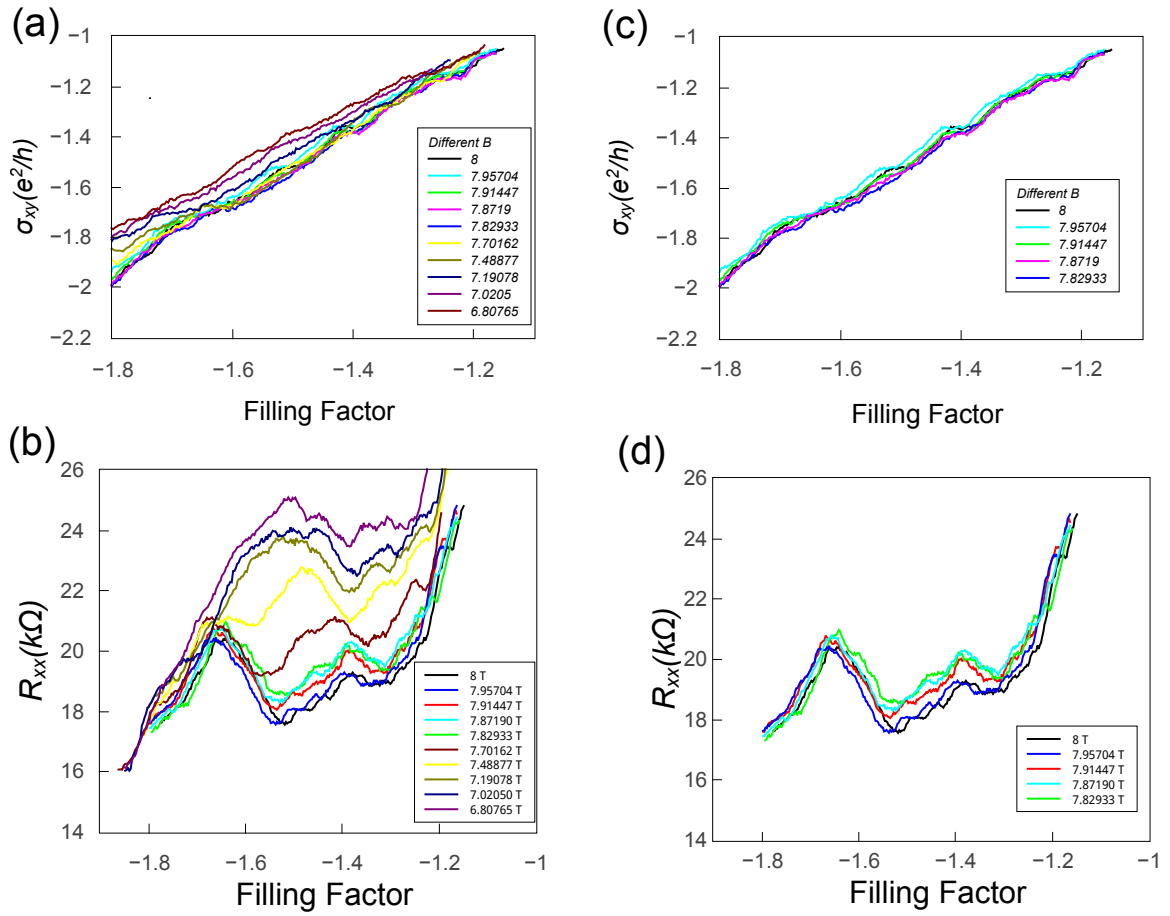


Figure 7.10: (a) The  $\sigma_{xy}$  vs. Filling Factor at different  $B$ . Increasing the magnetic field, the extra plateaus start to show up. (b) The  $R_{xx}$  vs. Filling Factor at same range of magnetic in (a). The extra dips disappear quickly when the  $B$  decreasing. (c) The  $\sigma_{xy}$  at high  $B$ . There are several plateaus very clearly visible between filling factor -1.2 to -1.8. (d) The  $R_{xx}$  with same  $B$  in (c).

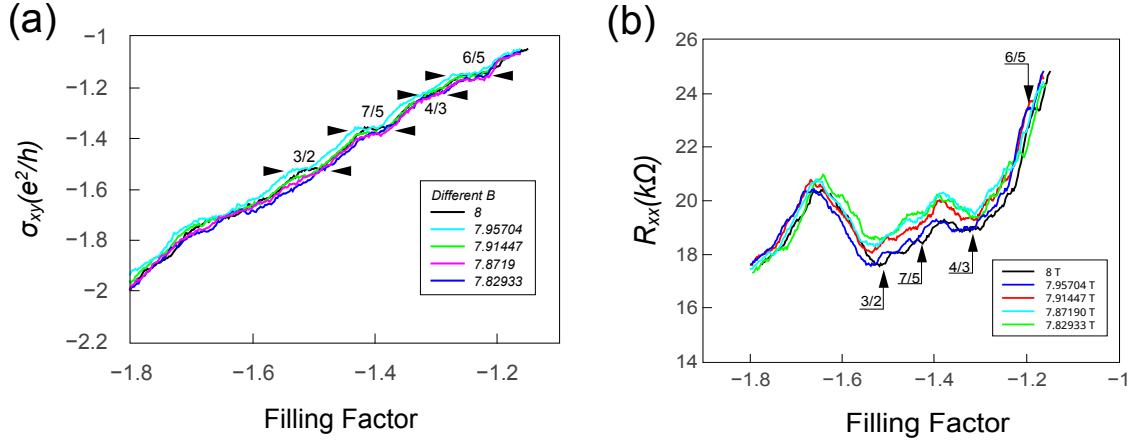


Figure 7.11: (a)  $\sigma_{xy}$  and (b)  $R_{xx}$  versus the Filling Factor at high  $B$  with FQH states numbers. Units of magnetic field is T.

From this figure, the order of energy gaps with different fractional filling factor can be estimated. The  $-3/2$  state disappear at the first when the  $B$  is lowered to 7.91447 T. Then the  $-7/5$  state disappear at  $B = 7.82933$  T while  $-6/5$  plateau is still there. This means the  $-3/2$  has the smallest gap and  $-6/5$  has the biggest gap while the gap size of  $-7/5$  is between these two. This order of sizes of energy gap is confirmed with Laughlin wave functions theory.

In Figure 7.11, both fractional plateaus and dips are in the right place. For example, in Figure 7.11 a, the plateaus will have the same filling factor and  $\sigma_{xy}$  (in units of  $e^2/h$ ).

Similar line traces are taken on the electron side in Figure 7.12. (a) and (b) shows the line trace of  $\sigma_{xy}$  with a large and small magnetic range. In (b), the plateaus of filling factor 1 and 2 are visible. When the data is zoom in between filling factor 0 and 1, the

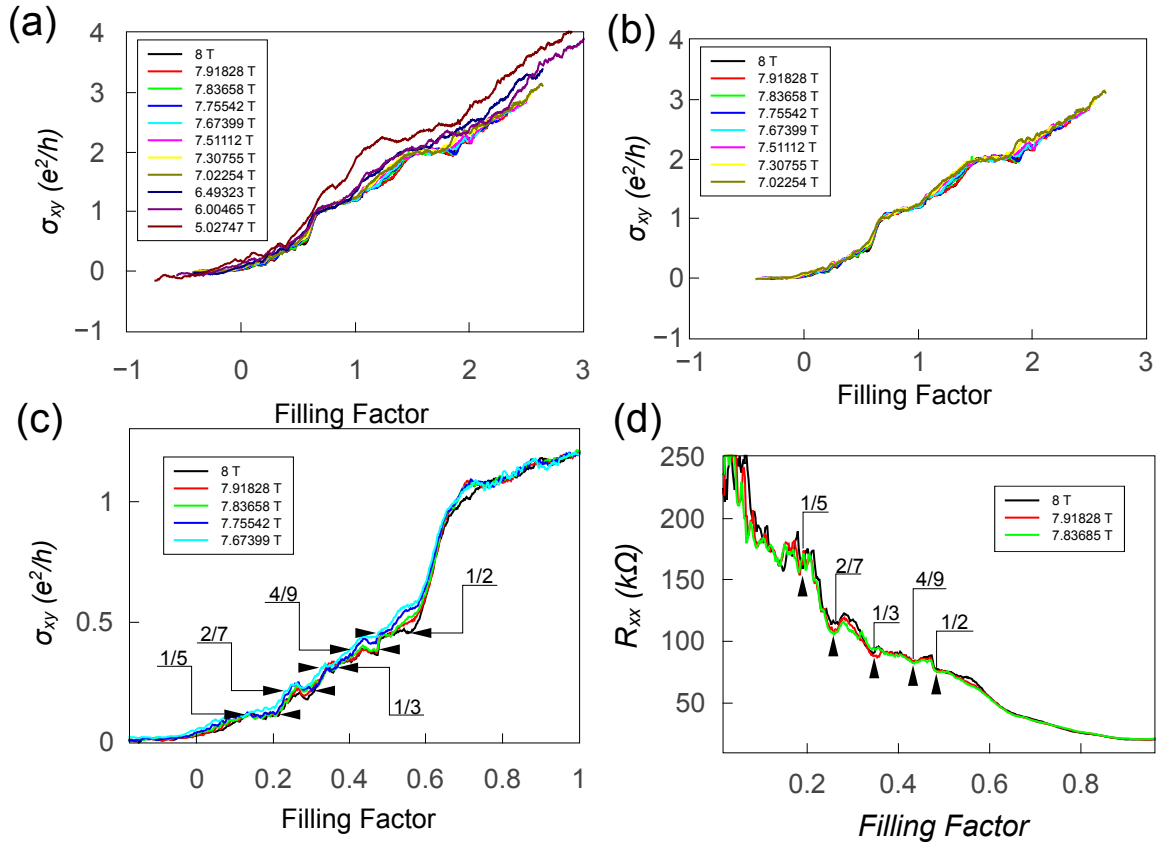


Figure 7.12: (a) and (b) shows the line trace of  $\sigma_{xy}$  with a large and small magnetic range. Zoomed-in data between filling factor 0 and 1 and the fractional plateaus are shown in figure (c) with filling factors. The dips in  $R_{xx}$  are shown in (d) with same filling factors like (c).

fractional plateaus are shown in figure (c) with filling factors. The dips in  $R_{xx}$  are shown in (d) with same filling factors like (c). The  $1/2$  FQH state is observed from the data.

## 7.5 FQHE by plotting $R_{xx}$ versus Filling Factor and Magnetic Field

Before we discuss the data, some theories about the odd and even denominator FQHE will be introduced.

At first, we introduce a model called the composite Fermion model for the FQHE [27] [28]. This model is based on the formation of composite particles (CP). The basic idea is there is 1 flux quantum for every available particle state in the Landau level. For example, for  $1/3$  quantum state, there are 3 times number of flux quantum of number of electrons. And for  $1/2$  quantum state, there are twice as many flux quanta as electrons. By adding the flux quanta, this model changes the complicated many-body electron system as a system of non-interacting CPs. In this theory's quantum statistics, an electron plus an even number of flux is a composite Fermion (CF), while an electron plus an odd number of flux is a composite Boson.

Now we try to explain the FQHE by using this Composite Fermion model. In the composite particle picture, the even denominator FQH state  $\nu = \frac{1}{2}$  is a ground state of independent CFs.

In Figure 7.13, electrons transform into composite fermions by capturing  $2m$  "flux quanta" of the external field. In (a), several electrons are under the external magnetic field  $B$ . In (b), which is the CP model's physics picture, the CPs are made by one electron and two flux quanta. And the effect magnetic field becomes  $B_{eff}$  which is  $B_{eff} = B - 2m\phi_0/A_0$  for each CP.  $A_0$  is the unit area and  $\phi_0$  is the flux quanta. In (c), 2CF is one electron two

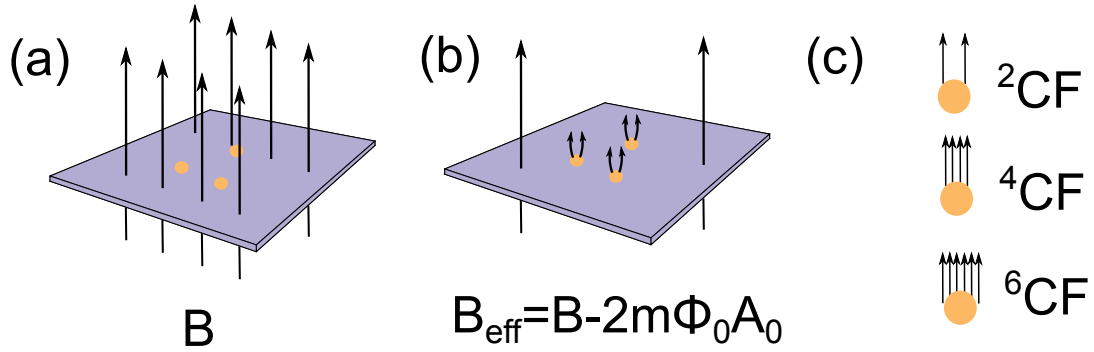


Figure 7.13: (a) Electrons under magnetic field  $B$ . (b) CPs under effective magnetic field  $B_{eff}$ . (c) Different CF with different quantum flux inside.

flux quanta ( $m=1$ ),  ${}^4\text{CF}$  is one electron four flux quanta ( $m=2$ ),  ${}^6\text{CF}$  is one electron six flux ( $m=3$ ) quanta and so on.

In this model, the FQH states are the IQH states for the CPs under a much smaller reduced effective magnetic field.

To understand this more easily, here we give the general condition restrict the FQHE with odd denominator fractional fillings,

$$\nu = \frac{p}{2mp \pm 1} \quad (7.6)$$

where  $m, p$  is integer.

So the  $\nu = \frac{1}{2}$  corresponds to a ground state of  $m=1$ . And the  $\nu = \frac{1}{3}$  equals to the  $p=1$  IQH state in equation 7.6. The  $\nu = \frac{2}{5}$  is the  $p=2$  IQH state in the CFs. From this physics picture,  $\nu = \frac{1}{3}$  and  $\nu = \frac{2}{3}$  are the particle-hole conjugate. So they obey the same physics. In this way, the theory can also explain why even denominator FQH states are more difficult to be observed [17].

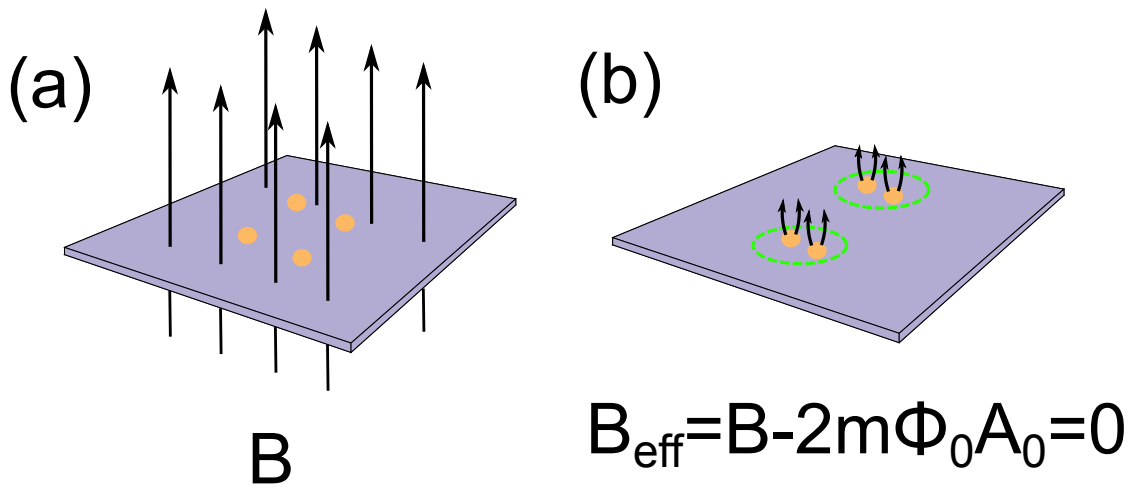


Figure 7.14: (a) Electrons under magnetic field  $B$ . (b) CFs under effective magnetic field  $B_{\text{eff}}$ . The CFs absorb all the magnetic field and give a zero effective field.

Speaking of the even denominator FQH state, it is first discovered by Willett *et al.* [69]. Extensive theoretical work indicated the even denominator state can be described by the Moore-Read Pfaffian wavefunction. This wavefunction describes a Laughlin wavefunction from a BCS-like pairing of composite Fermions (into quasi-Bosons). The physics picture of this model is shown in Figure 7.14. In this picture, CFs absorb interactions become the mass of composite fermions and two CFs combine together (green dashed line) become a quasi-Boson which may lead to BCS-like pair.

To see the fractional quantum hall states more clear, a color plot of  $R_{xx}$  with filling factor and magnetic field is given.

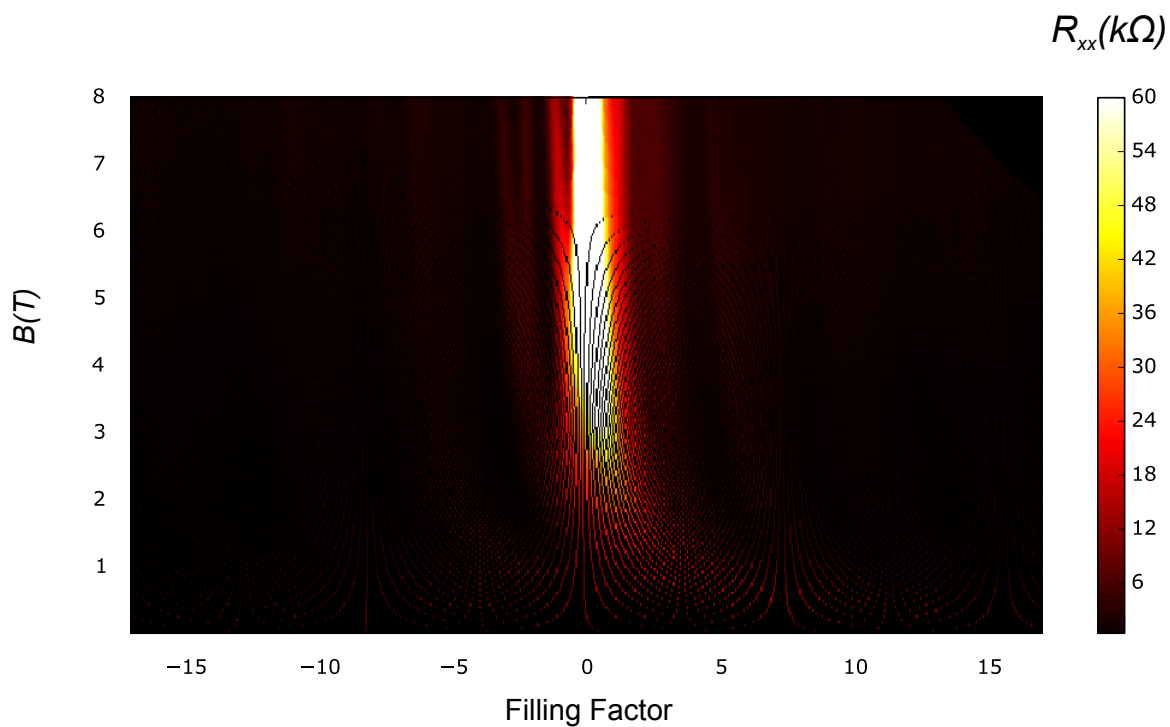


Figure 7.15: The color plot of  $R_{xx}$  with  $B$  and Filling Factor. Dark color is the gap and bright color is the peak of the  $R_{xx}$ . Every filling factor of 4, there is a big gap. And small symmetry-breaking gaps open at higher magnetic field.

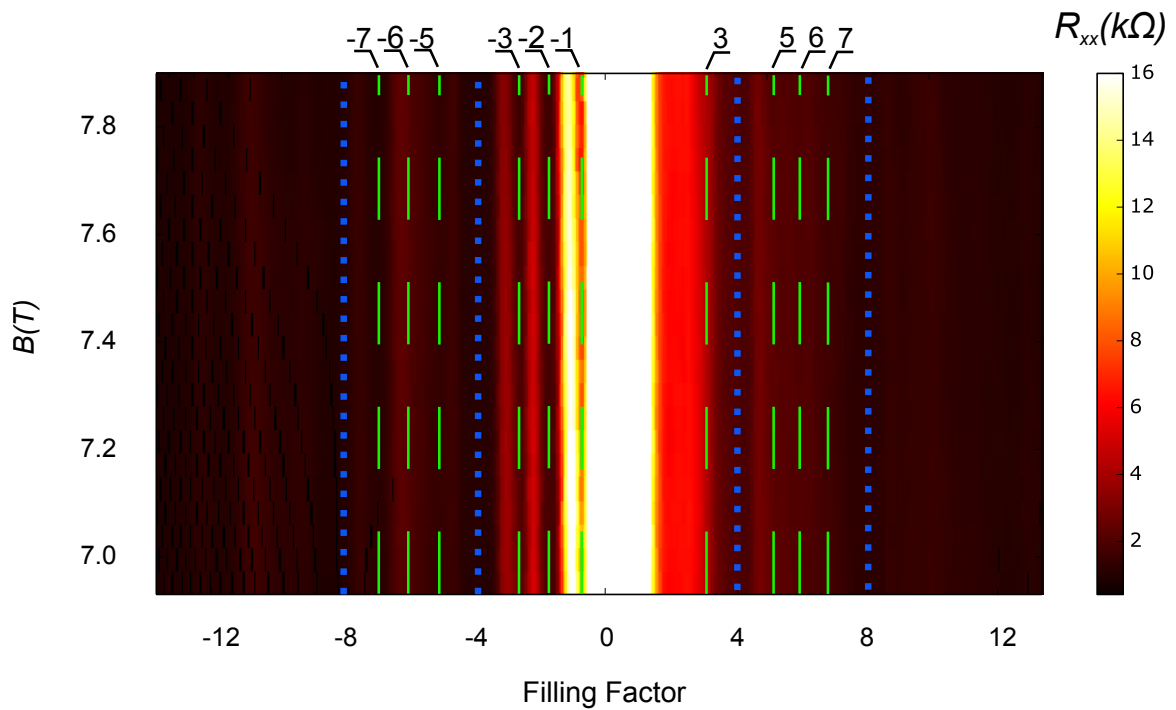


Figure 7.16: The color plot of  $R_{xx}$  at high magnetic field with Filling Factor. Every step of 4 in filling factor, there are big gaps. The filling factor of  $\pm 4$  and  $\pm 8$  are shown in blue dashed lines. Dashed green lines indicate the position of gaps with step of 1 in filling factor. The number of FF is shown on top of the figure. 1 and 2 are missing because of the color contract. The resistance is very high at around the Dirac point due to its high mobility.

In Figure 7.15, it shows a color plot of  $R_{xx}$  with  $B$  and filling factor. Dark color corresponds to the gap and bright color is the peak of the  $R_{xx}$ . Every filling factor change of 4, there is a big gap. And small gaps open at higher magnetic field.

Figure 7.16 shows a zoomed-in figure of Figure 7.15 at high magnetic field. The dark color is the gap and the bright color is the peak of the  $R_{xx}$ . Every step of 4 in filling factor, there are big gaps ( $\pm 4$ ,  $\pm 8$  and  $\pm 12$ ). The filling factor of  $\pm 4$  and  $\pm 8$  are shown in blue dashed lines. They are much bigger than the other gaps between  $-8$  and  $8$ . Dashed green lines indicate the position of gaps with a step of 1 in filling factor. The number of filling factor is shown on top of the figure. 1 and 2 are missing because of the color contrast. The resistance is super high and increase very fast at around the Dirac point due to its high mobility.

Then a slow scan has been taken in the small filling factor regions.

We focus on the electron side at first. Figure 7.17 shows the color plot of  $V_{xx}$  versus the filling factor and magnetic field above 6 T. The gap at filling factor 2 and 3 are very big and visible in dark color in Figure 7.17 (a). The gap of  $\nu = 1$  is the blue dashed line. Some black arrows on top of the figure show the possible FQH states. In this kind of figure, the FQH states should be a vertical feature. So some noises which shows a line feature with a slope will not be counted as a FQH state. Figure 7.17 (b) is a zoom in figure at high magnetic field and filling factor between 0 and 1. The green dashed line indicates the  $\nu = \frac{1}{3}$  state.  $\nu = \frac{1}{3}$  quantum state has the biggest gap except the IQH state between 0 and 1. This big gap has also been confirmed in this data. Except  $\nu = \frac{1}{3}$  gap, there are

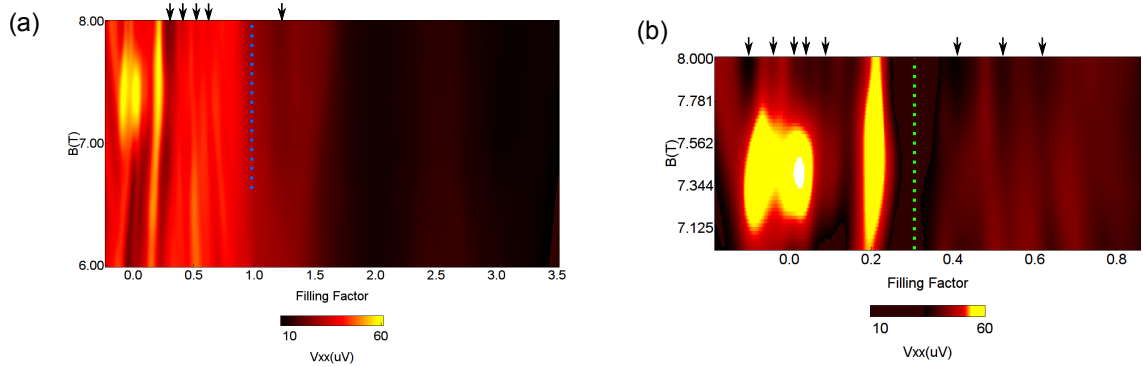


Figure 7.17: (a) The color plot of  $V_{xx}$  versus the filling factor and magnetic field above 6 T. (b) Zoom-in figure of (a). The green dashed line indicate the  $\nu = \frac{1}{3}$  state. Except  $\nu = \frac{1}{3}$  gap, there are several gaps (black arrows) in the figure.

several gaps (black arrows) in the figure. They are all vertical which means they could all be FQH states' gaps.

To confirm these possible FQH states, we plot a line trace of  $G_{xy}$  versus the filling factor also well as  $V_{xx}$  at the same time (Figure 7.18). The bottom figure is the color plot of  $V_{xx}$  versus the  $B$  and  $\nu$ . The fractional gaps are dark strips. The top figure is  $G_{xy}$  versus  $\nu$ . FQH states should be a plateau in this line trace. The dashed lines between two graphs are possible FQH states both shown as a dip in bottom figure and a plateau in top figure. At first, there are three clear fractional filling factor plateaus in the  $G_{xy}$  line trace. These ( $\nu = \frac{1}{3}$ ,  $\nu = \frac{1}{2}$ ,  $\nu = \frac{3}{5}$ ) states are connected to their concomitant gaps in the bottom figure with blue dashed lines and a red solid line indicate their plateaus. There are also some mini gaps and mini plateaus with their filling factors are marked with green lines, orange solid lines and orange numbers separately. At the  $G_{xy}$  line trace, each plateau (filling factor  $\nu$ ) also has the right quantum conductivity value ( $\nu e^2/h$ ).

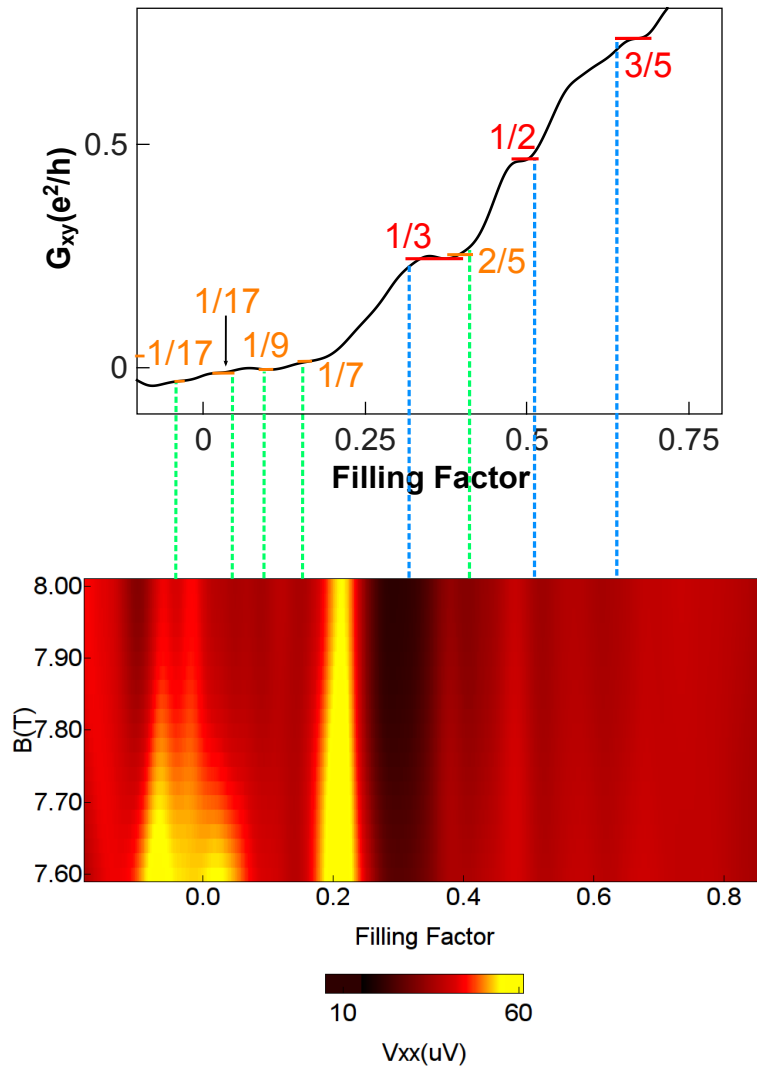


Figure 7.18: The top figure is  $G_{xy}$  versus  $\nu$ . The bottom figure is the color plot of  $V_{xx}$  versus the  $B$  and  $\nu$ . The FQH filling number is shown in figure. The red number is clear FQH states. The yellow numbers are some possible FQH states.

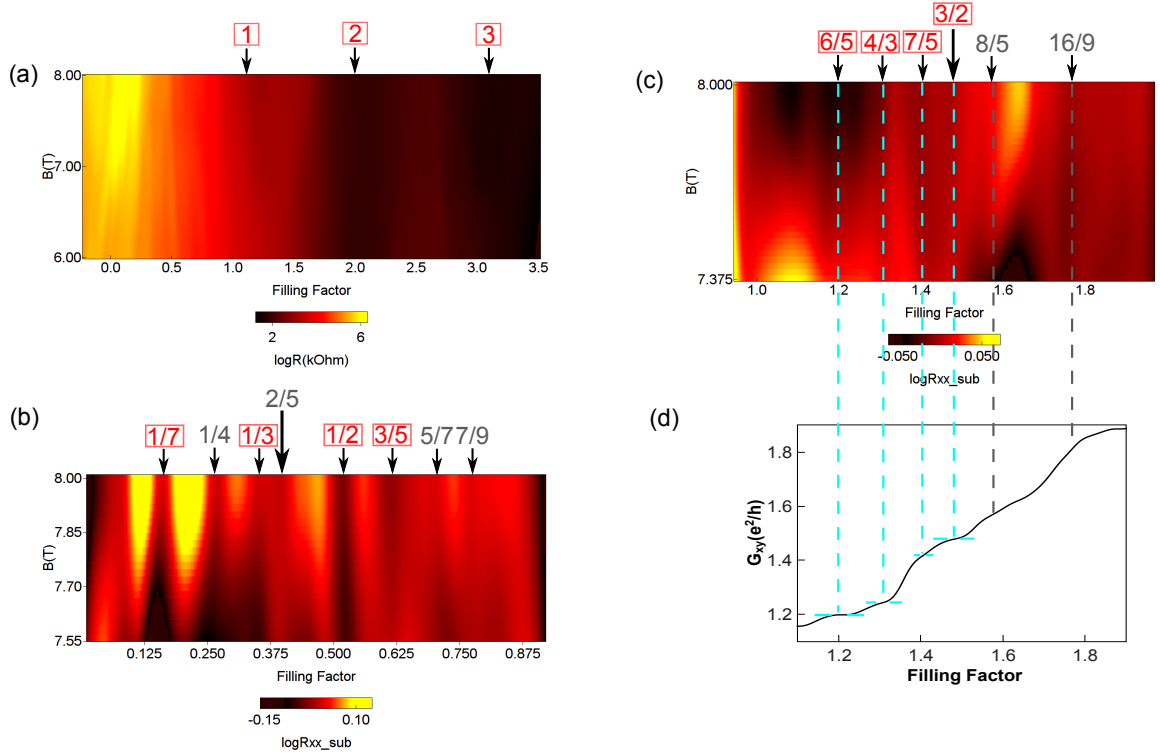


Figure 7.19: The color plot of  $\log R_{xx}$  (a) (b). And the FQH states between  $\nu = 1$  and  $\nu = 2$  shown in  $\log R_{xx}$  (c) and  $G_{xy}$  signals (d).

Also for the electron side, this time we focus on the longitudinal resistance  $R_{xx}$ . In Figure 7.19 (a),  $\log R_{xx}$  has been shown in a color plot with filling factor 0 to 4 and magnetic field 6 T to 8 T. The IQH states  $\nu = 1, 2, 3$  are shown with black arrows. In Figure 7.19 (b), it is a color plot of  $\log R_{xx}$  with the background subtraction. Clear gaps with a concomitant plateau in  $G_{xy}$  have been shown in red numbers, like  $\frac{1}{3}$ ,  $\frac{1}{2}$ ,  $\frac{1}{7}$ ,  $\frac{3}{5}$  and so on. Some other gaps are indicated with gray numbers. Figure (c) and (d) are the  $\log R_{xx}$  signal with background subtraction and line trace of  $G_{xy}$  in the range of filling factor between 1 and 2. The clear FQH states with dips in  $\log R_{xx}$  and plateaus in  $G_{xy}$  are pointed with red numbers. Other possible FQH states with clear dips but missing plateaus are pointed with gray numbers.

Figure 7.20 shows the color plot of  $\log R_{xx}$  with magnetic field and filling factor. In (a), the IQH states' gaps are visible.  $\nu = -4$  has the largest gap, then  $\nu = -2$  has the second largest gap,  $\nu = -3$  and  $\nu = -1$  has the third largest and smallest gap in these IQH states. (b) is the zoom-in figure with  $\nu$  is from -1 to 0. The data plotted is  $\log R_{xx}$  subtract the background signal. Some FQH states are visible. The  $\nu = -\frac{2}{3}$  has a visible large gap in the data. The gaps of  $\nu = -\frac{7}{9}$ ,  $\nu = -\frac{1}{2}$ ,  $\nu = -\frac{1}{3}$  and  $\nu = -\frac{1}{4}$  are also visible. (c) shows the same figure but different range ( $\nu = -2$  to  $\nu = -1$ ) like (b). Some vertical features may indicate the FQH states' gaps.  $\nu = -\frac{5}{3}$ ,  $\nu = -\frac{8}{5}$  and  $\nu = -\frac{4}{3}$  are strong. Some other gaps like  $\nu = -\frac{9}{5}$  and  $\nu = -\frac{3}{2}$  are also there. In (d), the range of  $\nu$  is -3 to -2. There are possible FQH states like  $\nu = -\frac{14}{5}$  and  $\nu = -\frac{7}{3}$ .

Figure 7.21 shows the same figures of (b) and (c) from Figure 7.19 with a concomitant  $G_{xy}$  versus  $\nu$  line trace plots. The FQH states with filling factor  $\nu = -\frac{7}{9}$ ,  $\nu = -\frac{2}{3}$ ,  $\nu = -\frac{5}{3}$ ,  $\nu = -\frac{8}{5}$  and  $\nu = -\frac{4}{3}$  have the concomitant plateaus in the transverse conductivity figures.  $\nu = -\frac{9}{5}$  and  $\nu = -\frac{3}{2}$  states possible have the transverse conductivity plateaus. However, the  $\nu = -\frac{1}{2}$ ,  $\nu = -\frac{1}{3}$  and  $\nu = -\frac{1}{4}$  can only observe gaps but no plateaus.

## 7.6 Conclusion

In conclusion, we have observed several FQH states in a high mobility bilayer graphene device, including several even denominator FQH states, like  $\frac{1}{2}$ . It is first time to observe an even denominator fractional quantum hall state at an encapsulated bilayer graphene sample.

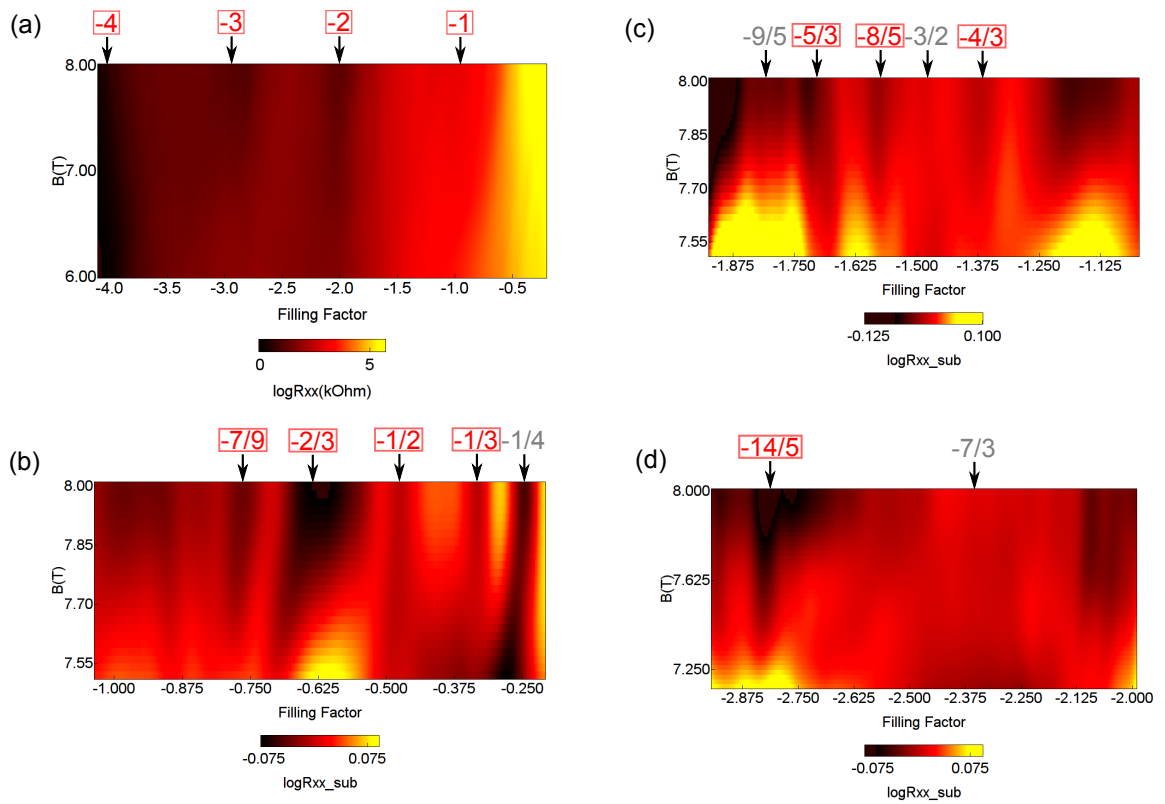


Figure 7.20: (a) The color plot of  $\log R_{xx}$  at the hole side ( $\nu$  from -4 to 0). (b) to (d) are plots of  $\log R_{xx}$  subtract the background within different ranges.

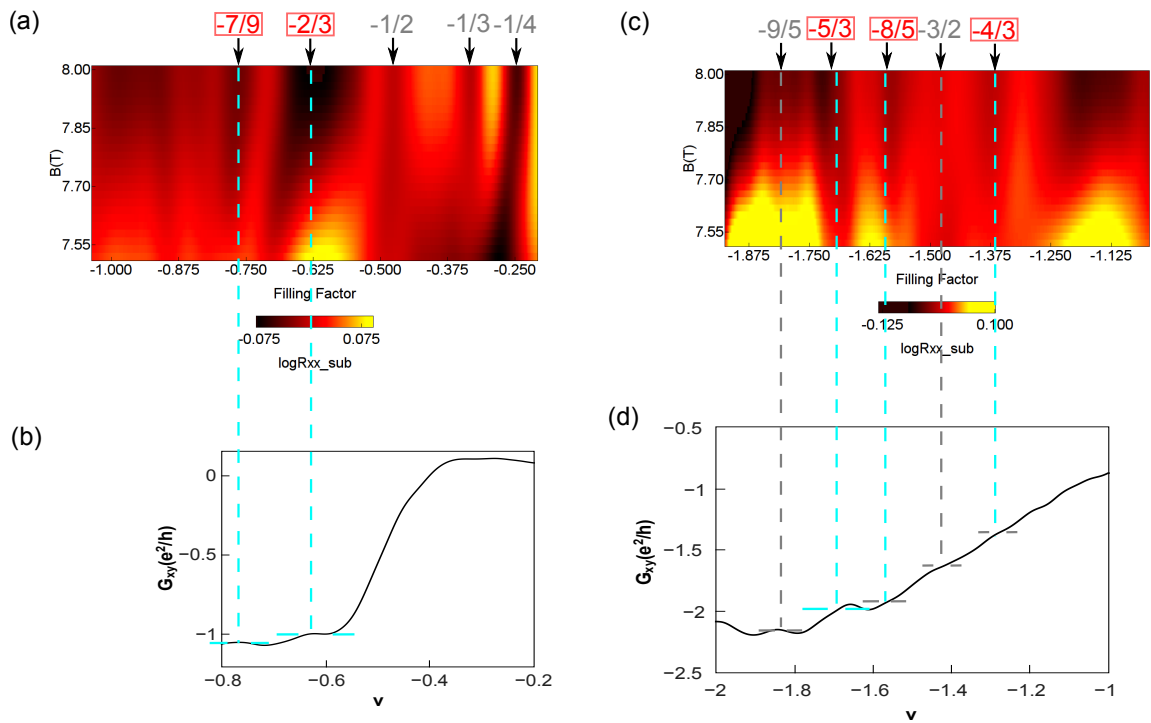


Figure 7.21: The color plot of  $\log R_{xx}$  with a subtracted background (a,c) and the concomitant  $G_{xy}$  versus  $\nu$  (b,d).

This bilayer graphene mobility (1 million  $\text{cm}^2\text{V}^{-1}\text{s}^{-1}$ ) reaches the highest mobility has been reported in graphene devices before. Some other measurements' results also show it is a high quality sample which makes it possible to observe FQH states at low magnetic fields (up to 8 T).

The observed FQH states in this experiment is shown in Table 7.6. According to the composite Fermions theory (equation 7.6),

ground state	$\frac{1}{2}$	p=1	p=2	p=3
m=1		$\frac{1}{3}$	$\frac{2}{5}$	$\frac{3}{5}$
m=2		$\frac{1}{5}$	$\frac{2}{9}, \frac{2}{7}$	
m=3		$\frac{1}{7}$		
m=4		$\frac{1}{9}$		
m=16		$\frac{1}{17}$		

## Chapter 8

# Conclusions

In this thesis, we studied the low temperature transport in graphene itself and its heterostructures. In graphene under one dimensional periodic potentials, electron collimation and extra Dirac points are studied. We also studied the transport in trilayer graphene aligned with BN. The Hofstadter butterfly and the Landau levels transitions are carefully analyzed. The third part of work is transport study in strained graphene. The experiment results give the evidence of the pseudo magnetic field. The next work is about the hetero-structure of black phosphorus (BP) and graphene. Some interesting anisotropic transport behaviours are introduced from BP to graphene. At the end, an ultra clean bilayer graphene device is reported. In this device, we observe fractional quantum hall effects. The even denominator fractional quantum hall state will be reported first time in an encapsulated bilayer graphene sample.

# Bibliography

- [1] Susan J. Angus. Gate defined quantum dots in intrinsic silicon. *NanoLetter*, 7:2051, 2007.
- [2] A.F.Young B. Hunt, J.D.Sanchez Yamagishi. Massive dirac fermions and hofstadter butterfly in a van der waals heterostructure. *Science*, 340:1427, 2013.
- [3] Felix Bloch. Über die quantenmechanik der elektronen in kristallgittern. *Zeitschrift für physik*, 52(7-8):555–600, 1929.
- [4] Kirill I Bolotin, Fereshte Ghahari, Michael D Shulman, Horst L Stormer, and Philip Kim. Observation of the fractional quantum hall effect in graphene. *Nature*, 462(7270):196–199, 2009.
- [5] J. Hone C. R. Dean. Boron nitride substrates for high quality graphene electronics. *Nature Nanotechnology*, 5:722, 2010.
- [6] P. Kim C. R. Dean. Hofstadters butterfly and the fractal quantum hall effect in moire superlattices. *Nature*, 497:598, 2013.
- [7] Yongqing Cai, Gang Zhang, and Yong-Wei Zhang. Electronic properties of phosphorene/graphene and phosphorene/hexagonal boron nitride heterostructures. *The Journal of Physical Chemistry C*, 119(24):13929–13936, 2015.
- [8] Andres Castellanos-Gomez, Leonardo Vicarelli, Elsa Prada, Joshua O Island, KL Narasimha-Acharya, Sofya I Blanter, Dirk J Groenendijk, Michele Buscema, Gary A Steele, JV Alvarez, et al. Isolation and characterization of few-layer black phosphorus. *2D Materials*, 1(2):025001, 2014.
- [9] Steven G. Louie Cheol Hwan Park. Anisotropic behaviours of massless dirac fermions in graphene under periodic potentials. *Nature Physics*, 4:213, 2008.
- [10] Steven G. Louie Cheol Hwan Park. Electron beam supercollimation in graphene superlattices. *Nanoletter*, 8:2920, 2008.
- [11] Steven G. Louie Cheol Hwan Park. Landau levels and quantum hall effect in graphene superlattices. *PHYSICAL REVIEW LETTERS*, 103:046808, 2009.

- [12] Jesper Nygard David H. Cobden. Shell filling in closed single wall carbon nanotube quantum dots. *PHYSICAL REVIEW LETTERS*, 89:046803, 2002.
- [13] Cory R Dean, Andrea F Young, Inanc Meric, Chris Lee, Lei Wang, S Sorgenfrei, K Watanabe, T Taniguchi, P Kim, KL Shepard, et al. Boron nitride substrates for high-quality graphene electronics. *Nature nanotechnology*, 5(10):722–726, 2010.
- [14] CR Dean, L Wang, P Maher, C Forsythe, F Ghahari, Y Gao, J Katoch, M Ishigami, P Moon, M Koshino, et al. Hofstadter’s butterfly and the fractal quantum hall effect in moire superlattices. *Nature*, 497(7451):598–602, 2013.
- [15] CR Dean, AF Young, Pet Cadden-Zimansky, L Wang, H Ren, K Watanabe, T Taniguchi, P Kim, J Hone, and KL Shepard. Multicomponent fractional quantum hall effect in graphene. *Nature Physics*, 7(9):693–696, 2011.
- [16] Régis Decker, Yang Wang, Victor W Brar, William Regan, Hsin-Zon Tsai, Qiong Wu, William Gannett, Alex Zettl, and Michael F Crommie. Local electronic properties of graphene on a bn substrate via scanning tunneling microscopy. *Nano letters*, 11(6):2291–2295, 2011.
- [17] RR Du, HL Stormer, DC Tsui, LN Pfeiffer, and KW West. Experimental evidence for new particles in the fractional quantum hall effect. *Physical review letters*, 70(19):2944, 1993.
- [18] Xu Du, Ivan Skachko, Fabian Duerr, Adina Luican, and Eva Y Andrei. Fractional quantum hall effect and insulating phase of dirac electrons in graphene. *Nature*, 462(7270):192–195, 2009.
- [19] U. FANO. Effects of configuration interaction on intensities and phase shifts. *PHYSICAL REVIEW LETTERS*, 124:1866, 1961.
- [20] Nathaniel Gillgren, Darshana Wickramaratne, Yanmeng Shi, Tim Espiritu, Jiawei Yang, Jin Hu, Jiang Wei, Xue Liu, Zhiqiang Mao, Kenji Watanabe, et al. Gate tunable quantum oscillations in air-stable and high mobility few-layer phosphorene heterostructures. *2D Materials*, 2(1):011001, 2014.
- [21] F Guinea, MI Katsnelson, and AK Geim. Energy gaps and a zero-field quantum hall effect in graphene by strain engineering. *Nature Physics*, 6(1):30–33, 2010.
- [22] Si-ping Han, Hareem T Maune, Robert D Barish, Marc Bockrath, and William A Goddard III. Dna-linker-induced surface assembly of ultra dense parallel single walled carbon nanotube arrays. *Nano letters*, 12(3):1129–1135, 2012.
- [23] Philip George Harper. Single band motion of conduction electrons in a uniform magnetic field. *Proceedings of the Physical Society. Section A*, 68(10):874, 1955.
- [24] Douglas R Hofstadter. Energy levels and wave functions of bloch electrons in rational and irrational magnetic fields. *Physical review B*, 14(6):2239, 1976.

- [25] B Hunt, JD Sanchez-Yamagishi, AF Young, M Yankowitz, Brian J LeRoy, K Watanabe, T Taniguchi, P Moon, M Koshino, P Jarillo-Herrero, et al. Massive dirac fermions and hofstadter butterfly in a van der waals heterostructure. *Science*, 340(6139):1427–1430, 2013.
- [26] K. Ensslin J. Guttinger. Spin states in graphene quantum dots. *PHYSICAL REVIEW LETTERS*, 105:116801, 2010.
- [27] Jainendra K Jain. Composite-fermion approach for the fractional quantum hall effect. *Physical review letters*, 63(2):199, 1989.
- [28] JK Jain. Theory of the fractional quantum hall effect. *Physical Review B*, 41(11):7653, 1990.
- [29] David Goldhaber Gordon Kathryn Todd. Quantum dot behavior in graphene nanoconstrictions. *NanoLetter*, 6:416, 2009.
- [30] Dong-Keun Ki, Vladimir I Falko, Dmitry A Abanin, and Alberto F Morpurgo. Observation of even denominator fractional quantum hall effect in suspended bilayer graphene. *Nano letters*, 14(4):2135–2139, 2014.
- [31] Nikolai N Klimov, Suyong Jung, Shuze Zhu, Teng Li, C Alan Wright, Santiago D Solares, David B Newell, Nikolai B Zhitenev, and Joseph A Stroscio. Electromechanical properties of graphene drumheads. *Science*, 336(6088):1557–1561, 2012.
- [32] Mikito Koshino and Edward McCann. Gate-induced interlayer asymmetry in ab-stacked trilayer graphene. *Physical Review B*, 79(12):125443, 2009.
- [33] A. K. Geim L. A. Ponomarenko. Chaotic dirac billiard in graphene quantum dots. *Science*, 320:356, 2008.
- [34] A. K. Geim L. A. Ponomarenko. Cloning of dirac fermions in graphene superlattices. *Nature*, 497:594, 2013.
- [35] LD Landau. Diamagnetismus der metalle. *Zeitschrift für Physik*, 64(9-10):629–637, 1930.
- [36] Robert B Laughlin. Anomalous quantum hall effect: an incompressible quantum fluid with fractionally charged excitations. *Physical Review Letters*, 50(18):1395, 1983.
- [37] Kayoung Lee, Babak Fallahazad, Jiamin Xue, David C Dillen, Kyoungwan Kim, Takashi Taniguchi, Kenji Watanabe, and Emanuel Tutuc. Chemical potential and quantum hall ferromagnetism in bilayer graphene. *Science*, 345(6192):58–61, 2014.
- [38] N Levy, SA Burke, KL Meaker, M Panlasigui, A Zettl, F Guinea, AH Castro Neto, and MF Crommie. Strain-induced pseudo-magnetic fields greater than 300 tesla in graphene nanobubbles. *Science*, 329(5991):544–547, 2010.

- [39] Likai Li, Fangyuan Yang, Guo Jun Ye, Zuocheng Zhang, Kenji Watanabe, Takashi Taniguchi, Yayu Wang, Xian Hui Chen, and Yuanbo Zhang. Quantum hall effect in black phosphorus two-dimensional electron gas. *arXiv preprint arXiv:1504.07155*, 2015.
- [40] Likai Li, Guo Jun Ye, Vy Tran, Ruixiang Fei, Guorui Chen, Huichao Wang, Jian Wang, Kenji Watanabe, Takashi Taniguchi, Li Yang, et al. Quantum oscillations in a two-dimensional electron gas in black phosphorus thin films. *Nature nanotechnology*, 10(7):608–613, 2015.
- [41] Likai Li, Yijun Yu, Guo Jun Ye, Qingqin Ge, Xuedong Ou, Hua Wu, Donglai Feng, Xian Hui Chen, and Yuanbo Zhang. Black phosphorus field-effect transistors. *Nature nanotechnology*, 9(5):372–377, 2014.
- [42] Han Liu, Adam T Neal, Zhen Zhu, Zhe Luo, Xianfan Xu, David Tománek, and Peide D Ye. Phosphorene: an unexplored 2d semiconductor with a high hole mobility. *ACS nano*, 8(4):4033–4041, 2014.
- [43] Zhiwen Shi Long Ju. Topological valley transport at bilayer graphene domain walls. *Nature*, 520:650, 2015.
- [44] AH MacDonald. Landau-level subband structure of electrons on a square lattice. *Physical Review B*, 28(12):6713, 1983.
- [45] Patrick Maher, Lei Wang, Yuanda Gao, Carlos Forsythe, Takashi Taniguchi, Kenji Watanabe, Dmitry Abanin, Zlatko Papić, Paul Cadden-Zimansky, James Hone, et al. Tunable fractional quantum hall phases in bilayer graphene. *Science*, 345(6192):61–64, 2014.
- [46] Paul L. McEuen Marc Bockrath. Single electron transport in ropes of carbon nanotubes. *Science*, 275:1922, 1997.
- [47] Hareem T Maune, Si-ping Han, Robert D Barish, Marc Bockrath, William A Goddard III, Paul WK Rothemund, and Erik Winfree. Self-assembly of carbon nanotubes into two-dimensional geometries using dna origami templates. *Nature nanotechnology*, 5(1):61–66, 2010.
- [48] Edward McCann and Vladimir I Falko. Landau-level degeneracy and quantum hall effect in a graphite bilayer. *Physical Review Letters*, 96(8):086805, 2006.
- [49] Artem Mishchenko, Yang Cao, GL Yu, Colin R Woods, Roman Vladislavovich Gorbachev, Konstantin S Novoselov, Andre K Geim, and Leonid S Levitov. Nonlocal response and anamorphosis: The case of few-layer black phosphorus. *Nano Letters*, 15(10):6991–6995, 2015.
- [50] AH Castro Neto, F Guinea, NMR Peres, Kostya S Novoselov, and Andre K Geim. The electronic properties of graphene. *Reviews of modern physics*, 81(1):109, 2009.

- [51] K. S. Novoselov, A. K. Geim, S. V. Morozov, D. Jiang, Y. Zhang, S. V. Dubonos, I. V. Grigorieva, and A. A. Firsov. Electric field effect in atomically thin carbon films. *Science*, 306(5696):666–669, 2004.
- [52] Kostya S Novoselov, Andre K Geim, SV Morozov, D Jiang, Y\_ Zhang, SV Dubonos, , IV Grigorieva, and AA Firsov. Electric field effect in atomically thin carbon films. *science*, 306(5696):666–669, 2004.
- [53] KS Novoselov, D Jiang, F Schedin, TJ Booth, VV Khotkevich, SV Morozov, and AK Geim. Two-dimensional atomic crystals. *Proceedings of the National Academy of Sciences of the United States of America*, 102(30):10451–10453, 2005.
- [54] JE Padilha, A Fazzio, and Antônio JR da Silva. Van der waals heterostructure of phosphorene and graphene: Tuning the schottky barrier and doping by electrostatic gating. *Physical review letters*, 114(6):066803, 2015.
- [55] Cheol-Hwan Park, Li Yang, Young-Woo Son, Marvin L Cohen, and Steven G Louie. New generation of massless dirac fermions in graphene under external periodic potentials. *Physical review letters*, 101(12):126804, 2008.
- [56] LA Ponomarenko, RV Gorbachev, GL Yu, DC Elias, R Jalil, AA Patel, A Mishchenko, AS Mayorov, CR Woods, JR Wallbank, et al. Cloning of dirac fermions in graphene superlattices. *Nature*, 497(7451):594–597, 2013.
- [57] Frank Schwierz. Graphene transistors. *Nature nanotechnology*, 5(7):487–496, 2010.
- [58] Keun-Young Shin, Jin-Yong Hong, and Jyongsik Jang. Flexible and transparent graphene films as acoustic actuator electrodes using inkjet printing. *Chem. Commun.*, 47(30):8527–8529, 2011.
- [59] Pooja Srivastava, KPSS Hembram, Hiroshi Mizuseki, Kwang-Ryeol Lee, Sang Soo Han, and Seungchul Kim. Tuning the electronic and magnetic properties of phosphorene by vacancies and adatoms. *The Journal of Physical Chemistry C*, 119(12):6530–6538, 2015.
- [60] Brian Standley, Wenzhong Bao, Hang Zhang, Jehoshua Bruck, Chun Ning Lau, and Marc Bockrath. Graphene-based atomic-scale switches. *Nano letters*, 8(10):3345–3349, 2008.
- [61] Thiti Taychatanapat, Kenji Watanabe, Takashi Taniguchi, and Pablo Jarillo-Herrero. Quantum hall effect and landau-level crossing of dirac fermions in trilayer graphene. *Nature Physics*, 7(8):621–625, 2011.
- [62] Takashi Taniguchi Thiti Taychatanapat, Kenji Watanabe<sup>3</sup> and Pablo Jarillo-Herrero. Electrically tunable transverse magnetic focusing in graphene. *Nature Physics*, 9:225, 2013.
- [63] Daniel C Tsui, Horst L Stormer, and Arthur C Gossard. Two-dimensional magneto-transport in the extreme quantum limit. *Physical Review Letters*, 48(22):1559, 1982.

- [64] Klaus von Klitzing. The quantized hall effect. *Reviews of Modern Physics*, 58(3):519, 1986.
- [65] Philip Richard Wallace. The band theory of graphite. *Physical Review*, 71(9):622, 1947.
- [66] L Wang, I Meric, PY Huang, Q Gao, Y Gao, H Tran, T Taniguchi, K Watanabe, LM Campos, DA Muller, et al. One-dimensional electrical contact to a two-dimensional material. *Science*, 342(6158):614–617, 2013.
- [67] Peng Wang, Bin Cheng, Oleg Martynov, Tengfei Miao, Lei Jing, Takashi Taniguchi, Kenji Watanabe, Vivek Aji, Chun Ning Lau, and Marc Bockrath. Topological winding number change and broken inversion symmetry in a hofstadters butterfly. *Nano Letters*, 15(10):6395–6399, 2015.
- [68] GH Wannier. A result not dependent on rationality for bloch electrons in a magnetic field. *physica status solidi (b)*, 88(2):757–765, 1978.
- [69] R Willett, JP Eisenstein, HL Störmer, DC Tsui, AC Gossard, and JH English. Observation of an even-denominator quantum number in the fractional quantum hall effect. *Physical review letters*, 59(15):1776, 1987.
- [70] CR Woods, L Britnell, A Eckmann, RS Ma, JC Lu, HM Guo, X Lin, GL Yu, Y Cao, RV Gorbachev, et al. Commensurate-incommensurate transition in graphene on hexagonal boron nitride. *Nature physics*, 10(6):451–456, 2014.
- [71] Yuanbo Zhang, Yan-Wen Tan, Horst L Stormer, and Philip Kim. Experimental observation of the quantum hall effect and berry’s phase in graphene. *Nature*, 438(7065):201–204, 2005.
- [72] K Zou, Fan Zhang, C Clapp, AH MacDonald, and J Zhu. Transport studies of dual-gated abc and aba trilayer graphene: band gap opening and band structure tuning in very large perpendicular electric fields. *Nano letters*, 13(2):369–373, 2013.